Internal mixing processes in massive stars: uncertainties and impact

Etienne Kaiser

Doctor of Philosophy

School of Physics and Chemical Sciences, Keele University

October 2022

Abstract

Massive stars are key contributors to the evolution of galaxies and many observed phenomena. Therefore, understanding them is crucial to explain the evolution of the Universe and its constituents. The evolution of massive stars is strongly influenced by internal mixing processes. In stellar evolution theory, these processes are simplified due to the assumption of spherical symmetry. This introduces many uncertainties. In this Thesis, I investigate two groups of internal mixing processes in massive stars: turbulent convection and rotation-induced mixing. The study focusses on convective boundary mixing and angular momentum transport. Concerning convective boundary mixing, I study how the location of the convective boundary and different amounts of convective boundary mixing affects the structure and evolution of massive stars. I find an uncertainty of up to $\sim$ 70% in the prediction of core masses at core helium depletion. Furthermore, the surface evolution of massive stars depends critically on the mixing choices. Comparison between model predictions and observations suggests that models require a larger amount of convective boundary mixing than currently adopted in the literature. Concerning angular momentum transport, I investigate angular momentum transport by rotation-induced instabilities and two different magnetic dynamos and how it is affected by related theoretical and implementation uncertainties. The three sets of models predict distinct ranges of the core rotation rate at core collapse. However, the strength and timing of angular momentum transport depends strongly on the transport mechanism and its uncertainty. Generally, the main transport of angular momentum occurs before core helium ignition and nearly no angular momentum is transported after core oxygen ignition. This Thesis shows that the evolution of massive stars is strongly influenced by the uncertainties linked to convective boundary mixing and rotation-induced mixing and more work is needed to provide reliable predictions for stellar evolution.

Acknowledgements

Science is never done alone and same goes for this Thesis. I could never have completed this dissertation without the advice, help and collaboration of many scientists and friends. I want to express my gratitude to all those who supported me. In particular, I want to thank my supervisor, mentor and Swiss friend Raphael Hirschi for his support, patience and the opportunities he created for me to grow as a scientist. I am grateful to the members of the NuGrid collaboration, the team at the Geneva Observatory, Chris Belczynski, Zsolt Keszthelyi, Dave Arnett with whom I had many interesting discussions, scientific and non-scientific. I also want to thank my family and the family Humphreys for their support, in particular Sophie Humphreys. I could have never done it without you.

Table of Contents

List of Figures

List of Tables

Chapter I

Introduction To Massive Stars

The understanding of massive stars is key to many aspects of astronomy, such as the evolution of galaxies, nucleosynthesis, supernovae, neutron stars, black holes, gravitational waves and other exotic objects. In this Chapter, an overview of the evolution and death of massive stars is given, setting the stage for this thesis. First, the life of non-rotating stars is discussed with a focus on the internal evolution and nucleosynthesis, followed by a brief summary of stellar winds and mass loss from massive stars. Then, the diversity of the final fates of massive stars is presented and two scenarios, the core-collapse and pair-instability supernova, are explored in more detail. Finally, the evolution of rotating massive stars is reviewed. In the last Section, the motivation and organisation of this work are outlined.

1 Why Study Massive Stars?

Since ancient times humans have been intrigued about their surroundings and wondered about the origin of life. This curiosity led them to eventually look into the sky and study the different stellar objects. While the path to life is complicated, it is currently thought that some of the building blocks used to form life are made in stars. In addition to the origin of life, human kind also depends on our neighbouring star, the Sun, because it enables life on the Earth and we depend on its radiated energy, hence, it is important to know what will happen to the Sun in the future.

A star is a gaseous cloud bound by its own gravity, which induces enough pressure in the central region to heat it up to temperatures where thermonuclear reactions can occur. Stars are nuclear reactors that synthesise new elements from old ones via fusion and other processes, thus slowly changing the matter they are made of. If the stars are able to return the newly synthesised material into the

galaxy, they actively contribute to the chemical evolution of the galaxy. This, for example, facilitates the formation of planets such as the Earth on which new life can form.

Stars are nuclear laboratories with extremely high temperatures and pressures. This enables scientists to test many different areas of physics under extreme conditions, such as nuclear physics, particle physics, thermodynamics, hydrodynamics and classical mechanics. Some stars even form very compact objects that become a test-bed for relativistic and quantum mechanics.

Massive stars are defined as stars with masses of at least eight times the mass of the Sun, $M \gtrsim 8\,\mathrm{M}_\odot$[1] (Smartt et al., 2009). Following the Harvard spectral classification, massive stars are classified as O and early B-type stars. Contrary to the Sun and other lower mass stars, which have a very long and calm life, massive stars have relatively short lifetimes. For example, on the main sequence[2], where stars spend most of their lives, massive stars have surface temperatures higher than $10,000\,\mathrm{K}$ whereas the Sun has a surface temperature of $\sim 5,800\,\mathrm{K}$.

Massive stars play a key role in the evolution of galaxies: They are fundamental for the production of heavy elements up to an atomic mass number of ~ 90 (Woosley et al., 2002) and they dominate the luminosity of stellar systems. The feedback from massive stars into the interstellar medium occurs via intense stellar winds, radiation and through their explosive deaths. Most massive stars end their lives as a supernova, one of the most powerful explosions in the universe. After their death they might leave behind a compact remnant, either a neutron star or a black hole, hence, they are the progenitor of compact objects and gravitational waves. Also, other energetic phenomena such as long gamma-ray bursts[3] are thought to originate from supernovae of stars in this mass range (Woosley & Bloom, 2006). Massive stars can trigger star formation activity via their strong radiation (Getman et al., 2009) and through their winds and supernova events (Preibisch & Zinnecker, 2007). The first generation of massive stars are thought to be the main driver of the reionisation of the Universe (Bromm & Larson, 2004; Sobral et al., 2015).

The evolution of massive stars, and all stars in general, is strongly affected by internal mixing processes. Thermally-driven turbulent convective mixing is often correlated with a nuclear burning region. Convection can provide more fuel into the burning region, prolonging the lifetime of a star. Also, it is one of the dominant energy transport processes, it mixes the interior and rearranges the structure of the star, for example by increasing the core masses. This will change the outcome of the star's later evolution, influence the way the star meets its end and the remnant, if any, that will be left after the catastrophic death. On the other hand, rotation-induced mixing can happen in any region of the star. Similar to thermally-driven mixing processes, it mixes the matter and changes the structure in

[1] One solar mass $\mathrm{M}_\odot$ is $1.99 \times 10^{30}\,\mathrm{kg}$. Solar values are generally indicated with the index $\odot$.

[2] The main sequence is a prominent band in the colour versus absolute magnitude diagram, or surface temperature versus luminosity diagram, of observed stars.

[3] Gamma-ray bursts are extremely energetic explosions that are thought to be generated during the collapse of rapidly rotating massive stars, see Section I.4. Their duration is of the order of seconds to minutes but they produce as much energy as the Sun during its entire existence.

stars, which prolongs the lifetime of each evolutionary stage and influences the way the star evolves. Both types of mixing consist of an ensemble of different processes. While a vast development has been made in the understanding of these processes, there are still a lot of open questions, inconsistencies and uncertainties.

In this work, some uncertainties from thermally-driven and rotation-induced mixing processes are investigated, specified and their implications for stellar evolution are explored. Furthermore, the aspects of the mixing processes leading to the largest uncertainties in the stellar model predictions are highlighted. Assessing the impact of the mixing uncertainties on the evolution of stars is an important step in several ways. Currently, there are many different published stellar evolution model grids that predict various outcomes. Knowing the uncertainties from the mixing processes and the different implementations allows for a better comparison of the grids and their reliability. Also, the knowledge of the uncertainties guides the path to improve the theory of mixing processes as it highlights which treatments need most improving and which are negligible. This also indicates the phases where multi-dimensional simulations are needed in order to better understand the operating processes. Last, but not least, specifying the uncertainties provides studies that use stellar evolution grids, for example galactic chemical evolution simulations, with necessary uncertainty for stellar model predictions.

2 The Evolution of Massive Stars

Stellar evolution is the process by which a star changes its structure and chemical composition over time through physical processes, including the interplay between nuclear reactions, gravity and energy transport mechanisms. The lifetime of a star is far too long for a human to observe and most changes occur on timescales too long to be detected. Therefore, in attempting to understand the physics of stars and their changes over time, scientists observe numerous stars at various points of their evolution. In parallel, they simulate the stellar structure using computed models, adding together the diverse features into one full model and compare the outcome with observations.

The evolution of massive stars can be crudely associated with three parameters - mass M, metallicity Z[4] and rotation rate Ω (e.g. Woosley et al., 2002; Maeder & Meynet, 2012). Binarity also plays an important role in the evolution of massive stars, see Section I.5, but in this thesis the focus will be on single stars.

Massive stars originate from cold dense clumps, with typical masses of $100-1000$ $M_\odot$ and temperatures of $10-20$ K inside giant molecular clouds (Zinnecker & Yorke, 2007). Gravitational instabilities or shock waves, for example by a nearby supernova, can trigger the collapse of such interstellar clouds into proto-stars. During proto-star evolution, the gas is opaque and the released gravitational energy is

[4] In an astrophysical context, the notion of metal applies to all elements heavier than helium.

kept inside, heating up the gas. This phase is accompanied by an accretion disc and bipolar outflows of matter. Thus, the star does not keep all the accreted mass but some is lost via the outflows. Once the star reaches the pre-main sequence, the contraction proceeds on the slower Kelvin-Helmholtz timescale and the gravitational energy released is roughly of the same order of magnitude as the energy radiated from the surface.

The evolution of a massive star begins when the energy generation due to thermonuclear burning processes opposes the gravitational contraction; the star is then said to be in hydrostatic equilibrium. The energy generation is a consequence of the increasing temperature and pressure in the central region of the star, allowing nuclear fusion and fission. Consequently, the composition slowly changes and the star evolves. Massive stars go through several burning phases, generally in a hydrostatic fashion, namely hydrogen-, helium-, carbon-, neon-, oxygen- and silicon burning. After silicon burning, the nuclear burning cannot provide the energy to keep a massive star in a hydrostatic balance. Therefore, the iron core formed during silicon burning gravitationally collapses, forming a compact object. If the iron core was not too massive, the additional infalling matter bounces when the core reaches nuclear densities, producing a spectacular supernova. This hydrodynamic phase might leave a neutron star or even a black hole at the end of the star's life.

Massive stars are generally more luminous than their lower mass counterparts. Consequently, they have to replenish the energy through nuclear burning faster, resulting in relatively shorter lifetimes. Ultimately the lifetime τ is roughly correlated with the initial mass of the star (Maeder, 2009)

$$\tau \propto \frac{M}{L} \propto M^{1-\alpha} \quad \text{with} \begin{cases} \alpha \approx 1.7 & \text{for } 0.6\,\mathrm{M}_\odot < M < 2\,\mathrm{M}_\odot \\ \alpha = 3 & \text{for } 2\,\mathrm{M}_\odot < M < 60\,\mathrm{M}_\odot \\ \alpha \approx 4 & \text{for } 60\,\mathrm{M}_\odot < M < 120\,\mathrm{M}_\odot. \end{cases} \tag{I.1}$$

For even higher masses, $\alpha \to 1$ (Yusof et al., 2013). Therefore, a $20\,\mathrm{M}_\odot$ star lives about 10^7 years which is around 100 times shorter than the lifetime of a $2\,\mathrm{M}_\odot$ star. The much shorter lifetime leads to the more immediate influence of massive stars on their surroundings and also why the early Universe was dominated by massive stars.

During main-sequence evolution where hydrogen is burnt in the core, massive stars are observed as O- and early B-type stars. Once the star exhausts its central hydrogen fuel it evolves past the main sequence into more rapid stages. There, massive stars are observed as Red or Blue Supergiants or more peculiar objects such as Wolf-Rayet stars and luminous blue variables. These advanced stages of stellar evolution are accompanied by strong and varying mass loss and luminosities. The final death of the star after silicon burning is accompanied by spectacular explosions. Also, other exotic appearances like pulsars, gamma-ray bursts or magnetars are thought to originate from massive stars

(e.g. Woosley, 1993; Lyutikov & Blackman, 2001; Woosley & Bloom, 2006; Turolla et al., 2015). Scientists are mostly limited by observations of the stellar surface, with the exception of asteroseismology that allows us to probe the interior of stars. However, stellar evolution is mainly driven by changes in the centre of the star, often depending on nuclear properties, and changes at the surface are a consequence of the interior evolution. Nevertheless, the conditions in the centre are affected by the physics of the surrounding layers. For that reason, a star has to be considered as a whole and the interaction of the various physical processes and layers have to be taken into account.

2.1 Nuclear Burning

One of the key ingredients of stellar models is the energy generation which keeps the star in a hydrostatic equilibrium during most of its evolution. This energy is generated by thermonuclear reactions, which are activated when the gravitational contraction pushes the temperature and pressure in the centre of a star above a certain threshold. The nuclear energy is radiated away and enables a balance between gravitational contraction and radiation pressure. The lost energy is resupplied by further thermonuclear reactions. Hence, these reactions slowly modify the composition in a burning region and shape the internal structure of stars. Ergo, they determine how stars evolve and their fate.

The interior of a star can be represented in the following, very simplified, way (Kippenhahn & Weigert, 1994). A star burns through its fuel[5] during a certain phase, depending on the physical properties, normally starting in or near the centre. Once the fuel is exhausted, the star lacks an energy source needed to maintain hydrostatic equilibrium. Consequently, the core contracts on the Kelvin-Helmholtz timescale τ_{KH}, defined as the ratio of the gravitational energy to the luminosity (e.g. Kippenhahn & Weigert, 1994). This increases the central temperature and pressure. Once the temperature and pressure are high enough to further fuse the ashes[6] of the previous burning phase, the next burning stage is ignited and the cycle restarts. The contraction also heats up the layers above the core, setting the conditions for thermonuclear burning in a shell. This leads to an "onion-like" structure. However, even though the burning zones are separated, they may influence each other through mixing processes - see Chapter II - or by local expansion and contraction[7]. For example, strong burning zone can lead to an expansion of the layers above it location. The expanding layers will reduce their temperature and pressure. Consequently, the new temperature might be lower than the ignition temperature of a previously active burning shell, which then ceases.

The order of the burning stages and the reactions taking place depend on the nuclear properties of the isotopes taking part in the reactions, such as the Coulomb-barriers, the nuclear cross-sections and

[5] The nuclei that are used as ingredients for the thermonuclear reactions.
[6] The end product(s) of a burning stage.
[7] Also, in reality stars are not completely spherically symmetric and asymmetries lead to a deviation from the "onion-structure".

Table I.1: The central densities, ρ_c, and the central temperature, T_c, both at the ignition of the burning stage, i.e. when 0.3% of the fuel is burnt, for a $15\,M_\odot$ (left) and a $25\,M_\odot$ (right) model. The respective third row shows the duration τ of the burning phase. The number in the bracket is the exponent while the number before is the multiplier. The stellar models presented here are the non-rotating models from Chapter IV.

	$15\,M_\odot$			$25\,M_\odot$		
Fuel	ρ_c (g cm^{-3})	T_c (K)	τ	ρ_c (g cm^{-3})	T_c (K)	τ
Hydrogen	6.99(0)	3.55(7)	1.40(7) yrs	4.52(0)	3.85(7)	7.54(6) yrs
Helium	8.49(2)	1.65(8)	0.91(6) yrs	4.64(2)	1.75(8)	0.57(6) yrs
Carbon	9.01(4)	6.60(8)	1.43(3) yrs	5.24(4)	7.14(8)	1.75(2) yrs
Neon	6.77(6)	1.26(9)	1.68(0) yrs	2.68(6)	1.37(9)	41 days
Oxygen	7.59(6)	1.95(9)	211 days	2.18(6)	1.80(9)	76 days
Silicon	4.84(7)	3.55(9)	37 hrs	7.61(7)	3.77(9)	18 hrs

reaction rates (Gamow-peak) and Gamow penetration-factors (see e.g. Povh et al., 2009). This leads to the well separated phases of nuclear burning.

For a polytrope of constant index it is possible to obtain a relation between the initial mass M, the central temperature T_c and the central density ρ_c (Kippenhahn & Weigert, 1994),

$$M^2 \sim \frac{T_c^3}{\rho_c^2}. \tag{I.2}$$

This relation implies that for a given burning stage, which is activated above a certain threshold in T_c given by thermonuclear properties, more massive stars burn at lower densities (see Table I.1). Furthermore, more massive stars have shorter burning times as the mass dependence pushes T_c higher for each burning stage (see Table I.1) and thermonuclear reaction rates depend exponentially on T_c (Kippenhahn & Weigert, 1994; Maeder, 2009). This is correlated to the shorter lifetimes of massive stars due to higher luminosities (see Eq. I.1). It should be noted that this approximative relation is applicable for the early evolution of a star. During the advanced stages, the complex structure of a star leads to a deviation of the oversimplified polytropic picture (see also Fig.(I.1b)).

2.1.1 Hydrogen Burning

The simplest nucleus initially available is hydrogen, consisting of a proton. So the first burning stage taking place is hydrogen burning, synthesising mainly ^{4}He. This burning stage proceeds via the pp-chain and the CNO-cycle. The CNO-cycle operates more effectively at higher temperatures, hence, it dominates in massive stars. The simplest pp-chain is activated at $T_c \sim 5 \times 10^6$ K by ^{1}He(p,e$^+\nu$)^{2}H(p,γ)^{3}He and is completed by ^{3}He(^{3}He,2p)^{4}He (Burbidge et al., 1957). There are alternatives for the second part over ^{7}Be and ^{7}Li or ^{7}Be and ^{8}B, respectively, but they require the existence of a significant amount of ^{3}He. The CNO-cycle, dominating at slightly higher temperatures of

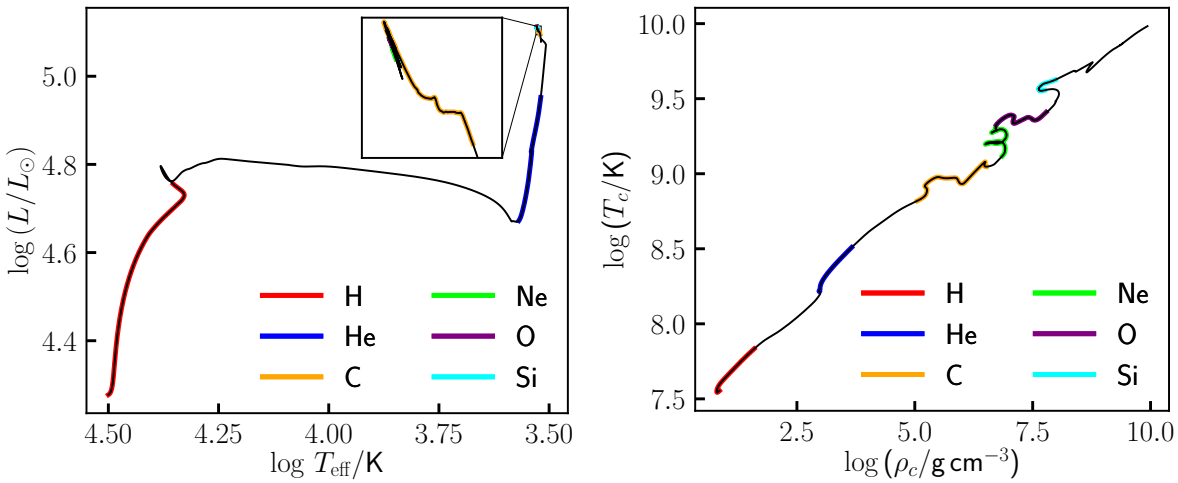

(a) Hertzsprung-Russell diagram

(b) T_c-ρ_c diagram

Figure I.1: The Herzsprung-Russel diagram and the T_c-ρ_c diagram of a 15 $M_\odot$ model showing its surface and central evolution, respectively. The colours indicate the burning phase in the centre.

$T_c \sim 16 \times 10^6$ K, synthesises helium via ^{12}C(p,γ)^{13}N(e$^+\nu_e$)^{13}C(p,γ)^{14}N(p,γ)^{15}O(e$^+\nu_e$)^{15}N(p,^{4}He)^{12}C (Burbidge et al., 1957). This catalytic cycle is controlled by the slowest reaction ^{14}N(p,γ)^{15}O. The CNO-cycle depends on the availability of metals. Therefore, it cannot be activated in stars with a metallicity close to zero[8], unless the catalysts are mixed into the burning shell during the later burning phases - see Section I.4.

Contrary to low-mass stars, massive stars have a convective core and a radiative envelope, meaning that the energy in the centre is mainly transported outwards via turbulent flows of matter - see Section II.1 - whereas in the envelope the energy is transported to the surface by the diffusion of photons. During core hydrogen burning the star is found on the main sequence in the Hertzsprung-Russell diagram, indicated with red colour in Fig.(I.1a). This diagram shows the relation between the surface temperature and the luminosity of the star. Stars with a larger initial mass have a higher luminosity and surface temperature. During the main-sequence evolution, the star moves slowly upwards to higher luminosities and lower surface temperature. The higher luminosity results from the fact that hydrogen is turned into helium, which increases the mean molecular weight μ, and that the luminosity scales with μ as $L \propto \mu^4$ (e.g. Kippenhahn & Weigert, 1994). On the other hand, the surface temperature decreases slightly because the higher luminosity pushes the star to a larger radius which makes the surface cooler.

Table I.1 shows that hydrogen burning is the longest burning stage and lasts about 90% of the star's life. This is a consequence of the binding energy per atomic number which decreases for heavier nuclei. Therefore, thermonuclear burning has to consume more nuclei in order to generate the same amount of energy per atomic number as heavier elements are synthesised, leading to shorter burning lifetimes

[8] In primordial stars the initial contraction is only stopped during core helium burning by the 3α process (e.g. Ekström et al., 2008), see Section I.2.1.2.

for the later stellar phases. For example, the binding energy per atomic number during core helium burning is roughly ten times lower than during core hydrogen burning. This leads to an approximately ten times shorter burning lifetime. This example can be generalised, because the binding energy per atomic number mostly decreases as the nuclei become heavier. Therefore, the burning lifetimes become shorter as the evolution proceeds, see Table I.1.

After hydrogen is exhausted in the core, the energy generation by thermonuclear burning together with the convective core ceases rather abruptly. The missing energy production in the centre leads to a phase where the core gravitationally contracts on the Kelvin-Helmholtz timescale. As a result, the increasing temperature leads to hydrogen burning ignition in a shell surrounding the core. This newly established energy source opposes the further contraction of the hydrogen envelope but the core continues to shrink. According to the Virial theorem[9] for a mono-atomic gas, half of the liberated gravitational energy turns into internal energy. Therefore, the core is heated up (see Fig.(I.1b)) while losing gravitational energy, hence, stars have a negative specific heat. The other half of the energy is radiated from the core into the envelope. On the other hand, the luminosity at the surface of the star remains roughly constant on this short evolutionary timescale (see Fig.(I.1a)). Therefore, following energy conservation, this leads to an expansion of the envelope. Ergo, during the short phase after main-sequence evolution the star has a contracting core accompanied by a expanding envelope above the hydrogen burning shell. The expansion of the envelope stops when it becomes convective, i.e. the energy excess is transported more efficiently to the surface - see Section II.1. This is the so-called "*mirror-principle*" (Kippenhahn & Weigert, 1994) and it can also be found in other evolutionary phases. The consequence of this scenario is that the surface temperature first increases, due to the whole contraction of the star, before it decreases to lower temperatures, a consequence of the quite extreme expansion of the envelope. In Fig.(I.1a), this corresponds to a short leftwards hook before the stellar track moves to the cooler part of the Hertzsprung-Russell diagram on the right side. During this evolutionary sequence the star becomes a red supergiant. The timescale of this evolutionary phase and how long the star stays on the hotter side of the Hertzsprung-Russell diagram as a blue supergiant is very uncertain and depends on input physics such as convection, nuclear physics, opacity and so forth (e.g. Langer & Maeder, 1995; Schootemeijer et al., 2019; Kaiser et al., 2020, and Chapter III).

2.1.2 Helium Burning

After hydrogen is depleted in the core, mainly ^{4}He is left (roughly $X_{\rm He} \sim 1 - Z_{\rm ini} \sim 98.6\%$). When the core is heated up due to contraction to about 10^8 K (see Table I.1 and Fig.(I.1b)) helium burning ignites. This burning process has to overcome the bottleneck around the atomic mass number 8.

[9]The Virial theorem relates the potential and the kinetic energy in equilibrium (see e.g. Collins, 1978). For a gravitational bound system, such as a star, it gives the connection between its gravitational and internal energy.

Fusing two ^{4}He produces ^{8}Be, which has a lifetime of $\sim 10^{-18}$ s (Magill et al., 2006) and therefore immediately decays back to two ^{4}He nuclei. However, this short lifetime is still sufficient to build up a small concentration of ^{8}Be, with a ^{8}Be to ^{4}He ratio of $\sim 10^{-9}$ (Salpeter, 1953). The high number densities of helium then allow for another ^{4}He nucleus to be captured, forming the ^{12}C nucleus (Burbidge et al., 1957). This reaction is called the 3α process.

Once there is enough ^{12}C synthesised, another reaction activates, the $^{12}\mathrm{C}(\alpha,\gamma)^{16}\mathrm{O}$ reaction where the newly produced carbon captures another helium nucleus (Burbidge et al., 1957). The 3α process and the $^{12}\mathrm{C}+\alpha$ reaction compete for the remaining ^{4}He. The first has a second-order dependence on the density, whereas the latter has a first order dependence (see Eq.(B.9)). Therefore, with an increasing abundance of carbon towards the end of the core helium burning stage, the α-capture on carbon dominates. Furthermore, the density dependence favours the latter reaction at higher entropy, i.e. in more massive stars.

Stars with an operating CNO-cycle during main sequence - see Section I.2.1.1 - will contain a non-negligible amount of ^{14}N in their cores[10] left over from the CNO-cycle (Arnould & Mowlavi, 1993). At the start of core helium burning, before the energy generation by the 3α process becomes noteworthy, the ^{14}N burns convectively via $^{14}\mathrm{N}(\alpha,\gamma)^{18}\mathrm{F}(\beta^+\nu)^{18}\mathrm{O}(\alpha,\gamma)^{22}\mathrm{Ne}$ (Cameron, 1960). The newly synthesised ^{22}Ne will capture another helium nucleus once the central temperature exceeds $\sim 2.5\times10^8$ K late during core helium burning via $^{22}\mathrm{Ne}(\alpha,\mathrm{n})^{25}\mathrm{Mg}$[11]. This neutron source creates the condition for the weak slow[12] neutron capture process (weak s-process) where the neutron is captured by seed nuclei synthesising isotopes up to A$\approx$ 90 (Burbidge et al., 1957; Couch et al., 1974; Arnett & Thielemann, 1985; Prantzos et al., 1990; Raiteri et al., 1991a; Kaeppeler et al., 1994; The et al., 2007; Frischknecht et al., 2016). Yet, only a part of the central ^{22}Ne manages to capture a helium nucleus during core helium burning. The leftover neon will capture an α during a subsequent carbon shell burning phase, where the αs are provided from the α-emission channel of the $^{12}\mathrm{C}+^{12}\mathrm{C}$ reaction, $^{12}\mathrm{C}(^{12}\mathrm{C},\alpha)^{20}\mathrm{Ne}$. This creates the condition for the weak s-process at higher temperatures and slightly different conditions (Couch et al., 1974; Prantzos et al., 1990; Raiteri et al., 1991b; Pignatari et al., 2010). This secondary neutron-source reaction competes during the late core helium burning stage with the $^{12}\mathrm{C}(\alpha,\gamma)^{16}\mathrm{O}$ reaction for the remaining helium nuclei.

The outcome of core helium burning affects the further evolution of massive stars in several ways. The size of the convective helium core defines the region in which the subsequent advanced evolutionary stages will occur. Next, the ratio of ^{12}C and ^{16}O not only sets the amount of fuel for the subsequent carbon and oxygen burning phases but it also influences the pre-supernova abundance (e.g. Thielemann & Arnett, 1985; Weaver & Woosley, 1993). Furthermore, the amount of ^{12}C available at the

[10] At solar metallicity about 1.4%, because most of the initial metal mass fraction are CNO elements, which are converted into ^{14}N by the CNO-cycle during the main-sequence evolution.

[11] Another $^{22}\mathrm{Ne}+\alpha$ reaction that is active in parallel is $^{22}\mathrm{Ne}(\alpha,\gamma)^{26}\mathrm{Al}$, reducing the neutron production.

[12] Slow compared to the β-decay of nuclei near the line of stability.

start of core carbon burning - see Section I.2.1.3.1 - determines whether carbon burns convectively or radiatively. This has consequences for the convective history and the stellar structure at core-collapse (see Section I.3 but also Ugliano et al., 2012; Sukhbold & Woosley, 2014; Ertl et al., 2016; Sukhbold et al., 2018; Chieffi & Limongi, 2020). Moreover, the different activity of the ^{22}Ne+α reaction during core helium or carbon shell burning will affect the nucleosynthesis and final weak s-process yields, because the burning conditions of the two sites differ and there are different isotopic abundances, e.g. neutron poison, in the two stages (Prantzos et al., 1990; Raiteri et al., 1991a,b; Pignatari et al., 2010). Unfortunately, the reaction rate of the ^{12}C$(\alpha,\gamma)^{16}$O reaction is subject to large uncertainties (a factor of a few, Caughlan & Fowler, 1988; Buchmann, 1996; deBoer et al., 2017; Rapagnani et al., 2017), resulting in quite big uncertainties for the further evolution of massive stars (e.g. Rauscher et al., 2002; West et al., 2013; Rauscher et al., 2016; Fields et al., 2018; Farmer et al., 2019).

The evolution of the star in the Hertzsprung-Russell diagram during core helium burning and the location where helium is ignited in the core depends on the mass, the physics used and the implementation thereof (see Chapters III and IV and also Davies & Dessart, 2018; Schootemeijer et al., 2019; Wagle et al., 2019; Kaiser et al., 2020). If the star at core helium ignition is still in the hot part of the Hertzsprung-Russell diagram, it might spend part of the core helium burning lifetime as a blue supergiant before it moves to the red supergiant branch. After the star reaches the cool part of the Hertzsprung-Russell diagram, the track rises steeply regardless of whether helium is ignited or not. Thereafter, it might start doing loops, whose orientation depends on the properties and the treatment of the models (e.g. opacity, treatment of convection, energy generation and composition, e.g. Kippenhahn & Weigert, 1994; Wagle et al., 2019). Stars with masses $M \gtrsim 40\,\mathrm{M}_\odot$ either lose too much mass to reach the red supergiant branch or only spend a short time there, losing a substantial amount of their mass, before becoming a Wolf-Rayet star - see Section I.2.2. These stars are more compact and therefore have higher surface temperatures, thus they are located in the left part of the Hertzsprung-Russell diagram. At lower metallicities, the stars generally stay more compact due to the lower opacity. Hence, they have slightly hotter surface temperatures and prefer the blue supergiant evolution.

2.1.3 Advanced Burning Stages

The evolution after core helium depletion is often referred to as advanced stages of evolution. During these advanced burning phases, the temperatures in the centre are hot enough for non-negligible neutrino production - see Section B.1.2.2 - and the dominant energy transport changes from photon to neutrino emission (e.g. Thielemann & Arnett, 1985; Woosley et al., 2002, - see also Section B.1.2.2). Neutrinos have a very small cross-section. Therefore, they immediately escape at the densities existing during the advanced burning stages. The more efficient energy transport leads to qualitatively different

burning stages. For example, because energy is transported away faster, the star has to provide more energy in order to stay in a hydrostatic equilibrium and burns faster through its fuel. Hence, the stellar lifetimes speed up (see Table I.1). The envelope cannot respond to the fast changes in the core. Consequently, the position of the star in the Hertzsprung-Russell diagram is nearly unchanged during those burning stages (see Fig.(I.1a)). This also relates to the fact that the final outcome of the advanced phases of stellar evolution is almost completely determined by the helium or the carbon-oxygen core after the helium burning phase rather than the initial mass on the main sequence (e.g. Thielemann et al., 2011).

During the advanced stellar evolution stages, the central temperatures and densities are much higher than during core hydrogen or helium burning. Furthermore, there is an increasing amount of potential seed nuclei and possible reactions that liberate neutrons, protons and α-particles. These conditions allow for diverse capture-reactions. Indeed, the nucleosynthesis during the advanced burning stages consists of a large variety of different nuclear reactions. It is during this later burning stages and the final explosive event - see Section I.3 - where most of the heavy elements with A$= 16 - 64$ are synthesised (Arnett & Thielemann, 1985; Thielemann & Arnett, 1985; Woosley et al., 2002; Langer, 2012; Pignatari et al., 2016; Ritter et al., 2018; Limongi & Chieffi, 2018).

After core helium burning, the further contraction increases the density to such levels that the free electrons in the centre become limited in their movement. This is a quantum mechanical effect where fermions, such as electrons, are limited to a finite volume at a high density. Therefore, electrons cannot be indefinitely close to each other and the state population of electrons is determined by the Pauli exclusion principle rather than the Boltzmann statistics, which is valid for low densities and high temperatures (e.g. Greiner et al., 1993). The consequence is an additional pressure, the degeneracy pressure, that counteracts the gravitational contraction. The maximum mass that can be supported by electron pressure is the Chandrasekhar mass,

$$M_{\rm Ch}(Y_{\rm e}, S_{\rm e}) = 1.44(2Y_{\rm e})^2 \left[1 + \left(\frac{S_{\rm e}}{\pi Y_{\rm e}}\right)^2\right] M_{\odot}, \tag{I.3}$$

where S_e is the entropy in electrons per baryon and Y_e the electron abundance. If the gravitational mass exceeds this limit, the core of the star can contract further and heat up the centre enough to ignite the following burning stages in non-degenerate conditions. This applies to stars with initial masses of $\gtrsim 10\,\mathrm{M}_{\odot}$. This effect can be seen in Fig.(I.1b) where the wiggles towards the right side indicate that the matter in the core becomes partly degenerate and a backwards loop and heating indicates the lifting of the degeneracy. Stars below this mass limit end their life as white dwarfs. However, stars with the mass of $\sim 9\,\mathrm{M}_{\odot}$ have another way to overcome the degeneracy and evolve through the advanced phases (Miyaji et al., 1980; Nomoto, 1984, 1987; Jones et al., 2013; Takahashi et al.,

2013; Schwab et al., 2015). In a degenerate electron gas the Fermi energy increases the energy of the degenerate electrons. If the Fermi energy is able to overcome the negative Q-value, electron captures on nuclei and protons become probable which would normally be forbidden. In a degenerate Ne-O-Mg core, for example, electron captures on ^{20}Ne and ^{25}Mg can become possible if the Fermi energy overcomes the negative Q-value. The captured electrons do not contribute to the degeneracy pressure anymore and the reduction of the supporting pressure leads to the collapse of the star, combining all further burning stages via a nuclear statistical equilibrium on a short collapse timescale (Miyaji et al., 1980; Nomoto, 1984, 1987). These stars are thought to leave an oxygen-neon-iron white dwarf behind (Jones et al., 2016, 2019).

On the other hand, there is also an upper mass limit above which the advanced phases proceed in a different manner. If a star is massive enough they enter the so-called pair-instability region, where high central temperatures and low densities lead to the thermal concentration of free electron-positron pairs (Rakavy & Shaviv, 1967). This results in a reduction of the thermal pressure and eventually to violent pulsations that remove a large part of the star's mass or, if the star is massive enough, entirely disrupt the star (Fraley, 1968; Fryer et al., 2001; Kasen et al., 2011; Waldman, 2008; Kozyreva et al., 2017; Gilmer et al., 2017; Woosley, 2017, 2019; Leung et al., 2019) - see Section I.3.2. At solar metallicity, massive stars lose enough mass through stellar winds to avoid the pair-instability scenario. However, at lower metallicity, where the winds are weaker - see Section I.2.2 - stars in the mass range of about $140 - 260\,\mathrm{M}_\odot$ encounter the pair-instability.

I.2.1.3.1 Carbon Burning If the carbon-oxygen core exceeds the Chandrasekhar limit, non-degenerate carbon burning ignites. During this burning phase, carbon is mainly burnt via the heavy-ion fusion reaction ^{12}C(^{12}C,γ)^{24}Mg*. The excited magnesium nuclei can decay through three channels, giving ^{23}Mg+n, ^{20}Ne+α or ^{23}Na+p (Arnett & Thielemann, 1985). Other interesting nuclei synthesised during carbon burning via neutron-, proton-, and α-captures are ^{16}O, ^{21,22}Ne, ^{24,25,26}Mg, ^{26,27}Al and some smaller amounts of ^{29,30}Si and ^{31}P (Arnett & Thielemann, 1985; Woosley et al., 2002).

In stars with $M \gtrsim 22\,\mathrm{M}_\odot$ carbon burns radiatively (Hirschi et al., 2004), meaning the energy transport is purely radiative, contrary to lower masses where the energy is transported by convection - see also Section II.1. This change arises because of the smaller carbon abundance available at core helium depletion with increasing stellar mass - see discussion in Section I.2.1.2. This change leads to a different outcome of the burning stage and its nucleosynthesis, since there is no mixing occurring that provides fresh fuel into the burning region. Furthermore, the structure of the star is shaped differently in the presence of pure radiative transport compared to a convective and radiative transport (see e.g. the discussions in Sukhbold & Woosley, 2014; Chieffi & Limongi, 2020). However, the mass limit where the switch occurs is sensitive to the uncertainties of stellar evolution such as the rate of the

$^{12}C(\alpha,\gamma)^{16}O$ reaction, which determines the abundance of carbon after core helium burning.

I.2.1.3.2 Neon & Oxygen Burning After carbon burning depletes, the central region consists mainly of ^{16}O, ^{20}Ne and ^{24}Mg. The "easiest" fusion reaction to take place next is the heavy-ion fusion of oxygen. However, before the central region reaches the temperature required for oxygen fusion, the photons from the high energy tail of the Planck distribution have enough energy to photodisintegrate ^{20}Ne. The ^{20}Ne is destroyed rather than the "simpler" ^{16}O nuclei, i.e. with the lower Coulomb-barrier, because neon has a much lower binding energy than oxygen and the photons with no electrical charge ignore the Coulomb-barrier. This photodisintegration period is called the neon burning phase and is initiated by the endothermic absorption of a photon by a neon isotope which then enters an exited state and nearly immediately decays by emitting an α-particle, $^{20}Ne(\gamma,\alpha)^{16}O$ (Cameron, 1959). The freed α-particles are recaptured by $^{16}O(\alpha,\gamma)^{20}Ne$, establishing an equilibrium whereafter the α-particles start to be captured by ^{20}Ne, synthesising ^{24}Mg (Arnett, 1974). Some secondary neon burning reactions can emit a neutron, however, the s-process production differs from the previous helium and carbon burning because of the efficient photodisintegration reactions and the different exposure timescales (Thielemann & Arnett, 1985). Other nucleosynthetically-interesting neon burning products, produced via capture reactions, are $^{28,29,30}Si$, ^{26}Al, ^{31}P and some additional numbers of ^{36}S, ^{40}K, ^{46}Ca, ^{58}Fe and $^{61,62,64}Ni$ (e.g. Woosley et al., 2002).

After neon is depleted in the core, oxygen burning ignites at slightly higher temperatures (see Table I.1). Oxygen burning proceeds via the heavy-ion fusion reaction $^{16}O + {}^{16}O$, synthesising $^{32}S^*$ (Arnett, 1972; Woosley et al., 1972). The excited sulfur decays through four possible channels, giving ^{28}Si, ^{31}S or $^{30,31}P$ (e.g. Woosley et al., 2002). Similar to the two previous advanced burning stages there are a number of secondary reactions that occur during oxygen burning. The outcome of the secondary reactions follows a certain trend. In a high temperature, low density environment the Coulomb-barriers are more easily overcome and heavier nuclei are synthesised. On the other hand, at slightly lower temperatures and higher densities the electrons become more degenerate, enhancing electron capture on nuclei, see discussion above. This results in a decrease of the electron abundance, Y_e, and slightly neutron-richer matter (Thielemann & Arnett, 1985). Depending on the conditions, the secondary reactions produce nuclei such as $^{32,33,34}S$, $^{35,37}Cl$, $^{36,38}Ar$, $^{39,41}K$ and $^{40,42}Ca$ (Woosley et al., 2002). The high temperatures achieved during the core oxygen burning phase favour the photodisintegration of the heavy nuclei produced from the slow s-process during the earlier burning phases into iron-peak nuclei (Thielemann & Arnett, 1985).

I.2.1.3.3 Silicon Burning Silicon burning proceeds similarly to neon burning via a photodisintegration process rather than a heavy-ion fusion reaction because of the high Coulomb barrier. The

high temperatures during this burning stage, see Table I.1, allow for the complete photodisintegration of silicon via $^{28}\mathrm{Si}(\gamma,\alpha)^{24}\mathrm{Mg}$ $(\gamma,\alpha)^{20}\mathrm{Ne}(\gamma,\alpha)^{16}\mathrm{O}(\gamma,\alpha)^{12}\mathrm{C}(\gamma,2\alpha)\alpha$. The freed α-particles and their associated nucleons are recaptured onto ^{28}Si and other nuclei to produce heavy nuclei (Bodansky et al., 1968; Weaver et al., 1978; Thielemann & Arnett, 1985). These heavy nuclei are also subject to further photodisintegration. Therefore, several groups of nuclei are linked via forward and reverse reactions with increasing temperature, creating a quasi-statistical equilibrium (Hix & Thielemann, 1996, 1999). It is not a full equilibrium because two main quasi-statistical equilibrium clusters form around ^{28}Si ($12 \leq Z \leq 20$) and ^{56}Ni ($22 \leq Z \leq 28$), separated by the proton magic number[13] $Z = 20$ (Bodansky et al., 1968; Weaver et al., 1978; Thielemann & Arnett, 1985). This bottleneck can be overcome by two possibilities, (i) in higher temperature environments the gap is bridged on the proton-rich side of the stability and (ii) at low temperature sufficient amounts of neutron-rich calcium nuclei were already synthesised in prior burning stages (Thielemann & Arnett, 1985). Once the temperature exceeds $T_9 \gtrsim 5$ the bottleneck can be bridged and all the nuclei are in a nuclear-statistical equilibrium via strong and electromagnetic interactions. With increasing temperature the mean atomic weight of the statistical equilibrium is gradually shifted towards the most tightly bound iron-group nuclei.

During the late phase of core silicon burning an amount of partly-degenerate electron-captures occur. As a result, the dominant product of silicon burning is not ^{56}Ni, but ^{54}Fe or even ^{56}Fe (e.g. Weaver et al., 1978). The other important burning products are $^{55-68}$Co, $^{56-69}$Ni, $^{53-62}$Fe, $^{53-63}$Mn, $^{64-74}$Cu, $^{49-54}$Sc, $^{50-58}$V, $^{52-59}$Cr, $^{49-54}$Ti, $^{74-80}$Ga, $^{77-80}$Ge, ^{83}Se, $^{80-83}$As and ^{75}Zn (Bodansky et al., 1968; Thielemann & Arnett, 1985; Woosley et al., 2002).

2.2 Mass Loss

Stellar winds and their treatment is one of the largest uncertainties of stellar evolution. While this subject would be enough to fill several other theses and is not the core of this work it nevertheless should be shortly discussed here in the context of massive star evolution to understand its impact. There are several reviews that discuss the physics of stellar winds of massive stars, see e.g. Kudritzki & Puls (2000); Puls et al. (2008); Crowther (2007); Vink (2008); Vink et al. (2011); Massey (2013); Smith (2014); Vink (2015).

Mass loss is an important ingredient in the evolution of massive stars. For example, a star with an initial mass of $60\,\mathrm{M}_\odot$ at solar metallicity loses more than half of its mass during the main-sequence evolution, see also Table V.1, and it is left with only about $\sim 20\,\mathrm{M}_\odot$ for the further stages. Compared to low mass stars such as the Sun, the mass-loss rate, $\dot{M}$, of OB stars during main-sequence evolution is about 10^7 times larger. The evolution of massive stars with masses larger than $\sim 30 - 40\,\mathrm{M}_\odot$ is

[13] A magic number is a number of nucleons so that they can fill a complete nuclear shell. Nuclei with magic numbers are more stable than others.

largely determined by the strength of their mass loss (e.g. Vink, 2008; Vink et al., 2011; Yusof et al., 2013; Köhler et al., 2015). The amount of mass lost during the early stages of evolution is crucial as it influences the later evolutionary stages. Strong stellar winds can remove the outer layers of a star, making possible evolutionary stages such as the Wolf-Rayet[14] and luminous blue variable[15] phases. This change in the advanced evolution, i.e. whether the star is a blue or red supergiant or is stripped from its envelope, will also influence the final fate of the star (e.g. Renzo et al., 2017) - see also Section I.3. It determines the stellar mass before the collapse and is therefore relevant for the possible fallback onto the proto-neutron star and it also affects the light curves and absorption lines, hence, the supernova type (Filippenko, 1997; Turatto, 2003).

Despite the importance of mass loss, there is still a tremendous uncertainty in its derived rates for massive stars, especially in post-main-sequence evolution. The uncertainty is the largest for the most luminous stars with $M \gtrsim 60\,\mathrm{M}_\odot$ (Woosley et al., 2002; Vink, 2008; Langer, 2012) for different reasons. Very massive stars are rare and therefore there are fewer empirical constraints and the physics of the stellar winds becomes more challenging. The luminosity of these stars is close to the Eddington-limit (Ulmer & Fitzpatrick, 1998), their winds become optically thick (de Koter et al., 1997; Vink et al., 2011) and their atmospheres are often enriched in helium (Mokiem et al., 2006). Also, the gravity of a very massive star does not follow a simple mass-luminosity relation (Gräfener et al., 2011).

The mass loss in massive stars is driven by the strong radiative output. The strong radiation pressure is so powerful that it can drive strong stellar winds, the so-called line-driven wind (Lucy & Solomon, 1970; Castor et al., 1975). Momentum is mainly transferred to matter via absorption of radiation by the spectral lines. Key parameters in determining the mass-loss rates are the metallicity Z, the luminosity L, the mass M and the surface temperature T_{eff}. The general consensus is that the mass-loss rates increase for more massive stars (Puls et al., 2008) and for more metal-rich stars (Mokiem et al., 2007). Stellar winds in different stages scale differently on these parameters. The relative importance of stellar winds to supernova explosions, regarding the chemical enrichment of the interstellar medium, increases with metallicity. Thus, stellar winds become more important at higher metallicity (Vink et al., 2001).

The radiation-driven winds from hot O- and B stars that still have their hydrogen envelope are relatively well understood (Kudritzki & Puls, 2000; Vink et al., 2000, 2001; Puls et al., 2008). The momentum transfer during the main sequence mainly occurs on metal lines, specifically on iron, despite its rarity. The reason are the many line transitions of the complex atomic structure, which

[14] Wolf-Rayet stars are massive stars that have experienced strong winds, which removed a substantial part of their envelopes. Thus, they have broad emission lines and an altered surface composition, reflecting the presence of ashes from nuclear burning. Hydrogen is either deficient, as in WN stars, or completely absent, as in WC and WO stars. The N, C and O subtypes of Wolf-Rayet stars indicate the presence of strong lines of nitrogen, carbon or oxygen in their spectra (e.g. Crowther, 2007)

[15] Luminous blue variables are massive evolved stars that show temporal variations in their spectra and brightness (Humphreys & Davidson, 1994; Vink, 2012; Weis & Bomans, 2020).

make it an efficient absorber of radiation. The momentum is then transferred to the bulk plasma via Coulomb collisions (Owocki & Puls, 2002). At lower metallicity other metals such as Cl, Ar, P, S or CNO elements become relevant. Therefore, the host galaxy's metallicity plays a crucial role for stellar winds, since stars that are born with lower Fe content lose less matter during their evolution, despite their larger content of CNO material (Vink, 2008). At present day, the fast and thin radiation-driven winds from hot O- and B-stars are commonly treated with a theoretical prescription for different masses M, luminosity L, surface temperature $T_{\rm eff}$ and metallicity Z as (Vink, 2008, 2011):

$$\dot{M} \propto Z^{0.6} L^{2.2} M^{-1.3} T_{\rm eff}^{1.1}. \tag{I.4}$$

Mokiem et al. (2006), for example, found an excellent agreement with the theoretical prescriptions by Vink et al. (2000, 2001) for observed stars with $\log L/L_\odot \gtrsim 5.4$.

The line-driven mass-loss rates are predicted to increase strongly when the surface temperature of a massive star decreases to lower values and the star crosses the bi-stability jump (Vink et al., 2010; Vink, 2018). The reason behind the jump in $\dot{M}$ is a change in the line-driving element Fe, where Fe iv recombines to Fe iii, so that the Fe lines fall into the range where the flux distribution is maximal and the absorption becomes more efficient. The bi-stability jump is relevant when a massive star evolves to lower $T_{\rm eff}$ around $\log T_{\rm eff} \approx 4.34$. Since stellar winds remove angular momentum from rotating stars, see Section I.4, the bi-stability jump might explain the general slow surface rotation of supergiants (Vink et al., 2010).

The post-main-sequence stellar winds depend on the phases the star evolves through. Massive stars below about $30-40\,{\rm M}_\odot$ at solar metallicity[16] do not lose a lot of mass on the main sequence. However, once these stars reach the red supergiant branch they experience relatively strong winds, where mass loss can potentially remove the entire hydrogen-rich envelope. In red supergiants, mass loss is driven by the absorption and diffusion of radiation by dust. The driving mechanism for red supergiant winds is still very uncertain (e.g. discussions in Mauron & Josselin, 2011; Puls et al., 2015), meaning that the mass-loss rates in this phase cannot be determined from first principles. Instead, stellar evolution models apply empirical recipes, e.g. from de Jager et al. (1988); Nieuwenhuijzen & de Jager (1990), which appear to be insensitive to metallicity. However, the red supergiant mass loss is poorly understood theoretically and work determining a description for $\dot{M}$ during this phase is still ongoing (e.g. Beasor et al., 2020). In cool red supergiants, the dust forms grains in the elevated atmospheres because of the cooler temperatures. These so-called dust-enshrouded red supergiants have strong mass-loss rates due to the high dust opacity (van Loon et al., 2005). The mass lost during the red supergiant evolution is crucial in determining the further evolution and fate of these stars (Georgy et al., 2013). On the other hand, the winds during the blue supergiant phase can generally

[16] At lower metallicity this range is higher.

be described by the prescription of Vink et al. (2001). However, some blue supergiants are Cepheids, which experience large amplitude pulsations, resulting in enhanced mass-loss rates (Neilson & Lester, 2008).

Massive stars above $30 - 40\,M_\odot$ at solar metallicity experience strong winds already during the main-sequence evolution which can strip the star of its envelope, exposing the star's core. These Wolf-Rayet stars (see e.g. Crowther, 2007, for a review on Wolf-Rayet stars) have high $\dot{M}$ because of their high luminosity to mass ratio. The mass-loss rates commonly used in stellar evolution models are empirical mass-loss recipes, e.g. from Nugis & Lamers (2000). According to Vink et al. (2011) the line-driven winds become optically thick for $\Gamma > 0.7$[17] which favours larger $\dot{M}$ compared to optically thin winds. While other authors find a transition at lower Γ (e.g. Bestenlehner et al., 2014), they agree that the Eddington factor becomes the most relevant parameter in determining the mass-loss rates of Wolf-Rayet stars (Gräfener et al., 2011; Vink et al., 2011; Bestenlehner et al., 2014; Bestenlehner, 2020).

3 Fate of Massive Stars

The evolution of massive stars can lead to nature's biggest explosions, an event with unique physical conditions, very high energy output and production site of many heavy elements. The explosion ejects the elements synthesised during the star's evolution into the interstellar medium (e.g. Thielemann et al., 1996), which contributes to galactic chemical evolution. The explosive events may leave a compact remnant such as a neutron star or a black hole or even more exotic objects such as magnetars and pulsars (e.g. Woosley, 1993; Lyutikov & Blackman, 2001; Woosley & Bloom, 2006; Turolla et al., 2015). If these compact objects are in a binary system they may merge and generate gravitational waves (e.g. Abbott et al., 2016; Belczynski et al., 2020a).

There are different fates a massive star can meet, chiefly depending on its initial mass and metallicity. The details of these events also depend on other physical processes, such as neutrino interactions, fluid instabilities, rotation, magnetic fields, mass loss and so on. Their impact and importance is debated and remains uncertain.

Fig.(I.2) depicts the fate of massive stars as a function of the initial mass and metallicity and Fig.(I.3) illustrates the compact remnant, if any, that will be formed in the process. While the various scenarios are explained in more detail in the following Subsections, Figs.(I.2) and (I.3) give a complete overview of the fate of massive stars and how it depends on metallicity and mass. In Section I.2.2, the mass and metallicity dependence of stellar winds is discussed. In summary stars experience stronger mass loss with increasing mass and metallicity. This is also reflected in Figs.(I.2) and (I.3).

At zero to low metallicity the stellar winds are weak and massive stars lose nearly no mass during

[17] Γ is the Eddington factor which is the ratio of the gravitational to radiative forces.

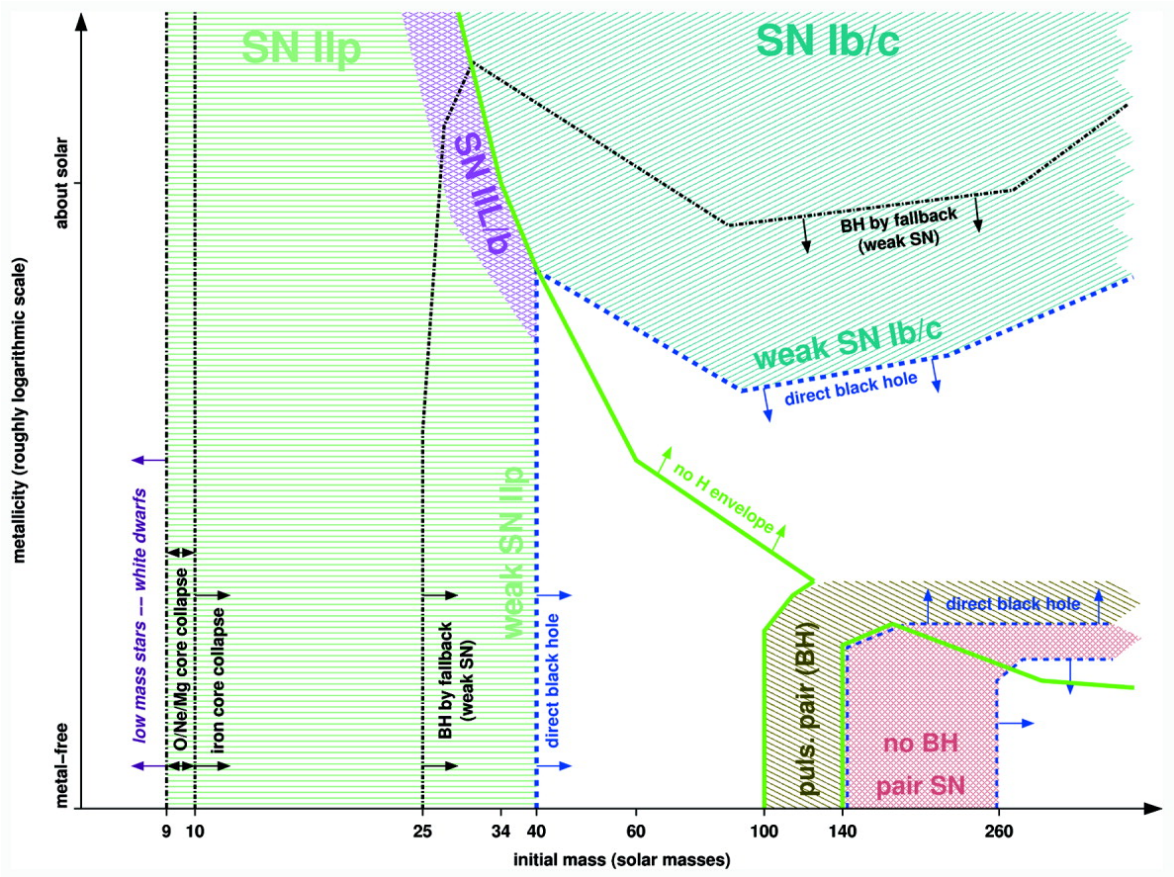

Figure I.2: The fate of single stars in relation to initial mass and metallicity. This figure presents the supernova types of the stars, if any, indicated by a colour shading for the different explosion types, explained in the text. The green line separates the stars that keep their hydrogen envelope and those that lose it. The dashed blue line borders the regime of direct black hole formation. The black dash-dotted lines distinguish the regions of stars that experience a supernova but form compact objects differently, specified by the label. Green horizontal hatching and purple cross-hatching depicts the regime where supernovae type II occur (for supernova classification, see e.g. Filippenko, 1997; Turatto, 2003). The stars that lose their hydrogen envelope and experience an explosion will be of type Ib or c, indicated by the dark green diagonal hatching. The brown diagonal hatching represents the pulsational pair-instability regime, right next to the pair-instability supernova region indicated by the red cross-hatching. Stars in regions with no colour shading experience either a direct collapse, where no supernova occurs because no shock wave is launched, or form a white dwarf (on the left side) where no supernova is launched. The figure is taken from Heger et al. (2003). More detailed explanations of the various processes can be found in the text. The acronyms in the figure have the following meaning; SN: supernova, puls. pair: pulsational pair-instability, pair SN: pair-instability supernova, BH: black hole.

their evolution. For example the metal-free stars in Fig.(I.2) retain their hydrogen-rich envelope for all masses; with the exception of stars entering the pulsational pair-instability regime - see Section I.3.2. Therefore the core and total mass of the metal-free stars scale with their initial mass. The mass-dependent fate of these stars can be summarised as follows (e.g. El Eid et al., 1983; Heger & Woosley, 2002; Umeda & Nomoto, 2002; Heger et al., 2003; Chatzopoulos & Wheeler, 2012; Yusof et al., 2013; Yoshida et al., 2016; Woosley, 2017, 2019; Farmer et al., 2019; Leung et al., 2019):

(i) $9\,\mathrm{M}_\odot \approx M$: Stars form degenerate oxygen-neon cores that collapse because of degenerate electron

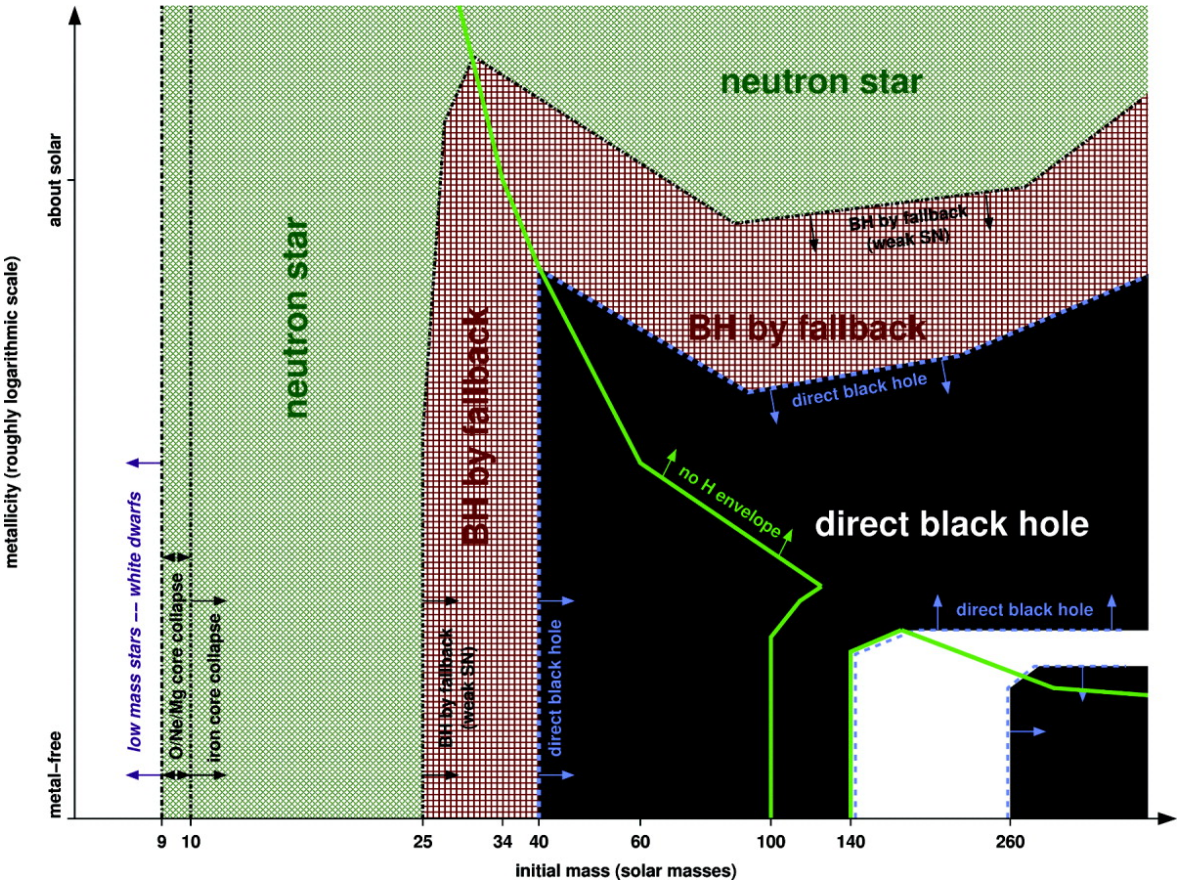

Figure I.3: The fate of single stars in relation to initial mass and metallicity. This figure shows the remnant, if any, of the explosive event. The various lines have the same meaning as in Fig.(I.2). The green cross-hatched region represents the stars that form a neutron star. The red cross-hatching indicates the regime where a black hole is formed due to fallback of matter onto the neutron star, whereas stars in the black zone will directly collapse into a black hole without launching a supernova shock wave. The white areas indicate where stars either form a white dwarf (*left*) or are completely disrupted by the pair-instability supernova (*right*). The figure is taken from Heger et al. (2003). More detailed explanations of the various processes can be found in the text.

capture (Miyaji et al., 1980; Nomoto, 1984, 1987; Jones et al., 2013; Takahashi et al., 2013; Schwab et al., 2015) - see also discussion in Section I.2.1.3. These stars leave a bound oxygen-neon-iron white dwarf behind (Jones et al., 2016, 2019).

(ii) $10\,\mathrm{M}_\odot \lesssim M \lesssim 40\,\mathrm{M}_\odot$: Stars in this mass range fom an iron core after core silicon depletion, which collapses and and releases a large amount of gravitational potential energy for a supernova explosion - see Section I.3.1 for more details. Stars in this mass range explode as a "*classical*" supernova type II, because they keep their hydrogen envelope. The explosion in the lower mass range, i.e. below ~ 20 - $25\,\mathrm{M}_\odot$, will successfully push the entire envelope away and the core forms a neutron star. On the other hand, for the higher masses the shock wave is not able to push all the infalling material away and some will fall back onto the neutron star. This pushes the configuration over the maximal stable neutron star mass and it collapses to a black hole (Woosley & Weaver, 1995; Fryer & Kalogera, 2001; Tauris et al., 2011), see also discussion at

the end of Section I.3.1.

(iii) $40\,\mathrm{M}_\odot \lesssim M \lesssim 100\,\mathrm{M}_\odot$: Contrary to (ii) the infalling mass of the stars in this mass range is too heavy to allow for a successful explosion. The result is a direct collapse to a black hole with no mass ejected (Fryer, 1999).

(iv) $100\,\mathrm{M}_\odot \lesssim M \lesssim 260\,\mathrm{M}_\odot$: The cores of these stars are massive enough for the star to enter the pair-instability region where the star is subject to violent pulsations, see Section I.3.2. For the lighter masses the pulsation are relatively weak and remove large parts of the envelope (Woosley et al., 2007; Waldman, 2008; Leung et al., 2019). These stars will then collapse to black holes. The pulsations in the higher mass stars are extreme enough to disrupt the entire star and no remnant is left (Fraley, 1968; El Eid et al., 1983; Bond et al., 1984; Fryer et al., 2001; Waldman, 2008; Woosley, 2017, 2019).

(v) $260\,\mathrm{M}_\odot \lesssim M$: Above this limit the stars are thought to directly collapse to a massive black hole without any explosion (Fryer et al., 2001; Heger & Woosley, 2002).

Increasing the metallicity enhances stellar winds, which in turn changes the final fate of a star. This is a consequence of the stronger mass loss that peels away the envelope, resulting in a lower total mass and smaller core masses. In the more extreme cases, the stellar wind is strong enough to remove the whole hydrogen envelope, see green line in Figs.(I.2) and (I.3), and erode part of the core during the Wolf-Rayet phase. The stellar winds depend on the mass and the metallicity of the star - see Section I.2.2. Therefore, the fate of the stars with $10\,\mathrm{M}_\odot \lesssim M \lesssim 20-25\,\mathrm{M}_\odot$ is not greatly affected by the metallicity and they are thought to produce a supernova type II with a neutron star remnant at all metallicities. However, at higher masses the effects of stellar winds become more prominent, which is underlined by the discrepancy of the vertical boundaries in Figs.(I.2) and (I.3) for the higher masses. At an intermediate metallicity, the stars do not form cores massive enough to enter the pair-instability regime but their core and envelope are still sufficient for the star to directly collapse to a black hole (Yusof et al., 2013; Leung et al., 2019). Langer et al. (2007) estimate that a metallicity smaller than $Z_\odot/3$ is needed to form cores massive enough to enter the pair-instability region. At high metallicity stellar winds effectively remove the outer layers of stars with $M \gtrsim 30\,\mathrm{M}_\odot$, preventing the formation of a carbon-oxygen core mass that enters the pair-instability regime, nor are these stars massive enough for a direct collapse to a black hole. However, black hole formation via fallback is still possible. These stars explode as supernove type Ib or c[18] (Woosley et al., 1993; Eldridge & Tout, 2004; Georgy et al., 2012), reflecting the missing hydrogen lines, and helium lines in the latter, in the spectrum of the light curve, and form most probably a neutron star with a small range where black holes are formed,

[18]Contrary to the supernova types mentioned above, which are all related to the core-collapse of a massive star, supernovae type Ia are thermonuclear explosions of accreting white dwarfs. It is historically in the same classification as type Ib and c because all their spectra miss hydrogen lines (e.g. Filippenko, 1997; Turatto, 2003).

i.e. the range where slightly more massive cores are formed - see Section I.3.1.

It has to be stressed that the picture of the fate, in particular the mass range and metallicity dependence, presented above and in Figs.(I.2) and (I.3) is fraught with uncertainty and should only be interpreted as indicating trends. For example internal mixing processes strongly affect the post-main-sequence evolution (e.g. Langer & Maeder, 1995; Schootemeijer et al., 2019; Higgins & Vink, 2019; Kaiser et al., 2020). The different evolutionary paths lead to different structures of the stars, final masses and surface abundances on which the final fate will depend (e.g. Georgy et al., 2012; Yoon et al., 2012; Eldridge et al., 2013). Also, the different scenarios build upon the mass-loss rates during the various evolutionary stages and the scaling of stellar winds with metallicity and mass which themselves are quite uncertain and widely debated - see Section I.2.2. Additionally, stellar rotation greatly affects the fate of massive stars by enhancing the mass loss and enlarging the core mass due to rotation-induced mixing. This will be discussed in Section I.4.

Binarity influences the way a star evolves, mainly due to mass transfer- see discussion in Section I.5. Therefore, duplicity reduces the amount of red supergiants and increases the predicted amount of Wolf-Rayet stars and supernovae type Ib/c (Podsiadlowski et al., 1992; Eldridge et al., 2008), which is more in agreement with observations. Moreover, it changes the pre-supernova structure (e.g. Schneider et al., 2021; Laplace et al., 2021; Zapartas et al., 2021), hence, it will affect the explodability of stars - see Section I.3.1. However, binarity alone cannot explain all the observations and further physics is necessary to find a better agreement, such as stellar rotation - see Section I.4.

3.1 Core-Collapse Supernovae

3.1.1 Collapse, Bounce and Shock Formation

After core silicon burning, which is discussed in Section I.2.1.3.3, the star is made up of a core consisting of iron-group elements. This so-called iron core is surrounded by an onion-layered structure of active burning shells and the ashes thereof. Since the iron-group nuclei have the highest binding energy (Fewell, 1995), exothermic fusion reactions are not possible anymore. Therefore the star loses the dominant energy source that opposes gravity. As a consequence, if the core exceeds the Chandrasekhar mass, Eq. (I.3), it starts to contract and this will eventually turn into a collapse. However, active burning shells in the core region after core silicon depletion support it against contraction and the star will not immediately begin to collapse (Woosley et al., 2002).

During the core oxygen and silicon burning phases in massive stars, the electrons may become moderately degenerate depending on the initial mass of the star. This leads to the electrons having an increased Fermi energy, as discussed in Section I.2.1.3, allowing for otherwise prohibited electron captures on the ashes of the burning stages. This slowly turns the stellar matter more neutron-rich, i.e.

the neutron excess η[19] increases and the electron mass fraction, Y_e, decreases (Arnett & Thielemann, 1985; Thielemann & Arnett, 1985). η and Y_e not only reflect the subtle details of the abundance but have important effects on the nucleosynthesis, the core size and the dynamic behaviour of the resulting core-collapse. For example, the Chandrasekhar mass depends on Y_e. Baade & Zwicky (1934) were the first to suggest that a supernova is energised by the gravitational collapse of a star to a neutron star; Fig.(I.4) presents the current understanding of the core collapse evolution. The collapse is triggered by degenerate electron captures, reducing the now dominant degeneracy pressure that opposes the gravitational contraction. The contraction raises the density and temperature, leading to a growth of the electron capture rates, which depends strongly on the energy ($\sim E_e^5$). This results in a speed up of the collapse (Langanke et al., 2003; Thielemann et al., 2011; Burrows & Vartanyan, 2020). Contrary, in very massive stars, where the density is lower and the temperature higher, the pressure reduction is dominated by endothermic photodisintegrations instead of electron captures (Weaver et al., 1978; Thielemann et al., 2011). This early phase of the final stage of stellar evolution, where the core reaches densities of $\sim 10^{10}\,\mathrm{g\,cm^{-3}}$, is known as the pre-supernova stage. During this phase the neutrinos are still able to freely escape. However, the weak interaction rates increase as the collapse proceeds and the neutrino mean free path shortens, until they are eventually trapped. At this point, the weak interactions of electron and neutrino captures come into an equilibrium. Hence, Y_e and the critical Chandrasekhar-limit stop shrinking.

During this dynamical phase the inner part of the core collapses homogeneously, with $v_{\mathrm{collapse}} \sim r$, while the velocity at the edge of the core becomes supersonic. Therefore, matter in the core, which is able to "communicate" at the speed of sound, cannot "communicate" with the free-falling envelope. When the infalling core reaches nuclear densities of $\rho_c \sim 2 \times 10^{14}\,\mathrm{g\,cm^{-3}}$, repulsive nuclear forces stop the collapse. The infalling matter bounces back and launches an outward moving pressure wave through the core (Colgate et al., 1961; Bethe et al., 1979; Bethe, 1990), which turns into a shock wave when it reaches the supersonic infalling edge of the core. However, this shock wave does not have enough energy to launch the explosion (e.g. Myra & Bludman, 1989; Bethe, 1990) and is stalled, due to dissociation of heavy nuclei at the shock front and neutrino losses from the post-shock region, after it passed through about $0.25 - 0.5\,M_\odot$. Meanwhile, in the centre a proto-neutron star is formed.

The collapse happens on a very short, dynamical timescale which is a few hundreds of milliseconds from the onset of the collapse and it is reduced to a few milliseconds when the core bounces back at nuclear densities (e.g. Liebendörfer et al., 2003). Summing up, some hundreds milliseconds after the collapse was triggered, there is a hot and dense proto-neutron star, accreting matter, and a stalled shock, which has to be revived in order to obtain a successful explosion. The accreted matter on the surface of the proto-neutron star is cooled down by neutrino emission. For a long time it was

[19] The neutron excess is the sum over all species i, $\eta = \sum_i (N_i - Z_i) Y_i$ with the number abundance Y_i of the nuclear species i, the number of neutrons N_i and the number of protons Z_i (Arnett & Thielemann, 1985).

thought that this emission is the energy that revives the stalled shock (Bethe, 1990) and blows off the envelope. However, 1-dimensional simulations show that the energy deposition by neutrinos alone is not sufficient (Liebendörfer et al., 2001) and another effect is needed, possibly in combination with the neutrino energy deposition (Woosley & Janka, 2005; O'Connor & Ott, 2011). Possible effects that might help revive the shock are (i) convection between the proto-neutron star and the accretion front which increases the neutrino energy deposition, (ii) asymmetric instabilities of the accretion shock that could push the shock to larger radii, (iii) regions of inverted gravitational and density gradients subject to the Rayleigh-Taylor instability or (iv) asymmetric infall of shells (e.g. Falk & Arnett, 1973; Burrows et al., 1995; Fryer & Heger, 2000; Blondin et al., 2003; Scheck et al., 2004; Janka et al., 2005; Janka, 2012; Couch et al., 2015; Janka et al., 2016; Hix et al., 2016; Müller et al., 2017). Magnetic fields and rotation might also play a crucial role in exploding massive stars (e.g. Fryer & Heger, 2000; Piro & Ott, 2011; Janka et al., 2016; Summa et al., 2018). Indeed, multi-dimensional effects are crucial for a successful explosion and the neutrino-driven mechanism, in combination with other instabilities and asymmetries, is the most promising scenario[20] (e.g. Janka et al., 2016; Hix et al., 2016; Müller, 2020; Burrows & Vartanyan, 2020). Also, asymmetries in the supernova progenitor can enhance the neutrino-driven turbulent convection in the post-shock region, which aids the possible explosion (Kazeroni & Abdikamalov, 2020). However, while there exists a growing set of 2- and 3-dimensional core-collapse supernova explosion simulations, the full solution to the problem has not been solved yet in a self-consistent way (e.g. Nakamura et al., 2015; Janka et al., 2016; Bruenn et al., 2016; Burrows et al., 2018; Müller, 2020; Burrows & Vartanyan, 2020). For a recent review of the *state-of-the-art* simulations of core-collapse supernovae and their understanding, see e.g. Müller (2020); Burrows & Vartanyan (2020).

In the end, a process, or the combination of several processes, leads to the observed supernova explosion (e.g. Smartt et al., 2009). In this dynamical phase, a shock wave propagates outwards and pushes the surrounding layers into the interstellar medium, where it contributes to the galactic chemical evolution. The outward moving shock sets the condition for explosive burning, leading to the production of heavy elements in particular neutron- and proton-rich isotopes - see Section I.3.1.4. The composition of the ejecta is determined by the neutron excess η of the pre-explosive composition since the timescale of the explosive event is too short to change η (Thielemann & Arnett, 1985). The core-collapse event contributes to the galactic evolution via ejecta of nearly unburned matter from the outer stellar zones and explosively processed matter from the inner ejected zones (e.g. Thielemann et al., 1996). The outward moving shock, even if initially considered spherically symmetric, develops non-spherical instabilities. Those instabilities affect the propagation of the shock and introduce mixing. The non-spherical effects are important to understand observations, such as supernova 1987A,

[20] Multi-dimensional effects are not only crucial for the neutrino-driven explosions but also for alternative scenarios, for example the magnetohydrodynamic mechanism (Akiyama et al., 2003; Winteler et al., 2012)

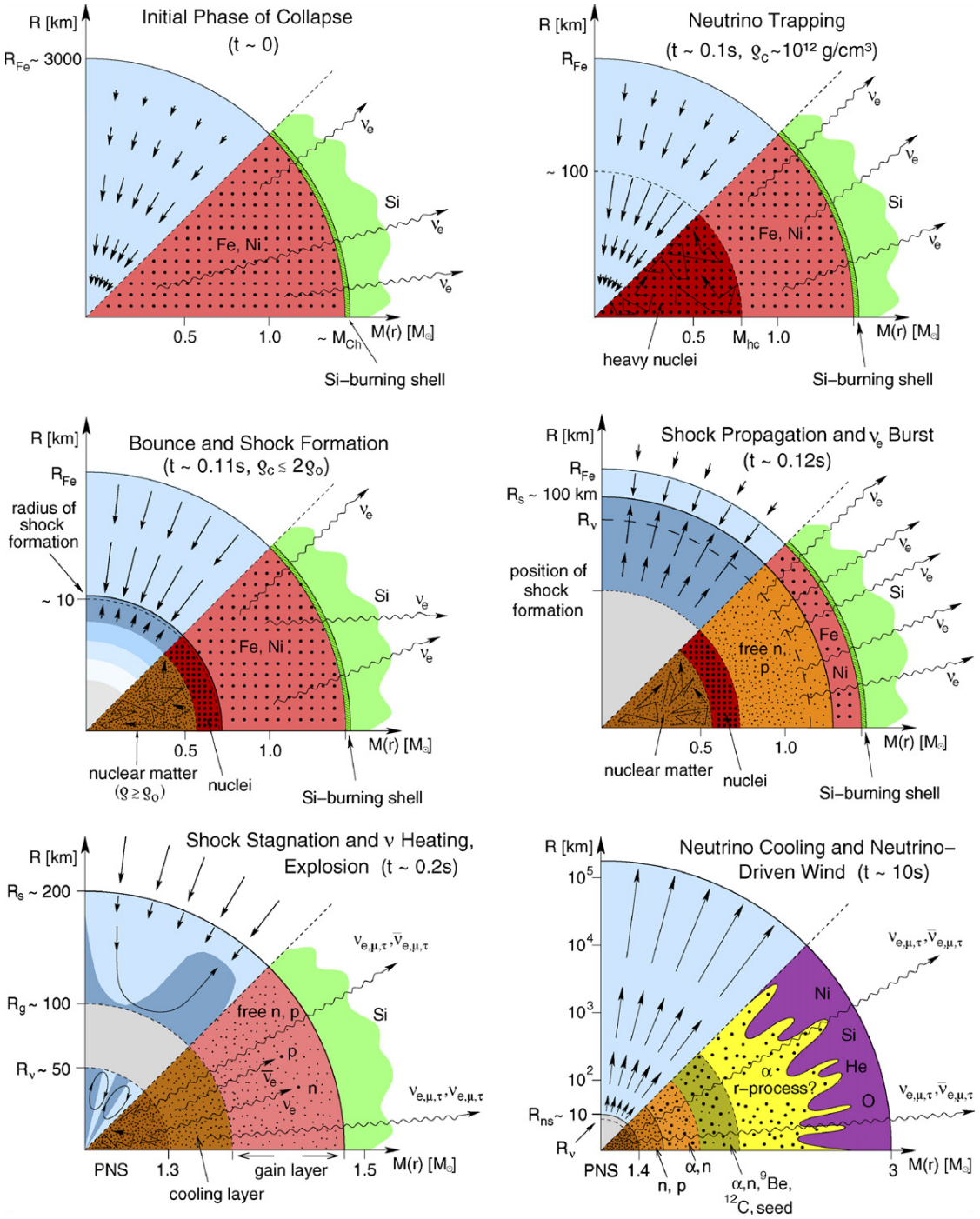

Figure I.4: A schematic representation of the evolutionary phases of a core collapse supernova, starting with the collapse of the core, through the bounce and formation of the shock up to the neutrino-driven wind during the neutrino-cooling phase of the proto-neutron star. Each panel is separated in an upper part, which shows the dynamics with the arrow indicating the velocity vectors, and a lower part, presenting the nuclear composition and the nuclear and weak processes. The vertical axis gives the corresponding radii whereas the horizontal axis shows the mass coordinates. The accronyms have the following meanings: $R_{\rm Fe}$ - iron core radius, $R_{\rm S}$ - shock radius, $R_{\rm g}$ - gain radius[a], $R_{\rm ns}$ - neutron star radius, R_ν - neutrinosphere, $\nu_{e,\mu,\tau}$ - electron, muon and tau neutrinos. The figure is taken from Janka et al. (2007).

[a] Only if the neutrino heating is sufficiently strong, an explosion can be triggered (see text below and Bethe & Wilson, 1985; Burrows & Goshy, 1993; Janka, 2001). Strong heating of the accreted matter reduces the infall speed and prolongs the neutrino-heating time. On the other hand, strong cooling can accelerate the accretion flow through the gain layer, which reduces the neutrino-heating time. The gain radius $R_{\rm g}$ is defined as the radial coordinate where the neutrino heating and the neutrino cooling, both per nucleon, are equal.

e.g. the light curve or the details of the spectrum (see discussions in e.g. Woosley et al., 2002; Smartt et al., 2009; Smartt, 2009; Langer, 2012).

3.1.2 The Progenitor of Core-Collapse Supernovae

The diversity of the supernova light curves and spectra reflects the different envelope properties of the progenitor stars, such as the envelope mass, the radius and chemical composition (Young, 2004). On the other hand, the observed explosion energies, the amount of radioactive nickel and the geometry of the ejecta are determined by the core properties of the progenitor, essentially by the core mass, density structure, spin and magnetic field (e.g. Woosley et al., 2002; Kasen & Woosley, 2009). Therefore it is essential to know, for example, whether the star evolves as a blue or red supergiant after the main sequence as it will affect its supernova progenitor structure, in particular the compactness, core masses and the total mass of the star. This in turn influences the explosion type and the compact remnant. The long-standing disagreement whether a star will be a blue or red supergiant - see Chapters III and IV but also for example the reviews Maeder & Meynet (2012); Langer (2012) - prevents a reliable prediction concerning the nature of the supernova progenitor in different environments. Also, while red supergiants in the Local Group are observed with masses up to $25\,M_\odot$ Smartt et al. (2009) found a lack of supernova II-P[21] above $\sim 17\,M_\odot$. They call this the "*red supergiant problem*" for which they did not find a satisfactory explanation. Suggested explanations include the modification of our understanding of stellar physics, such as mass-loss rates (Yoon & Cantiello, 2010; Georgy, 2012; Meynet et al., 2015) or the threshold mass for black-hole formation (Smartt et al., 2009), and systematic effects that lead to underestimation of the supernova progenitor mass, such as errors in the bolometric corrections (Davies et al., 2013) or the amount of circumstellar extinction (Walmswell & Eldridge, 2012)[22]. None of these explanations can satisfactorily explain the discrepancy (see e.g. discussion in Davies, 2017), however, some authors argue that the statistical significance of the "*red supergiant problem*" is within two standard deviations (Davies & Beasor, 2020a), thus, that there is no "*problem*". This claim is in controversy (Kochanek, 2020; Davies & Beasor, 2020b). Nevertheless, recent observations found a new type of pulsating yellow supergiant[23] (Dorn-Wallenstein et al., 2020). They identify these stars as post red supergiant stars, i.e. the star evolved back towards the hotter part of the Hertzsprung-Russell diagram after losing a large part of their envelope during the red supergiant phase. Furthermore, the authors estimate the lowest mass of the observed pulsating yellow supergiants to be close to the highest mass of the red supergiant supernova progenitor. Therefore, the missing red supergiant supernova progenitor could in fact be red supergiants that evolve to the yellow

[21] This is the most common core-collapse supernova and is thought to be produced by red supergiants.
[22] While binary evolution should also be considered as a solution to the "*red supergiant problem*", Zapartas et al. (2021) discuss that binarity does not significantly affect the issue.
[23] A yellow supergiant is an evolved post-main-sequence star. They are more compact than red supergiants and have a slightly hotter surface temperature, i.e. $3.9 \gtrsim \log T_{\rm eff} \gtrsim 3.66$ (Parsons, 1971).

supergiant phase shortly before the supernova event. However, the detailed evolutionary scenario is still unclear and further theoretical and observational work needs to be done. A possibility could include pre-supernova outbursts shortly before the collapse (Fuller, 2017; Leung & Fuller, 2020) - see also discussions in Chapters III and IV.

3.1.3 Explodability and Black Hole Formation

After a shock wave was successfully launched, a stable neutron star is formed. However, a stellar mass black hole is the outcome of the core-collapse if (O'Connor & Ott, 2011)

(i) The shock energy is not enough to eject all of the accreted matter of the proto-neutron star. In this case the matter will fall back onto the nascent neutron star which collapses further to a black hole.

(ii) Nuclear phase transitions occur during the proto-neutron star cooling.

(iii) The explosion mechanism fails to revive the stalled shock. Then, accretion of material pushes the proto-neutron star over its maximum mass of $M_{NS,max} \sim 2.1\,M_\odot$, whereby it collapses to a black hole (e.g. Woosley & Weaver, 1995).

The black hole formation is not instantaneous in ordinary massive stars but is always preceded by a proto-neutron star phase, with neutrino cooling and gravitational wave emission, until the proto-neutron star is engulfed by the black hole horizon.

A major question is the mapping between the progenitor mass and the outcome of the core-collapse supernova event, i.e. at which progenitor mass does the scenario of a successful explosion with a neutron star turn into a black hole as the final fate. This is still debated and there might not even exist such a clear limit, see below.

As discussed above, a core-collapse supernova is a multi-dimensional process and asymmetries are crucial in launching the explosion. 1-dimensional models are unable to reproduce these characteristic features, such as the coexistence of accretion flows and expanding plumes shortly after the onset of the explosion (see e.g. discussion and references in Müller, 2020) However, recent 3-dimensional simulations show a pronounced sphericity, hence the average condition resembles a shock expansion obtained under the assumption of spherical symmetry. This supports pragmatic 1-dimensional parametrised explosion studies, allowing the investigation of large sets of core-collapse supernova progenitors.

Many recent studies of 1-dimensional progenitors of core-collapse supernovae show a non-linear behaviour of the pre-supernova compactness and the explodability as a function of the initial mass of the star (O'Connor & Ott, 2011; Ugliano et al., 2012; Sukhbold & Woosley, 2014; Sukhbold et al., 2016; Müller et al., 2016; Ertl et al., 2016; Sukhbold et al., 2018; Ebinger et al., 2019; Chieffi & Limongi, 2020). The non-linearity is sensitively linked to the convective history during the advanced phases of stellar evolution, for example the change from convective to radiative core carbon burning or the

relative timing of the convective zones with respect to each other. While some authors find a nearly chaotic behaviour (e.g. Sukhbold & Woosley, 2014; Sukhbold et al., 2016, 2018), others argue that this chaotic behaviour is due to the improper treatment of the numerics (e.g. Chieffi & Limongi, 2020, M. Limongi, private communication). In general, there is an increase of the explosion energy up to about $\sim 18 - 20\,M_{\odot}$ (e.g. Sukhbold et al., 2016; Ebinger et al., 2019) and beyond $\sim 20\,\mathrm{M}_{\odot}$ there is a transition to black hole formation. This picture seems to be in line with observations (e.g. Smartt, 2015). However, theoretical models predict "*islands of explodability*" above $20\,\mathrm{M}_{\odot}$ where successful explosions are obtained, while black hole formation can also be obtained for a few lower mass models (Sukhbold & Woosley, 2014; Sukhbold et al., 2016; Müller et al., 2016; Ertl et al., 2016; Sukhbold et al., 2018; Ebinger et al., 2019; Chieffi & Limongi, 2020). The observational constraints, on the other hand, are quite consistent with black hole formation above $\sim 18\,\mathrm{M}_{\odot}$ (e.g. Smartt, 2015). This contradiction between observations and model prediction is still under debate. Above $\sim 35\,\mathrm{M}_{\odot}$ the models predict a general tendency of black hole formation. While the details of the models depend on the physics such as metallicity, treatment of rotation, mass-loss rates, nuclear reaction rates, etc., the general trend remains (e.g. Ebinger et al., 2017). How rotation and magnetic fields affect this picture is still debated - see Section I.4 and Chapter IV.

3.1.4 Explosive Burning

Many of the hydrostatic thermonuclear burning processed described in Section I.2 also occur under explosive conditions. The key difference to the hydrostatic burning is that the temperature reaches much higher values as the post-bounce shock moves through the interior of the star and the burning proceeds on a much shorter timescale. The timescales are much shorter than the $\beta^{+/-}$-decay half-life times, leading to a significant production of unstable neutron-rich isotopes, via the rapid neutron capture process (r-process), or proton-rich nuclei, via proton capture processes (e.g. νp-process), during the explosive phase, see below. The fuel for the explosive nucleosynthesis consists of the ashes of the prior hydrostatic burning phases discussed in Section I.2, mainly nuclei with $N = Z$ like ^{12}C, ^{16}O, ^{20}Ne, ^{25}Mg or ^{28}Si, resulting again in nuclei with $N = Z$. For example the products of explosive oxygen and silicon burning are similar to the hydrostatic burning case with a slightly modified isotopic pattern (e.g. Woosley et al., 1973). Also, at higher densities, captures of degenerate electrons are important, shifting $Z \rightarrow Z - 1$, as discussed above.

Explosive silicon burning proceeds slightly differently from its hydrostatic version, discussed in Section I.2.1.3.3, and it can be separated in three different regimes depending on the temperature and density (Woosley et al., 1973; Hix & Thielemann, 1999); (i) at lower temperatures, roughly $T < 5\times10^{9}$, cooling of the burning region due to expansion halts the burning of silicon prematurely. This so-called *incomplete silicon burning* results in a larger concentration of intermediate mass elements than suggested

by the nuclear statistical equilibrium. For higher temperatures, silicon is completely exhausted and a full nuclear statistical equilibrium is reached. However, (ii) at lower densities, roughly $\rho < 10^8\,\mathrm{g\,cm^{-3}}$, the nuclear abundance consists of a large number of light nuclei, especially ^{4}He. The inability of the triple-α reaction to keep the light nuclei and the nuclei beyond $A = 12$ in a nuclear statistical equilibrium, because of the quadratic dependence of the reaction rate, prevents the incorporation of the lighter nuclei into heavier nuclei. This results in a large ^{4}He abundance after freeze-out, hence, an *α-rich freeze-out*. On the other hand, (iii) at higher densities a full nuclear statistical equilibrium is reached, where the light nuclei form heavier nuclei as the temperature drops. This is referred to as *normal freeze-out*.

After the freeze-out large ratios of neutrons to seed-nuclei can be obtained due to the electron captures $p + e^- \rightarrow n + \nu_e$, which neutronise matter (Burbidge et al., 1957). Under these conditions it is possible to experience r-process production, synthesising the heaviest neutron-rich nuclei (Woosley & Hoffman, 1992). The difference to the s-process discussed in Section I.2.1.2 is that the neutron flux is much higher and occurs in a hotter environment. This allows the production of nuclei far from stability with extremely short β-decay half-lives. These nuclei then β-decay back into stable heavy nuclei. While it is thought that the scenario of two merging neutron stars is the main site for the r-process (Arcavi et al., 2017; Kasen et al., 2017; Smartt et al., 2017; Pian et al., 2017; Thielemann et al., 2017b; Côté et al., 2018; Frebel & Beers, 2018) it cannot be the only source of the r-process and other scenarios, possibly rare classes of supernovae, are responsible for a non-negligible amount of r-process production, especially in the early Universe (Winteler et al., 2012; Thielemann et al., 2017a; Côté et al., 2019). Historically, neutrino-driven winds in regular core-collapse supernovae have been discussed as possible sites for the r-process (Woosley et al., 1994; Takahashi et al., 1994; Farouqi et al., 2010). However, this site is contradicted by observational constraints and simulations show at most a weak r-process (Martínez-Pinedo et al., 2012; Roberts et al., 2012), which is responsible for only lighter nuclei with $A < 130$ (Wanajo & Ishimaru, 2005; Shibagaki et al., 2016).

During the explosive supernova event, a range of proton-rich nuclei are synthesised. Contrary to the r-process, proton captures are limited due to the increasing Coulomb-barrier of the heavier elements. Therefore, only light elements can be synthesised via direct proton captures (e.g. Rauscher, 2010). The heavier proton-rich isotopes are produced by a combination of several processes. One is the γ-process, also known as p-process, where energetic photons photodisintegrate neutron-rich elements, synthesising proton-rich isotopes (Rauscher et al., 2002; Arnould & Goriely, 2003; Rauscher, 2010). This process is possible in layers where the supernova shock wave moves through, but also in hydrostatic burning phases such as the oxygen-neon layers in massive stars (e.g. Rauscher et al., 2002). The different sites will obviously influence the resulting proton-rich abundances, i.e. the different temperature and timescale or the available seed nuclei. The latter implies that this production is

secondary because it relies on the production of seed nuclei from another process. On the other hand, in the innermost ejected layers of core-collapse supernovae very proton-rich conditions are found due to the interaction of the neutrino winds with matter. Therefore, as matter freezes out from nuclear statistical equilibrium, sequences of rapid proton-captures and β-decays along the proton drip line produce proton-rich nuclei. The proton-captures are hindered by (γ,p)-reactions but can be bypassed by (n,p) reactions, where a constant neutron flux is provided by $\overline{\nu}_e + p \rightarrow e^+ + n$. This process is termed the νp-process (Fröhlich et al., 2006) and produces light proton-rich isotopes.

3.2 Pair Instability

In helium cores with masses larger than $\sim 40\,\mathrm{M}_\odot$ the high central temperatures and low central densities lead to the thermal concentration of free electron-positron pairs in the core before oxygen ignition (Rakavy & Shaviv, 1967). This effect is the so-called *pair-instability* and it reduces the thermal energy which normally would contribute to pressure. Therefore, the pressure in the core does not increase fast enough to counter its contraction. The strength of the instability determines the contraction speed of the core to higher temperatures, during which the core amasses a considerable amount of momentum. The rising temperature during the fast contraction causes oxygen and in some cases silicon to rapidly burn in an explosive manner - see Section I.3.1.4. The further outcome of this instability depends on the mass of the contracting core, the energy generated by the burning and when it ignites. In particular the extra energy from burning and the partial recovery from the instability when the photons become relativistic might slow down the collapse. If the burning is able to be active long enough before the collapse is stopped, it has generated enough energy to reverse the collapse into an explosion. On the other hand, if the helium core mass is large enough, i.e. above $\sim 133\,\mathrm{M}_\odot$, the contraction cannot be halted and the core continues collapsing to a black hole (Fryer et al., 2001). Therefore, the pair-instability region is limited to the mass range of $\mathrm{M_{He}} \sim 40 - 133\,\mathrm{M}_\odot$.

In case an explosion occurs, it can be of two varieties. If the thermodynamic burning is able to deposit enough energy then the reversed shock wave can unbind the whole star in a single pulse, resulting in a powerful *pair-instability supernova* exceeding 10^{53} ergs (Fraley, 1968; El Eid et al., 1983; Bond et al., 1984; Fryer et al., 2001; Waldman, 2008). If the energy deposition is not enough to entirely disrupt the star, it will nonetheless expand violently, throwing off a large part of its outer layers (Barkat et al., 1967; Woosley et al., 2007; Kozyreva et al., 2017; Gilmer et al., 2017; Leung et al., 2019). The amount of ejected mass by these thermonuclear outbursts can vary, from a very mild ejection, where nearly no matter is lost, up to extremely large ones with over 10^{51} ergs in one pulse. After the pulse the star will slowly contract until the pair-instability is encountered again and the process repeats itself. The star continues pulsating until enough mass has been ejected and entropy in form of neutrinos has been lost so that the pair-instability is avoided. This typically needs a reduction of the helium

core mass to about $40\,M_\odot$ or below. In general, the lower mass range experiences more but weaker pulsations but more in numbers, whereas the heavier stars go through fewer but stronger pulsations (e.g. Woosley, 2017, 2019; Leung et al., 2019). The remaining, compact star then evolves smoothly until it has formed an iron-core after silicon burning, which gravitationally collapses to a black hole (Woosley et al., 2007; Waldman, 2008; Powell et al., 2021); partial mass ejection is possible but this is still an open question. This is often called *pulsational pair-instability supernova*.

Generally, helium core masses between $40\,M_\odot$ and $133\,M_\odot$ encounter the pair-instability followed by mass ejection (Bond et al., 1984; Heger & Woosley, 2002; Chatzopoulos & Wheeler, 2012; Woosley, 2017, 2019; Leung et al., 2019). From this mass range, helium cores with $64\,M_\odot \lesssim M \lesssim 133\,M_\odot$ will produce a pair-instability supernova. Helium cores in the mass range $40-64\,M_\odot$ experience violent pulsations but they are not strong enough to entirely disrupt the star, hence they produce a pulsational pair-instability supernova. These mass-limits are sensitive to the input physics (Farmer et al., 2019; Renzo et al., 2020; Umeda et al., 2020).

The pair-instability supernova entirely disrupts the star and does not leave any compact remnant. Therefore, there will be a gap in the distribution of black hole masses, the *pair-instability mass-gap*, and no black hole with a mass between $\sim 50\,M_\odot$ and $\sim 150\,M_\odot$ is expected from a theoretical point of view. However, a recent discovery of a binary black hole merger with two black hole components of $85\,M_\odot$ and $66\,M_\odot$ challenges this view (Abbott et al., 2020a,b).

In the previous paragraph, the pair-instability region is only given in terms of the helium core mass because of two reasons. First, while it would be possible to map the helium core mass to the initial mass of a star, this correlation depends on the metallicity. Furthermore, it would be very uncertain due to the missing details, such as the internal mixing processes and mass loss. Second, many recent studies of the (pulsational) pair-instability supernova limit themselves to pure helium stars (e.g. Heger & Woosley, 2002; Woosley, 2017, 2019; Farmer et al., 2019; Renzo et al., 2020, to name a few). This avoids the calculation of the numerically unstable envelope of the very massive stars and reflects the possible binary interaction where it is thought that the hydrogen envelope is removed by the more compact partner. While the hydrogen envelope might not affect the pair-instability region, the final black hole mass of the stars might be affected and massive single stars could produce black holes that lie in the pair-instability mass-gap (see e.g. Belczynski et al., 2020b; Farrell et al., 2020).

At solar metallicity, strong stellar winds remove the entire hydrogen envelope and part of the core mass of very massive stars (e.g. Yusof et al., 2013; Leung et al., 2019). These stars therefore avoid the pair instability. Only stars with a metallicity below $\sim Z_\odot/3$ retain enough mass to enter the pair-instability regime (Langer et al., 2007).

4 Rotation in Massive Stars

Stars rotate. This is a long-known fact and it was first observed by spectroscopy. The wider lines in spectroscopic observations due to the Doppler effect allow us to measure the surface rotation rates. Massive stars rotate with typical rotation rates between $0 - 250\,\mathrm{km\,s^{-1}}$ on the main sequence with an average rotation rate at the equator of $200\,\mathrm{km\,s^{-1}}$ (e.g. Huang & Gies, 2006a; Hunter et al., 2008; Dufton et al., 2013). Such observations also show that the post-main-sequence surface rotation rate is relatively small with $0 - 100\,\mathrm{km\,s^{-1}}$ (e.g. Huang & Gies, 2006b; Dufton et al., 2006; McEvoy et al., 2015).

Asteroseismology (e.g. Beck et al., 2011), the study of stellar oscillations, allows observers to gain information about the internal structure of stars. Therefore, asteroseismic observations can determine the internal rotation rate of stars (e.g. Beck et al., 2014; Deheuvels et al., 2014; Aerts et al., 2017). These measurements show that main-sequence stars rotate nearly uniformly, but during the post main sequence the core spins up and the envelope slows down, resulting in differential rotation.

In addition to the direct observations of rotation mentioned above, there are also more indirect hints of rotation-induced effects. For example, nitrogen and helium enhancements at the surface of massive main-sequence stars (e.g. Gies & Lambert, 1992), however, this could also be a result of binary interaction. Other examples are the number ratios of Wolf-Rayet to O-stars, of blue to red supergiants and of supernovae Ib to Ic, which are better reproduced by rotating models (Maeder & Meynet, 2001; Meynet & Maeder, 2003, 2005). Also, the dependency of long gamma-ray bursts on metallicity shows a better agreement with rotation (Yoon et al., 2006) and the nucleosynthetic signature of very metal-poor stars is better explained with fast rotating massive stars than non-rotating stars (Chiappini et al., 2011).

Rotation changes the way of stellar evolution and therefore, rotational effects need to be included in stellar evolution theory.

4.1 Effects of Rotation on Structure

Including rotation in stellar evolution simulations changes the structure of stars and how they evolve. The general effects of rotation can roughly be summarised as follows (see e.g. the review of Maeder, 2009):

(i) Rotation changes the equilibrium configuration of stars. The gravitational force, which points directly towards the centre in non-rotating stars, is modified by the centrifugal force. Consequently the hydrostatic equilibrium changes to $\nabla P = \rho \mathbf{g}_{\mathrm{eff}}$, with the effective gravity $\mathbf{g}_{\mathrm{eff}}$ which results from the gravitational and centrifugal acceleration. For solid body rotation or a rota-

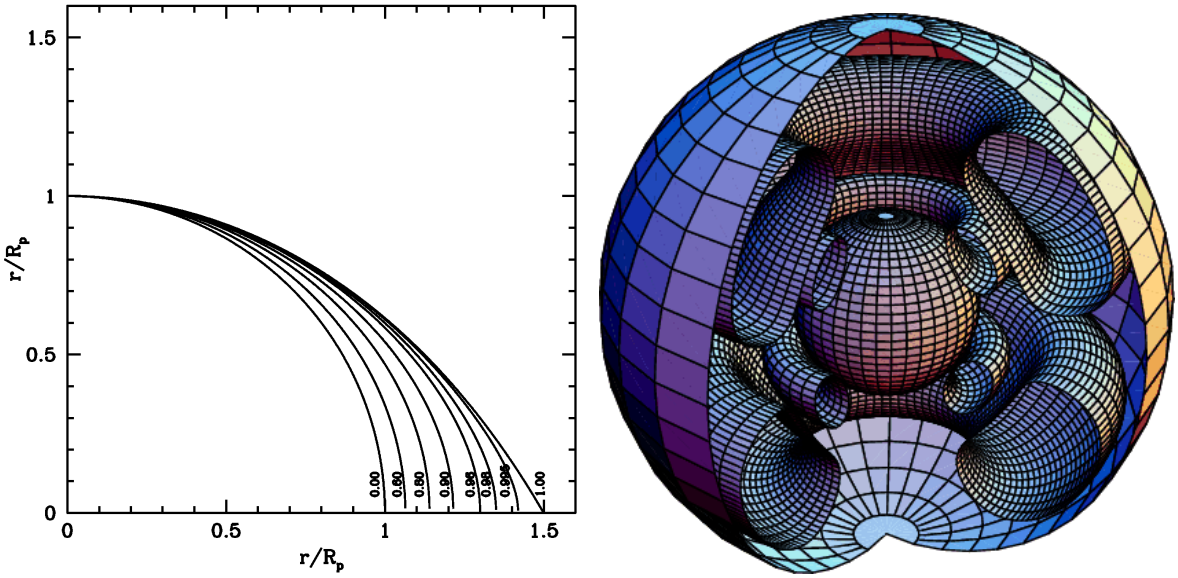

(a) Equipotential with varying ω

(b) The meridional circulation

Figure I.5: (a) The shape of the surface equipotential for different rotation rates $\omega = \frac{\Omega}{\Omega_{\rm crit}}$, labelled at the bottom of each curve. The radii on both axes are given as a fraction of the polar radius, where the polar radius is plotted on the y-axis and the equatorial axis on the x-axis. The figure is taken from Georgy et al. (2011).
(b) A representation of the streamlines of the meridional circulation in a $20\,M_\odot$ star at solar metallicity and $v_{\rm ini} = 300\,{\rm km\,s^{-1}}$ at the start of hydrogen burning as a function of M_r. The inner sphere is the boundary of the convective core and the outer boundary is the surface of the star. On the outer streamlines in the upper right corner matter turns counter clockwise whereas on the inner it turns clockwise. The figure is taken from Meynet & Maeder (2002).

tion rate constant on cylindrical surfaces, the modified hydrostatic equation implies that the pressure is constant on an equipotential, i.e. a surface with the same potential. Therefore, the equipotentials and isobars match, which is said to be barotropic. Also, for these two rotation laws, the temperature and density are constant on isobars. The stellar surface, for example, is an equipotential. Contrary, for shellular rotation, where the rotation rate is constant on isobaric shells, the surfaces of constant pressure intersect the equipotentials but do not coincide, i.e. the star is baroclinic. In this case, the temperature and pressure are not constant on isobars.

Another result of the additional centrifugal acceleration is that the effective gravity changes with latitude; it is highest at the poles and decreases towards the equator. Consequently, a rotating star is more extended at the equator than at the pole due to the reduced gravity (see Fig.(I.5a)). The deformation is more extreme for a faster rotation rate. What is more, the centrifugal force lets stars behave as if they have a reduced effective mass (Endal & Sofia, 1976; Meynet & Maeder, 1997). The rotation rate at which the centrifugal force becomes equal to the gravitational attraction at the equator is the star's critical rotation velocity. Above this break-up velocity, there is no stable configuration for the star.

Rotation also affects the thermal equilibrium in stars. Similar to the surface equipotential, the equipotentials in the interior are distorted; they are closer to each other at the polar than at the

equatorial region. Since the radiative flux at some latitude is proportional to the local gradient between the equipotentials, there is an excess of flux in the polar region and a deficiency in the equatorial region[24]. This thermal imbalance creates large circulation motions in the meridian planes, which transport chemical elements and angular momentum (see Fig.(I.5b) and Section II.2.2)). Moreover, the von Zeipel theorem (von Zeipel, 1924a) relates the radiative flux on the surface of a rotating star to the local effective gravity. This leads to the surface temperature $T_{\rm eff}$ being proportional to $g_{\rm eff}$, thus, the star is hotter at the polar region and cooler at the equator (von Zeipel, 1924b). This effect is called gravity-darkening.

(ii) Rotation affects the stellar winds discussed in Section I.2.2 in two ways (Maeder & Meynet, 2000b); first it increases the average mass-loss rate for a given luminosity and surface temperature (see Fig.(I.7)). Second, the hotter polar regions have a higher radiation pressure, making the stellar winds anisotropic (Georgy, 2010). In stars that evolve near the Eddington-limit the radiation pressure reduces the threshold of the critical break-up rotation velocity discussed in point i. Therefore, even a modest rotation rate could potentially significantly increase the mass-loss rates (Maeder & Meynet, 2000b; Gagnier et al., 2019). However, the dependence of the mass-loss rates on the changes of the equilibrium configuration of rotating stars and vice versa, how rotation depends on the mass-loss rates, i.e. by removing angular momentum, is not completely understood yet (Vink et al., 2010; Müller & Vink, 2014).

(iii) Rotation drives global internal circulation currents due to the thermal imbalance explained in point i - see also Section II.2.2. In addition to that, the rotation rate throughout the star is often not constant with layers rotating at different speeds. This differential rotation leads to several kinds of instabilities which result in turbulent motions. One dominant process, for example, is the shear turbulence, where a shear between two layers with different rotation speeds induces mixing. All these processes mix the chemical elements and transport angular momentum - see Chapter II.2.

(iv) Rotation interacts with magnetic fields. This may couple layers that rotate at different rates, leading to solid body rotation. External magnetic fields might also interact with the surrounding stellar medium and brake down rotating stars. Section II.3 discusses magnetic fields in rotating stars, possible dynamos and their impact.

4.2 The Evolution of Rotating Stars

How does the picture of stellar evolution discussed in Section I.2 change in the presence of rotation? Rotation mainly influences the evolution of a star during core hydrogen burning, and maybe core helium burning, because this is the longest burning stage. The impact of rotation during the more

[24] Assuming there is no local energy source or sink.

advanced stellar stages is minor because the timescales of the rotational effects are much longer than the evolutionary timescales. The evolutionary path of massive rotating stars can be divided into two groups (Hirschi et al., 2004); in stars with $M \lesssim 30\,\mathrm{M}_\odot$ at solar metallicity rotation-induced mixing dominates and in stars with $M \gtrsim 30\,\mathrm{M}_\odot$ the rotation-enhanced mass loss dominates. The effects of rotation-induced mixing become more important in the more massive stars at lower metallicity, where the mass loss is weaker and less angular momentum is lost through stellar winds (Hirschi, 2007).

4.2.1 Evolution of Rotation

The distribution of angular momentum in a star at different phases is crucial to simulate the evolution of a rotating star. It is important to treat the evolution of angular momentum self-consistently because the rotation rate determines the behaviour of rotation-induced instabilities, which themselves transport angular momentum, as mentioned above and discussed in more detail in Chapter II. While turbulent convection is the most efficient angular momentum transport mechanism, it has been shown that in the radiative layers of rotating massive stars angular momentum is dominantly transported by the meridional currents and the rotational shear instability (Meynet & Maeder, 2000; Heger et al., 2000). This changes the rotation rate in different layers and rotation modifies itself.
The knowledge of the interior distribution of rotational velocity is important to estimate the total angular momentum content of the star on the zero-age main sequence. Nowadays, it is often assumed that a star is formed with solid body rotation. This is a very simplifying assumption but the exact shape of the profile is not very important. Indeed, the initial angular momentum distribution inside the star converges rapidly towards an equilibrium profile due to two opposing effects; the meridional currents tend to increase the gradient in the rotation rate whereas the rotational shear tends to decrease this gradient (Denissenkov et al., 1999; Meynet & Maeder, 2000; Maeder, 2009).

With the knowledge of the initial rotation rate on the zero-age main sequence, stellar models can be used to predict the evolution of the rotation rate. Fig.(I.6a) depicts the evolution of the surface rotation velocity of various models. The evolution from the start on the left until there is a sharp peak in the surface rotation rate is the main-sequence evolution. The evolution of the surface rotation rate during the main-sequence is an interplay between the meridional flows, which transport angular momentum to the surface, and stellar winds, removing angular momentum. This interplay becomes more obvious when comparing the models with "*standard*" mass loss, indicated by the solid lines, to the model without mass loss, $\dot{M} = 0$ in Fig.(I.6a). In the latter, the surface velocity increases until it reaches the critical break-up velocity near the end of the main-sequence phase (Meynet & Maeder, 2000). A consequence of the interaction of meridional flows and mass loss is that in models at solar metallicity with "*standard*" mass loss the surface velocity decreases as a function of time. This reduction is stronger for larger initial masses because of the stronger stellar winds that remove angular

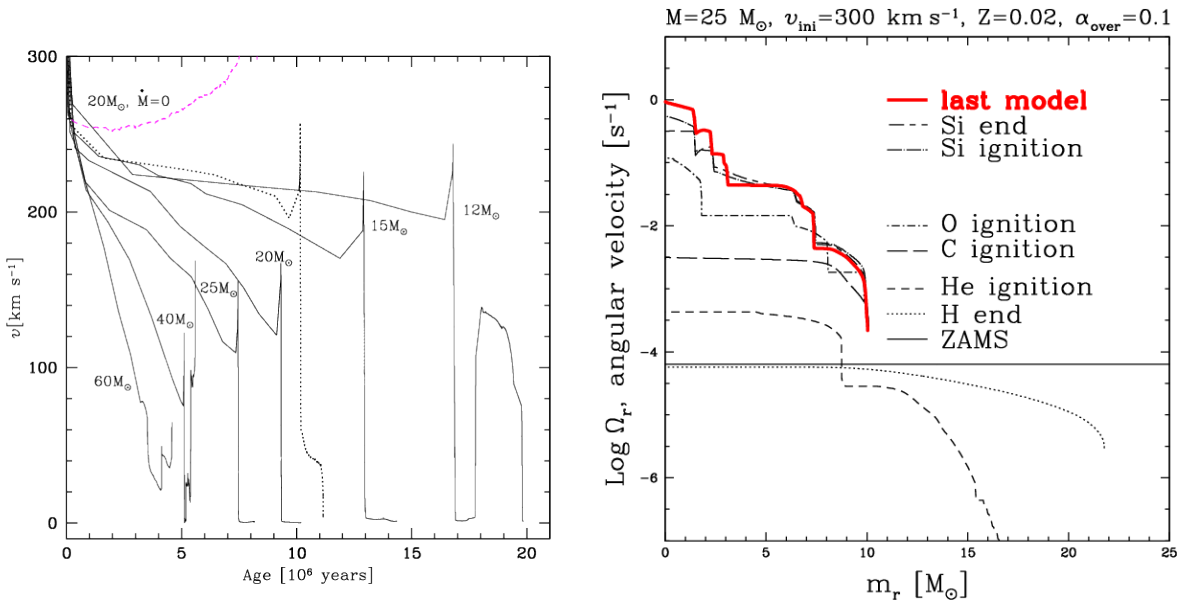

(a) Evolution of the surface rotation velocity

(b) Rotation profile at different stellar stages

Figure I.6: (a) Evolution of the surface equatorial velocity as a function of time for stars of different initial masses and an initial velocity of $v_{\rm ini} = 300\,{\rm km\,s^{-1}}$. The continuous lines refer to solar metallicity models, the dotted line corresponds to a $20\,{\rm M}_\odot$ model with $Z = 0.004$ and the dashed pink line corresponds to a $20\,{\rm M}_\odot$ model without mass loss. The figure was taken from Meynet & Maeder (2000). (b) The angular velocity as a function of the Lagrangian mass coordinate m_r inside a $25\,{\rm M}_\odot$ model with an initial velocity $v_{\rm ini} = 300\,{\rm km\,s^{-1}}$ at various evolutionary stages. Figure was taken from Hirschi et al. (2004).

momentum from the surface. By comparing the $20\,{\rm M}_\odot$ model at solar metallicity and $Z = 0.004$, the dotted line in Fig.(I.6a), it becomes also apparent that there is less reduction of the surface rotation velocity at lower metallicity due to the weaker winds. Therefore, models at lower metallicity or lower initial mass can reach the critical break-up velocity more easily during the main-sequence evolution. Such a scenario would impact the evolutionary and structural properties of the star.

The peak in the surface rotation velocity at the end of the main sequence in Fig.(I.6a) is a consequence of an overall contraction after core hydrogen depletion. The immediate reduction of $v_{\rm surf}$ thereafter results from the expansion of the star during the redwards evolution, because angular momentum is conserved. Accordingly, the surface rotation velocity in all the stellar models becomes small, whatever the initial rotation was (Meynet & Maeder, 2000).

The evolution of the interior rotation profile is shown in Fig.(I.6b) in the form of the angular velocity, Ω, in a $25\,{\rm M}_\odot$ model for different stages. The change of Ω results from many different processes; (i) shear erodes Ω-gradients while meridional circulation flows erode or build them. (ii) Convection enforces solid body rotation, resulting in a constant Ω. (iii) Contraction and expansion, respectively increases or decreases Ω due to local angular momentum conservation and (iv) mass loss removes angular momentum from the surface, reducing Ω. The combination of these processes lead to an overall decrease of Ω during the main-sequence evolution (Meynet & Maeder, 2000; Hirschi et al.,

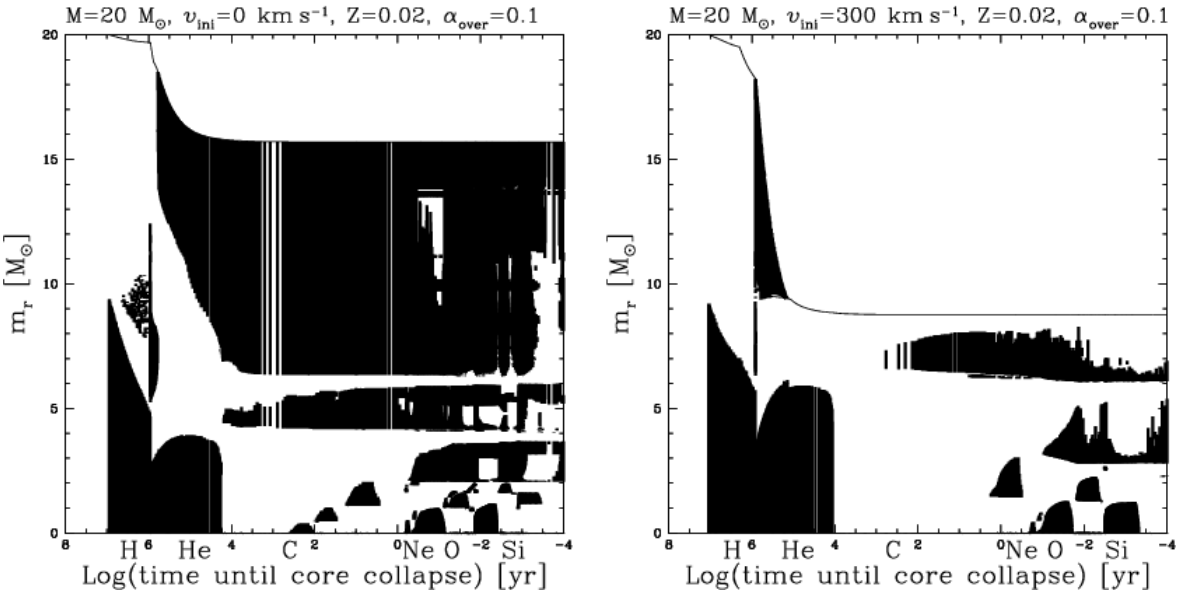

Figure I.7: Kippenhahn diagrams with the Lagrangian mass coordinate on the y-axis, showing the structural evolution as a function of the time left until core-collapse. The central burning phases are indicated below the x-axis. The black shading depicts convective zones and the top black line shows the surface of the star. The left figure shows a non-rotating $20\,M_\odot$ model, whereas on the right a rotating $20\,M_\odot$ model is presented. The key parameters are given on top of the plots. The figure was taken from Hirschi et al. (2004).

2004). However, the post-main-sequence evolutionary timescale is shorter than the timescale of the secular rotation-induced angular momentum transport processes and therefore the evolution seen in Fig.(I.6b) is mainly determined by (ii), (iii) and (iv) (Meynet & Maeder, 2000).

The stellar models in Fig.(I.6) do not include magnetic fields. If magnetic fields are accounted for, the evolution of rotation is different. A $15\,M_\odot$ model with $v_{\rm ini} = 300\,{\rm km\,s^{-1}}$, for example, would evolve nearly as a solid body during the main sequence, meaning Ω would be nearly constant. During the post-main-sequence evolution differential rotation develops, as a result of the spinning up of the core and slowing down of the envelope, when the star evolves towards the red supergiant branch. However, when magnetic fields are included the ratio of core to envelope rotation rate is much smaller than shown in Fig.(I.6b) - see discussions in Section II.3 and Chapter IV.

4.2.2 Effects of Rotation on the Evolution of Massive Stars

Rotation-induced mixing provides the burning zone with more fuel, prolonging the burning lifetime (Meynet & Maeder, 2000; Heger et al., 2000). The higher amount of fuel also enhances the energy production by thermonuclear burning, leading to a higher local luminosity. Consequently, the star has larger convective cores as shown in Fig.(I.7), where the rotating model shows larger convective cores than the non-rotating model. Accordingly, the nuclear burning shells are further out and they are also more separated from each other as can be seen in Fig.(I.7) during the advanced stellar stages. This becomes more extreme with increasing rotation rate. Also, the two diagrams depict that the rotating

star loses more mass. This is a result of two effects. First, rotation enhances mass loss as discussed in Section I.4.1. Second, the rotating model has a hydrogen burning shell that is further out. Therefore it becomes a red supergiant slightly earlier than the non-rotating model, see discussion below, and experiences the stronger red supergiant stellar winds for a longer time.

In non-rotating stars, the luminosity increases during the main-sequence evolution as a result of the growing mean molecular weight in the core - see Section I.2.1.1. As a consequence, the pressure on the core is reduced. At the same time, the conversion of hydrogen into helium decreases the opacity. The latter two dominate over the increase of the core luminosity in a massive star, leading to a receding convective core during the main-sequence evolution. Furthermore, the higher luminosity enlarges the radius of the star which results in a cooler surface temperature. Rotation-induced mixing adds two modifications. First, it enables more fuel to be transported into the burning region. Therefore, a more massive helium core is formed and the star has a higher luminosity. Second, if rotational mixing is efficient, it mixes helium in the radiative zone and thus reduces the opacity throughout the interior of the star. The two modifications result in a slower receding convective hydrogen core, for fast rotation the convective core can even grow initially. A higher luminosity also implies larger radii, thus, rotating stars evolve to lower surface temperatures during the main sequence. However, fast rotating stars stay more compact during the main sequence, because rotational mixing reduces the opacity in the envelope, and it evolves to slightly higher surface temperatures.

Rotation also influences the post-main-sequence evolution, whether the star will follow the usual red-wards post-main-sequence evolution in the Hertzsprung-Russell diagram (see Fig.(I.1a)) or it evolves towards the hotter side in a more homogeneous evolution, becoming a blue supergiant and likely producing a Wolf-Rayet star, see also the discussion further down. Noticeably, for a low or intermediate rotation rate the red-wards evolution is favoured. This is a consequence of the effects of internal mixing and of the enhanced mass loss - see Section I.4.1. The first point reduces the extension of the convective zone associated with the post-main-sequence hydrogen burning shell, which the star needs to stay in the blue part of the Hertzsprung-Russell diagram, and produces a larger helium core at core hydrogen depletion. Therefore, the contracting core after the terminal-age main sequence will be larger and have less support against gravitational contraction, leading to a faster red-wards evolution[25]. As a matter of fact, the ratio of blue to red supergiants in rotational models is smaller for higher rotational velocity, which is more in agreement with the observations (Heger et al., 2000; Meynet & Maeder, 2000). Furthermore, rotating models give a decreasing blue to red supergiant ratio with decreasing metallicity, implying a larger number of red supergiants at low Z (Maeder & Meynet, 2001). Finally, rotation lowers the threshold of Wolf-Rayet star formation, at solar metallicity for example from $\sim 37\,M_\odot$ to $\sim 22\,M_\odot$ (Meynet & Maeder, 2003, 2005; Georgy et al., 2013).

[25]This is a similar effect as for larger amounts of convective boundary mixing discussed in Chapter III, where a redwards evolution is favoured for larger amounts of convective boundary mixing.

Rotation also affects the nucleosynthesis and yields of stars. For example the larger convective cores and the rotation-induced mixing increase the availability of fuel, leading to a larger production of carbon and oxygen, and other α-nuclei, during core helium burning. Furthermore, the $^{12}C(\alpha,\gamma)^{16}O$ reaction is more active at the end of core helium burning, creating a lower carbon to oxygen mass fraction (Maeder & Meynet, 2000b; Heger & Langer, 2000). This effect can be seen in Fig.(I.7); in the non-rotating model core carbon burning occurs convectively whereas in the rotating models it proceeds radiatively, which is a result of the lower amount of carbon left at the end of core helium burning (Hirschi et al., 2004). Rotation-induced mixing between different burning sites can open new channels of nucleosynthesis. The interaction between hydrogen and helium burning regions, for example, leads to enhanced formation of ^{14}C, ^{18}O and ^{19}F (Maeder & Meynet, 2000a; Heger & Langer, 2000). Also, the interaction between the hydrogen and helium burning regions can mix freshly synthesised carbon and oxygen into the hydrogen shell. Consequently, the burning shell is strongly boosted, especially at lower metallicity, because the CNO-cycle strongly depends on the availability of the catalysts. This further creates a convective shell with a primary ^{14}N production. While low-metallicity intermediate mass stars are the main producers of primary ^{14}N, rotating massive stars also contribute to the generation of this isotope (Meynet & Maeder, 2002).The interaction between the convective hydrogen shell and helium core also leads to a large production of primary ^{22}Ne at all metallicities, which is the main source of the weak s-process in massive stars, see Section I.2.1.2. Therefore, the weak s-process production in rotating massive stars is boosted (Frischknecht et al., 2012; Choplin et al., 2018). The weak s-process activity at solar metallicity is modest and the production stops at the strontium peak as in the non-rotating models. However, at very low metallicity, where the amount of heavy seed nuclei is limited, the weak s-process production reaches barium. Thus, heavier elements are synthesised by the s-process at very low metallicity (Frischknecht et al., 2016; Banerjee et al., 2019). Although, this scenario is very sensitive to metallicity and initial rotation rate.

Rotational mixing can change the surface composition during the main sequence. This would not be possible in non-rotating massive stars until the red supergiant branch, where the envelope becomes convective. For example, rotating massive stars alternate their CNO surface abundance by increasing the helium and nitrogen mass fractions and reducing the hydrogen, carbon and oxygen mass fractions (Meynet & Maeder, 2000; Heger & Langer, 2000; Hirschi et al., 2005a). The enrichment is higher for larger masses, lower metallicities and higher initial velocities. The surface enrichments in stars are mainly important during the early evolutionary stages, predominantly during the main sequence. During the advanced burning stages, the rotational velocities converge towards low values, independent of the initial rotation rate, and their impact is therefore reduced, see Section I.4.2.1. Nevertheless, a high helium and nitrogen surface enrichment indicates a fast rotation in the past, even if the star only rotates very slowly.

Hunter et al. (2008) compared the observed surface enrichments with the predictions of stellar evolution models in order to test rotation-induced mixing. They plot the surface nitrogen abundance ($12 + \log[N/H]$) as a function of the projected rotational velocity ($v \sin i$), which is the so-called *Hunter diagram*. Although they attempted to constrain the stellar evolution models to the observations, they can only match 60% of the data, with several discrepant groups during core hydrogen burning and during the supergiant evolution. Other authors also find inadequacies of stellar evolution models to represent the surface enrichment in rotating massive stars (e.g. Markova et al., 2018). Possible explanations for the discrepancy include binarity or magnetic fields but it could also relate to a missing piece in the understanding of rotation-induced mixing. The subject is still an ongoing discussion (e.g. Song et al., 2018; Markova et al., 2018; Carneiro et al., 2019; Keszthelyi et al., 2019; Schneider et al., 2020; Bouret et al., 2021).

Efficient rotational mixing not only affects the surface composition but also reduces the opacity in the envelope of the star, see discussion above. Therefore, moderate or rapid rotating stars are hotter on their surface, because $T_{\rm eff} \propto 1/\text{opacity}$, and more compact, following $R \propto L^{1/2}T^{-2}$ (e.g. Kippenhahn & Weigert, 1994). Thus, rotation favours a more blueward evolution to the hotter side of the Hertzsprung-Russell diagram, increasing the blue to red supergiant ratio (Meynet & Maeder, 2000; Maeder & Meynet, 2001). Also, the mixing of chemicals in the radiative zones of massive stars may prevent the establishment of a chemical stratification when the timescale of rotation-induced mixing is shorter than the nuclear timescale, i.e. during the main-sequence evolution. Consequently, the star can efficiently mix the whole interior and evolves nearly chemically homogeneously (Eddington, 1929; Maeder, 1987b). This so-called quasi chemical-homogeneous evolution depends on the mass, metallicity, rotation rate and also the numerical implementation of the physics, for the latter see the discussion in Chapters II and B. Generally, quasi chemical-homogeneous evolution is favoured at lower metallicity due to the reduced angular momentum loss through stellar winds (Maeder, 1987b; Yoon & Langer, 2005; Yoon et al., 2006, 2012). At low metallicity, even moderately fast rotators can undergo efficient rotation-induced mixing, resulting in quasi chemically-homogeneous evolution (e.g. Szécsi et al., 2015). Nevertheless, quasi chemical-homogeneous evolution is also possible at solar metallicity, which is consistent with discoveries of long-duration gamma-ray burst in (super) solar metallicity galaxies, but it is much rarer (Levesque, 2010) and a high rotation rate is needed (Yoon et al., 2006). The fraction of homogeneous evolving stars increases as the metallicity decreases. Therefore, rotation induced chemically homogeneous evolution might be an important mode of massive star evolution at low metallicity and it is able to explain many otherwise peculiar observations (e.g. Walborn et al., 2004; Sander et al., 2012; Martins et al., 2013). Furthermore, while the bulk of observed stars rotate slowly, with a rotation rate less than 20% of their break-up velocity, there is a significant fraction of massive stars that rotate rapidly (Ramírez-Agudelo et al., 2013), which might evolve quasi chemically

homogeneously at higher metallicity.

Rotation changes the fate of massive stars. A slow or medium rotation rate favours the formation of red supergiants which are less compact. The faster redward evolution changes the pre-supernova structure of the star, in particular the compactness, core mass and total mass. Therefore it shifts the *initial mass-supernova progenitor-explosion type* correlation. Furthermore, rotation-induced mixing favours the entry into the Wolf-Rayet phase in two ways, it modifies the chemical composition in the radiative envelope and it increases the core mass. While in the non-rotating scenario, a star can only enter the Wolf-Rayet phase when the stellar wind has peeled of the outer hydrogen layer, the rotating model can obtain the characteristic surface abundance with the effects of rotation-induced mixing and mass loss. Therefore, rotating models can also produce Wolf-Rayet stars at lower metallicity, when mass loss is reduced, by following the homogeneous evolution discussed above. The different structure of the progenitors also changes the explosive event itself. Indeed, rotating models predict a higher occurrence of supernovae type Ib and Ic (Georgy et al., 2009). Observations show an increase of the supernova type Ib and Ic to II with metallicity due to stronger stellar winds (e.g. Prantzos & Boissier, 2003). This trend can be better reproduced with rotating models[26] (Meynet & Maeder, 2005; Hirschi et al., 2005b; Georgy et al., 2009). Rotation also changes the initial mass of the stars that enter the pair-instability regime by enlarging the core mass. In addition, the scenario of quasi-chemical homogeneous evolution reduces the threshold of stars that experience the pair-instability (e.g. Chatzopoulos & Wheeler, 2012). The typical spectrum of a type Ic supernova is associated with long gamma-ray bursts (Woosley & Bloom, 2006). Gamma-ray bursts are primarily found at low metallicity (e.g. Modjaz et al., 2008), where rotation-induced chemical mixing is more efficient and the stars are able to maintain a high angular momentum in the core. Therefore, quasi-chemical homogeneous evolved stars are potential progenitors of long gamma-ray bursts (Woosley & Heger, 2006; Yoon et al., 2006, 2012). Chemically homogeneous stars are hotter, more luminous and more compact, following the same argument from above. Therefore, two massive stars in a binary system are compact enough to avoid mass transfer (de Mink et al., 2009). Consequently, this scenario can lead to two massive helium stars where both eventually collapse to a black hole. This is a potential channel to a black hole binary system, which is the progenitor of a black hole merger and source of gravitational waves (Mandel & de Mink, 2016).

Generally, stellar models that include rotation are able to better reproduce many observations than models without rotation. However, some problems remain. For example, the improvement of rotation explains the number of Wolf-Rayet subtypes at solar and lower metallicity and the trend of the observed ratios as a function of metallicity (Meynet & Maeder, 2003, 2005; Langer, 2012), but it produces too many nitrogen enhanced Wolf-Rayet (WN) stars at solar and higher metallicities (Meynet

[26]This trend can also be reproduced by invoking a close binary-star, where the hydrogen-rich envelope is removed through binary interaction (e.g. Eldridge et al., 2008), hence, the solution is not singular.

& Maeder, 2005). Also, Eldridge & Vink (2006) show that rotating models cannot simultaneously reproduce the dependency of the ratio of Wolf-Rayet subtypes on the metallicity and the number ratio of Wolf-Rayet to O-type stars. Another problem is the fact that there is still a discrepancy between the observed rotation rates of evolved stars and the ones predicted by stellar evolution theory, also with the inclusion of a magnetic dynamo which is thought to efficiently slow down the stellar core, see also Chapter II. In particular, rotating models fail to reproduce the slow rotation rate of white dwarfs, neutron stars and black holes (e.g. Heger et al., 2005; Suijs et al., 2008; Hirschi & Maeder, 2010) and the internal rotation profiles of subgiants or red giants (e.g. Eggenberger et al., 2005, 2019a; Cantiello et al., 2014). More recent improvements of angular momentum transport, e.g. the Fuller-modified Taylor-Spruit dynamo process (Fuller et al., 2019, see also Chapter II), enables stellar cores to spin down more efficiently but it cannot explain observed rotation profiles in low mass stars in its current form (e.g. den Hartogh et al., 2019; Eggenberger et al., 2019c). Therefore, an additional angular momentum transport mechanism is needed. Currently discussed possibilities are magnetic torques (Spruit, 2002; Maeder & Meynet, 2004; Spada et al., 2016; Fuller et al., 2019) and gravity waves (Talon & Charbonnel, 2005; Belyaev et al., 2013; Fuller et al., 2015b; Pinçon et al., 2017; Edelmann et al., 2019). Another open question is the dependence of the mass-loss rates on the changes of the equilibrium configuration of rotating stars (Müller & Vink, 2014) and vice-versa, how rotation depends on the mass-loss rates, i.e. by removing angular momentum (Vink et al., 2010), which is not well understood.

5 This Work

The overview of stellar evolution given in the previous sections shows that there are still major uncertainties regarding the evolution of massive stars. In particular, the uncertainty of internal mixing processes such as turbulent convection and rotation, the treatment of stellar atmospheres and winds and the uncertainty of nuclear reaction rates have a vast impact on the evolution and fate of stars. Also, while it was not discussed in the previous sections, the treatment of binarity is another big question, which still needs to be addressed.

While 1-dimensional stellar evolution models will never be perfect descriptions of a 3-dimensional star, they can at least describe its average evolution in a reliable way. Therefore, the theories of the various physical processes have to be consistent and preferably based on physics rather than parametrisation. A first crucial step in the direction of improving stellar evolution models is to know which physical processes lead to the largest uncertainties, hence, affect the prediction of stellar evolution the most. In this work I investigate some uncertainties related to the internal mixing processes. In the context of convection, the focus lies on convective boundary mixing by assessing the impact of its strength

and the different criteria of the convective boundary. In the framework of rotation-induced mixing processes, I compare different treatments of angular momentum transport, mainly by magnetic dynamos.

This work is organised as follows; in Chapter II the theory of internal mixing processes is discussed in more detail. Appendix B gives an overview on the stellar evolution code `MESA` which is used for this work and how the physics of Chapter II is numerically implemented. Chapters III and IV present the results of my thesis. In Chapter III the uncertainty of convective boundary mixing is discussed, which was published in Kaiser et al. (2020), and Chapter IV presents the investigation of the different flavours of angular momentum transport.

It should be noted that a large fraction of massive stars, i.e. more than 70%, are members of a close binary system (Sana et al., 2012). Binarity impacts the evolution of the two companion stars via mass transfer, possible common envelope evolution or merger. Binary interaction influences the observed population of massive stars, e.g. supergiants, Wolf-Rayet stars or supernovae. Binary evolution is also crucial for the understanding of progenitors of gravitational waves. In this thesis, however, only single stars and their evolution are considered, despite the impact of binarity on massive star evolution. This is done because of several reasons. First, binary evolution and interaction itself is quite uncertain. Furthermore, the interaction also depends on the physics of single stars. For example, rotation and convection influence the blue versus red supergiant evolution and thus the radial extent of a star. This, on the other hand, affects the amount of interaction between the two companion stars. Therefore, it is less problematic to study the uncertainty of the internal mixing processes first, before applying it to the problem of binary interaction. Also, no stellar model to date includes all the physics needed to describe a star. Simplifications are made to study certain problems. Finally, this thesis mostly focusses on the interior evolution of massive stars. Therefore, the main findings of this work are still applicable in a binary system.

Chapter II

Internal Mixing Processes

Internal mixing processes crucially affect the structure of a star and change their evolution. Thermally-driven mixing processes arise as a consequence of local heat excess, leading to turbulent energy transport and turnover of matter. At the convective boundary matter is turbulently entrained and internal gravity waves are generated. Rotation-induced mixing processes, on the other hand, are produced either due to the changes by rotation to the hydrostatic equilibrium or by differential rotation. Both processes mix the chemical composition in a star and transport angular momentum. Rotation also interacts with magnetic fields, creating a possible dynamo action which couples the core and envelope and leads to near-solid body rotation. The first two sections of this chapter give an overview of both mixing processes. The last section summarises the interaction between stellar rotation and magnetic fields and discusses different magnetic dynamo processes.

1 Thermally-Driven Mixing

In most physical systems, a heat excess, which cannot be regulated by radiative transfer alone, leads to instability and finally to turbulent convective motions, i.e. the turnover of matter in a region where energy cannot be transported by radiation alone. This turbulent energy transport and radiation are the two main energy transport processes in stars. In addition, convective motions efficiently mix the chemical composition and transport angular momentum. At the boundary between convectively unstable and stable regions, where the convective flow turns, new material is entrained into the convective region and internal gravity waves are generated, the latter being observable by asteroseismology. Thermally-driven mixing shapes the interior of stars and replenishes fuel into the burning region, thus,

is a crucial process in stellar physics and evolution.

Turbulent convection is a chaotic, non-linear process (e.g. Landau & Lifschitz, 1966; Pope, 2000). For example Figs.(7) and (11) from Cristini et al. (2017) illustrate the chaotic behaviour of the turbulent flow[1]. The coherent structures in the figures, forming rolls and plumes, are strongly dynamic; they appear, break apart and are formed elsewhere. The interaction between the coherent structures leads to an intermittency of the turbulent convective flow in space and time (Tennekes & Lumley, 1972) and there is a balance between turbulent driving and damping (Warhaft, 2002). Also, the boundary layers between the stable and turbulent region are dynamic, see Section II.1.3. There is a growing number of multi-D hydrodynamic simulations studying stellar convection that show these characteristics (e.g. Asplund et al., 1999; Herwig et al., 2006; Meakin & Arnett, 2007; Magic et al., 2013; Woodward et al., 2015; Cristini et al., 2017; Freytag et al., 2017; Jones et al., 2017; Mocák et al., 2018; Arnett et al., 2019; Yadav et al., 2020).

Turbulent convection is clearly a 3-dimensional (3D) process operating on a timescale of seconds up to a year. On the other hand, the life of a star is at least millions of years. Therefore, in order to simulate the long evolutionary timescale, stellar evolution models are limited to one dimension and the complex 3D turbulent process has to be approximated by 1-dimensional (1D) prescriptions.

Standard 1D stellar evolution models are calculated in spherical symmetry and the convective energy transport and mixing are often approximated with the mixing-length theory (MLT, Vitense, 1953; Böhm-Vitense, 1958). This theory represents the convective flow with fluid elements that move up and down and transport energy and material. While this approximation works surprisingly well for the bulk of weakly stratified convective regions, it neglects several important facts of turbulent convection, such as the convective boundary (Renzini, 1987). In an attempt to correct for these issues additional theories are used, for example the different boundary mixing prescriptions discussed in Section II.1.3 or methods to treat the superadiabatic convection in radiation-dominated regions - see discussion in Sections III.2 and III.7.

In this Section the thermally-driven mixing processes are discussed, starting with the consideration of local stability to determine whether global flows develop. The theory of the mixing-length is introduced and how it accounts for mixing and energy transport. The last two subsections present the current treatment of convective boundaries and the inefficient mixing process called semiconvection.

1.1 Local Stability

Using linear perturbation theory, the stability of a layer can be expressed in terms of the Brunt-Väisälä frequency, which is the oscillation frequency of a displaced fluid element around its equilibrium

[1]Movies of the 3D simulations by Cristini et al. (2017) are available at http://www.astro.keele.ac.uk/shyne/321D/convection-and-convective-boundary-mixing/visualisations

position. The square of the Brunt-Väisälä frequency for a fluid element with an internal density $\rho_{\rm int}$ oscillating in a medium with density $\rho_{\rm ext}$ can be written as

$$N^2 = \frac{g}{\rho_{\rm int}} \left(\frac{d\rho_{\rm int}}{dr} - \frac{d\rho_{\rm ext}}{dr} \right) \equiv \frac{g}{\rho_{\rm int}} \frac{d(\Delta\rho)}{dr}, \tag{II.1}$$

with the gravitational acceleration g, so that the stability or instability of the fluid element is defined as

$$\frac{d(\Delta\rho)}{dr} \begin{cases} > 0 \Rightarrow \text{stable}, \\ < 0 \Rightarrow \text{unstable}. \end{cases} \tag{II.2}$$

This criterion compares the density change in the displaced fluid element and of the surrounding medium over a small distance dr. If there is a larger change of the density inside the fluid element compared to its surroundings, corresponding to a negative $\frac{d(\Delta\rho)}{dr}$, then the fluid element will be lighter and experience unstabilising buoyant forces. Vice versa, if the density in the fluid element changes less than the density in the surrounding medium, which corresponds to a positive $\frac{d(\Delta\rho)}{dr}$, then the fluid element is lighter and will be stabilised. Therefore the squared buoyancy frequency determines whether an oscillatory motion of a fluid element around its equilibrium position is damped and stabilised or whether it grows and moves away from it.

In stellar evolution theory it is convenient to express a process in terms of the basic structure variables[2]. The density is not a structure variable but the temperature is. Therefore, it is advantageous to express Eq.(II.1) in terms of temperature gradients (see e.g. Kippenhahn & Weigert, 1994; Maeder, 2009, for the derivation),

$$N^2 = N_{\rm T}^2 + N_\mu^2 = \frac{g\delta}{H_P} \left(\nabla_{\rm int} - \nabla + \frac{\varphi}{\delta} \nabla_\mu \right), \qquad N_{\rm T}^2 = \frac{g\delta}{H_P} (\nabla_{\rm int} - \nabla), \qquad N_\mu^2 = \frac{g\varphi}{H_P} \nabla_\mu, \tag{II.3}$$

, where H_P is the local pressure scale height, with the two components for the thermal and chemical composition stratification, the temperature gradients

$$\nabla_{\rm int} \equiv \frac{d\ln T_{\rm int}}{d\ln P}, \qquad \nabla \equiv \frac{d\ln T_{\rm ext}}{d\ln P}, \qquad \nabla_\mu \equiv \frac{d\ln \mu_{\rm ext}}{d\ln P}, \tag{II.4}$$

where T is the temperature and P is the pressure, and the thermodynamic quantities

$$\delta \equiv -\left(\frac{\partial \ln \rho}{\partial \ln T} \right), \qquad \varphi \equiv \left(\frac{\partial \ln \rho}{\partial \ln \mu} \right). \tag{II.5}$$

[2]Structure variables are the mass M, pressure P, temperature T and luminosity L and they can be obtained by solving the stellar structure equations, see Section B.1.2. Other variables are calculated from the structure variables. The density for example is determined from P and T using the equation of state.

The condition for stability, Eq.(II.2), can thus be written as

$$\nabla < \nabla_{\rm int} + \frac{\varphi}{\delta}\nabla_{\mu}. \tag{II.6}$$

This is the famous Ledoux criterion. A positive gradient in chemical composition favours convective stability by increasing the restoring buoyancy force. In a chemically homogeneous medium, i.e. when $\nabla_{\mu} = 0$, Eq.(II.6) becomes

$$\nabla < \nabla_{\rm int}, \tag{II.7}$$

which is known as the Schwarzschild criterion.

It is possible to define an adiabatic and radiative temperature gradient (e.g. Kippenhahn & Weigert, 1994),

$$\nabla_{\rm ad} = \left(\frac{\partial \ln T}{\partial \ln P}\right)_{\rm ad} = \frac{P\delta}{C_P \rho T}, \; \nabla_{\rm rad} = \frac{3}{16\pi acG}\frac{\kappa l P}{m T^4}, \tag{II.8}$$

with the specific heat at constant pressure C_P, the opacity κ, the luminosity in a given layer l, the Stefan-Boltzmann constant a, the speed of light c and the gravitational constant G. In a convective zone the four temperature gradients follow the relation (Kippenhahn & Weigert, 1994; Maeder, 2009)

$$\nabla_{\rm rad} > \nabla > \nabla_{\rm int} > \nabla_{\rm ad}. \tag{II.9}$$

In the stellar interior[3] convection is nearly adiabatic and an order of magnitude estimate shows that $(\nabla - \nabla_{\rm int})/\nabla \approx 10^{-8}$ (Maeder, 2009), hence, $\nabla \approx \nabla_{\rm int} = \nabla_{\rm ad}$. Therefore, Eq.(II.9) simplifies to

$$\nabla_{\rm rad} > \nabla_{\rm ad}, \tag{II.10}$$

which is the Schwarzschild criterion for instability in the stellar interior. This criterion basically states that if the energy excess cannot be transported by radiation alone convective motions set in. Arguing similarly, the Ledoux criterion for convective instability in the stellar interior can be written as

$$\nabla_{\rm rad} > \nabla_{\rm ad} + \frac{\varphi}{\delta}\nabla_{\mu}. \tag{II.11}$$

The convection in the outer layers of a star are not adiabatic. There, the energy lost by a turbulent fluid element has to be taken into account as it is transported, see below.

The two stability criteria determine the location where the acceleration of the convective flow drops to zero. In 1D stellar evolution, this point is often, maybe falsely, labelled as the convective boundary. The question of the *"correct"* convective boundary criterion to be used in stellar evolution calculations has been discussed for several decades. For example the study of Georgy et al. (2014) indicates that

[3]Roughly the region below the layers where hydrogen and helium are not fully ionised anymore.

the Ledoux criterion better reproduces observations of blue supergiants. Yet, the solution they found is not unique and there might be another solution with the Schwarzschild criterion. In a purely linear theory, in which the two criteria were derived, it is correct to use the Ledoux criterion, in order to take care of possible chemical composition gradients. Convection, however, is a 3D process which drives non-linear intermittency and fluctuations. As a result, the convective boundary bends and stretches as it evolves, contrary to the fixed boundary location given by Eqs.(II.11) and (II.10) which is sharp and spherically symmetric. Consequently, the chemical composition gradient near the convective boundary is erased and the location of the boundary in 3D simulations agrees on average more with the Schwarzschild criterion location (Meakin & Arnett, 2007; Arnett et al., 2019). This is an initial value problem; the convective boundary of the growing instability starts at the location determined by the Ledoux criterion. Intermittency and fluctuations at the convective boundary move the boundary to the Schwarzschild solution on a finite timescale. Thus, it is not sure which criterion has to be used for convective regions that only exist on a short time scale. This transition needs further 3D hydrodynamic simulations for verification and to test the transition speed.

1.2 Convection in Stellar Evolution

In a region which is unstable according to the Ledoux or the Schwarzschild criterion, Eqs.(II.11) and (II.10), turbulent convective motions set in. This turbulent fluid flow efficiently transports energy, in addition to mixing the chemical species. The average convective flux in a layer results from the motion of the fluid elements with an average velocity $\bar{v}$ and an average temperature excess $\overline{\Delta T}$. In the 1D picture developed here, the flow consists of upward moving hotter and downward moving cooler fluid elements, which both contribute to the outward transport of energy, thus, a regulation of the excess. The convective flux, calculated as "mass×velocity×driving gradient", is (Vitense, 1953)

$$F_{\rm conv} = C_P \rho \bar{v} \overline{\Delta T} \tag{II.12}$$

in the units of energy per units of horizontal surface and time. In order to calculate the flux, the average velocity of the turbulent flow and the average temperature excess have to be determined first. The convective flow not only depends on local properties but also on processes in surrounding layers, hence, it is a non-local process. Most stellar evolution models, however, assume a local theory, i.e. the properties of convection only depends on local properties, which comes with great simplifications for the computations but it is a crude oversimplification of the physics. The most common formulation is the mixing-length theory (MLT, Vitense, 1953; Böhm-Vitense, 1958). There it is assumed that the fluid element moves over an average distance $\ell_{\rm MLT}$, the mixing-length, without losing its identity before it dissolves into its new surroundings, depositing energy and chemical elements. The mixing-length is

of the order of the pressure scale height, $\ell_{\rm MLT} = \alpha_{\rm MLT} H_P$, where $\alpha_{\rm MLT}$ is an adjustable parameter of order unity and needs to be calibrated. Current estimates lead to a value of $\alpha_{\rm MLT} \approx 1.6 - 1.7$ (e.g. Ludwig et al., 1999; Ekström et al., 2012; Trampedach et al., 2014). Arnett et al. (2018) find for strongly stratified convection an asymptotic limit for the dissipation length of a turbulent flow, which they identify with $\ell_{\rm MLT} \sim 5/3 H_P$.

For a fluid element that moves a distance $\ell_{\rm MLT}$, the average velocity $\bar{v}$ and temperature excess $\overline{\Delta T}$ can be estimated as (Eqs.(6) and (7a) from Vitense, 1953)

$$\overline{\Delta T} \approx \Delta T \frac{\ell_{\rm MLT}}{2} = (\nabla - \nabla_{\rm int}) \frac{T}{H_P} \frac{\ell_{\rm MLT}}{2} \tag{II.13}$$

and

$$\bar{v}^2 = v^2 \frac{\ell_{\rm MLT}^2}{4} = g\delta(\nabla - \nabla_{\rm int}) \frac{\ell_{\rm MLT}^2}{8 H_P}. \tag{II.14}$$

In the case of a non-negligible temperature excess with respect to the local temperature, the convection cannot be considered adiabatic anymore and the temperature gradients ∇ and $\nabla_{\rm int}$ need to be calculated explicitly. This can be done by combining the equation for the total flux, i.e. $F_{\rm tot} = F_{\rm rad} + F_{\rm conv}$, and by considering the energy lost as the fluid element moves over a distance (e.g. Kippenhahn & Weigert, 1994; Maeder, 2009). In order to solve the problem, two more suitable relations are needed. Generally, these are (i) the ratio between the energy excess of a fluid element to the energy radiated away during its lifetime and (ii) the excess rate of energy generation minus the excess rate of energy loss by radiation of the fluid element relative to its surrounding. This gives the same number of equations as unknowns, hence, the two temperature gradients ∇ and $\nabla_{\rm int}$ can be determined, see Section B.1.3.1 for more details.

The knowledge of ∇ and $\nabla_{\rm int}$ in the convective zone allows to express the convective velocity (Eq.(II.14)) and the convective flux (Eq.(II.12)) in a non-adiabatic case. Furthermore, the determination of ∇ in the different regimes,

$$\begin{aligned} \text{adiabatic convection} &\rightarrow \nabla \equiv \nabla_{\rm ad}, \\ \text{non-adiabatic convection} &\rightarrow \nabla_{\rm rad} > \nabla > \nabla_{\rm int} > \nabla_{\rm ad}, \\ \text{radiative} &\rightarrow \nabla \equiv \nabla_{\rm rad}, \end{aligned} \tag{II.15}$$

allows to calculate the energy transport in a region with the stellar structure equation in Eq.(B.4). Finally, $F_{\rm conv}$ allows to calculate the transport of chemical species and angular momentum in the convective region. The mixing of chemical species is most commonly done by a diffusion equation, see Appendix C.3.1,

$$\rho \frac{\partial}{\partial t} X = \frac{1}{r^2} \frac{\partial}{\partial r} (r^2 \rho D_{\rm MLT} \frac{\partial}{\partial r} X), \tag{II.16}$$

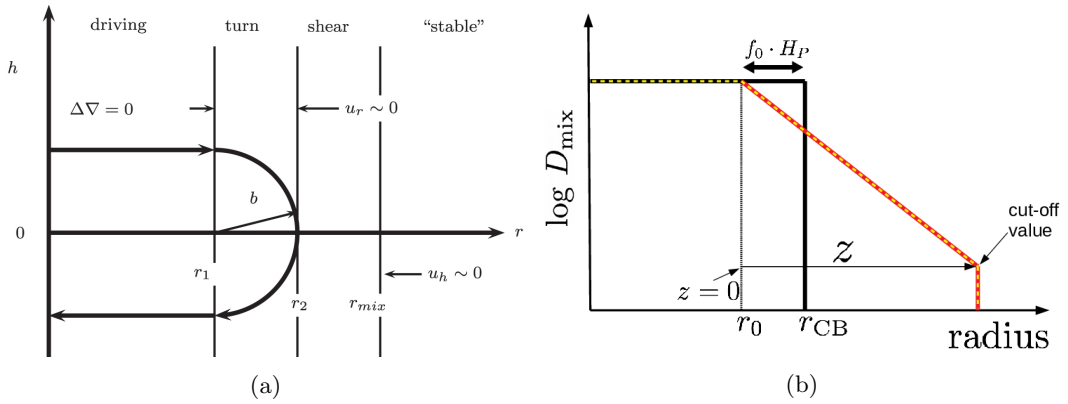

Figure II.1: (a) Simplified schematic representation of a convective boundary. The radial direction is denoted by r and the horizontal by h. The arrows give a schematic flow pattern which is sub-divided into the various regimes explained in the text. u_r is the radial velocity component and u_h the horizontal one. The figure is taken from Arnett et al. (2015). (b) A schematic illustration of the construction of the convective boundary with the exponential decaying diffusive scheme (see Eq.(II.17)). The fat black line depicts the diffusion coefficient from the mixing coefficient, with a sharp drop at the convective boundary location $r_{\rm CBM}$ given by the Ledoux or the Schwarzschild criterion. The fat red line indicates the exponential decrease of the diffusion coefficient to the convective boundary mixing scheme. It starts inside the convective region at r_0, illustrated by the dashed black line. The final diffusion coefficient for convective mixing is shown with a yellow dashed line. The variables are explained in the text.

with the diffusion coefficient $D_{\rm MLT} = \frac{1}{3}\ell_{\rm MLT}\bar{v}$. In the presence of rotation, the transport of angular momentum can be considered similar but it is often assumed that convective regions rotate as solid bodies - see discussion in Sections II.2 and B.1.5.

1.3 Convective Boundary Mixing

The convective boundary criteria in Section II.1.1 determine the location where the buoyant driving force of the turbulent flow changes sign, i.e. where it becomes a damping force. In this sense, the Ledoux and Schwarzschild criteria are local criteria. However, convection not only depends on local forces but is coupled to neighbouring layers via momentum transfer, inertia and equation of continuity. Therefore, a fluid element that was accelerated elsewhere "*overshoots*" the convective boundary until its radial motion is stopped and reversed.

3D simulations show nicely[4] how the flow approaches the boundary and then u-turns. In these simulations, several sub-regions in the boundary layer can be observed. A schematic representation of a 3D convective boundary is shown in Fig.(II.1a) which can be divided into the following regions (Arnett et al., 2015, other authors, e.g. Cai (2020), find similar partitioned layers):

(a) The driving region - this is the turbulent convective region where the superadiabatic excess is positive and the material is unstable due to buoyant driving. This region is fully mixed and it is the "convective" region associated with MLT.

[4] A visualisation of the simulations by Cristini et al. (2017) can be found at http://www.astro.keele.ac.uk/shyne/321D/convection-and-convective-boundary-mixing/visualisations.

(b) The turning region - as a consequence of a pressure excess and the buoyant force changing sign the turbulent flow turns around. This region is well mixed.

(c) The shear region - the radial velocity is going to zero and the horizontal velocity dominates. The horizontal flow may create Kelvin-Helmholtz instabilities which entrain material from the stable region into the convective region.

(d) The stable region - the radiative region beyond the turbulent convective regime. Gravity waves are generated, a result of the convective flow joining the stable region (Landau & Lifschitz, 1966), which can lead to chemical mixing in the stable "radiative" region (e.g. Rogers & McElwaine, 2017). Otherwise, there is no mixing in this region.

Contrary to the convective boundary discussed in Section II.1.1 these layers are not static but dynamic and subject to fluctuations (Cristini et al., 2017). Recent 3D simulations of turbulent convection (e.g. Meakin & Arnett, 2007; Woodward et al., 2015; Cristini et al., 2017; Jones et al., 2017) show that there is indeed a turbulent convective, a turning and a shear region.

In the 1D prescription of the MLT discussed in Section II.1.2 the velocity at the convective boundary drops from a finite value to zero, as if the fluid flow rams into a solid barrier. This problem arises because the MLT only considers regions (a) and (d) in the schematic picture outlined above (Renzini, 1987). In order to account for convective boundary mixing in the framework of the MLT, i.e. regions (b) and (c), an additional theory, or a combination of several, has to be used, patching together the mixing after the convective boundary.

In the following, the mixing after the convective boundary is called convective boundary mixing (CBM), which describes an ensemble of physical processes responsible for the mixing. We avoid the term *"overshoot"* in this context on purpose, despite its wide use in the literature, because it describes a particular physical process, the vertical motion driven by buoyancy, which is part of CBM but not the whole story. Semiconvection is mentioned separately in Section II.1.4 because this mixing process only occurs in the context of the Ledoux criterion.

In a 1D prescription of convection only the radial velocity is considered. For that reason, convection is often falsely[5] thought of as a radial up-down movement. At the 1D convective boundary, the acceleration of the radial upwards motion becomes zero. However, the radial velocity is not zero at this point and the fluid overshoots the convective boundary as a consequence of the Newtonian laws (Canuto, 1998). This lead to the idea of "overshoot", an attempt to locally account for CBM (e.g. Shaviv & Salpeter, 1973; Maeder, 1975).

Observations show the evidence that CBM exists (see e.g. discussion in Zahn, 1991, Section 2). For example, CBM is needed in stellar models to reproduce the main-sequence width (e.g. Maeder, 1975;

[5]3D simulations clearly show the complexity of the turbulent flow with coherent dynamic structures (e.g. Arnett et al., 2019, but also see movies at http://www.astro.keele.ac.uk/shyne/321D/convection-and-convective-boundary-mixing/visualisations).

Bertelli et al., 1984; Ekström et al., 2012) and asteroseismic observations (e.g. Straka et al., 2005; Meynet et al., 2009; Moravveji et al., 2015, 2016; Arnett & Moravveji, 2017). Also, observations of eclipsing binaries show the need to include convective boundary mixing (e.g. Tkachenko et al., 2020). Currently, there exist different prescriptions and implementations in 1D stellar evolution codes to account for CBM. The most commonly used prescriptions are (i) the convective penetration (Zahn, 1991) or penetrative "overshoot" (commonly referred to as "step-overshoot") and (ii) the exponentially decaying diffusive boundary mixing (Herwig et al., 1997). In the formalism of Zahn (1991) the efficient heat transport across the convective border with $\nabla \approx \nabla_{\rm ad}$ is called penetrative "overshoot". Other implementations use inefficient heat transport with $\nabla \approx \nabla_{\rm rad}$, which is commonly called "overshoot" but the use of terminology is often imprecise. The penetrative "overshoot" extends the fully mixed region after the convective boundary by a fraction of the pressure scale height, $d_{\rm ov} = \alpha_{\rm ov} H_P$. The parameter $\alpha_{\rm ov}$ needs to be calibrated against observations - see the discussion further down. On the other hand, the prescription by Herwig et al. (1997) treats the convective boundary mixing as a diffusive process. The strength of the diffusive mixing decreases exponentially from the convective boundary, which is inspired by the exponentially decaying velocity fields seen in the multi-dimensional simulations by Freytag et al. (1996). The diffusion coefficient $D_{\rm CBM}$ is calculated as (Herwig et al., 1997)

$$D_{\rm CBM} = D_0(f_0) \cdot \exp\left(\frac{-2z}{f_{\rm CBM} \cdot H_P^{\rm CB}}\right) \tag{II.17}$$

Fig.(II.1b) schematically illustrates the resulting diffusion coefficient and the dependence of the various variables, which are explained in the following. The diffusion coefficient is a function of distance $z = r - r_0(f_0)$ from a point close to the edge of the convective boundary. $f_{\rm CBM}$ is a free parameter which expresses the length scale of the extra mixing as a fraction of the pressure scale height at the convective boundary, $H_{\rm P}^{\rm CB}$. $D_0(f_0)$ is the diffusion coefficient from the MLT, taken at the location $r_0(f_0) = r_{\rm CB} - f_0 \cdot H_P$ inside the convective zone, where $r_{\rm CB}$ is the location of the convective boundary determined by the boundary criterion and f_0 is an additional free parameter[6]. This is done because the diffusion coefficient from MLT drops sharply towards zero at the convective boundary. The new diffusion coefficient is then applied starting at $r(f_0)$, thus inside the convective zone.

The amount of CBM that is applied, i.e. the calibration of α_{ov} or $f_{\rm CBM}$[7], varies a lot throughout the literature. Ekström et al. (2012) fit their amount of CBM to the main-sequence width of low mass stars with $\alpha_{ov} = 0.1$. Brott et al. (2011) constrain CBM with the observed drop of the rotation rates for massive stars with a surface gravity of $\log g < 3.2$ and find $\alpha_{ov} = 0.335$. Recently, Schootemeijer et al. (2019) compared a grid of stellar models with varying amounts of internal mixing to observa-

[6]The implementation of the "step-overshoot" in the `MESA` code depends on a similar second parameter - see Section B.1.3.2.

[7]The two free parameters in the two prescriptions can be mapped with a mapping (conversion) factor between $10-15$ (Herwig et al., 1997; Noels et al., 2010; Moravveji et al., 2016; Claret & Torres, 2017).

tions of massive stars in the Small Magellanic Cloud and conclude that $0.22 \lesssim \alpha_{ov} \lesssim 0.35$ is needed to match observed numbers of blue to red supergiants. Higgins & Vink (2019), on the other hand, constrain massive star evolution with a Galactic binary system. They need $\alpha_{ov} = 0.5$ (and rotation - see Section II.2) in order to reproduce the system. Herwig (2000) find that $f_{\rm CBM} = 0.016$ is needed for convective core hydrogen burning in intermediate mass stars to reproduce the main-sequence width. Claret & Torres (2017, 2018) do a semi-empirical mass calibration of $f_{\rm CBM}$ and find a dependence of $f_{\rm CBM}$ on the stellar mass, with a strong increase of $f_{\rm CBM}$ up to about $2\,{\rm M}_{\odot}$ where it levels off at a value of $f_{\rm CBM} \sim 0.0164 - 0.0181$. Costa et al. (2019) reanalyse the sample of Claret & Torres (2017, 2018) and find a wide distribution of $0.3 - 0.4 < \alpha_{ov} < 0.8$ for masses $M > 1.9\,{\rm M}_{\odot}$. When they include rotation, the models agree with the observed data when $\alpha_{ov} = 0.4$. Castro et al. (2014) suggest, based on the observational spectroscopic Hertzsprung-Russell diagram of Galactic massive stars, that the amount of CBM increases with initial mass in order to fit their empirical terminal-age main-sequence. Other studies (e.g. Vink et al., 2010; McEvoy et al., 2015), however, do not find a clear boundary corresponding to the terminal-age main-sequence. Nevertheless, McEvoy et al. (2015) find hints for a broader main-sequence width than adopted in the literature. Denissenkov et al. (2019), on the other hand, scale the $f_{\rm CBM}$ with the driving luminosity, $f_{\rm CBM} \propto L^{1/3}$. This relation also hints towards larger amounts of convective boundary mixing with increasing initial mass as these stars show a higher driving luminosity. The values commonly used in theoretical "*state-of-the-art*" evolution calculations of massive stars range from $f_{\rm CBM} = 0.004$ (e.g. Farmer et al., 2016; Fields et al., 2018) up to $f_{\rm CBM} = 0.022$ (e.g. Jones et al., 2015) or $f_{\rm CBM} = 0.025$ (e.g. Sukhbold & Woosley, 2014), with intermediate values around $f_{\rm CBM} = 0.014 - 0.016$ (e.g. Choi et al., 2016; Pignatari et al., 2016; Ritter et al., 2018). These values are significantly lower than the values for massive stars constrained by observations and the difference will influence the structure and evolution of these stars - see Chapter III.

Moravveji et al. (2015) tested the penetrative and exponential decaying "overshoot" against asteroseismic observations. They found a better fit with the exponentially decaying "overshoot". Furthermore, Arnett & Moravveji (2017) show that the asteroseismic models from Moravveji et al. (2015, 2016) with the exponentially decaying "overshoot" prescription create a chemical composition profile similar to the profile in 3D hydrodynamic simulations. On the contrary, the penetrative "overshoot" creates a step in the chemical composition profile, which is not supported by asteroseismology or 3D simulations.

Stellar models that include one of the two CBM prescriptions, the penetrative "overshoot" or the exponential decaying diffusive scheme, may be able to match some observations but they are not able to reproduce the average shape of the complex convective boundary structure seen in 3D simulations (e.g. Cristini et al., 2017; Jones et al., 2017). Also, the CBM model prescriptions are used regardless of

possible chemical composition gradients at the convective boundary. Those might affect the amount of CBM but will not prevent it entirely (Canuto, 1998).

1.4 Semiconvection

In a region of the star with a strong gradient in chemical composition the scenario can arise where the Ledoux criterion predicts stability and the Schwarzschild criterion instability,

$$\nabla_{\rm int} < \nabla < \nabla_{\rm int} + \frac{\varphi}{\delta}\nabla_\mu. \tag{II.18}$$

This condition implies that a perturbed fluid element is stabilised by the chemical composition gradient, hence, the perturbed fluid element has a higher atomic weight and is brought back to its equilibrium position by gravity (Kato, 1966). However, following the Schwarzschild criterion, the fluid element is hotter than its surrounding medium and it will radiate energy. Consequently, the density in the fluid element increases, which causes the restoring force to rise and the element is brought further back than its equilibrium position. In this new surrounding, however, the element is lighter and moves upwards again, leading to an oscillatory movement around the element's equilibrium position. This oscillatory movement slowly erodes the chemical composition gradient, thus, the restoring force decreases, which may lead to a growth in amplitude of the oscillation. The timescale of the growth of the amplitude depends on the time the mass element takes to adjust thermally to its surroundings (Kippenhahn & Weigert, 1994). The growing oscillation leads to a region with slow chemical mixing called semiconvection. Whether the semiconvective region is stabilised or becomes convective depends on the changes of the gradients entering Eq.(II.18).

Several methods have been developed to deal with semiconvective regions. For example, Schwarzschild & Härm (1958) assume that matter is redistributed, which reduces ∇_μ, until the condition $\nabla_{\rm ad} = \nabla_{\rm rad}$ is met. Langer et al. (1983) treat the semiconvective mixing as a diffusive process with the diffusion coefficient

$$D_{\rm sc} = \alpha_{\rm sc}\frac{K}{6C_P\rho} \times \frac{\nabla - \nabla_{\rm ad}}{\nabla_{\rm ad} - \nabla + \frac{\varphi}{\delta}\nabla_\mu}, \tag{II.19}$$

with the radiative conductivity K. The semiconvective diffusion coefficient is scaled by the semiconvective efficiency parameter $\alpha_{\rm sc}$. Langer et al. (1985) estimate $\alpha_{\rm sc}$ to be of the order of 0.1 but more recent studies conclude that $\alpha_{\rm sc} > 1.0$ is needed in order to reproduce observations (e.g. Schootemeijer et al., 2019). The semiconvective diffusion coefficient assumes the adiabatic limit. The more general $D_{\rm sc}$ away from the adiabatic limit would be (Maeder, 2009)

$$D_{\rm sc} = \frac{2\Gamma}{\Gamma + 1} \times \frac{K}{C_P\rho} \times \frac{\nabla - \nabla_{\rm int}}{\nabla_{\rm ad} - \nabla + \frac{\varphi}{\delta}\nabla_\mu}, \tag{II.20}$$

with the factor to account for radiative losses

$$\Gamma \equiv \frac{\text{energy transported}}{\text{energy lost}} = \frac{3\rho^2 C_P \kappa}{4acT^3}\frac{\bar{v}\ell}{6} \quad \text{, i.e.} \quad N_{\rm T}^2 = \frac{\Gamma}{\Gamma+1} N_{\rm T,ad}^2 \tag{II.21}$$

Spruit (1992) derived a mixing coefficient on the assumption of layered convection. There, the transport across the stable layers between layers with mixing proceeds via microscopic diffusion. The diffusion coefficient can be written as

$$D_{\rm sc} \propto \sqrt{K K_{\rm diff}} \frac{\nabla_{\rm rad} - \nabla_{\rm ad}}{\nabla_\mu}, \tag{II.22}$$

with the microscopic diffusion coefficient $K_{\rm diff}$. However, simulations show that a layered structure, as assumed by Spruit (1992), is rapidly destroyed.

The amount of semiconvective mixing, if any, is still an unsolved problem (e.g. Langer, 2012, and references therein). The importance of semiconvection during the evolution of a massive star will be investigated in Chapter III.

1.5 Discussion on Thermally-Driven Mixing Processes

It is worth mentioning that there are some non-local turbulent convection theories for 1D stellar evolution (e.g. Shaviv & Salpeter, 1973; Xiong et al., 1997; Canuto, 1999; Deng et al., 2006; Canuto, 2011; Gabriel & Belkacem, 2018). For example Canuto (1999, 2011) developed a self-consistent turbulent convection theory with a two-component fluid, which however is very difficult to apply in stellar evolution calculations. The difficulty lies in two facts, (i) the equations to solve in the turbulent convection models are highly non-linear and unstable in numerical simulations and (ii) the complexity to include the turbulent convective model, because in order to solve these equations the parameters of the stellar structure are needed. In order to solve the equations of stellar structure, the temperature gradient is necessary, which however is determined by the turbulent convective model. Therefore, in order to solve the turbulent convective model, one must simultaneously solve the equation of turbulent convection and the stellar structure, which is enormously challenging.

Convective boundary mixing is still an open question. 3D hydrodynamic simulations allow to investigate the dynamics of turbulent boundaries, understand their behaviour and develop theories (e.g. Arnett et al., 2019, 2018). While these theories may explain the physics of the convective boundaries in 3D, current *state-of-the-art* stellar evolution theory has to rely on 1D models due to the high computation cost and small timesteps of 3D hydrodynamic simulations. Hence, the average 3D behaviour has to be incorporated into 1D codes.

Commonly used prescriptions for convective boundary mixing are phenomenological, based on the fact that observations and 3D simulations suggest the existence of turbulent mixing after the boundary, but there is a lack of theory. While it is possible to match observations by simply extending the convective core by a fraction of the pressure scale height, it is important to remember that this is only a constraint of the effects of convective boundary mixing, i.e. larger convective cores and higher luminosity, but not the physics of convective boundary mixing itself. Moreover, constraining the convective boundary mixing parametrisation for a certain star during a certain evolutionary stage does not mean that other stars, or even the same star during a different evolutionary phase, experiences the same amount of convective boundary mixing - see discussion in Chapter III. Also, an unphysical treatment of the boundary might affect the chemical composition at the boundary location, which consequently influences the convective history during the advanced evolutionary phases and changes the pre-supernova structure.

Several new prescriptions are being developed for 1D stellar evolution calculations. For example, Meakin & Arnett (2007) suggest a turbulent entrainment law at the convective boundary based on 3D hydrodynamic simulations. This prescription calculates the amount of entrained material at the convective boundary based on the stiffness of the boundary and the turbulent convective velocity. Recently, Pratt et al. (2017) proposed a diffusion coefficient based on a Gumbel distribution of the penetration probability in 2D hydrodynamic simulations. Korre et al. (2019) suggest a diffusive Gaussian model, similar to the exponential diffusive model from Herwig et al. (1997). However, instead of having a free parameter to calculate the distance of the mixing they suggest to calculate the length scale with properties of the boundary such as the convective velocity and the superadiabatic excess. Some authors also combine several prescriptions in order to mimic the convective boundary with the turning and the shear regions seen in 3D simulations. Michielsen et al. (2019), for example, combine the penetrative "overshoot" and the exponential diffusive model.

2 Rotation-Induced Mixing

In Section I.4 a short overview on rotation and how it influences the evolution of a star has been given. It is apparent that stars rotate, which leads to a change of their equilibrium configuration and thermal imbalance due to the additional centrifugal force. This can introduce instabilities. Furthermore, rotation in stars is generally not constant but different layers rotate at different angular speeds. This differential rotation may also introduce a number of instabilities. The rotation-induced instabilities can lead to chemical mixing and transport of angular momentum in the interior of stars. Theses mixing processes are especially important in radiative zones of a star where otherwise no mixing would occur. This drastically changes the structure and evolution of a star, as seen in Section I.4.

Similar to thermally-driven mixing, rotation is a multi-D process and therefore approximative theoretical prescriptions are needed in a 1D stellar evolution code. On top of that, due to the historical development, there exist different ways to describe the large scale meridional flow - see Section II.2.2. Moreover, the various stellar evolution codes implement the same physics differently - see discussion in Section B.1. Therefore, the predictions of rotating stellar models depend not only on the physical processes considered but also on how they are implemented in a stellar evolution code.

In most stellar evolution codes, the rotation-induced chemical mixing is described as a diffusive process following Endal & Sofia (1978). In this case, the diffusion coefficient from rotational mixing is the sum of all diffusion coefficients generated from each instability. In some cases the implementation of the rotation-induced chemical mixing is an "*order-of-magnitude*" estimate (Heger et al., 2000) and the sum is multiplied by a correction factor - see Section B.1. On the other hand, there are two popular ways to treat angular momentum transport by rotation. One calculates the angular momentum transport as a purely diffusive process (Endal & Sofia, 1978; Pinsonneault et al., 1989; Heger et al., 2000), whereas the other applies an advective-diffusive scheme (Chaboyer & Zahn, 1992; Zahn, 1992). While the advective term arises from the meridional circulation, the diffusion coefficient for the diffusive term is, similar to the pure diffusive case, the sum over the remaining rotation-induced transport processes.

In this Section, an overview of all the commonly considered rotation-induced instabilities is given and their mixing efficiency is discussed. A discussion about their implementation and treatment in stellar evolution codes can be found in Section B.1.

2.1 Solberg-Høiland Instability

The Brunt-Väisälä frequency N^2 in Section II.1.1 was derived in the absence of rotation. In a rotating medium, however, a displaced fluid element experiences in addition to gravity and buoyancy force a centrifugal force (Wasiutynski, 1946). This modifies the Brunt-Väisälä frequency, hence, the condition for convective stability. This condition for stability against axisymmetric adiabatic perturbations is the Solberg-Høiland criterion. At the equator, the condition for stability is (Endal & Sofia, 1978)

$$R_{\rm SH} \equiv \frac{g\delta}{H_P}\left(\nabla_{\rm ad} - \nabla + \frac{\varphi}{\delta}\nabla_\mu\right) + \frac{1}{r^3}\frac{d}{dr}(r^2\Omega)^2 \geq 0. \tag{II.23}$$

If the specific angular momentum $j \sim r^2\Omega$ is constant in a region, Eq.(II.23) reduces to the Ledoux criterion (Eq.(II.6)). This instability occurs in regions of decreasing specific angular momentum, according to the second term on the left hand side, and is suppressed in thermally stratified layers. This instability occurs on the dynamical timescale $\tau_{\rm dyn} = \sqrt{r^3/(Gm)}$.

The corresponding diffusion coefficient of the Solber-Høiland instability is estimated as the product

of the spatial extent of the unstable region $r_{\rm inst}$, limited by the pressure scale height, and a factor that determines the intensity of the instability, divided by the local dynamical timescale (Heger et al., 2000),

$$D_{\rm SHI} = \left\{ \min(r_{\rm inst}, H_P) \left[\frac{r R_{\rm SH}}{g} \right] \right\}^2 / \tau_{\rm dyn}. \tag{II.24}$$

The implementation using Eq.(II.24) means that the instability is smoothly turned on from stable ($R_{\rm SH} = 0$) and becomes more intense the more the stability criterion is violated.

2.2 Eddington-Sweet Circulation

A rotating star cannot be in thermal and hydrostatic equilibrium at the same time: In a rotating star, the centrifugal acceleration leads to oblate equipotentials and isobars towards the equator - see Section I.4. Since the radiative flux is proportional to the effective gravity, which is proportional to the equipotential density, there is a flux excess at the poles and a deficiency at the equator. This thermal imbalance causes large-scale circulation (von Zeipel, 1924a,b; Eddington, 1925; Sweet, 1950; Kippenhahn & Moellenhoff, 1974; Kippenhahn, 1974), which is called Eddington-Sweet circulation or Meridional circulation[8].

Kippenhahn & Moellenhoff (1974); Kippenhahn (1974) estimated the radial velocity of the circulation as

$$v_{\rm E} = \frac{\nabla_{\rm ad}}{\delta(\nabla_{\rm ad} - \nabla)} \frac{\Omega^2 r^3 l}{(Gm)^2} \left[\frac{2\varepsilon r^2}{l} - \frac{2r^2}{m} - \frac{3}{4\pi\rho r} \right], \tag{II.25}$$

with the local luminosity l and the nuclear energy generation rate ε per gram and second. A gradient in chemical composition can suppress or even inhibit the circulation, because the flow has to work against a potential (Mestel, 1953). Formally, this effect is written as a "stabilising" circulation velocity v_μ that brakes the Eddington-Sweet circulation by friction (Kippenhahn, 1974)

$$v_\mu \equiv \frac{H_P}{\tau^*_{\rm KH}} \frac{\varphi \nabla_\mu}{\delta(\nabla - \nabla_{\rm ad})}. \tag{II.26}$$

$\tau^*_{\rm KH}$ is the local Kelvin-Helmholtz timescale to estimate the timescale for the local thermal adjustment of the currents (Pinsonneault et al., 1989)

$$\tau^*_{\rm KH} = \frac{Gm^2}{r(l - m\varepsilon_\nu)}, \tag{II.27}$$

with the energy generation via neutrinos ε_ν[9] which reduces the thermal timescale in the advanced stellar phases.

[8] In the literature, there seems to be a separation of the two naming conventions: Eddington-Sweet circulation is often associated with the circulation as described in Kippenhahn & Moellenhoff (1974); Kippenhahn (1974); Endal & Sofia (1978); Heger et al. (2000). On the other hand, meridional circulation is linked with the solution of Zahn (1992). Out of convenience, this nomenclature is kept throughout this work.

[9] The neutrino energy generation is negative because neutrinos transport energy away.

Since the mixing of chemicals and transport of angular momentum is treated in a diffusive manner in the MESA code used in this thesis (see Appendix B) the sign of the Eddington-Sweet circulation does not matter but the braking μ-gradient velocity will always point the opposite way to $v_{\rm E}$. Therefore, the effective Eddington-Sweet circulation net-velocity is determined by (Endal & Sofia, 1978)

$$v_{\rm ES} \equiv \max\left\{|v_{\rm E}| - |v_\mu|, 0\right\} \tag{II.28}$$

The diffusion coefficient is then calculated as the product of the circulation velocity $v_{\rm ES}$ and the path length of the distributing currents (Endal & Sofia, 1978)

$$D_{\rm ES} \equiv \min\left\{r_{\rm inst}, H_{v,\rm ES}\right\} v_{\rm ES} \tag{II.29}$$

with the velocity scale height $H_{v,\rm ES}$

$$H_{v,\rm ES} = \left|\frac{dr}{d\ln\, v_{\rm ES}}\right| \tag{II.30}$$

and the minimum extent of the instability $r_{\rm inst}$.

Zahn (1992) solved the problem of meridional circulation in a self-consistent picture without making a rudimentary comparison of "velocities" - see Eqs.(II.26) and (II.28). He showed that the equation of energy conservation, the Poisson equation and the conservation of angular momentum have to be treated simultaneously. While the vertical transport of matter is still treated as a diffusion process, the vertical transport of angular momentum is described by an advective-diffusive equation (Chaboyer & Zahn, 1992; Zahn, 1992), which in the case of shellular rotation, a rotation law where the rotation rate is constant on isobaric shells (see Section II.2.3), can be written in Eulerian coordinates as

$$\frac{\partial}{\partial t}\left(\rho r^2 \overline{\Omega}\right)_r = \frac{1}{5r^2}\frac{\partial}{\partial r}\left[\rho r^4 \overline{\Omega}\left(U(r) - \dot{r}\right)\right] + \frac{1}{r^2}\frac{\partial}{\partial r}\left[\rho D r^4 \frac{\partial \overline{\Omega}}{\partial r}\right]. \tag{II.31}$$

Here, D is the diffusion coefficient resulting from the sum of the various transport processes other than the meridional circulation[10], $\overline{\Omega}$ is the average value of Ω on an isobar, $\dot{r}$ is the change of the radius due to expansion or contraction of the star and $U(r)$ is the amplitude of the radial component of the meridional circulation velocity (see e.g. Maeder & Meynet, 2012, for a review). If Eq.(II.31) is written in Lagrangian formulation the effects of expansion or contraction will be automatically included and the $\dot{r}$ vanishes. The first term on the right hand side is the advection term, indicating the transport by a velocity current, while the second term is the already discussed diffusive term.

It is more physical to treat the meridional circulation as an advective process rather than a diffusive one because it describes the transport by a velocity current rather than the movement of angular

[10]The diffusion coefficients will be in an advective-diffusive scheme and different from the ones derived in this chapter (see e.g. Ekström et al., 2012, for the GENEC variant).

momentum from a location with high concentration to an area of low concentration (Zahn, 1992). However, it is numerically more expensive to include in a stellar evolution code since a fourth order differential equation needs to be solved. Potter et al. (2012a,b) compared the advective-diffusive and the purely diffusive schemes for angular momentum transport. While they found differences between the models on the main-sequence, the authors were unable to identify a preferred implementation and the different models lead to similar qualitative conclusions. Also, if a magnetic dynamo operates (see Section II.3) the magnetic coupling of differential rotating layers will dominate the transport of angular momentum. Therefore, the difference of angular momentum transport between the advective-diffusive and the purely diffusive scheme is negligible.

2.3 Horizontal Turbulence

Differential rotation gives rise to shear instabilities between layers with different rotation velocity, creating turbulent motions. In a radiative region, where a thermal gradient stabilises motions in the vertical direction, the turbulence is much stronger in the horizontal than in the vertical direction[11] (Zahn, 1992). The horizontal turbulence is characterised by a diffusion coefficient, which also expresses the horizontal viscosity. The expression of this coefficient, however, is uncertain and three different forms have been proposed (Zahn, 1992; Maeder, 2003; Mathis et al., 2004). The horizontal turbulent coupling favours a constant angular velocity on isobars. This enforces shellular rotation, a rotation law where the rotation rate is constant on isobaric shells, i.e. $\Omega \equiv \Omega(P) \equiv \Omega(\overline{r})$ with the average radius $\overline{r}$ of a isobaric shell (Zahn, 1992), contrary to cylindrical rotation for example. The inclusion of this rotation law brings many simplifications, for example when formulating the equations of stellar structure - see Section B.1.2. Therefore, this form of rotation law is often used in stellar evolution codes.

Some observations support the existence of horizontal turbulent motions. For example, the solar tachocline[12] is very thin according to helioseismic observations, which can be achieved with horizontal turbulence (Spiegel & Zahn, 1992). Also, observations of the surface CNO elements are in favour of the horizontal turbulence as explained in the following. It was shown that when only the large scale meridional or Eddington-Sweet circulation is included in models, the predictions of surface CNO elements are overestimated (e.g. Charbonneau et al., 1989). The solution is that while meridional or Eddington-Sweet currents transport both, angular momentum and chemical elements, the two transport processes interact differently with the horizontal turbulence. Chaboyer & Zahn (1992) showed that the combination of the transport of chemical elements by the meridional circulation and the horizontal turbulence is equivalent to a diffusion process (see also Fig.(11.10) in Maeder, 2009). The

[11] Vertical means along the radial direction and horizontal is on an isobar.

[12] The solar tachocline is the region where the solid body rotation in the radiative solar core transitions into the convective envelope, where rotation varies with latitude.

resulting effective diffusivity by meridional circulation in presence of horizontal turbulence is much smaller than if the circulation would be applied alone, thus, the horizontal turbulence strongly inhibits the transport of the chemical elements by the meridional circulation. This is not the case for the transport of angular momentum. For the chemical elements, both the advective and diffusive processes operate on the same quantity, the abundance X_i. In contrast, for angular momentum the diffusive term acts on the derivative of Ω while the advective term acts on the angular momentum $(r\,\sin\theta)^2\Omega$. Consequently, horizontal turbulence favours the horizontal uniformity of Ω and the meridional circulation transports angular momentum, hence, angular momentum transport remains an advective process and horizontal turbulence does not greatly affect it (Chaboyer & Zahn, 1992). Therefore, the inclusion of horizontal turbulence will reduce the predicted surface CNO abundances but not influence the transport of angular momentum and observations are better reproduced (Meynet & Maeder, 2000).

2.4 Shear Instabilities

In their interior rotating stars have density and angular velocity gradients, resulting from their stratified structure. If this stable structure is perturbed instabilities can set in. For example, if a denser fluid is pushed by a lighter one against gravitational acceleration the Rayleigh-Taylor instability occurs. Another instability arises if two neighbouring regions rotate with different velocities, the Kelvin-Helmholtz instability. The balance between the two instabilities needs to be studied in detail. While a velocity gradient between differentially rotating layers may trigger an instability, a density stratification favours stability. The condition that expresses the stability is the Richardson criterion (e.g. Endal & Sofia, 1978), where instability leads to the dynamical shear instability. However, heat losses and diffusion may change the stability of fluid elements, leading to the so-called secular shear instability.

2.4.1 Dynamical Shear Instability

The Richardson criterion was first derived by Chandrasekhar (1961). A velocity gradient between differential rotating layers provides energy to overcome the gravitational potential for the fluid element to adiabatically turnover. Assuming there are two neighbouring fluid elements at locations z and $z+\delta z$ with velocities v and $v+\delta v$, the work per unit volume to be done against gravity to exchange the two elements is

$$\delta W_{\rm grav} = g\delta\rho\delta z;\ \text{with}\ \delta\rho = \left(\frac{d\rho_{\rm int}}{dz} - \frac{d\rho_{\rm ext}}{dz}\right), \tag{II.32}$$

with the density excess $\delta\rho$ (see Section II.1.1) at the end of the displacement. After their displacement, both elements have the average velocity $1/2(v+\delta v)$. The kinetic energy per unit volume available to

provide work against the gravitational potential is the difference between the total initial and total final kinetic energy,

$$\delta E_{\rm kin} = \frac{1}{2}\rho\left[v^2 + (v+\delta v)^2 - 2\cdot(v+\frac{1}{2}\delta v)^2\right] = \frac{1}{4}\rho(\delta v)^2. \tag{II.33}$$

The instability occurs when the kinetic energy from differential rotation overcomes the work against the gravitational potential, hence, $\delta E_{\rm kin} > \delta W_{\rm grav}$ and which becomes for infinitesimal small variations

$$\mathcal{R}i_{\rm crit} = \frac{1}{4} > \frac{g}{\rho}\frac{N^2}{(\partial v/\partial z)^2} \equiv \mathcal{R}i, \tag{II.34}$$

with the critical Richardson number $\mathcal{R}i_{\rm crit}$ and the stabilising buoyancy frequency. Here, the gravity entering the Brunt-Väisälä frequency is the effective gravity to account for the rotational distortion. The Richardson criterion does not account for thermal effects. This assumption is only valid if the instability works on a fast, dynamic timescale, i.e. when the Peclet number[13] is much larger than 1. This condition is met, for example, during the advanced pre-supernova phases in massive rotating stars.

Different formulations of the dynamical shear diffusion coefficients $D_{\rm DSI}$ can be found in the literature (Zahn, 1992; Maeder, 1997; Heger et al., 2000; Brüggen & Hillebrandt, 2001; Hirschi et al., 2004). The diffusion coefficient of the dynamical shear instability used in this work is estimated similarly to the diffusion coefficient of the Solberg-Høiland instability in Section II.2.1 (Endal & Sofia, 1978; Pinsonneault et al., 1989; Heger et al., 2000),

$$D_{\rm DSI} = \left\{\min(r_{\rm inst}, H_P)\left[1 - \max(\frac{\mathcal{R}i}{\mathcal{R}i_{\rm crit}}, 0)\right]\right\}^2 / \tau_{\rm dyn}. \tag{II.35}$$

The term in the second bracket allows for a smooth transition from a stable region ($\mathcal{R}i_{\rm crit} < \mathcal{R}i$) to the unstable region and increases the mixing as the instability increases.

2.4.2 Secular Shear Instability

The assumption that the thermal timescale is negligible is not necessarily the case. Therefore, more generally heat losses and heat diffusion need to be taken into account. These effects reduce the thermal stratification and the shear instability can occur in regions that are stable according to the Richardson criterion derived in Eq.(II.34). This process operates on a thermal timescale and is therefore a secular process, hence the name secular shear instability.

The stability criterion for the secular shear instability needs to consider the stabilisation of thermal stratification including heat losses and the stabilising gradient in chemical composition. Endal & Sofia

[13] The Peclet number is the ratio of the thermal to the dynamical timescale, $\mathcal{P}e = v\ell/K$, with the radiative conductivity K.

(1978) include two conditions, that need to be violated simultaneously for the secular shear instability to set in.

The Prandtl number $\mathcal{P}r$ is the ratio of thermal diffusion time scale to the angular momentum diffusion time scale and can be calculated by dividing the kinematic viscosity by the thermal diffusivity. A strong thermal diffusion thus results in a small Prandtl number, $\mathcal{P}r \ll 1$ and the stabilising effect of the density gradient is removed, resulting in a stronger secular shear. The first criterion for instability against secular shear is (Endal & Sofia, 1978)

$$\mathcal{R}i_{\mathrm{SSI},1} \equiv \frac{\mathcal{R}_{\mathrm{crit}}}{8}\mathcal{P}r\mathcal{R}i < \frac{1}{4}, \tag{II.36}$$

with the critical Reynolds number[14] $\mathcal{R}_{\mathrm{crit}} \approx 10^3$ (Zahn, 1974).

The stability condition for $\mathcal{R}i_{\mathrm{SSI},1}$ implies that any differential rotation is unstable in the inviscid limit ($\mathcal{P}r \to 0$), despite any stabilising gradient in chemical composition. However, this is not correct because the timescale for chemical diffusion is longer than the thermal timescale. In order to account for the effect of the μ-gradient, the second condition for instability is the Richardson criterion in Eq.(II.34) but only the ∇_μ in N^2 is considered (Endal & Sofia, 1978; Heger et al., 2000),

$$\mathcal{R}i_{\mathrm{SSI},2} \equiv \frac{g^2\varphi}{\rho H_P}\frac{\nabla_\mu}{(\partial v/\partial z)^2} < \frac{1}{4}. \tag{II.37}$$

If both criteria, Eqs.(II.36) and (II.37), are met the secular shear instability arises. The growth timescale of this instability, $\tau_{\mathrm{SSI}} \sim \mathcal{R}_{\mathrm{crit}}/|d\Omega/d\ln r|$, is long compared to the dynamical timescale but shorter than the Kelvin-Helmholtz timescale. The velocity of the instability, which is needed to estimate a diffusion coefficient, can be calculated from the ratio of the size scale, $r_{\mathrm{inst}} \sim \sqrt{\nu d\mathcal{R}_{\mathrm{crit}}/|d\Omega/d\ln r|}$ and the timescale,

$$v_{\mathrm{SSI}} = \sqrt{\frac{\nu}{\mathcal{R}_{\mathrm{crit}}}\frac{d\Omega}{d\ln r}}. \tag{II.38}$$

The diffusion coefficient is then computed by

$$D_{\mathrm{SSI}} \equiv \min(v_{\mathrm{SSI}}, c_s)\min(H_{v,\mathrm{SSI}}, H_P)\left[1 - \frac{\max(\mathcal{R}i_{\mathrm{SSI},1}, \mathcal{R}i_{\mathrm{SSI},2})}{\mathcal{R}i_{\mathrm{crit}}}\right]^2, \tag{II.39}$$

with the speed of sound, c_s, and the velocity scale height of the flow, $H_{v,\mathrm{SSI}} \equiv |dr/d\ln v_{\mathrm{SSI}}|$. Similar to the dynamical shear instability, the diffusion coefficient smoothly increases as the stability criterion is more violated.

The horizontal turbulence from Section II.2.3 reduces the chemical composition gradients and temperature stratification (Maeder, 1997). Consequently, the limiting chemical composition gradient in

[14] The Reynolds number is the ratio of inertial to viscous forces. This number helps in predicting flow patterns, i.e. at a high Reynolds number a fluid flow tends to be turbulent.

$\mathcal{R}i_{\mathrm{SSI},2}$ is reduced and might not completely suppress the occurrence of the shear instability, thus, some mixing can occur. In order to take the reduction of the chemical composition gradient and the temperature stratification into account, Heger et al. (2000) introduce two parameters $\in [0,1]$, which they multiply to chemical mixing efficiency and the ∇_μ, respectively - see also discussions in Chapters B and IV.

2.5 Baroclinic Instabilities

A star with solid body rotation or a cylindrical rotation law is barotropic and ρ, P and T are constant on equipotentials - see Section I.4. In other cases of differential rotation, such as shellular rotation, quantities other than the pressure vary with latitude and the star is baroclinic. The variation of the different quantities with latitude depends on the gradient of Ω. This baroclinicity introduces various instabilities such as the Goldreich-Schubert-Fricke instability, the ABCD instability (Spruit et al., 1983) and the triple-diffusive instability (Knobloch & Spruit, 1983). The latter two instabilities currently lack reliable estimates of their mixing efficiencies. Therefore, their inclusion into stellar evolution codes is unjustified (Heger et al., 2000).

2.5.1 Goldreich-Schubert-Fricke Instability

The Goldreich-Schubert-Fricke instability arises when there is an angle between surfaces of constant specific angular momentum and the rotation axis (Goldreich & Schubert, 1967; Fricke, 1968). The conditions for stability are

$$\frac{\partial j}{\partial r} \geq 0 \qquad \text{and} \qquad \frac{\partial \Omega}{\partial z} = 0. \tag{II.40}$$

The first condition is the secular version of the Solberg-Høiland criterion, where thermal conduction removed the stabilising temperature gradients. The second condition leads to a baroclinic instability if the rotation rate depends on the distance from the equatorial plane. A displaced fluid element will have a larger amount of angular velocity than its surrounding and the excess centrifugal force on this element will further displace it. Accordingly, if the rotation profile is not conservative, meridional flows will be driven which tend to enforce uniform rotation in chemically homogeneous regions (Endal & Sofia, 1978). The stabilising buoyancy force on the displaced element can be removed by heat losses on a thermal timescale. The larger the angle between the rotation axis and the lines of constant rotation, the stronger this instability will be and its dependence on differential rotation is stronger than for the Eddington-Sweet circulation. The circulation velocity can be estimated as (Endal & Sofia, 1978)

$$v_{\mathrm{g}} = \frac{2H_T}{H_j}\frac{d\ln\Omega}{d\ln r} v_{\mathrm{E}}, \tag{II.41}$$

with the Eddington-Sweet circulation velocity $v_{\rm E}$, Eq.(II.25), the temperature scale height $H_T \equiv -(dr)/(d\ln T)$ and the angular momentum scale height $H_j \equiv (dr)/(d\ln j)$. The Goldreich-Schubert-Fricke instability has the same dependence on the chemical composition gradient as the Eddington-Sweet circulation, hence, the total circulation velocity is calculated in the same way,

$$v_{\rm GSF} \equiv \max\{|v_{\rm g}| - |v_\mu|, 0\} \tag{II.42}$$

and so is the diffusion coefficient

$$D_{\rm GSF} \equiv \min\{r_{\rm inst}, H_{v,\rm GSF}\}\, v_{\rm GSF} \tag{II.43}$$

with the velocity scale height $H_{v,\rm GSF}$

$$H_{v,\rm GSF} = \left| \frac{dr}{d\ln v_{\rm GSF}} \right|. \tag{II.44}$$

2.6 Discussion on Rotation-Induced Hydrodynamic Mixing

The treatment of the mixing processes in 1D stellar evolution codes includes many uncertainties. The uncertainties arise because of the approximate and parametrised way the processes are included in stellar modelling. For example Edelmann et al. (2017) compare 2D and 1D simulations of the dynamical shear instability and conclude that the dynamical process operates on a much faster timescale than the evolutionary timesteps in the 1D simulations. As a result, the estimated mixing efficiency will be overestimated in 1D simulations. Another example is the treatment of a possible chemical composition gradient. In the rotational instabilities discussed above, this gradient is taken into consideration by writing it formally as a "breaking-velocity". This obviously is not the proper treatment, which leads for example to the scenario that a chemical composition gradient can completely suppress rotation-induced mixing - see discussion in Chapter IV. Other uncertainties are due to the different schemes used, either a purely diffusive or an advective-diffusive scheme, and approximations within these schemes. For example, Heger et al. (2000) names the derived diffusive descriptions of the rotation-induced mixing processes "*order-of-magnitude*" estimates and therefore scales the sum of their diffusion coefficients with a parameter - see Section B.1.4. This, however, leads to the question how much they have to be scaled, if the scaling applies the same way in different stars and whether all the estimates have to be scaled by the same amount. On the other hand, in the advective-diffusive scheme, there exist different prescriptions to express the horizontal turbulent coefficient (Zahn, 1992; Maeder, 2003; Mathis et al., 2004) and two different expressions of the shear turbulence (Maeder, 1997; Talon & Zahn, 1997). Also, in both the purely diffusive and the advective-diffusive schemes, the

various rotation-induced instabilities are considered separate and their effects are summed together. This neglects any interaction between them. Maeder et al. (2013) show that the different instabilities interact with each other and should not be taken into account separately.

The transport of angular momentum by hydrodynamic instabilities alone is not sufficient and the predicted core rotation rates from 1D calculations are too fast compared to observations (e.g. Heger et al., 2000; Suijs et al., 2008; Eggenberger et al., 2012; Mosser et al., 2012; Cantiello et al., 2014). Therefore, an additional mechanism needs to be included. Potential candidates are magnetic dynamos (see Section II.3 and e.g. Spruit, 2002; Fuller et al., 2019) and gravity waves (e.g. Talon & Charbonnel, 2005; Belyaev et al., 2013; Fuller et al., 2015b; Edelmann et al., 2019). For a recent review on rotation rates in lower mass stars inferred by asteroseismology and angular momentum transport mechanisms see e.g. Aerts et al. (2019).

3 Magnetic Fields

Stellar observations show the existence of surface magnetic fields in stars across the Hertzsprung-Russell diagram and in compact remnants, allowing to measure and characterise them (e.g. Donati & Landstreet, 2009; Mathys, 2012; Ferrario, 2018). The presence of magnetic fields in massive stars is often accompanied with slow rotation and a chemically peculiar photosphere (Walder et al., 2012). Only a small amount of O- and B-stars ($\lesssim 10\%$) are reported to have large-scale surface magnetic fields (Donati & Landstreet, 2009; Fossati et al., 2015). Strong magnetic fields in the cores of stars have been potentially indirectly detected through asteroseismology, where the magnetic field is thought to have suppressed dipole oscillatory modes (Fuller et al., 2015a).

There exist two configurations of magnetism: the long-lived, stable and the short-lived, dynamical configurations. The stable configurations are thought to be fossil fields, which originate from the magnetic field in the interstellar medium and get amplified during the formation of a star (e.g. Braithwaite & Nordlund, 2006). Dynamical field configurations, on the other hand, are thought to be driven by instabilities and dynamos in rotating stars (Tayler, 1973; Wright, 1973). The understanding of both types of magnetic configuration is still ongoing (see e.g. Walder et al., 2012, for a review).

Magnetic fields are often one of the least explored topics in stellar evolution theory. Nevertheless, magnetic fields play a crucial role in some specific problems of stellar evolution. For example, magnetic fields can transport angular momentum by torques further reducing the core rotation, or the interaction between rotation and magnetic fields can wind up the magnetic field lines causing instabilities by magnetic buoyancy. Even initially weak magnetic fields in the interior of stars are expected to affect the angular momentum transport (Mestel, 1953), which then leads to further changes such as

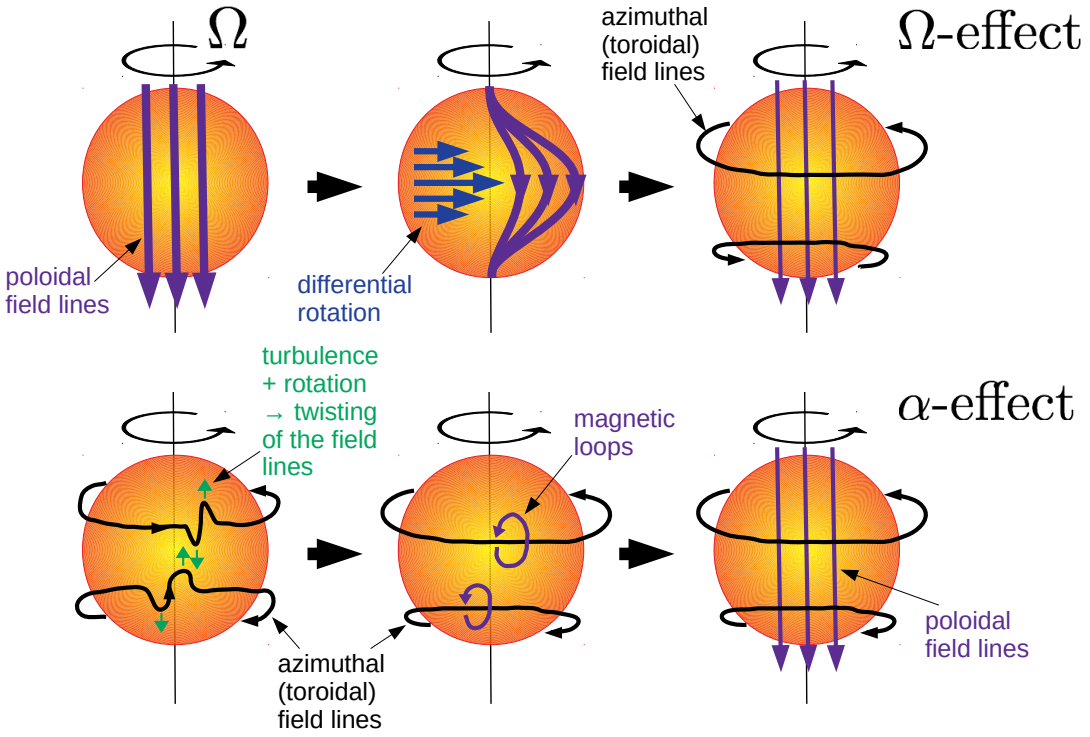

Figure II.2: A schematic representation of the Ω-effect and α-effect. The black and purple lines indicate magnetic field lines.

transport of chemical elements and mass-loss. Magnetic fields affect the final fate of massive stars and exotic objects such as gamma-ray bursts (e.g. Woosley & Bloom, 2006) and magnetars (e.g. Woosley, 1993; Lyutikov & Blackman, 2001; Woosley & Bloom, 2006; Turolla et al., 2015).

3.1 Magnetic Instabilities and Dynamo Processes

In general, a magnetic dynamo is a process where a magnetic field is preserved against ohmic dissipation by a fluid flow and is amplified in the process by field line stretching. In principle, a dynamo converts kinetic energy into magnetic energy. The challenge with massive stars is that their envelopes are radiative, at least most of their life on the main-sequence, therefore the solar-type dynamo[15] cannot be applied. Alternative explanations are a different kind of dynamos or the above-mentioned fossil fields, maybe even a combination of both. The precise origin of both alternatives is still under debate. One of the problems is the stability of the magnetic fields involved in the dynamo process. While dynamo theories generally rely on instabilities of the magnetic field to close the dynamo loop,

[15]In the Sun shear and turbulence near the surface convective zone may create loops in the toroidal or poloidal field lines. [Both, poloidal and toroidal, refer to directions relative to a torus. The poloidal direction is the short way around the surface of the torus, whereas the toroidal direction follows the outer radius around the torus. Historically, these coordinates have been used in context of the Earth's magnetic field, with toroidal being parallel to lines of latitude and poloidal being the direction of the magnetic field.] These loops then generate an electrical current, which according to Ampères' law creates a field of the opposite component (α effect). Furthermore, poloidal field lines in a differentially rotating star are stretched, creating toroidal components (Ω effect) - see also Fig.(II.2).

fossil field theories depend on stable field configuration so that it lasts for the lifetime of a star. It has been shown that magnetic fields with mixed poloidal and toroidal components are stable and that initially unordered fields often relax to this long-lasting mixed topology (Braithwaite & Spruit, 2004; Braithwaite & Nordlund, 2006). On the other hand, pure poloidal fields are unstable if some field lines close outside of the star (Wright, 1973) and a pure toroidal field is unstable to non-axisymmetric perturbations (Tayler, 1973; Wright, 1973).

In the convective core of massive stars a dynamo process is likely to exist (Charbonneau & MacGregor, 2001; Brun et al., 2005), however, it is currently not clear if these generated fields can reach the surface. In case of rotating stars, differential rotation can generate a dynamo action in the radiative zone, the so-called Tayler-Spruit dynamo, but it is dependent on the gradient in the rotation rate (Spruit, 1999, 2002). In this case, the magnetic energy is generated from differential rotation.

An operating dynamo process in the interior of a differentially rotating star creates a torque. This torque can couple the differential rotating layers and reduce the degree of differential rotation, if it acts on a faster timescale than the process that creates the differential rotation, i.e. spin-down or stellar evolution timescale. This may lead to near-solid body rotation - see also Chapter IV.

3.1.1 Tayler Instability

There are several magnetic instabilities that may occur, which all produce displacements that affect rotation and the magnetic fields. The most important one is the Tayler instability, because this instability has the lowest threshold and the shortest timescale of the known magnetic instabilities. Tayler (1973) showed for a non-rotating star that a purely toroidal magnetic field $B_\varphi(r,\theta)$ is unstable on the Alfvén timescale $\tau_\mathrm{A} = \omega_\mathrm{A}^{-1} = R/v_\mathrm{A}$ [16] in a stably stratified medium, even if the field is weak. Assuming a simple picture with an azimuthal magnetic field (see e.g. Fig.(II.2)) where the field lines are ordered concentric around the rotation axis as shown in Fig.(II.3). Between the magnetic loops there is a magnetic pressure $P_\mathcal{M} = B^2/(8\pi)$. As a consequence, the loops move apart sideways from the axis of rotation in a disordered way. The instability is mostly restricted to horizontal surfaces where it avoids work against the stable stratification.

Pitts & Tayler (1985) showed that the Tayler instability also occurs in rotating stars. There, however, the growth time of the Tayler instability is $\sigma_\mathrm{B} = \omega_\mathrm{A}^2/\Omega$ instead of ω_A because the oriolis force reduces the growth rate of the instability. This argument assumes that $\omega_\mathrm{A} \ll \Omega$, which is generally the case with the ordering (Spruit, 2002)

$$N \gg \Omega \gg \omega_\mathrm{A}. \tag{II.45}$$

[16] with the Alfvén frequency, ω_A, and the Alfvén velocity, $v_\mathrm{A}^2 = B^2/(4\pi\rho) \equiv (\text{tension})/\rho$, the velocity with which the magnetic perturbation of the magnetic field propagates along the field lines, i.e. it characterises magnetic equilibrium in a non-rotating star.

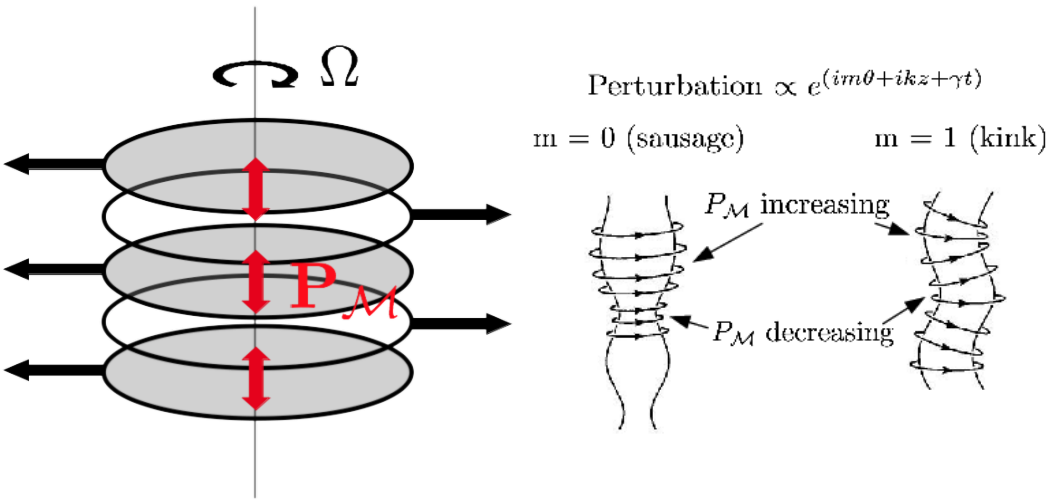

Figure II.3: *Left*: A schematic representation of the Tayler instability. The concentric rings around the rotation axis, indicated with the rotation velocity Ω, represent an azimuthal magnetic field, which is exposed to a magnetic pressure, indicated by the red arrows. As a result, the magnetic loops move apart sideways (black arrows) as an unordered $m = 1$ instability. Adapted from Spruit (1999).
Right: Schematic representation of magnetohydrodynamic instabilities near the rotation axis of a star. The magnetic field lines are indicated with arrows on the "rings". The figure shows the $m = 0$ disturbance, which requires motion along the rotation axis, and the $m = 1$ instability, which involves motion mostly perpendicular to the rotation axis. Adopted from Tayler (1973).

Considering thermal effects, the minimum Alfvén frequency for the Tayler instability to occur can be found by equating the minimal amplitude of the instability so that it is not damped and the condition that the magnetic energy has to be larger than the kinetic energy of the restoring forces. This gives the condition (Spruit, 1999)

$$\frac{\omega_{\rm A}}{\Omega} > \left(\frac{N}{\Omega}\right)^{1/2} \left(\frac{\eta}{K}\right)^{1/4} \left(\frac{\eta}{r^2\Omega}\right)^{1/4}, \tag{II.46}$$

with the magnetic diffusivity η and the thermal diffusivity K.

In a slowly rotating star, however, the condition changes to $\omega_{\rm A} > \Omega$. In this case, the Richardson criterion (Eq.(II.34)) is first met and the shear instability arises before the Tayler instability sets in.

3.1.2 Tayler-Spruit Dynamo

The first proposed magnetic dynamo operating in the radiative region of a differential rotating star, often called Tayler-Spruit dynamo, was suggested by Spruit (1999, 2002). The driving magnetic instability of this dynamo process is the Tayler instability, discussed in Section II.3.1.1.

In a schematic picture, the magnetic dynamo loop works in the following way. For simplicity, the initial configuration is a star with a shellular rotation $\Omega(r)$ and an initially weak poloidal magnetic field[17]. Differential rotation winds up the radial component B_r of the poloidal field, forming an azimuthal

[17] A strong field would lead to magnetic coupling between differential rotating layers, hence, the star would rotate as, or close to, a solid body. Furthermore, a weak magnetic fields obeys the condition $\omega_{\rm A} \ll \Omega$.

field B_φ after a few rotation periods. The field components evolve as (Spruit, 1999)

$$\frac{\partial B_r}{\partial t} = 0, \quad \frac{\partial B_\theta}{\partial t} = 0, \quad \frac{\partial B_\varphi}{\partial t} = r \sin\theta \, \mathbf{B}_P \nabla\Omega, \tag{II.47}$$

with the poloidal field $\mathbf{B}_P$ and the angle of latitude θ. After a few differential turns the field component B_φ is

$$B_\varphi = r \sin\theta \int_0^t |\nabla\Omega| dt \times \left\{ \mathbf{B}_P \frac{\nabla\Omega}{|\nabla\Omega|} \right\}, \tag{II.48}$$

were the term $r \sin\theta \int_0^t |\nabla\Omega| dt$ is a factor that accounts for the number of differential revolution, i.e. the number of rotations due to differential rotation , normalised by 2π and $\nabla\Omega/|\nabla\Omega|$ is a unit vector in the direction of the gradient of Ω, i.e. orthogonal to the horizontal layers. In simple terms, the initially weak magnetic field is amplified depending on the differential rotation and number of differential turns, meaning that the rotation energy is transferred into magnetic energy[18]. The azimuthal magnetic component, B_φ, grows linearly in time and eventually dominates over B_r. At some point, B_φ becomes unstable to the Tayler instability discussed in Section II.3.1.1. While this instability mainly generates horizontal components of the magnetic field, it also produces a small amount of B_r, which is limited by the action of the buoyancy work. The radial component of the field is further wound up by differential rotation, amplifying the field component B_φ. The toroidal field is once again unstable, closing the dynamo loop. The maximal amplitude of the magnetic field generated by this dynamo action is limited by dissipation effects. The horizontal component of the magnetic field favours shellar rotation whereas the vertical component favours solid body rotation.

In his work, Spruit (2002) considered two cases, *case 0* where the chemical composition gradient dominates over the thermal gradient and *case 1* with $\nabla_\mu = 0$. In the following the two cases are considered and indicated with the subscript 0 and 1, respectively. The condition for the occurrence of the Tayler instability (Eq.(II.46)) is for *case 1* were thermal diffusion reduces the stabilising stratification. In *case 0*, $(\eta/K) = 1$. Spruit (1999) assumed $\eta/K \ll 1$ for the derivation of Eq.(II.46), hence it is less restrictive. Therefore, the Tayler instability sets in at lower field strengths in *case 1* than in *case 0*. Spruit (2002) derives the amplitudes of the dynamo-generated field for a steady equilibrium where the amplification timescale due to the dynamo matches the damping timescale due to magnetic diffusivity. He finds for the saturated field components generated by the dynamo process in *case 0*

$$B_{\varphi,0} = (4\pi\rho)^{\frac{1}{2}} rq\frac{\Omega^2}{N}, \qquad B_{r,0} = q\left(\frac{\Omega}{N}\right)^2 B_{\varphi,0} \tag{II.49}$$

[18]This is fundamentally different from, for example, the solar dynamo, where the dynamo is driven by the convective velocity field.

and in *case 1*

$$B_{\varphi,1} = (4\pi\rho)^{\frac{1}{2}}\, r q^{\frac{1}{2}} \Omega \left(\frac{\Omega}{N}\right)^{\frac{1}{8}} \left(\frac{K}{r^2 N}\right)^{\frac{1}{8}}, \qquad B_{r,1} = \left(\frac{\Omega}{N}\right)^{\frac{1}{4}} \left(\frac{K}{r^2 N}\right)^{\frac{1}{4}} B_{\varphi,1}. \tag{II.50}$$

q is the dimensionless differential rotation rate or shear

$$q = \frac{\partial \ln \Omega}{\partial \ln r}. \tag{II.51}$$

The dynamo process generates magnetic energy from differential rotation. Therefore, in order for the dynamo process to operate there has to be a minimum amount of differential rotation. Spruit (2002) derived the minimal necessary shear for the Tayler-Spruit dynamo to be active as

$$q_0 = \left(\frac{N}{\Omega}\right)^{\frac{7}{4}} \left(\frac{\eta}{r^2 N}\right)^{\frac{1}{4}}, \qquad q_1 = q_0 \left(\frac{\eta}{K}\right)^{\frac{3}{4}}. \tag{II.52}$$

If the shear is below this limit, then the differential rotation is not strong enough to amplify the magnetic field in the dynamo loop.

It is worth noting that Maeder & Meynet (2004) avoid the simplification to assume that either the temperature gradient or a gradient in chemical composition dominates and derive the Tayler-Spruit dynamo theory for the general case. This also includes non-adiabatic effects, which favour the growth of the magnetic fields. However, the solution of Maeder & Meynet (2004) requires a fourth- order differential equation to be solved which is computational expensive and can make the code unstable.

II.3.1.2.1 Angular Momentum Transport by the Tayler-Spruit Dynamo

The main implication of the dynamo process and the magnetic field it produces is the ability to transport angular momentum. This is especially crucial in radiative layers where otherwise only the less efficient rotation-induced hydrodynamic instabilities transport angular momentum. The magnetic coupling is strong enough to favour a solid body rotation and efficiently spin down the cores. This results in a faster surface rotation, which favours mass and angular momentum loss.

The torque by volume unity, $\mathcal{S}_B$, induced by the magnetic fields can be obtained by writing the Lorentz force and the Maxwell equation $(4\pi/c)\mathbf{j} = \nabla \times \mathbf{B}$,

$$\mathcal{S}_{\mathrm{B}} = \mathbf{r} \times \mathbf{F}_{\mathrm{L}} = \frac{1}{c}\mathbf{r} \times (\mathbf{j} \times \mathbf{B}) = \frac{1}{4\pi}\mathbf{r} \times ((\nabla \times \mathbf{B}) \times \mathbf{B}), \tag{II.53}$$

which can be written approximately[19] in modulus form as $\mathcal{S}_{\mathrm{B}} \approx (1/4\pi) B_r B_\varphi$, hence, for the two cases

[19] This form is a dimensional estimate by taking $r \cdot \frac{\delta B}{\delta r} \cdot B \approx \delta B \cdot B$

of Spruit (2002)

$$\mathcal{S}_{\mathrm{B},0} \approx \rho\Omega^2 r^2 q^3 \left(\frac{\Omega}{N}\right)^4, \qquad \mathcal{S}_{\mathrm{B},1} \approx \rho\Omega^2 r^2 q \left(\frac{\Omega}{N}\right)^{\frac{1}{2}} \left(\frac{K}{r^2 N}\right)^{\frac{1}{2}}. \tag{II.54}$$

The stress can be expressed in terms of the kinematic viscosity $\nu = \eta/\rho$, which relates the shear and the magnetic torque as $\mathcal{S}_{\mathrm{B}} = \rho\nu r\partial\Omega/\partial r \equiv \rho\nu\Omega q$. Combining this and Eq.(II.54) yields the viscosities for the angular momentum transport,

$$\nu_0 = r^2\Omega q^2 \left(\frac{\Omega}{N}\right)^4, \qquad \nu_1 = r^2\Omega \left(\frac{\Omega}{N}\right)^{\frac{1}{2}} \left(\frac{K}{r^2 N}\right)^{\frac{1}{2}}. \tag{II.55}$$

Surprisingly, if the dynamo is active, i.e. the shear satisfies the condition $q > q_1$, the effective viscosity in *case 1* is independent of the shear rate. These viscosities determine the radial transport of angular momentum under the assumption of shellular rotation.

Under the assumption of a monotonic dependence of the stress on the chemical and thermal stratifications, Spruit (2002) suggest a patching formula to connect the two limiting cases. The minimum shear for the dynamo to operate can be taken as the sum $q_{\min} = q_0 + q_1$, which takes into account that the dynamo action is only possible when $\nabla\Omega$ is strong enough to overcome the chemical and compositional stratification. The effective viscosity produced by the Tayler-Spruit dynamo-generated magnetic field can then be patched together[20] with the modified viscosities of the two limiting cases, ν_0 and ν_1, as

$$\nu_{\mathrm{AM,TS}} = \frac{\nu_{\mathrm{N}_\mu} \cdot \nu_{\mathrm{N_T}}}{\nu_{\mathrm{N}_\mu} + \nu_{\mathrm{N_T}}} f(q), \tag{II.56}$$

with

$$\nu_{\mathrm{N}_\mu} = r^2\Omega q^2 \left(\frac{\Omega}{N_\mu}\right)^4, \qquad \nu_{\mathrm{N_T}} = r^2\Omega \max\left\{\left(\frac{\Omega}{N_{\mathrm{T}}}\right)^{\frac{1}{2}} \left(\frac{K}{r^2 N_{\mathrm{T}}}\right)^{\frac{1}{2}}, q^2 \left(\frac{\Omega}{N_{\mathrm{T}}}\right)^4\right\}. \tag{II.57}$$

The max-function for $\nu_{\mathrm{N_T}}$ is included to correct for the error in its derivation of not including cases where thermal diffusion has no effect (Spruit, 2002). The factor in Eq.(II.56) includes the stabilising effects of the chemical composition and the thermal stratification at the same time. The function $f(q)$ causes the viscosity to decrease smoothly when the shear approaches the minimum amount required for the dynamo action to operate and is zero if the dynamo does not operate,

$$f(q) = \begin{cases} 1 - q_{\min}/q & (q > q_{\min}) \\ 0 & (q \leq q_{\min}) \end{cases} \tag{II.58}$$

[20] Spruit (2002) admits the algebraic complexity of an expression for the general case and, considering the sophistication of the analysis, presents a simpler patching formula to connect *case 0* and *case 1*. Note however, that Maeder & Meynet (2004) derived the Tayler-Spruit dynamo for the general case.

The viscosity for angular momentum transport can then be included in the diffusion equation to calculate the change in angular momentum - see Appendix C.3.2.

II.3.1.2.2 Chemical Mixing by the Tayler-Spruit Dynamo

The dynamo process described above creates fluid motion that can mix the chemical elements. In the radial direction the mixing is generated by the same displacements that produce the magnetic diffusivity. Therefore, the effective diffusivity of the Tayler-Spruit dynamo $D_{\rm TS}$ can be set equal to the effective magnetic diffusivity within a factor of unity (§3.2 Spruit, 2002). This results in a similar patched form for the effective diffusivity,

$$D_{\rm TS} = \frac{D_{\rm N_\mu} \cdot D_{\rm N_T}}{D_{\rm N_\mu} + D_{\rm N_T}} f(q), \tag{II.59}$$

with $f(q)$ defined in Eq.(II.58) and

$$D_{\rm N_\mu} = r^2 \Omega q^4 \left(\frac{\Omega}{N_\mu}\right)^6, \qquad D_{\rm N_T} = r^2 \Omega \max\left\{ q \left(\frac{\Omega}{N_{\rm T}}\right)^{\frac{3}{4}} \left(\frac{K}{r^2 N_{\rm T}}\right)^{\frac{3}{4}}, q^4 \left(\frac{\Omega}{N_{\rm T}}\right)^6 \right\}. \tag{II.60}$$

The comparison of $\nu_{\rm TS}$ and $D_{\rm TS}$ shows that the latter is generally smaller, since $\Omega \ll N$. This is because angular momentum is transported by magnetic stresses whereas the chemical mixing is produced by Reynolds stresses from the fluid flow.

3.1.3 Fuller-modified Tayler-Spruit Dynamo

The Tayler-Spruit dynamo discussed in Section II.3.1.2 enables more angular momentum transport in stars. Comparisons with observations, however, suggest that this dynamo process alone does not transport enough angular momentum - see discussion in Section II.3.2. Furthermore, there are also problems with the Tayler-Spruit dynamo as proposed by Spruit (1999, 2002). The Tayler instability grows fastest in the non-axisymmetric $m = 1$ mode (Tayler, 1973, ; see Fig.(II.3)). Hence, the B_r magnetic field component generated by the instability is non-axisymmetric (Zahn et al., 2007). Consequently, the winding up of B_r will not give an axisymmetric net increase in the B_φ magnetic field component and the axisymmetric components of B_r and B_φ are not necessarily related via Eqs.(II.49) or (II.50). Also, Spruit (2002) might overestimate the damping rate of large background fields B_φ that vary on much larger lengthscales than the displacement of the Tayler instability l_r (Denissenkov & Pinsonneault, 2007), which is normally taken as the typical lengthscale for damping, $\gamma_{\rm damp} \sim \eta_{\rm eff}/l_r^2$, with an effective turbulent diffusivity $\eta_{\rm eff}$. Such a large scale field is more or less constant on the displacement lengthscale. Thus, displacements do not mix the field's lines of opposite polarity and no magnetic reconnection or dissipation occurs. Fuller et al. (2019) show that loops in the field can still dissipate via reconnection after mitigation to the poles where the loop has a smaller

spatial extent. This mechanism, however, causes less damping of the large scale component of B_φ. Therefore, the saturated values of the magnetic field components can reach larger values and produce stronger magnetic torques.

Based on these issues, Fuller et al. (2019) calculate the damping of the perturbed non-linear fields from the Tayler instability, δB. They find a non-linear energy dissipation rate of

$$\dot{E}_{\rm damp} \sim \frac{\delta v_{\rm A}}{r} |\delta B_\perp|^2, \tag{II.61}$$

with the perturbed Alfvén frequency $\delta v_{\rm A} \sim \delta B/\sqrt{4\pi\rho}$ and the horizontal component of the perturbed magnetic field $\delta B_\perp$. This is one of the key differences to Spruit (2002) who uses (i) the large-scale background magnetic field B_φ to determine the energy dissipation and (ii) for the turbulent damping rate at saturation the growth rate of the magnetic field, $\dot{E}_{\rm damp} \sim \sigma_B |\delta B_\varphi|^2 = (\omega_{\rm A}^2/\Omega)|\delta B_\varphi|^2$. Fuller et al. (2019) argues that this is unphysical because it is the Alfvén waves that travel on B_φ that are damped after cascading to small scales, not B_φ itself.

At saturation of the instability a statistically stationary state is reached where the growth rate is equal to the damping rate, $(\omega_{\rm A}^2/\Omega) \sim (\delta v_{\rm A}/r)$, and the perturbed and background fields are related by $\delta B_\perp \sim (\omega_{\rm A}/\Omega) B_\varphi$. Hence, the non-linear energy dissipation rate can be written as a function of the background field

$$\dot{E}_{\rm damp} \sim \frac{\omega_{\rm A}^4}{\Omega^3} |B_\varphi|^2. \tag{II.62}$$

In the picture of Fuller et al. (2019), the energy from differential rotation is converted into magnetic energy by winding up a radial field into a toroidal field. The latter is then unstable to the Tayler instability, which converts the magnetic field energy into magnetic and kinetic energy of the perturbed magnetic and velocity field. These perturbations are then damped into heat by the turbulent cascade. Therefore, in the stationary state, the rate of the amplifying energy, $\dot{E}_{\rm amp} \sim 2 B_\varphi \dot{B}_\varphi \sim q\Omega B_\varphi B_r$, must be the same as the energy dissipation rate, giving

$$q\Omega B_\varphi B_r \sim \frac{\omega_{\rm A}^4}{\Omega^3} |B_\varphi|^2 \tag{II.63}$$

Combining the above equations and the ratio[21] $(B_r/B_\varphi) \sim \omega_{\rm A}/N_{\rm eff}$, with the effective Brunt-Väisälä frequency $N_{\rm eff} \simeq \frac{\eta}{K} N_T^2 + N_\mu^2$ (see Eq.(II.3) but also the discussion in Fuller et al. (2019), Appendix C)

[21] This ratio is the same as for the Tayler-Spruit dynamo. However, there it is only valid for the non-axisymmetric component of B_r, whereas in the Fuller-modified case it relates the axisymmetric component of B_r and B_φ.

to account for radiative losses, it is possible to write the amplitudes of the fields at equilibrium

$$\frac{B_\varphi}{\sqrt{4\pi\rho r^2}} = \omega_\mathrm{A} \sim \Omega \left(\frac{q\Omega}{N_\mathrm{eff}}\right)^{\frac{1}{3}}, \quad \frac{B_r}{\sqrt{4\pi\rho r^2}} \sim \Omega \left(\frac{q^2\Omega^5}{N_\mathrm{eff}^5}\right)^{\frac{1}{3}},$$
$$\frac{\delta B_\perp}{\sqrt{4\pi\rho r^2}} \sim \frac{\delta v_\mathrm{A}}{r} \sim \Omega \left(\frac{q\Omega}{N_\mathrm{eff}}\right)^{\frac{2}{3}}, \quad \frac{\delta v_\perp}{r} \sim \Omega \frac{q\Omega}{N_\mathrm{eff}}. \tag{II.64}$$

II.3.1.3.1 Angular Momentum Transport with the Fuller-modified Tayler-Spruit dynamo

The fields in Eq.(II.64) couple differentially rotating layers, similar to the Tayler-Spruit dynamo in Section II.3.1.2.1, and transport angular momentum. The angular momentum transport can be calculated in the same way as for the Tayler-Spruit dynamo by first calculating the magnetic torque

$$\mathcal{S}_B \sim B_\varphi B_r \sim 4\pi\rho r^2 q\Omega^2 \left(\frac{\Omega}{N_\mathrm{eff}}\right)^2 \tag{II.65}$$

which then relates to an effective diffusivity of angular momentum

$$\nu_\mathrm{AM,TSF} = \frac{\mathcal{S}_B}{4\pi\rho q\Omega} = \alpha^3 r^2 \Omega \left(\frac{\Omega}{N_\mathrm{eff}}\right)^2 \tag{II.66}$$

The factor α is introduced to account for the prefactors in the magnetic energy dissipation balance, which is difficult to predict in an analytical argument (Fuller et al., 2019). α parametrises the result via the saturated Alfvén frequency,

$$\omega_\mathrm{A} = \alpha\Omega \left(\frac{q\Omega}{N_\mathrm{eff}}\right)^{\frac{1}{3}}, \tag{II.67}$$

and is of order unity to fit observational data (Fuller et al., 2019).

As for the Tayler-Spruit dynamo, the Fuller-modified dynamo needs a minimum amount of differential rotation in order to operate, which is obtained by combining the condition for instability, Eq.(II.46), and the saturated Alfvén frequency, Eq.(II.67), giving

$$q_\mathrm{min} = \frac{1}{\alpha^3}\left(\frac{N_\mathrm{eff}}{\Omega}\right)^{\frac{5}{2}} \left(\frac{\eta}{r^2\Omega}\right)^{\frac{3}{4}}. \tag{II.68}$$

II.3.1.3.2 Chemical Mixing by the Fuller-modified Tayler-Spruit Dynamo

Fuller et al. (2019) estimated the effective diffusivity of the Fuller-modified Tayler-Spruit dynamo as

$$D_{TSF} \sim r^2\Omega \left(\frac{\Omega}{N_\mathrm{eff}}\right)^2 \left(\frac{q\Omega}{N_\mathrm{eff}}\right)^{\frac{5}{3}}. \tag{II.69}$$

The ratio of the effective chemical mixing diffusivity to effective angular momentum diffusivity is

$D_{\rm TSF}/\nu_{AM,TSF} \sim (q\Omega/N_{\rm eff})^{5/3}$. In most stars $\Omega/N_{\rm eff}$ is tiny, hence, the chemical mixing by the dynamo process is less important than angular momentum transport. Generally[22], the timescale for chemical mixing is longer than the Ohmic diffusion timescale, which is longer than the stellar evolution timescale (Cantiello et al., 2016). Therefore, the chemical mixing is negligible (Fuller et al., 2019).

3.2 Discussion on Magnetic Fields

Stellar models that include the Tayler-Spruit dynamo are able to efficiently extract angular momentum from the core. For example, this allows the explanation of the near solid body rotation of the Sun (Eggenberger et al., 2005). A more efficient angular momentum transport will also predict slower rotation rates of neutron stars and black holes. However, while the Tayler-Spruit dynamo is efficient at extracting angular momentum from the core of a star, it fails to reproduce the slow rotation rate of white dwarfs, neutron stars and black holes (Heger et al., 2005; Suijs et al., 2008) or the internal rotation profiles of sub-giants or red giants (e.g. Eggenberger et al., 2012, 2019a,b; Cantiello et al., 2014). The Fuller-modified Tayler-Spruit dynamo enables to spin down stellar cores more efficiently and it can match the rotation rates of neutron stars (Fuller et al., 2019; Ma & Fuller, 2019) but it cannot explain the observed rotation profiles in low mass stars in its current form (e.g. den Hartogh et al., 2019; Eggenberger et al., 2019c). The problem is that it cannot simultaneously reproduce the trend of the asteroseismic measurements in the sub-giant and giant stars.

The existence of the Tayler-Spruit dynamo is still strongly debated. Magnetohydrodynamic simulations of instabilities in the radiative zone of a differentially rotating star of Braithwaite & Nordlund (2006); Zahn et al. (2007) show the presence of the Tayler instability. However, while the simulations of Braithwaite & Nordlund (2006) find the existence of a dynamo loop, the results by Zahn et al. (2007) do not show any dynamo action. Also, Rüdiger et al. (2012) analyse the linear theory of the Tayler instability and do not find any dynamo action resulting from this instability.

Also, there are other open questions correlated to a magnetic dynamo process. For example little is known about either the strength of the initial field or the efficiency of instabilities in amplifying the magnetic fields.

There are other magnetic instabilities that might operate in stars (see e.g. Spruit, 1999). For example, in a differential rotating star where the angular momentum decreases outwards, a weak magnetic field is unstable to the magneto-rotational or magnetic shear instability (Velikhov, 1959): Radial motion of a fluid element in a magnetic differentially rotating region is opposed by two effects: (i) the magnetic field enforces rigid rotation and (ii) the stretched field lines try to bring back the fluid element. While (ii) favours stability, (i) leads to an instability because the fluid element has an excess of angular momentum, similar to the second term in Eq.(II.23). Wheeler et al. (2015) found that the magneto-

[22] unless $q \gg 1$ or $N_{\rm eff} \ll N$.

rotational instability operates in massive stars during the post-main-sequence evolution throughout the intermediate stages, where it can additionally slow down the core rotation. The instability only occurs in regions with sufficient shear to overcome the stabilising buoyancy. Therefore the instability is rather sensitive to convective boundary uncertainties. However, the Tayler-Spruit dynamo is more efficient at transporting angular momentum than the magneto-rotational instability because it is active over a larger spatial extent and less intermittent. Furthermore, it has a lower threshold to be activated. Hence, in most cases it reduces the shear before the magneto-rotational instability arises. Another example is the magneto-rotational turbulence, which is created by the redistribution of the magnetic flux, that can also drive the generation of a large-scale magnetic flux, the so-called α-effect (Brandenburg, 2001). This process can generate both, poloidal and toroidal fields. However, the toroidal field is more efficiently generated by shear in differentially rotating stars, which is called the Ω-effect. Therefore, the α-effect is only applied for the generation of a poloidal field. The combination of the two processes creates a dynamo loop, the α-Ω dynamo. While Potter et al. (2012c) find that the α-Ω dynamo allows a better comparison with the observed nitrogen surface enrichment in less massive stars, they also find that the α-Ω dynamo cannot sustain itself in stars with masses $M \gtrsim 15\,\mathrm{M}_\odot$.

More recently, Takahashi & Langer (2020) proposed a magneto-rotational scheme which treats the interplay between magnetic fields, rotation, mass-loss and changes in the density and temperature in a self-consistent manner. They derived the magnetic field components from the mean-field magneto-hydrodynamic equation using Alfvén's theorem. In this framework, angular momentum transport due to the Lorentz force is formulated in a conservative form. Their work so-far is limited to the evolution of a low mass star, which reproduces the core and envelope rotation periods observed by asteroseismology. Whether this formalism is able to explain the missing angular momentum transport in massive stars will be answered by future studies.

4 Discussion

A consequence of a magnetic dynamo is the fact that shear mixing by differential rotation is reduced. However, the Eddington-Sweet circulation (or meridional circulation) is more rapid in rigid rotating models than in the differentially rotating ones (Maeder & Meynet, 2005). Consequently, in a model with strong magnetic coupling, thus closer to solid body rotation, there is more mixing in the radiative zones due to the meridional flows. This leads to higher surface enrichments and higher surface velocities in magnetic models than in non-magnetic ones. However, the interaction between the Tayler-Spruit dynamo and the large-scale meridional circulation is not well understood. For example does a strong magnetic field reduce or even damp the slower hydrodynamic flow?

Stars at solar metallicity with masses above $\gtrsim 40\,M_\odot$ experience strong stellar winds that remove large parts of the envelope, if not all, already during the main-sequence. This mass-loss also removes angular momentum from the surface. Since magnetic fields couple the core and envelope, the core will also reduce its rotation rate substantially. Therefore, the stellar cores tend to rotate slowly in these stars, which helps to explain the rotation rate of young pulsars (Heger et al., 2005) but impedes the explanation of the progenitors of collapsars to produce long soft gamma-ray bursts as proposed by Woosley et al. (1993). Only stars with initially very rapid rotation might produce a collapsar (Hirschi et al., 2005b; Yoon & Langer, 2005), thus, magnetic fields reduce the gamma-ray burst rate prediction.

The different mixing processes are generally treated separately, in reality however they do affect each other. An example is the interaction between convective boundary mixing, rotation and magnetic fields. While the problem of convective boundary mixing is occupying scientists already for decades, the interaction of this process with the effects of rotation and magnetic fields adds another layer of complexity to the problem (see for example Korre et al., 2021; Varma & Müller, 2021). As a consequence of the effective angular momentum transport by turbulent convection, there might be a shear layer building up between the convective region and the radiative zone. This generates shear mixing and possibly activates a magnetic dynamo. How the two turbulent flows, convective boundary mixing and rotation-induced shear interact with each other and how they are affected by the possible magnetic field is still an unanswered question. Moreover, rotation affects other instabilities, such as the thermal-driven mixing processes, stellar winds and so forth. For example, convection in the core of rotating massive stars becomes anisotropic due to the rotational deformation of the core. This anisotropy results in a misalignment between the thermal gradient and the thermal flux, which leads to baroclinicity and circulation currents in the radiative zone, inducing a much stronger meridional flow (Jermyn et al., 2018). Therefore, despite the fast development concerning stellar convection, rotation and magnetic fields in recent years, there is still a lot of work to do.

Chapter III

The Relative Importance of Convective Uncertainties

In this Chapter, I investigate the impact of uncertainties due to convective boundary mixing, commonly called "overshoot", namely the criterion for the boundary location and the amount of mixing beyond the convective boundary, on stellar structure and evolution. For this I calculate two grids of stellar evolution models with the `MESA` stellar evolution code, one with the *Ledoux* and the other one with the *Schwarzschild* boundary criterion, and for each vary the amount of convective boundary mixing. I calculate each grid with the initial masses 15, 20 and 25 $M_\odot$. The evolution of the stellar models is followed from the start of hydrogen burning to the end of helium burning. The impact on nucleosynthesis during helium burning is also investigated. I find a broadening of the main sequence with an increasing amount of convective boundary mixing, which is in better agreement with observations. Furthermore during the core hydrogen burning phase there is a convergence between the *Ledoux* and *Schwarzschild* models due to convective boundary mixing. The uncertainties of the intermediate convective zone causes the models to diverge again after the main sequence. The behaviour of this convective zone strongly affects the surface evolution of the model, i.e. how fast it evolves red-ward. The amount of convective boundary mixing impacts the size of the convective cores and the nucleosynthesis, e.g. the ^{12}C to ^{16}O ratio and the weak s-process. Lastly, I determine the uncertainty that the range of parameter values investigated introduce and find differences of up to 70% for the core masses and the total mass of the star.

The majority of the content of this Chapter was published in Kaiser et al. (2020).

1 Introduction

Convection is one of the key physical processes in stars. In massive stars for example, several recent studies have shown the sensitivity of the pre-supernova structure and their explosion likelihood to the details of their complex convective history (Ugliano et al., 2012; Sukhbold & Woosley, 2014; Müller et al., 2016; Sukhbold et al., 2016; Ertl et al., 2016; Sukhbold et al., 2018; Chieffi & Limongi, 2019). In this Chapter, I investigate the the relative importance of the modelling uncertainties linked with convective boundary mixing and their impact. In particular, I focus on the location of the convective boundary ("*Schwarzschild* versus *Ledoux* criterion") and the amount of convective boundary mixing - see Sections II.1.1 and II.1.3.

This Chapter focusses on the early stellar stages, starting at the zero-age main-sequence and ending at core helium depletion. The goal is (i) to highlight, which aspects of the convective boundary physics lead to the largest uncertainties in the model prediction as well as (ii) which observational test and 3D hydrodynamic simulations may help constrain convective modelling in 1D stellar evolution models. I do not use any "new" physics nor do I claim to use the "right" physics. I simply use the choices that are frequently found in the literature. This study therefore helps to estimate the uncertainty of model predictions found in the literature.

This Chapter is structured as follows. In Section III.2, I outline the input physics and numerics used for the simulations. In Sections III.3 to III.6, I present the impact of the variations on the stellar models and their evolution. Finally, in Section III.7, the results are discussed and some quantities are compared to the literature. The theory of convective mixing is discussed in Section II.1.

2 Physical Ingredients

In order to study the impact of convective boundary uncertainties in massive star models, I computed a set of non-rotating stellar models at solar metallicity with three initial masses, $15, 20$, and $25\,\mathrm{M}_{\odot}$. The simulations were computed using the `MESA` software instrument for stellar evolution (Paxton et al., 2011, 2013, 2015, 2018), revision 10108 - see Appendix B.

The radiative opacities were calculated using the tables of Asplund et al. (2009) and if $\log T_{\mathrm{eff}} \leq 3.8\,\mathrm{K}$ the opacity tables from Ferguson et al. (2005) with photospheric metals from Asplund et al. (2009) were used.

In order to account for the thermonuclear reactions I used a network consisting of 206 isotopes from hydrogen up to the iron group (see Fig. (III.1)). This network calls all possible reactions and their rates linking the isotopes selected in the network, including the weak reactions. Therefore it is suitable to

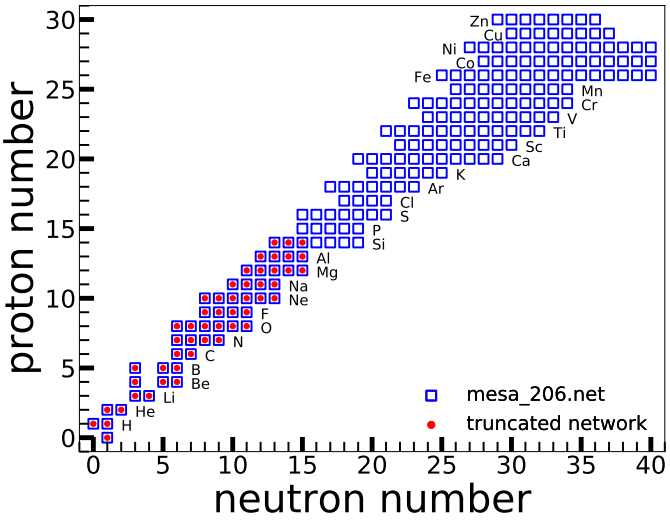

Figure III.1: The isotopes included in the two nuclear reaction networks used in this work, the `mesa_206.net` (empty squares) and the truncated version (filled dots).

calculate the energy generation for all the main burning stages during stellar evolution. Furthermore, the 206 isotope network allows to calculate the stellar evolution up to core-collapse[1]; it contains most of the reactions that affect the structure, such as α-captures on ^{14}N and ^{22}Ne during helium burning - see discussion in Section III.5 - and is able to properly calculate the neutronisation of matter in the core, usually tracked using the electron fraction Y_e. Lastly, Farmer et al. (2016) showed that key quantities of the stellar models converge at the 10% level when using an isotope network of at least $\sim$ 127 isotopes. The stellar models with no convective boundary mixing, $f_{\rm CBM} = 0.0$, were calculated with a truncated network because I only use them for comparison reasons. The truncated network consists of all the elements up to aluminium in `mesa_206.net` and additionally silicon $27, 28, 29$ (compare in Fig. (III.1)). It is therefore suitable to calculate all the necessary reactions during the hydrogen and helium burning phases and does not introduce a difference to the `mesa_206.net`. The reaction rates are taken from the `JINA REACLIB` (Cyburt et al., 2010, see also Section B.1.2.1).

The initial metal abundances were taken from Asplund et al. (2009) with some elements (He, C, N, O, Ne, Mg, Al, Si, S, Ar, Fe) updated based on Nieva & Przybilla (2012) and Przybilla et al. (2013). The mass loss by stellar winds was accounted for with `MESA`'s `Dutch` mass loss scheme - see Section B.1.6. All the mass loss rates were scaled with a factor of $\eta_{\rm wind} = 0.85$. This reduction factor was introduced by Maeder & Meynet (2001, see their Section 2.2 for details) for empirical mass loss rates. While this reduction factor is not necessary for theoretical mass loss rates such as Vink et al. (2000, 2001), we used it for all phases to have mass loss rates similar to published GENEC models (GENEC applies the factor 0.85 during the main sequence, e.g. Ekström et al., 2012) and MESA models (e.g.

[1]I limited the discussion in this Chapter to the evolution between core hydrogen ignition and core helium depletion, because the evolution of the convective history during the advanced phases is complicated and it is difficult to disentangle the uncertainties of convective boundary mixing. Furthermore, Davis et al. (2019) studied the impact of different amounts of convective boundary mixing during the advanced burning stages.

Farmer et al., 2016; Ritter et al., 2018, apply a factor of 0.8).

Some of the models generate enough luminosity so that in their radiation pressure dominated envelope a gas pressure and density inversion occurs - see Section B.1.3.4. These models become numerically unstable and the timesteps become prohibitively short. In order to keep the numerics stable and the timesteps at a reasonable limit we use `MESA`'s `MLT++` (Paxton et al., 2013, and Section B.1.3.4) in all models that apply the largest amount of convective boundary mixing and also in the 20 and 25 $M_\odot$ models with the second largest amount - see below. The treatment of `MLT++` allows the calculation of these models until the end of core helium burning with reasonable timesteps. Tests of the `MLT++` formalism in 15 $M_\odot$ models do not show any significant differences in the structure and evolution but see discussion in Section III.7.

The MESA models assume hydrostatic equilibrium and apply the mixing-length theory variation of Henyey et al. (1965) - see Section B.1.3.2. The mixing length was set to $\ell_{\rm MLT} = 1.6\,H_P$, where H_P is the pressure scale height. This is the same value used by Ekström et al. (2012). Furthermore, for strongly stratified convection Arnett et al. (2018) find an asymptotic limit for the dissipation length of a turbulent flow, which they identify with $\ell_{\rm MLT} \sim H_\rho \sim 5/3\,H_P$, which is close to $1.6\,H_P$. The mixing of the nuclear species in `MESA` is assumed to be a diffusive process. In this Chapter, the diffusion coefficient in the convective region is calculated by $D_{\rm mix} = \frac{1}{3}\ell_{\rm MLT} v_{\rm MLT}$, where $v_{\rm MLT}$ is the velocity determined by the mixing-length theory - see Section B.1.3.1.

We use the same resolution, at which our models seem to converge, in all calculations except the 15 $M_\odot$ models with no convective boundary mixing. In these models, the resolution needed to be increased in order to properly resolve the boundary of the convective zones. The details can be found in the inlists[2], which also contain all the other user-specified settings that differ from the default.

2.1 Convective Boundary Mixing Uncertainties

In this study, I investigate two uncertainties due to convective boundary mixing: (i) the determination of the convective boundary location and (ii) different amounts of extra mixing after the convective boundary.

As discussed in Section II.1, the determination of the convective boundary is not included in the mixing-length theory and either the *Ledoux* or the *Schwarzschild* criterion has to be used. Every model was calculated twice, once applying the *Ledoux* and once the *Schwarzschild* criterion to address this uncertainty.

An investigation of the second point is a much more extensive task because convective boundary mixing is poorly understood, hence connected with several uncertain aspects. The uncertainties arise from (a) the poor knowledge of the convective boundary and the breakdown into 1D, thus, how to

[2]The inlists can be found on http://doi.org/10.5281/zenodo.3871897.

describe and implement the physics in 1D, (b) the parametrisation of the convective boundary mixing prescriptions and (c) the different implementations of the same theory in the various stellar evolution codes, see e.g. discussions in Jones et al. (2015); Stancliffe et al. (2016). In this work, I limit the investigation to one convective boundary mixing prescription and investigate the impact of different choices of the free parameters within this setting.

Following the discussion in Section II.1.3, I apply the exponentially decaying convective boundary mixing prescription by Herwig et al. (1997) (see Eq.(II.17)), which is based on hydrodynamic simulations. Since the interior of the star is simulated, where the instabilities at the convective boundary behave different than in the surface convection simulations from Freytag et al. (1996), I refer to the resulting mixing after the convective boundary as convective boundary mixing. This includes an ensemble of different physical processes which might cause mixing across the convective boundary and is not only limited to an "overshooting" of the convective flow at the boundary. Even if the convective flow is simulated as a radial up-down movement in 1D stellar evolution it is still necessary to think of convection as a 3D process.

In the convective boundary mixing zone, the temperature gradient is set equal to the radiative one. The chemical composition, on the other hand, is mixed using the diffusion coefficient determined by Eq. (II.17). The diffusive mixing after the convective boundary is cut-off at a certain value, which we chose to be $D_{\rm cut} = 10^2\,{\rm cm^2\,s^{-1}}$, in order to avoid the long exponential tail. This treatment of convective boundary mixing is applied to all boundaries of all convective zones.

D_0 in Eq.(II.17) has to be taken "close" to the edge of the convective boundary (Herwig, 2000), which is equivalent to a small f_0 parameter. It is often not discussed how "close" and only the $f_{\rm CBM}$ parameter is mentioned, despite the importance of f_0. Changing the f_0 parameter in Eq. (II.17) from 0.02 to 0.002, gives a different location (i) where D_0 is taken from and (ii) where to begin the exponential decrease of the diffusion coefficient (compare Fig.(II.1b)). The impact of the first point is negligible since the mixing-length theory predicts an approximately constant diffusion coefficient. The second point, however, is not negligible. The fact that the diffusion coefficient begins to decrease deeper in the convective region and is cut off after it drops below a certain value means that the mixing efficiency inside the convective zone recedes and there is less and weaker mixing after the convective boundary.

In Section II.1.3, the values for $f_{\rm CBM}$ used in the literature were discussed. In order to cover the range of $f_{\rm CBM}$ adopted in the literature and the constraints from observations I applied the values $(0.004, 0.01, 0.022, 0.035, 0.05)$. Moreover, for comparison, I also calculated all the models with an initial mass of $15\,{\rm M_\odot}$ with no convective boundary mixing. Additionally, two values for f_0, 0.002 and 0.02, are tested in the $15\,{\rm M_\odot}$ models with $f_{\rm CBM} \leq 0.022$. I only test the two values of f_0 with small values of $f_{\rm CBM}$ because the relative importance of f_0 becomes negligible in models with large amounts of convective boundary mixing - see e.g. Table III.1. The 20 and $25\,{\rm M_\odot}$ models are only simulated

with $f_0 = 0.002$.

Regions which are unstable according to the *Schwarzschild* criterion but stable according to the *Ledoux* criterion undergo slow semiconvective mixing. Semiconvection in the models is applied as presented in Section B.1.3.3. The amount of semiconvective mixing, if it occurs, is still an unsolved problem (e.g. Langer, 2012, and references therein), hence $\alpha_{\rm sc}$ is uncertain. Langer et al. (1985) estimate the semiconvective efficiency to be of the order of 0.1. The values used in the literature vary greatly, ranging from small values of $\alpha_{\rm sc} = 0.01 - 0.02$ (e.g. Farmer et al., 2016; Limongi & Chieffi, 2018) up to 1.0 (e.g. Brott et al., 2011), with intermediate values of ~ 0.1 (e.g. Sukhbold & Woosley, 2014; Choi et al., 2016). Schootemeijer et al. (2019) explore in their calculations a large range of $\alpha_{\rm sc} = 0.01 - 300$ and conclude that $\alpha_{\rm sc} > 1.0$ is needed to reproduce the blue to red supergiant ratio in the Small Magellanic Cloud. I used two values for $\alpha_{\rm sc}$, 0.4, fast semiconvection, and 0.004, slow semiconvection, in my $15\,{\rm M}_\odot$ models. The 20 and $25\,{\rm M}_\odot$ models were only calculated with $\alpha_{\rm sc} = 0.4$ because the relative importance of semiconvection decreases with increasing amount of mixing at the convective boundary - see Sections III.3, III.4 and III.5. Therefore, the two values of $\alpha_{\rm sc}$ would predict a similar outcome. Similarly, Schootemeijer et al. (2019) find that in their massive star models of the Small Magellanic Cloud semiconvection rarely develops for large amount of convective boundary mixing and only plays a role after the main sequence. Moreover, Langer et al. (1985) show that while semiconvection can occur prominently during the main-sequence evolution in their massive star models the evolution during this phase is nearly independent of the choice of $\alpha_{\rm sc}$.

3 Core Hydrogen Burning

In the core hydrogen burning phase, hydrogen is fused into helium which is discussed in Section I.2.1.1. This increases the mean molecular weight μ and decreases the opacity κ. The first leads to an increase in luminosity, because $\ell_{\rm rad} \propto \mu^4$ (e.g. Kippenhahn & Weigert, 1994), hence, a reduction of the pressure onto the core. The decrease of the opacity and pressure dominate over the increase of the core luminosity in a massive star. Therefore, since $\nabla_{\rm rad} \propto \kappa \ell_{\rm rad} P$ (e.g. Kippenhahn & Weigert, 1994), the radiative temperature gradient decreases. On the other hand, the adiabatic temperature gradient, $\nabla_{\rm ad}$, remains roughly constant in the interior of the star. This continuously stabilises the material at the convective boundary against convection according to the stability criterion - see Section II.1.1 - and the mass of the convective hydrogen in a massive star decreases during its main-sequence lifetime. A consequence of the decreasing convective core is a decreasing mean molecular weight above the convective core. The resulting μ-gradient creates the difference between the two boundary criteria.

Fig. (III.2) shows the location of the convective boundary in stellar evolution models with an initial mass of $15\,{\rm M}_\odot$, either given by the *Ledoux* or the *Schwarzschild* boundary criterion, for various

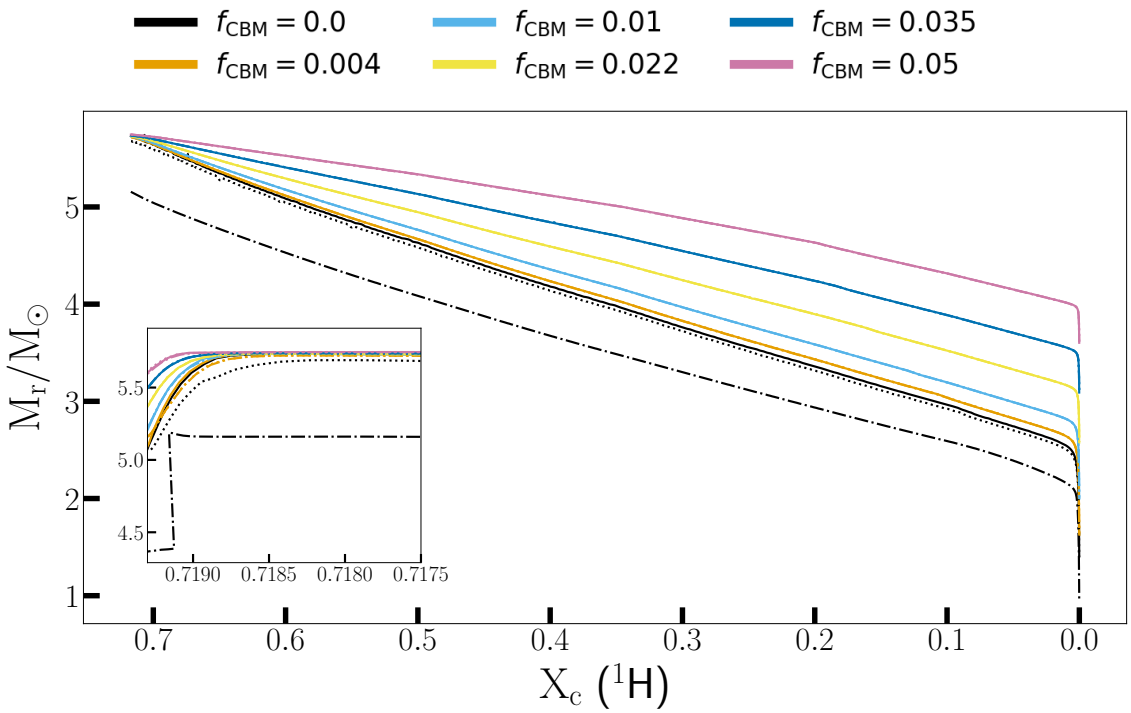

Figure III.2: The location of the convective hydrogen core boundary, determined by either the *Ledoux* or *Schwarzschild* criterion, as a function of the central hydrogen mass fraction. All tracks are $15\,M_\odot$ models with $f_0 = 0.002$. The solid lines indicate Schwarzschild models and the other lines are Ledoux models with either $\alpha_{sc} = 0.4$ (dotted line) or $\alpha_{sc} = 0.004$ (dash-dotted line). The colour scheme shows the different choices of f_{CBM}. The inset window presents the evolution of the convective boundary location right before it reaches the zero-age main sequence.

amounts of extra mixing and $f_0 = 0.002$. The location presented in Fig. (III.2) is the pure *Ledoux* or *Schwarzschild* boundary excluding the convective boundary mixing region. It is apparent that the location of the convective boundary is further out with more mixing. This is a consequence of the larger mixed region after the convective boundary. The inset window in Fig. (III.2) presents a zoom on the final growth of the convective hydrogen core before the zero-age main sequence. It shows that all the $15\,M_\odot$ models, except the Ledoux model with no convective boundary mixing and slow semiconvection, have a nearly equal convective hydrogen core size at the zero-age main sequence. Therefore, the differences arising during the main-sequence evolution are due to the larger f_{CBM} values. More convective boundary mixing increases the overall size of the convective zone, ingesting more fuel into the burning zone in the centre. This creates a higher hydrogen burning luminosity. Consequently the decrease in the radiative temperature gradient is relatively slower, which results in a larger convective hydrogen core - see also Table III.1.

The models with no convective boundary mixing, black lines in Fig. (III.2), predict different locations of the convective boundary by either using the *Ledoux* or the *Schwarzschild* criterion. In the Schwarzschild model the chemical composition gradient is ignored. Therefore, the convective core can grow freely during the pre-main-sequence evolution. The Ledoux models estimate a different

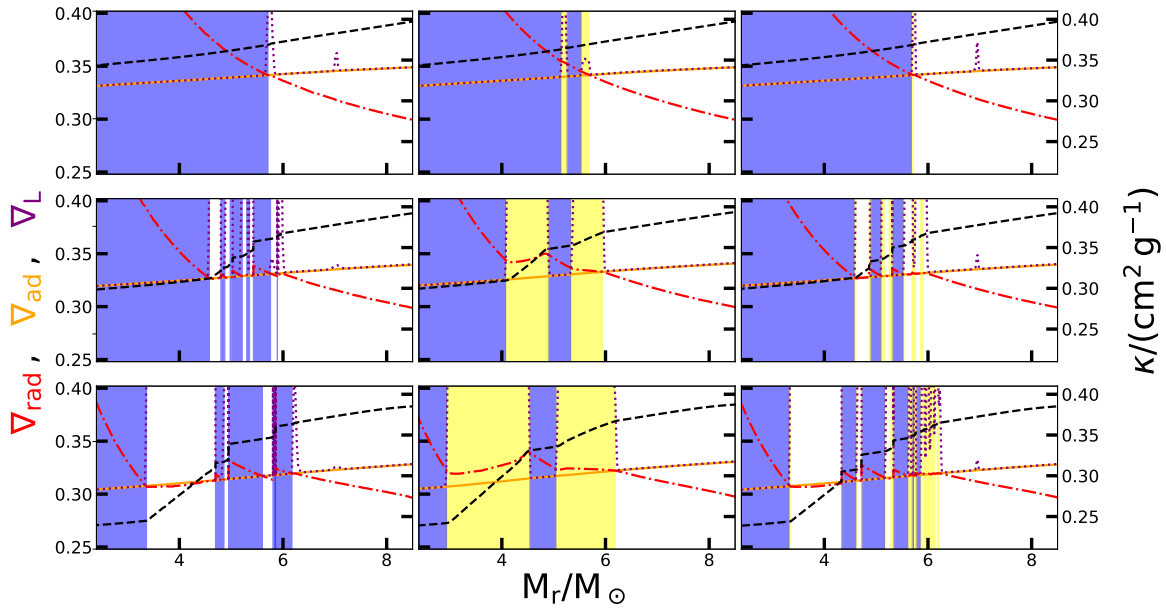

Figure III.3: Profiles of the temperature gradients at the boundary of the convective core as a function of Lagrangian mass coordinates. Shown are the $15\,M_\odot$ Schwarzschild (left column) and the Ledoux models with $\alpha_{sc} = 0.004$ (middle column) and $\alpha_{sc} = 0.4$ (right column) all with no convective boundary mixing. The top row is at the zero-age main sequence, $X_c(^1H) = 0.717$, the middle row at $X_c(^1H) = 0.5$ and the bottom row at $X_c(^1H) = 0.2$. Convective regions are indicated by blue shading, whereas yellow shows semiconvective regions. Additionally, the opacity is plotted as a function of mass coordinate (black dashed line). The ∇_L in the Schwarzschild model is only included for comparison and not used in the calculation.

boundary location depending on the semiconvective efficiency. The Ledoux model with inefficient semiconvection, $\alpha_{sc} = 0.004$, shows a convective core which is smaller. This is because during the pre-main sequence, where the convective core grows, a strong chemical composition gradient limits its size - see inset window in Fig. (III.2). A semiconvective layer develops above the convective core but semiconvection is not efficient enough to completely remove the chemical stratification. As a result, this model has a smaller convective core during the whole main-sequence evolution. If semiconvection is efficient, $\alpha_{sc} = 0.4$, the μ-gradient in the layer above the core is erased and the convective core can grow more. Therefore, the Ledoux model with efficient semiconvection has a convective hydrogen core size more similar to the Schwarzschild model at the zero-age main sequence. Afterwards, during the main-sequence evolution, the Schwarzschild model and the Ledoux model with $\alpha_{sc} = 0.4$ evolve their decreasing convective core similarly. This also is presented in Fig. (III.3) where the radial profile of the temperature gradients, the chemical composition gradient and the opacity are shown. The two models (left and right columns) behave similarly because in the latter there is a thin semiconvective zone (in yellow) right at the convective core boundary, which constantly mixes the region above the core. The Ledoux model with $\alpha_{sc} = 0.004$ evolves through the main sequence with a smaller convective core and a large μ-gradient above it (middle column in Fig. (III.3)). These differences affect the helium core mass at core hydrogen depletion - see Table III.1 - and the luminosity during the main sequence

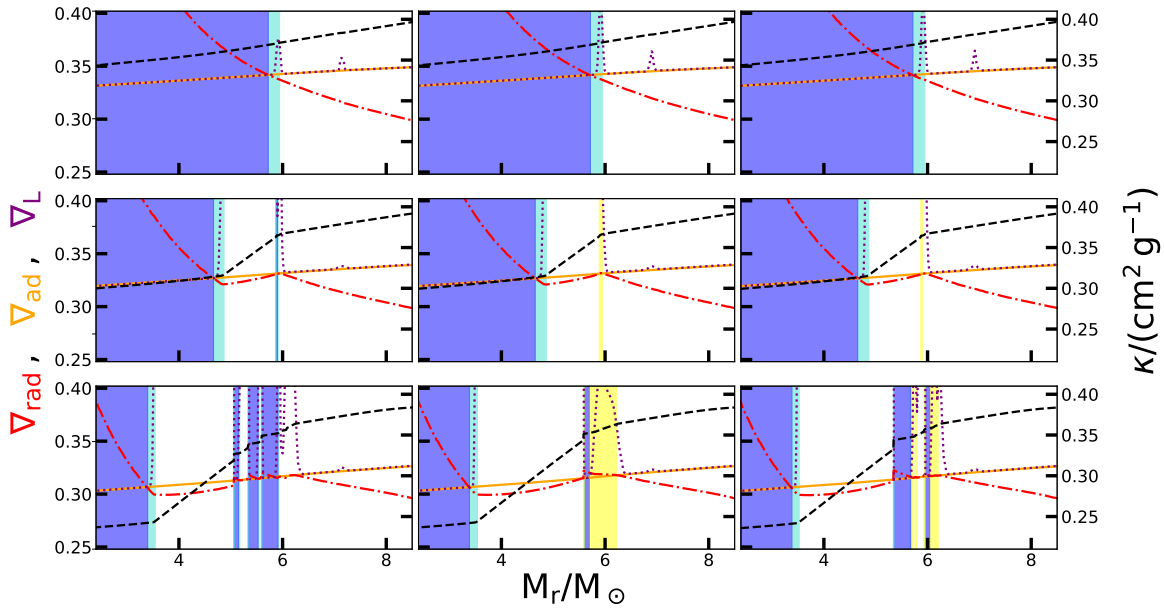

Figure III.4: The same as Fig. (III.3) but with $f_{\rm CBM} = 0.004$. The convective boundary mixing region is indicated by turquoise.

(Fig. (III.15)) which in turn impact the further evolution.

Fig. (III.3) might suggest that the Ledoux model with inefficient semiconvection (middle column) develops a chemical composition gradient within the convective zone which then is split up during the main-sequence evolution. Careful investigation reveals that the inner (left) location is the upper limit of the convective core, whose growth is limited due to the strong, narrow peak of the μ-gradient at the edge of the convective core. The convective region above the core develops during the pre-main sequence, which results in the convective layer after the μ-gradient peaks in the middle column, top panel.

Convective boundary mixing extends the region above the core that is well mixed. Therefore, changes in the chemical composition and the increase of opacity are pushed further away from the boundary location obtained from the stability criteria. Consequently, $\nabla_{\rm rad}$ decreases further after the convective boundary. Fig. (III.4), which shows the same stellar models as Fig. (III.3) but with $f_{\rm CBM} = 0.004$ instead of 0.0, illustrates this behaviour. Moreover, the chemical composition gradient at the convective boundary vanishes, $\nabla_\mu \approx 0$, and its increase further out is not a step-function anymore but it follows more a sigmoid shape. As a result, the convective hydrogen core boundary predicted by the *Ledoux* and *Schwarzschild* criterion in Fig. (III.2) converge. Obviously, the convergence between the two stability criteria is consistent when more convective boundary mixing is applied as shown in Figs. (III.2) and (III.5). The convergence of the two boundary criteria is also apparent in the Hertzsprung-Russell diagram (Fig. (III.7a)), where the evolutionary tracks with convective boundary mixing perfectly overlap during the main sequence. Furthermore, they predict the same helium core mass at the end of hydrogen burning - see Table III.1.

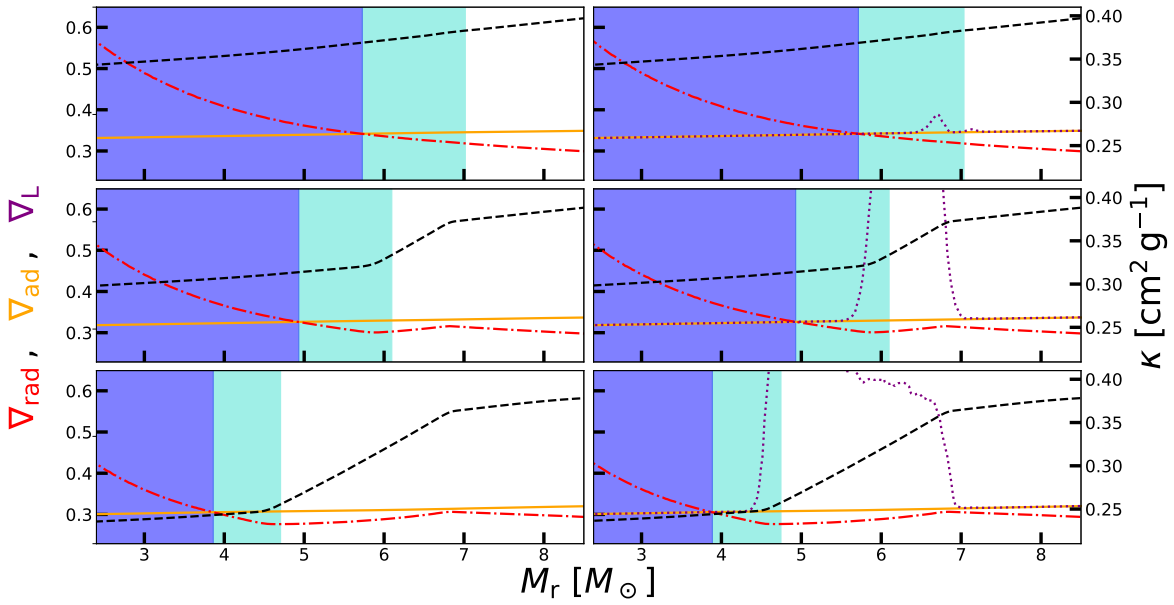

Figure III.5: The same as Fig. (III.4) but with $f_{\rm CBM} = 0.022$ and only the *Schwarzschild* model (left) and the *Ledoux* model with fast semiconvection (right) are shown.

Semiconvection only influences the convective hydrogen core size when there is no convective boundary mixing in the $15\,M_\odot$ models. There, a chemical composition gradient on the radiative side of the boundary limits the growth of the convective hydrogen core depending on the semiconvective efficiency - see Figs. (III.2) and (III.3) with $\alpha_{\rm sc} = 0.004$ and 0.4. However, as discussed before, convective boundary mixing removes the chemical stratification on the radiative side of the convective boundary. Additionally, the radiative temperature gradient further decreases in the convective boundary region, which creates the condition $\nabla_{\rm ad} - \nabla_{\rm rad} > 0$ beyond the convective boundary (Figs. (III.4) and (III.5)). For that reason there is no semiconvective zone right after the convective core region when convective boundary mixing is applied and the convective hydrogen core size is independent of semiconvection and its efficiency.

The differences of the convective boundary region discussed above have an effect on the main-sequence evolution. The larger convective cores enable more hydrogen fuel to be ingested into the central burning region. Subsequently, the helium core mass at the end of core hydrogen burning increases with more convective boundary mixing - refer to Table III.1. Furthermore, the luminosity generated by core hydrogen burning is higher and the increased radiation pressure leads to a slightly larger radius of the star. The consequence is that the track in the Hertzsprung-Russell diagram in Fig. (III.7a) is steeper and reaches lower effective temperatures at the end of the main sequence - see also Table III.1 - hence, the main-sequence width broadens, especially for the models with large amount of convective boundary mixing. Moreover, the increased amount of hydrogen available in the core burning region enhances the main-sequence lifetime as shown in Table III.1.

The behaviour of the convective hydrogen core and its response to convective boundary mixing un-

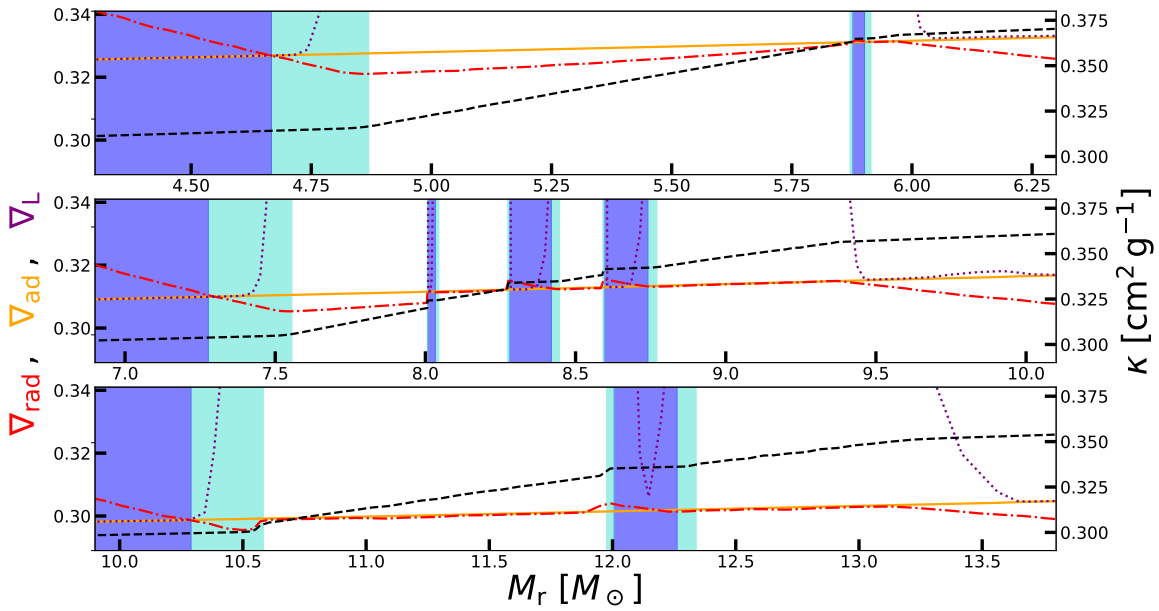

Figure III.6: Snapshots of the temperature gradients at the boundary of the convective core as a function of Lagrangian coordinates of the 15, top, 20, middle, and 25 $M_\odot$, bottom, Schwarzschild models, all with $f_{\rm CBM} = 0.004$ and $f_0 = 0.002$. The snapshots were all taken when the central hydrogen mass fraction drops below 0.5. Convective regions are indicated by blue shading, whereas turquoise shows convective boundary regions and yellow semiconvective regions. Additionally, the opacity is plotted as function of mass coordinate on the right axis of each figure (the black dashed line). Beware the different intervals of the x-axis due to the different initial masses, the y-axes have the same range for comparison reasons.

certainties found for the 15 $M_\odot$ models is similar for stellar models with initial masses of 20 and 25 $M_\odot$ (see Fig.(III.6)). There is, however, a small difference in the *Schwarzschild* and the *Ledoux* model. The thin convective layers found above the convective hydrogen core, the *convective fingers* - see discussion further down - penetrate slightly deeper in the models with larger initial masses and sometimes touch the convective core. This transports fuel into the convective core which leads to an increase of the convective core. The timing and intensity of the "touching" is different for the *Ledoux* and *Schwarzschild* models and depends on the initial mass. Therefore, the initially converged boundary locations diverge once more and the models end up with slightly different helium core masses at the end of core hydrogen burning - see Table III.1. A similar scenario is observed by e.g. Farmer et al. (2016) (their Fig. (3) for a star with an initial mass of 30 $M_\odot$) and Clarkson & Herwig (2020). There, however, the process is much more intense and the increase of the convective hydrogen core is larger compared to my cases. Whether such a merging scenario is realistic needs to be determined, though, with more realistic boundary physics (e.g. the Richarson number instead of the *Ledoux* or *Schwarzschild* criterion; Turner, 1973) instead of simply adding the diffusion coefficients together.

The 20 and 25 $M_\odot$ models show a larger dispersion of minimum effective temperatures reached at the end of the main-sequence evolution - see Fig.(III.7a) and Table III.1. This indicates that, if the $f_{\rm CBM}$ value is indeed as large as recent observational calibrations discussed in Section II.1.3, the widening

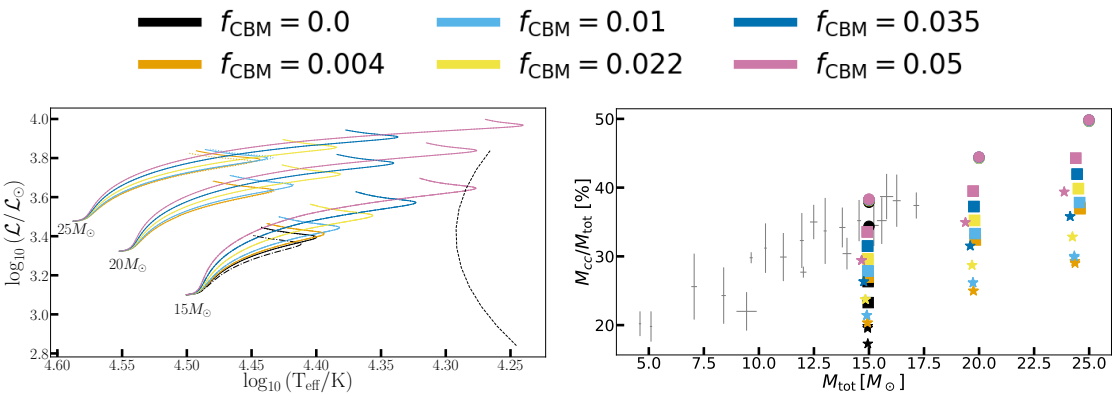

(a) (b)

Figure III.7: (a) The spectroscopic Hertzsprung-Russell diagram including the models with the three initial masses, 15, 20 and 25 $M_\odot$, and the various values for $f_{\rm CBM}$ indicated by the colour scheme. The tracks show the evolution from the zero-age to the terminal-age main sequence. The linestyle indicates the boundary criterion, where the Schwarzschild models have solid, the Ledoux models with $\alpha_{\rm sc} = 0.004$ dash-dotted and the Ledoux models with $\alpha_{\rm sc} = 0.4$ dotted lines. The thin dashed black line on the right hand side represents the empirical terminal-age main sequence determined by Castro et al. (2014). The "spectroscopic luminosity" is defined as $\mathcal{L} \equiv \frac{T_{\rm eff}^4}{g} = \frac{1}{4\pi\sigma G}\frac{L}{M}$. (b) The fraction of the convective core mass, M_{cc}, as a function of the total mass of the star. M_{cc} from all the models in this Chapter are plotted at three different stages: the zero-age main sequence (circles) and when the central hydrogen mass fraction drops below 0.35 (squares) and below 0.1 (stars). The amount of convective boundary mixing is indicated by the colour scheme. The grey crosses are the observed eclipsing binaries and their convective core mass estimates from Tkachenko et al. (2020).

of the main-sequence is more extreme for higher initial masses. Furthermore, the line of the terminal-age main sequence is slightly bent towards cooler temperatures rather than to hotter temperatures with increasing initial mass with increasing $f_{\rm CBM}$ as suggested by recent observations (Castro et al., 2014; McEvoy et al., 2015). This indicates that stars might experience a larger amount of convective boundary mixing than currently applied in most published theoretical stellar models. Fig.(III.7b), which compares the convective core masses to asteroseismic observations, supports this view, since only the 15 $M_\odot$ models with large $f_{\rm CBM}$ are able to match the data unless the stars are close to the zero-age main sequence. Fig.(III.7b) does not constrain the models with larger initial masses due to the limit of the sample.

Comparing the different $\log_{10} T_{\rm eff,min}^{\rm MS}$ values in Table III.1 reveals that the main-sequence width is nearly independent of the convective boundary criterion and the semiconvective efficiency. This is because during the main-sequence evolution (i) there is a convergence between the two boundary criteria and (ii) the relative importance of semiconvection is massively reduced with increasing convective boundary mixing - see discussion above.

In Section III.2.1 we mentioned the importance of another free parameter, f_0, in the exponentially decreasing diffusive convective boundary mixing scheme. Changing this parameter from our default value of 0.002 to 0.02 decreases the amount of mixing beyond the convective core. Consequently, slightly less fuel is brought down into the burning region, resulting in a lower $\nabla_{\rm rad}$, hence, the con-

vective boundary location decreases faster during the main-sequence evolution for the same $f_{\rm CBM}$. This flattens the main-sequence evolution track in the Hertzsprung-Russell diagram and reduces the main-sequence width. Moreover, the helium core mass at core hydrogen depletion is smaller, see Table III.1. However, the differences due to the two f_0 values decrease with increasing $f_{\rm CBM}$, because the f_0 is smaller relative to the $f_{\rm CBM}$ parameter. Therefore, the impact of the earlier decrease of the diffusion coefficient is reduced.

3.1 Convective Fingers

In the region above the convective hydrogen core, the radiative temperature gradient has a profile close to the adiabatic one, $\nabla_{\rm rad} \approx \nabla_{\rm ad}$ (see in Figs. (III.3), (III.4), (III.5) and (III.6)). Such a convective neutral region above the convective hydrogen core in massive stars was first predicted by Schwarzschild & Härm (1958). In their argument they use the fact that (1) the opacity is dominated by electron scattering, $\kappa \propto 1 + {\rm X}(^1{\rm H})$, and that (2) a hydrogen-rich mixture has more free electrons per unit mass than a helium-rich. The hydrogen burning leads to a helium-richer convective core than the overlying radiative layers. Consequently, the opacity is higher in the radiative side of the convective boundary than in the convective zone. Accordingly, the radiative temperature gradient, $\nabla_{\rm rad} \propto \kappa$, has a flatter profile, or even slightly increases, in the region above the receding convective hydrogen core. Schwarzschild & Härm (1958) propose that this zone above the convective core is slowly mixed to maintain convective neutrality. My simulations with no convective boundary mixing (Fig. (III.3)) show a similar behaviour: At the zero-age main sequence (top row) the temperature gradient above the convective core decreases outwards (increasing mass coordinate). During the main-sequence evolution the convective core slowly retreats, leaving behind a composition gradient between the helium and hydrogen gas mixtures, which increases the opacity. Consequently, the radiative temperature gradient above the receding convective hydrogen core is close to adiabatic. Hence, small discontinuities in the opacity profile, which create small local peaks in the radiative temperature gradient, violate the *Schwarzschild* stability criterion. This results in a thin layer with mixing, that reduces the radiative temperature gradient back to the adiabatic one. At the boundary of these mixed layers, a new discontinuity in opacity is created and the process repeats itself there. This creates a finger-like structure in the region above the core (e.g. Langer et al., 1985). The difference between the *Ledoux* and *Schwarzschild* criteria is the type of mixing in the thin layers. In the Schwarzschild models the *convective fingers* are always convectively mixed. In the Ledoux models, however, the layer appears as a semiconvective layer because of the strong chemical stratification above the receding hydrogen core. If semiconvection is not efficient, a large semiconvective region develops above the convective core because the mixing is not able to completely remove the chemical composition gradient. If semiconvection is more efficient, it is able to remove the chemical composition gradient. It should be

noted that semiconvection, as we use it, only mixes the chemical composition but not the entropy - see Section B.1.3.3. Therefore, the layer becomes convectively unstable because $\nabla_{\rm rad} > \nabla_{\rm ad}$ still holds. Thus, a similar finger-like convective-semiconvective structure as in the Schwarzschild models develops (Fig. (III.3)).

Convective boundary mixing (i) pushes the transition from the helium-rich mixture in the convective core to the hydrogen-rich mixture in the envelope further away from the convective boundary (compare Figs. (III.4) and (III.5)) and (ii) creates a smoother transition due to the exponential nature of the convective boundary mixing. The latter creates a more continuous opacity profile, therefore a smoother $\nabla_{\rm rad}$ profile. The first point, on the other hand, causes the opacity to increase further away from the boundary. This allows the radiative temperature gradient to further decrease in the convective boundary mixing region before it rises once more due to the increase of opacity. Hence, the appearance of *convective fingers* is either further out (Fig. (III.4)) or they never occur because $\nabla_{\rm rad}$ drops enough for the region above the core to stay convectively stable (Fig. (III.5)). Thus, the spatial area where *convective fingers* occur, if any, is reduced with increasing amount of mixing at the convective boundary. For $f_{\rm CBM} \gtrsim 0.01$ there are no *convective fingers* in my $15\,{\rm M}_\odot$ models.

The 20 and $25\,{\rm M}_\odot$ models exhibit a similar behaviour regarding the mixing in the zone beyond the convective core as the $15\,{\rm M}_\odot$ models but there are some important differences. Stars with a larger initial mass generate a higher luminous output. Hence, $\nabla_{\rm rad} \propto \ell_{\rm rad}$ is much closer to convective neutrality in the radiative zone beyond the convective core (see Fig. (III.6)). Therefore, in models with a larger initial mass, smaller changes in the entropy immediately create a situation where the stability criteria predict convection or semiconvection. Consequently, the *convective fingers* are much more present in the simulations with the same $f_{\rm CBM}$ but higher initial masses. As a result, the limit of convective boundary mixing above which no *convective fingers* or semiconvective layers appear above the convective hydrogen core increases with initial mass. In the $20\,{\rm M}_\odot$ models I do not find *convective fingers* for $f_{\rm CBM} \gtrsim 0.022$ and in the $25\,{\rm M}_\odot$ models for $f_{\rm CBM} \gtrsim 0.035$.

4 The Intermediate Convective Zone

After hydrogen is depleted in the core of the star, the convective core completely recedes and the star enters a short but crucial phase, which influences its fate - see also Section I.2.1.1. Since there is no nuclear energy generation left in the core, the star contracts, releasing gravitational energy. As a consequence of the Virial theorem, energy conservation and contraction on a short timescale the outer layer expands and cools down (mirror principle - e.g. Kippenhahn & Weigert, 1994). The layers above the previous hydrogen core, where there is still hydrogen left, heat up due to the contraction and set the condition for hydrogen burning. This hydrogen burning shell is accompanied by a convective

region - the intermediate convective zone (Figs. (III.8), (III.9) and (III.11)).

It is during this phase that the star leaves the main sequence and, in the mass range studied here, crosses the Hertzsprung-Russell diagram to the red super-giant branch, as shown in Fig. (III.15). The details of this phase depend strongly on the duration, location and size of the intermediate convective zone with respect to the hydrogen burning shell. The properties of the intermediate convective zone, in turn, depend strongly on the choices of the convective boundary criterion and the amount of extra mixing at the boundary. If the intermediate convective zone only exists above the hydrogen burning shell, the latter can only consume the hydrogen at its location via nuclear burning and is consequently relatively weak. However, an overlap of the two creates a situation where the convective zone ingests fuel into the burning shell. This results in a much stronger burning shell which provides more support to the core against the gravitational pressure from the outer layers.

Figs. (III.8) and (III.9) present structure evolution diagrams focussed on the intermediate convective zone in the $15\,M_\odot$ models. They show the amount of overlap between the intermediate convective zone and the hydrogen burning shell. Furthermore they visualise the size and give a hint of the duration of the intermediate convective zone. Fig. (III.10) presents the different post-main-sequence luminosities of the simulations. Shown are the total luminosity and the luminosities generated by hydrogen and helium burning. The difference between the luminosities from the two burning types and the total luminosity is due to changes of the gravitational potential. The sudden drop in luminosity powered by hydrogen burning, if any, indicates the end of the boost of the intermediate convective zone, thus, its duration.

In the $15\,M_\odot$ models with no convective boundary mixing there is a clear difference between the Schwarzschild and the Ledoux models. The intermediate convective zone in the Schwarzschild model has an initial overlap with the hydrogen burning shell, whereas the Ledoux models develop an intermediate convective zone outside of the hydrogen burning shell. This difference arises because of the chemical stratification which prevents convection in the Ledoux models. These findings are similar to Langer et al. (1985), Georgy et al. (2014) and Davies & Dessart (2018) who found that the depth at which the intermediate convective zone forms is sensitive to the stability criterion used. The comparison between the Ledoux model with $\alpha_{\rm sc} = 0.4$ and $\alpha_{\rm sc} = 0.004$, both with no convective boundary mixing, reveals that the intermediate convective zone appears at the same location. The difference between the two *Ledoux* models is introduced by the mixing efficiency of semiconvection. Slow semiconvection is not able to remove the chemical composition gradient. Therefore, the intermediate convective region consists mainly of a semiconvective region in the Ledoux model with slow semiconvection. In the case with efficient semiconvection, the *convective fingers* partly removed the chemical composition gradient. Hence, the intermediate convective zone is mostly convective. These differences affect the time when the surface is enriched with hydrogen burning products, since the large

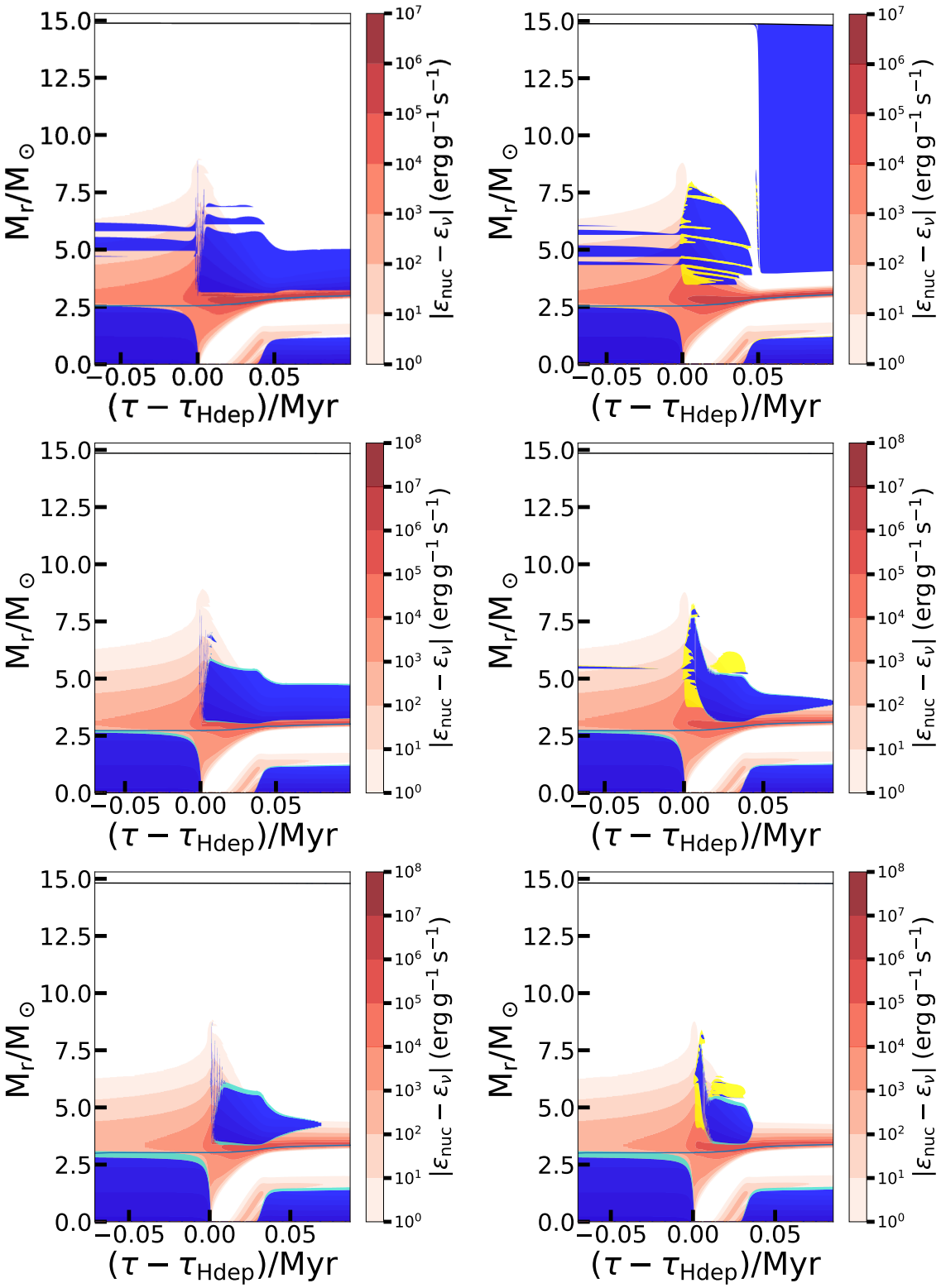

Figure III.8: Structure evolution diagrams, also known as Kippenhahn diagrams, of the 15 $M_\odot$ models showing the intermediate convective zone. The left column presents the Schwarzschild model and the right column the Ledoux models with $\alpha_{sc} = 0.4$. The f_{CBM} increases top to bottom with (0.0, 0.004, 0.01). The blue region indicates convective regions, whereas the convective boundary region is shown in turquoise and semiconvection in the Ledoux models is shown in yellow. The red shading indicates the energy generation. The time on the x-axis is with respect to the time of core hydrogen depletion, τ_{Hdep}. The structure evolution diagrams are limited to the evolution between the locations where $X_c(^1H) < 0.01$ and $X_c(^4He) > 0.95$.

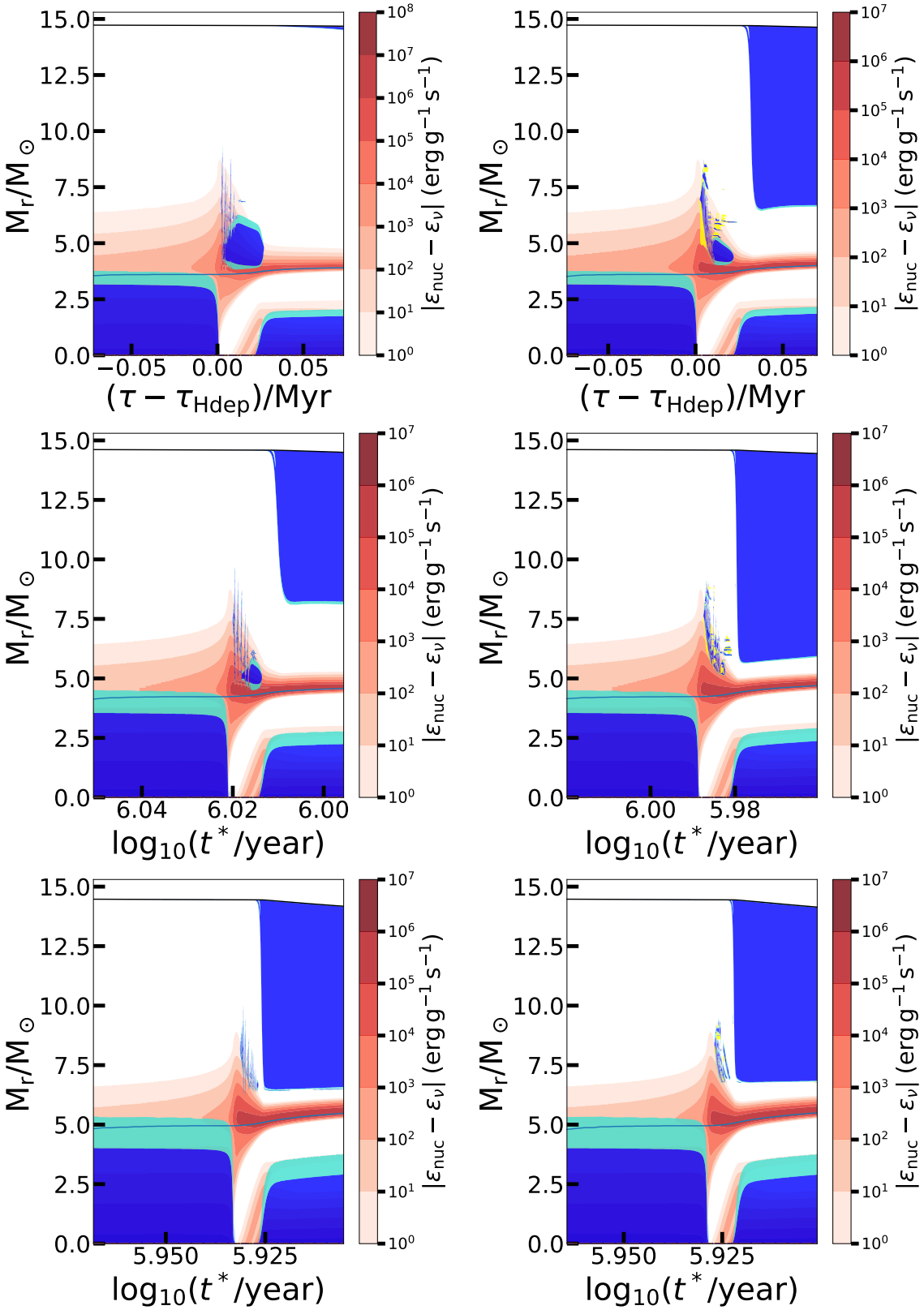

Figure III.9: Same as Fig. (III.8) but for f_{CBM} top to bottom equal to (0.022, 0.035, 0.05).

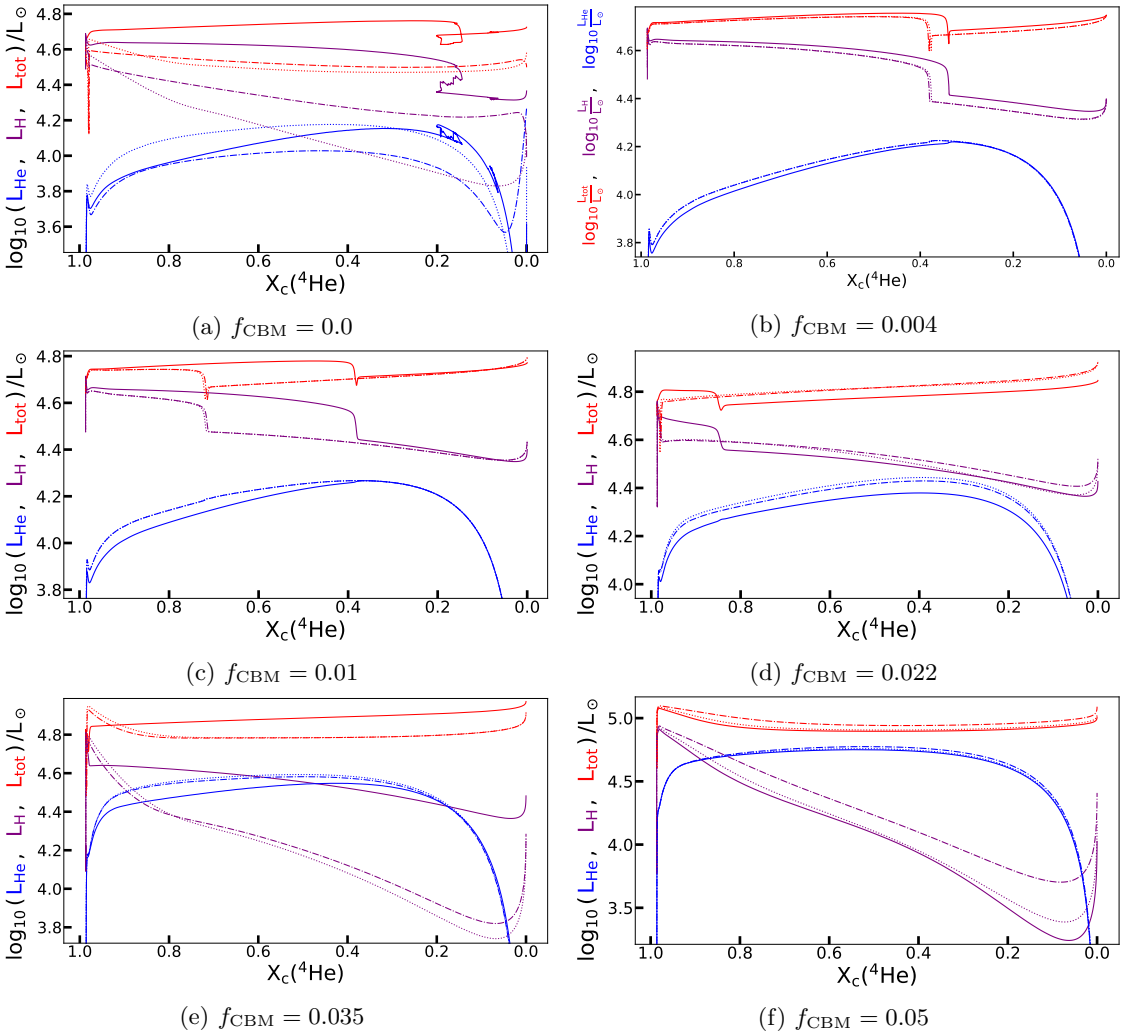

(a) $f_{\mathrm{CBM}} = 0.0$ (b) $f_{\mathrm{CBM}} = 0.004$

(c) $f_{\mathrm{CBM}} = 0.01$ (d) $f_{\mathrm{CBM}} = 0.022$

(e) $f_{\mathrm{CBM}} = 0.035$ (f) $f_{\mathrm{CBM}} = 0.05$

Figure III.10: The total luminosity, L_{tot} (red), and the luminosity generated by hydrogen and helium burning, L_{H} (purple) and L_{He} (blue) respectively, as a function of the central helium mass fraction. All the figures show $15\,M_{\odot}$ models with varying f_{CBM}. Within one panel, all boundary criteria are shown, the *Schwarzschild* (solid) and the Ledoux one, the latter with $\alpha_{\mathrm{sc}} = 0.004$ (dash-dotted) and $\alpha_{\mathrm{sc}} = 0.4$ (dotted).

surface convective zone penetrates into these layers shortly after the disappearance of the intermediate convective region (Fig. (III.8) right upper corner). Furthermore, the energy transport in this region is more efficient when semiconvective layers, which only mix the chemical composition, are turned into convective layers. This slightly increases the luminosity as can be seen in Fig. (III.10), which in turn influences the mass loss rates. However, the impact is modest.

Convective boundary mixing changes this picture. The extra mixing at the boundary (i) removes possible chemical stratification. Furthermore it increases the region with efficient mixing, hence, (ii) the energy excess is regulated faster and (iii) more fuel is provided for the burning shell. The latter simply increases the amount of boosting of the hydrogen shell. This is indicated by the hydrogen burning luminosity in Fig. (III.10), where the simulations with an overlap between the intermediate convective zone and the hydrogen shell have a higher L_{H} for the duration of the intermediate convec-

tive zone before the hydrogen powered luminosity drops. The second point decreases the lifetime of the intermediate convective core by increasing the region with efficient energy transport, thus, $\nabla_{\rm rad}$ drops faster. This is illustrated in Figs. (III.8) and (III.9), where the models with larger values of $f_{\rm CBM}$ have a shorter duration of the intermediate convective zone. Furthermore, in Fig. (III.10) the luminosity powered by the hydrogen burning shell experiences the drop earlier with higher $f_{\rm CBM}$. In the most extreme cases with $f_{\rm CBM} = 0.05$ and the Ledoux models with $f_{\rm CBM} = 0.035$ the envelope to core ratio is too small to produce a proper intermediate convective zone that ever overlaps with the hydrogen shell. In these models, L_H constantly drops because the burning shell depletes its fuel, very similar to the Ledoux models with no convective boundary mixing. The first point crucially impacts the Ledoux models, because it efficiently removes the μ-gradient at the convective boundary, which prevents the intermediate convective zone from moving inward. Consequently, the intermediate convective zone moves downwards in mass coordinates and eventually[3] overlaps with the hydrogen burning shell (compare Fig. (III.8) right column top to bottom). In the Ledoux models there is always a short semiconvective region before the intermediate convective zone penetrates downward. However, semiconvection is not efficient enough for the $\alpha_{\rm sc}$ values tested in this work to erase the chemical stratification by themselves because of the short timescale of this evolutionary phase. Moreover, when moving downwards the intermediate convective zone leaves behind a chemical composition gradient. Therefore, the intermediate convective zone has, when it starts boosting the burning shell, a semiconvective zone at its upper boundary. These semiconvective regions, however, become smaller as $f_{\rm CBM}$ is increased and disappear for the two largest values used. In contrast, the intermediate convective zone in the Schwarzschild models include this region, hence, they span a wider region and are able to boost the hydrogen shell for a longer time. This creates the difference in the luminosity powered by hydrogen burning between the *Ledoux* and *Schwarzschild* criterion in Fig. (III.10).

It should be noted that the impact of the above mentioned points (ii) and (iii) affect the intermediate convective zone differently; (ii) reduces the duration of the convective shell, whereas (iii) boosts the hydrogen burning region more, which in turn leads to a longer duration of the intermediate convective zone. In the Schwarzschild model (ii) leads to a decrease of the duration of the intermediate convective zone (compare Figs. (III.8), (III.9) and (III.10)). In the Ledoux models, on the other hand, at low $f_{\rm CBM}$ (i) dominates. This leads to a boost of the intermediate convective zone due to the ingestion of fuel into the burning shell. When increasing the amount of convective boundary mixing, the point (ii) starts to reduce the duration of the intermediate convective zone, similar to the Schwarzschild models.

Convective boundary mixing does not change the initial location of the intermediate convective

[3]The downward movement is not instantaneous because only the μ-gradient in the convective boundary layer is erased. Hence, the overlap of the intermediate convective zone and the hydrogen shell in the Ledoux models, if any, is always delayed compared to the Schwarzschild models (compare left and right column in Fig. (III.8)).

zone. The *Ledoux* criterion always predicts the initial location above the hydrogen shell, whereas the *Schwarzschild* criterion always predicts an overlap (see Figs. (III.8) and (III.9)) except when the envelope to core ratio is too small to produce an intermediate convective zone as in the models with $f_{\rm CBM} = 0.05$. This difference, and point (ii) above, also lead to the two behaviours, overlap and no overlap, in the $15\,M_\odot$ models with $f_{\rm CBM} = 0.035$ in Fig. (III.9), where the intermediate convective zone in the Ledoux model does not overlap but in the Schwarzschild model it does.

Davies & Dessart (2018) predict the first overlap of the intermediate convective zone and the hydrogen burning shell in their Ledoux models around $16\,M_\odot$. I show here that the lowest initial mass that shows an overlap is dependent on the amount of mixing at the convective boundary. Furthermore, an overall result is that the differences of the intermediate convective zone in the $15\,M_\odot$ models due to the choice of the stability criterion decrease with increasing amount of convective boundary mixing, and for $f_{\rm CBM} = 0.05$ Figs. (III.9) and (III.10) show similar results.

The intermediate convective zone exhibits the same dependence on convective boundary mixing in the 20 and $25\,M_\odot$ models as in the $15\,M_\odot$ models. There are, however, some important differences. As discussed in Section III.3, in stars with higher initial masses (a) the luminosity is higher and (b) the *convective fingers* above the convective core are more pronounced. (a) leads to an increased radiative temperature gradient in the region above the hydrogen burning shell. Consequently, the intermediate convective zone spans a larger radial distance in the models with higher initial masses (see Fig. (III.11)). Therefore, more fuel is provided for the hydrogen burning shell and it is boosted longer. This in turn prolongs the lifetime of the intermediate convective zone, leading to a convective region that can be present during nearly all of the core helium burning lifetime - see Table III.1. In general, the relative duration of the intermediate convective zone with respect to the core helium burning duration increases with initial mass and, in accordance with the previous discussion, decreases with $f_{\rm CBM}$. (b) may lead to *convective fingers* that exist until the appearance of the intermediate convective zone, as shown in Fig. (III.11, top row). These convective layers partly remove the chemical composition profile left behind by the receding convective hydrogen core. This mainly influences the Ledoux models, where the intermediate convective zone overlaps much faster with the hydrogen burning shell compared to the Ledoux model with no convective fingers, nearly at the same time as in the Schwarzschild model. Moreover, the intermediate convective zone in the Ledoux model is slightly bigger compared to the Schwarzschild model because of the slightly higher temperature at the location of the hydrogen shell. Therefore, it can replenish the hydrogen shell with fuel for longer and is active for longer compared to the Schwarzschild models of the same initial mass. This leads to an intermediate convective zone that lasts longer in the Ledoux models than in the Schwarzschild models with higher initial masses.

In the $20\,M_\odot$ model with $f_{\rm CBM} = 0.022$ there are no *convective fingers* at the same mass coordinate

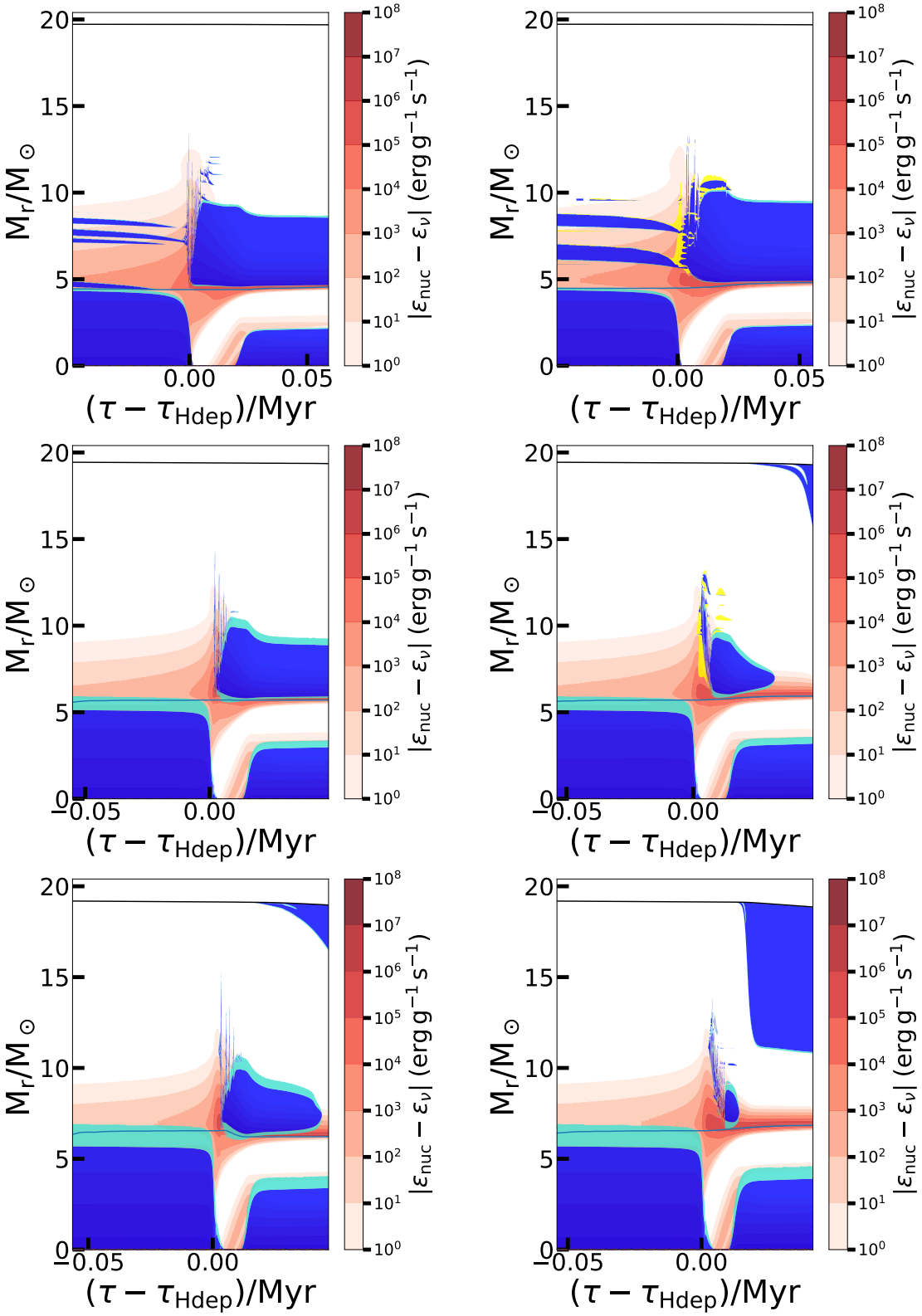

Figure III.11: Structure evolution diagram of the 20 $M_\odot$ simulations showing the intermediate convective zone as in Fig. (III.8). The left column presents the Schwarzschild model and the right column the Ledoux models with $\alpha_{sc} = 0.4$. The top row uses $f_{CBM} = 0.004$, the middle $f_{CBM} = 0.022$ and the bottom $f_{CBM} = 0.035$.

where the intermediate convective zone eventually appears. Consequently, the Ledoux model behaves very similar to the $15\,M_\odot$ model. As a result, the drops in luminosity of the Ledoux model are much earlier compared to the models with less convective boundary mixing.

The $25\,M_\odot$ Ledoux model with $f_{\rm CBM} = 0.01$ defies the general trend by creating an intermediate convective zone which lasts longer than the core helium burning (similar to Ritter et al., 2018, theri Fig.(11)).

The different behaviour in depth and duration of the intermediate convective zone has an important impact on the further evolution of the star. In summary, the intermediate convective zone influences the strength of the hydrogen burning shell. This shell supports the contracting core underneath against the gravitational pressure from the outer layers, which affects the way the star evolves through the Hertzsprung gap and sets the structure for its further evolution, e.g. the convective helium core (Section III.5) or the surface evolution (Section III.6).

5 Core Helium Burning

5.1 Convective Helium Core

During the helium burning stage, the convective helium core constantly grows in mass. This is because of (i) the increase of the core luminosity due to the active hydrogen burning shell which continuously synthesises hydrogen into helium, thus increasing the helium core mass, (ii) the increase of opacity and mean molecular weight due to the conversion of helium into carbon and oxygen and (iii) the density dependence of the 3α (second order) and $^{12}C(\alpha,\gamma)^{16}O$ (first order) reaction rate - see also Section I.2.1.2.

Fig. (III.12) presents the location of the convective helium core boundary as a function of the central helium mass fraction. The boundary shown is the convective core determined by the stability criterion without the boundary mixing region. The size and growth of the convective helium core depends on (i) the amount of mixing at the convective boundary, (ii) the strength and location of the hydrogen shell discussed in Section III.4 and (iii) on the choice of the stability criterion. Fig. (III.12) clearly illustrates that the convective core is larger in the models with more convective boundary mixing for a given convective boundary criterion. It furthermore shows that the different sizes of the convective cores arise mainly during their initial growth. During the rest of the core helium burning phase the cores grow at a similar rate. Interestingly, the models applying the *Ledoux* criterion predict a faster initial growth of the convective core than the corresponding Schwarzschild models, with the exception of the models with no convective boundary mixing and the models with $f_{\rm CBM} = 0.05$. In the latter the Schwarzschild model initially predicts a convective helium core which is only slightly larger before

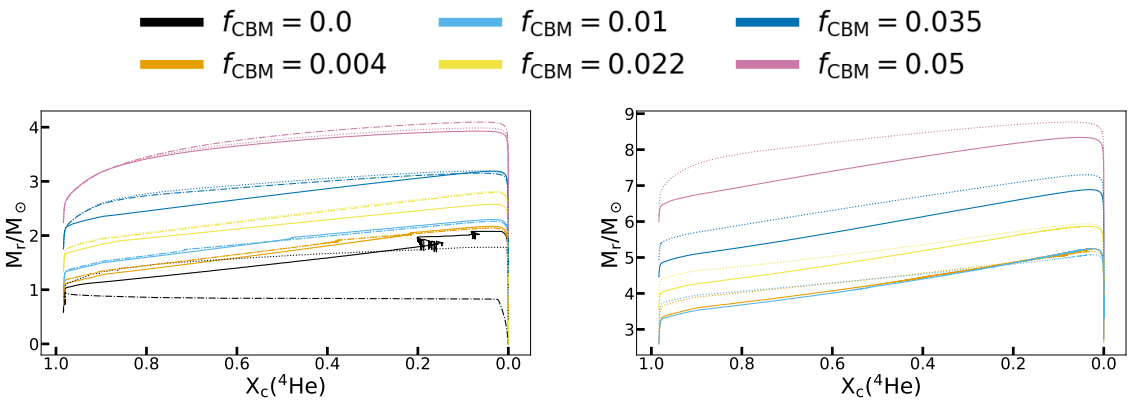

(a) 15 $M_\odot$ (b) 25 $M_\odot$

Figure III.12: The location of the convective helium core boundary, determined either by the *Ledoux* or the *Schwarzschild* criterion, as a function of the central helium mass fraction. Shown are the 15 and 25 $M_\odot$ models. The boundary criterion is shown by the linestyle, where a solid line indicates the Schwarzschild criterion and the Ledoux criterion is shown with a dash-dotted ($\alpha_{sc} = 0.004$) or a dotted line ($\alpha_{sc} = 0.4$). The colour scheme indicates the value of f_{CBM}.

the helium core in the Ledoux models overtake it. The initial size of the convective core depends strongly on the activity of the hydrogen shell, which itself is strongly affected by the intermediate convective zone as discussed in Section III.4. A stronger hydrogen shell supports the core against the gravitational pressure from the outer layers. Consequently, the helium core contracts less and the burning is slightly less energetic, hence, because of $\nabla_{rad} \propto \ell$, the convective helium core is smaller.

A larger amount of convective boundary mixing increases the mixed zone above the convective core and smooths the chemical composition gradient at the boundary. The first point provides the central burning region with fuel, increasing the energy generation. This results in a higher luminosity (L_{He} in Fig. (III.10)) thus a larger convective core. The second point removes the limiting chemical stratification in the Ledoux models. Consequently, the growth of the convective core in these models is less limited than in the models with no convective boundary mixing. Additionally, the semiconvective regions above the convective core disappear in the models with convective boundary mixing because the μ-gradient is only non-zero in the radiative layers. Therefore, the relative importance of semiconvection on the evolution of the convective helium core in the simulation with convective boundary mixing is reduced. The small differences between the Ledoux models with convective boundary mixing and different semiconvective efficiency arise from the different strength of the hydrogen burning shell - see Section III.4.

After its initial growth the convective core mass continues to increase because of the growth of the helium core mass due to the active hydrogen shell and the increase in opacity. This nearly constant increase is occasionally disrupted by kinks, for example in the Schwarzschild model with $f_{CBM} = 0.022$ at $X_c(^4He) \sim 0.87$ in Fig. (III.12), which are a consequence of the convective core regulating itself to the changes of the energy generation in the hydrogen shell or the opacity in the core.

The kinks around $X_c(^4He) \sim 0.7$ and 0.5 for the models with $f_{CBM} = 0.01$, around $X_c(^4He) \sim 0.35$ for the models with $f_{CBM} = 0.004$ occur due to vibrational up-down movements of the convective boundary. This ingests a larger amount of fuel into the convective zone and finally increases the zone as a consequence of the higher energy generation. I omit the discussion here whether these are *core breathing pulses* (Castellani et al., 1985) or numerical artefacts (e.g. Constantino et al., 2016; Farmer et al., 2016) and call these events *core breathing pulses* out of convenience. The presence of the *core breathing pulses* is discussed in Section III.7. However, I want to outline that the intensity of these *core breathing pulses* decreases, or they even vanish, with increasing amount of convective boundary mixing, e.g. $f_{CBM} \geqslant 0.022$ for the $15\,M_\odot$ models. The messy behaviour of the $15\,M_\odot$ Schwarzschild model with no convective boundary mixing is due to a fast, nearly step-like, increase of the convective core.

The differences in the convective core size of the $15\,M_\odot$ models with the same amount of convective boundary mixing but different boundary criteria, which are more dominant for $f_{CBM} \gtrsim 0.022$, arise because of the different (i) amounts of energy generation and (ii) radial location of the hydrogen burning shell. (i) supports the core more or less against the gravitational pressure of the outer layers, where a higher energy output by the burning shell leads to a smaller convective core. (ii), on the other hand, changes the helium core mass. If the burning shell is further out or moves outwards faster due to a smaller amount of fuel available, the core mass is bigger, hence a higher helium burning luminosity and a larger convective core. This dependency is apparent when comparing Figs. (III.8), (III.9), (III.10) and (III.12). The behaviour is not linear because the interaction between the intermediate convective zone and the hydrogen burning region is not linear. Therefore, contrary to the trend of finding convergence between the two convective stability criteria with an increasing amount of convective boundary mixing during core hydrogen burning, the different sizes of the convective helium core between the Schwarzschild and the Ledoux models varies more for $f_{CBM} \gtrsim 0.022$, with the exception of the case with no convective boundary mixing.

These uncertainties of the convective helium core affect the helium and carbon-oxygen core masses - see also Table III.1. This will influence the further central evolution and affect the pre-supernova structure, which depends on the helium core mass.

In the Ledoux models with no convective boundary mixing the convective core grows to a size of about $1\,M_\odot$ (Fig. (III.12)) black dashed and dash-dotted lines, before the chemical stratification limits the increase of the convective core in the Ledoux models. The radiative temperature gradient continues to increase and a semiconvective region develops above the core. The semiconvection in the model with $\alpha_{sc} = 0.004$ is not efficient enough to fully remove the restricting μ-gradient above the convective core and the convective helium core stops growing for the rest of the burning phase. Above the convective core, however, several sandwiched layers of semiconvection and convection occur, which increase

in number with time, because the semiconvective process slowly erases the chemical stratification[4]. In the model with fast semiconvection, $\alpha_{\rm sc} = 0.4$, the stratification is steadily removed by a thin semiconvective layer just above the convective core. This, however, leads to a wiggly convective core boundary but the core can initially grow very similarly to the convective core in the Schwarzschild model. The Schwarzschild model with no convective boundary mixing ignores the μ-gradient and initially grows similarly to the other Schwarzschild models with convective boundary mixing. At around $X_c(^4\mathrm{He})\approx 0.9$ in Fig. (III.12), the convective core growth plateaus before it continues to grow further at $X_c(^4\mathrm{He})\approx 0.8$. This is a result of the hydrogen shell, which is boosted there as a result of the interaction with the intermediate convective zone. Consequently, the Ledoux model with fast semiconvection predicts a bigger convective helium core at the beginning of core helium burning. As the evolution proceeds, however, a chemical composition gradient builds up above the core, which becomes too strong for semiconvection to erase. This reduces the increase of the convective core. The convective core in the Schwarzschild model on the other hand grows further, predicting a overall larger convective helium core than in the Ledoux models - compare Table III.1.

The chaotic behaviour of the core boundary around $X_c(^4\mathrm{He})\approx 0.1$ in the Schwarzschild model with no convective boundary mixing (solid black line in Fig. (III.12)) is due to a convective pillar that rises on top of the convective core, much stronger than the *core breathing pulses* previously mentioned. We tested this behaviour against an increased resolution but the feature remained.

The right panel in Fig. (III.12) shows the convective helium core boundary of the various $25\,\mathrm{M}_\odot$ models. The convective helium core grows with time as in the $15\,\mathrm{M}_\odot$ models but there are some important differences, which are more prominent in the models with larger $f_{\rm CBM}$. These differences, apart from the generally larger convective helium core with increasing initial mass, are due to the different behaviour of the intermediate convective zone.

In the $25\,\mathrm{M}_\odot$ case, the initial growth of the convective helium core is larger in all Ledoux models than in the Schwarzschild models with the same amount of convective boundary mixing. This is because the hydrogen shell is less active in the latter and slightly closer to the convective core. This is a consequence of the different evolution of the intermediate convective zone similar to Fig. (III.11, middle and bottom row). Therefore, the Ledoux models predict a larger convective helium core than the Schwarzschild models with the same amount of convective boundary mixing. The gap is larger for higher $f_{\rm CBM}$ values. Interestingly, the behaviour of the intermediate convective zone in the $25\,\mathrm{M}_\odot$ models leads to convective helium cores more similar in the Schwarzschild models with $f_{\rm CBM} = 0.004$ and 0.01 than with their Ledoux counterparts and vice versa for the Ledoux models (Fig. (III.12) and Table III.1). The convective core in the Schwarzschild models experiences a faster growth starting around $X_c(^4\mathrm{He}) \sim 0.5$. There the hydrogen shell narrows and with it the intermediate convective zone.

[4]When the μ-gradient decreases the term $(\nabla_{\rm L} - \nabla)^{-1}$ in Eq. (II.19) increases, which enhances the semiconvective mixing in this layer. The result is a very spiky chemical composition profile.

Consequently the core generates more energy and the convective region grows. This finally leads to similar core masses at the end of core helium burning for all the $25\,M_\odot$ models with $f_{\rm CBM} = 0.004$, 0.01 and 0.022. On the other hand, in the $25\,M_\odot$ models with $f_{\rm CBM} = 0.035$ and 0.05 the initial difference of the convective core sizes between the Ledoux and Schwarzschild models is large and the Ledoux models predict larger helium core masses.

The behaviour of the convective helium core in the $20\,M_\odot$ models is a mixture of the behaviours of the models for the two other initial masses. The simulations with $f_{\rm CBM} = 0.004$ behave similarly to the $25\,M_\odot$ case with the exception of stronger *core breathing pulses*. The calculations with $f_{\rm CBM} = 0.022$ are similar to the $15\,M_\odot$ models with the difference that the hydrogen shell is at about the same location in the Ledoux and Schwarzschild models. Therefore the convective core size grows at a similar rate, apart from an increase around $X_c(^4\mathrm{He}) \sim 0.6$, which is due to the disappearance of the intermediate convective zone; this is no *core breathing pulse*. The $20\,M_\odot$ models with the two largest values of $f_{\rm CBM}$ show a different intermediate convective zone and hence different convective helium cores depending on the boundary criterion, again similar to the $25\,M_\odot$ models.

The convective core in the $20\,M_\odot$ models with $f_{\rm CBM} = 0.01$ is the exception from the above discussion. There the Schwarzschild model predicts a larger convective helium core than the Ledoux models. This is because of the larger intermediate convective zone in the Ledoux models compared to the Schwarzschild model. Therefore, the Schwarzschild model provides more energy from central helium burning compared to the Ledoux model, hence, the relatively smaller convective core in the latter.

5.2 Nucleosynthesis during Core Helium Burning

The two dominant reactions by which helium burns are the triple-α process, $3\alpha \rightarrow {}^{12}\mathrm{C}$, and α capture on carbon, ${}^{12}\mathrm{C}(\alpha,\gamma){}^{16}\mathrm{O}$ - see also Section I.2.1.2 for more details on this burning phase. The first reaction has a second order dependence on density whereas the latter a first order (e.g. Kippenhahn & Weigert, 1994; Arnett & Thielemann, 1985; Woosley et al., 2002). Therefore, with increasing abundance of ${}^{12}\mathrm{C}$ towards the end of core helium burning, the second reaction dominates. Furthermore, the density dependency favours the latter reaction at higher entropy, i.e. higher masses. Stars at solar metallicity additionally contain some ${}^{14}\mathrm{N}$ in their cores, $\sim 1.4\%$, which is left over from the CNO-cycle during the main sequence (Arnould & Mowlavi, 1993). At the start of core helium burning, before the energy generation by the triple-α process becomes noteworthy, the ${}^{14}\mathrm{N}$ burns convectively away via ${}^{14}\mathrm{N}(\alpha,\gamma){}^{18}\mathrm{F}(\beta^+\nu){}^{18}\mathrm{O}(\alpha,\gamma){}^{22}\mathrm{Ne}$ (Cameron, 1960). The synthesised ${}^{22}\mathrm{Ne}$ will capture another α nucleus once the central temperature exceeds $\sim 2.5 \times 10^8$ K via ${}^{22}\mathrm{Ne}(\alpha,\mathrm{n}){}^{25}\mathrm{Mg}$, creating the condition for the weak slow neutron capture process (weak s-process; Couch et al., 1974; Arnett & Thielemann, 1985; Prantzos et al., 1990; Kaeppeler et al., 1994; Frischknecht et al., 2016). Yet only a part of the

Table III.1: Properties of the stellar models at core helium depletion.

model	$f_{\rm CBM}$ & $\alpha_{\rm sc}$	$M_{\rm final}$ ($M_\odot$)	M_α [a] ($M_\odot$)	M_α ($M_\odot$)	$M_{\rm CO}$ ($M_\odot$)	$\tau_{\rm H}$ (Myrs)	$\tau_{\rm He}$ (Myrs)	$\tau_{\rm BSG}/\tau_{\rm He}$ [b]	$\log_{10} T_{\rm eff,min}^{\rm MS}$ [c] (K)
$15M_\odot$,	$f_{\rm CBM}=0.0$	14.35	2.55	4.07	2.08	11.08	1.47	0.78	4.40
Schwarzschild,	$f_{\rm CBM}=0.004$	13.83	2.73	4.08	2.14	11.40	1.48	0.54	4.39
$f_0=0.002$	$f_{\rm CBM}=0.01$	13.43	3.03	4.28	2.34	11.93	1.34	0.36	4.38
	$f_{\rm CBM}=0.022$	12.34	3.60	4.68	2.75	12.86	1.19	0.02	4.36
	$f_{\rm CBM}=0.035$	11.23	4.23	5.39	3.45	13.74	1.03	0.02	4.32
	$f_{\rm CBM}=0.05$	11.13	4.95	6.22	4.33	14.60	0.84	0.01	4.28
$15M_\odot$,	$f_{\rm CBM}=0.004$	14.28	2.65	4.05	2.10	11.28	1.52	0.77	4.40
Schwarzschild,	$f_{\rm CBM}=0.01$	13.61	2.96	4.24	2.29	11.83	1.39	0.46	4.38
$f_0=0.02$	$f_{\rm CBM}=0.022$	12.47	3.59	4.65	2.72	12.81	1.20	0.02	4.36
$15M_\odot$,	$f_{\rm CBM}=0.0$, $\alpha_{\rm sc}=0.004$	14.30	2.21	3.51	0.56	10.47	0.93	0.02	4.41
Ledoux	$f_{\rm CBM}=0.0$, $\alpha_{\rm sc}=0.4$	14.09	2.54	3.73	2.13	11.07	1.26	0.01	4.40
$f_0=0.002$	$f_{\rm CBM}=0.004$, $\alpha_{\rm sc}=0.004$	13.85	2.72	4.07	2.13	11.40	1.44	0.49	4.39
	$f_{\rm CBM}=0.004$, $\alpha_{\rm sc}=0.4$	13.85	2.72	4.07	2.13	11.40	1.44	0.49	4.39
	$f_{\rm CBM}=0.01$, $\alpha_{\rm sc}=0.004$	13.18	3.02	4.24	2.31	11.93	1.34	0.15	4.38
	$f_{\rm CBM}=0.01$, $\alpha_{\rm sc}=0.4$	13.18	3.02	4.24	2.31	11.93	1.33	0.15	4.38
	$f_{\rm CBM}=0.022$, $\alpha_{\rm sc}=0.004$	11.88	3.60	4.92	2.94	12.86	1.16	0.01	4.36
	$f_{\rm CBM}=0.022$, $\alpha_{\rm sc}=0.4$	11.92	3.60	4.96	2.98	12.86	1.14	0.01	4.36
	$f_{\rm CBM}=0.035$, $\alpha_{\rm sc}=0.004$	12.46	4.23	5.30	3.40	13.74	0.95	0.02	4.32
	$f_{\rm CBM}=0.035$, $\alpha_{\rm sc}=0.4$	12.41	4.23	5.34	3.44	13.74	0.94	0.02	4.32
	$f_{\rm CBM}=0.05$, $\alpha_{\rm sc}=0.004$	10.39	4.96	6.41	4.50	14.60	0.84	0.01	4.28
	$f_{\rm CBM}=0.05$, $\alpha_{\rm sc}=0.4$	10.90	4.95	6.28	4.39	14.60	0.83	0.01	4.28
$15M_\odot$,	$f_{\rm CBM}=0.004$, $\alpha_{\rm sc}=0.004$	13.63	2.64	4.06	2.14	11.25	1.27	0.01	4.40
Ledoux,	$f_{\rm CBM}=0.01$, $\alpha_{\rm sc}=0.004$	13.40	2.96	4.20	2.27	11.82	1.35	0.27	4.38
$f_0=0.02$	$f_{\rm CBM}=0.022$, $\alpha_{\rm sc}=0.004$	11.90	3.59	4.91	2.94	12.82	1.16	0.01	4.36
$20M_\odot$,	$f_{\rm CBM}=0.004$	17.37	4.39	5.94	3.63	8.12	0.99	0.64	4.43
Schwarzschild,	$f_{\rm CBM}=0.01$	17.49	4.89	6.24	3.95	8.40	0.89	0.64	4.42
$f_0=0.002$	$f_{\rm CBM}=0.022$	14.48	5.70	6.71	4.45	8.95	0.82	0.17	4.38
	$f_{\rm CBM}=0.035$	11.93	6.54	7.35	5.13	9.46	0.78	0.02	4.34
	$f_{\rm CBM}=0.05$	10.95	7.49	8.74	6.52	9.97	0.66	0.01	4.27
$20M_\odot$,	$f_{\rm CBM}=0.004$, $\alpha_{\rm sc}=0.4$	18.90	4.49	5.89	3.58	8.09	0.96	0.92	4.43
Ledoux,	$f_{\rm CBM}=0.01$, $\alpha_{\rm sc}=0.4$	18.66	4.90	6.13	3.86	8.40	0.92	0.87	4.42
$f_0=0.002$	$f_{\rm CBM}=0.022$, $\alpha_{\rm sc}=0.4$	13.02	5.70	6.90	4.61	8.95	0.79	0.02	4.38
	$f_{\rm CBM}=0.035$, $\alpha_{\rm sc}=0.4$	10.84	6.54	8.01	5.71	9.46	0.72	0.02	4.34
	$f_{\rm CBM}=0.05$, $\alpha_{\rm sc}=0.4$	11.02	7.50	8.83	6.64	9.97	0.63	0.01	4.28
$25M_\odot$,	$f_{\rm CBM}=0.004$	17.10	6.54	7.84	5.24	6.63	0.75	0.36	4.44
Schwarzschild,	$f_{\rm CBM}=0.01$	15.69	6.85	7.86	5.31	6.70	0.77	0.26	4.44
$f_0=0.002$	$f_{\rm CBM}=0.022$	12.57	7.95	8.54	6.05	7.08	0.69	0.02	4.38
	$f_{\rm CBM}=0.035$	14.03	9.00	9.73	7.24	7.43	0.64	0.02	4.34
	$f_{\rm CBM}=0.05$	12.69	10.16	11.27	8.86	7.78	0.55	0.01	4.24
$25M_\odot$,	$f_{\rm CBM}=0.004$, $\alpha_{\rm sc}=0.4$	21.35	6.43	7.77	5.18	6.53	0.71	0.72	4.45
Ledoux,	$f_{\rm CBM}=0.01$, $\alpha_{\rm sc}=0.4$	21.59	6.91	7.72	5.15	6.70	0.70	0.78	4.43
$f_0=0.002$	$f_{\rm CBM}=0.022$, $\alpha_{\rm sc}=0.4$	14.87	7.94	8.59	6.11	7.08	0.66	0.12	4.38
	$f_{\rm CBM}=0.035$, $\alpha_{\rm sc}=0.4$	13.70	9.00	9.88	7.39	7.43	0.61	0.02	4.33
	$f_{\rm CBM}=0.05$, $\alpha_{\rm sc}=0.4$	12.76	10.16	11.68	9.25	7.78	0.52	0.04	4.24

Notes: Shown are the total star mass, $M_{\rm tot}$, the helium core mass, M_α, the carbon-oxygen core mass, $M_{\rm CO}$, the main-sequence lifetime, $\tau_{\rm H}$, the core helium burning lifetime, $\tau_{\rm He}$ and the blue supergiant to core helium burning lifetime, $\tau_{\rm BSG}/\tau$He. The core mass is defined as the location where the abundance of the main fuel in the burning process, which creates the main end product of the burning phase, is below 0.1 and the abundance of the end product is above 0.01.

[a] Hydrogen free core at hydrogen depletion.

[b] $\tau_{\rm BSG}$, the blue supergiant lifetime is defined as the time when the star (i) has left the main-sequence stage of core hydrogen burning, (ii) the surface temperature is in the range $4.4 > \log_{10} T_{\rm eff} > 3.9$ and (iii) it is not an extremely helium-enriched Wolf-Rayet-like star, i.e. $X_{\rm surf}(^1{\rm He}) > 0.3$.

[c] The logarithm of the minimum effective temperature during the main-sequence evolution. The terminal-age main-sequence is defined as the time when the central hydrogen mass fraction drops below 10^{-5}.

central ^{22}Ne captures an α nucleus during core helium burning. The leftover ^{22}Ne will capture an α during carbon shell burning, where the αs are provided from the α-emission channel of the ^{12}C+^{12}C reaction. This creates the condition for the weak s-process at higher temperatures and slightly different conditions (e.g. Couch et al., 1974; Prantzos et al., 1990; Raiteri et al., 1991b; Pignatari et al., 2010). This secondary neutron-source reaction competes during the late core helium burning with the ^{12}C$(\alpha,\gamma)^{16}$O reaction for the remaining α nuclei.

The outcome of core helium burning affects the further evolution of the star in several ways. The ^{12}C to ^{16}O ratio at core helium depletion depends strongly on the nucleosynthesis and its uncertainties (e.g. Arnett & Thielemann, 1985; Fields et al., 2018). The outcome not only sets the fuel for the subsequent carbon and oxygen burning phases but also influences the pre-supernova abundances (e.g. Thielemann & Arnett, 1985; Woosley et al., 2002). Furthermore, the amount of ^{12}C available at core carbon burning ignition determines whether carbon burns convectively or radiatively, which has consequences for the convective history and the stellar structure at core collapse (Ugliano et al., 2012; Sukhbold & Woosley, 2014; Müller et al., 2016; Sukhbold et al., 2016; Ertl et al., 2016; Sukhbold et al., 2018; Chieffi & Limongi, 2019). Moreover, the different activity of the ^{22}Ne+α reaction during core helium or shell carbon burning will affect the nucleosynthesis and final weak s-process yields, because the burning conditions differ and there are different isotopic abundances, e.g. neutron poison, in the two stages (Prantzos et al., 1990; Raiteri et al., 1991a,b; Pignatari et al., 2010).

Convective boundary mixing increases the effective size of the convective helium core (Fig. (III.12)) which slightly changes the central conditions. Furthermore, the convective stability criterion influences the size of the convective core and when it grows - see discussion in Section III.5.1. These facts affect the amount of α nuclei available during a certain period of core helium burning and the central conditions. This impacts the ^{12}C to ^{16}O ratio and the amount of ^{22}Ne capturing an α nucleus, thus, the efficiency of the weak s-process during core helium burning (see also e.g. Costa et al., 2006).

Fig. (III.13) presents the ^{12}C and ^{16}O mass fraction in the centre of the star at core helium depletion as a function of the carbon-oxygen core mass for the different initial masses. In the 15 $M_\odot$ models the ^{12}C mass fraction decreases and the ^{16}O mass fraction increases with increasing $f_{\rm CBM}$. The 15 $M_\odot$ models with the two highest values of $f_{\rm CBM}$ follow this trend but are shifted to slightly larger ^{12}C and smaller ^{16}O mass fractions. The first trend is a consequence of the increasing convective core mass during core helium burning with larger $f_{\rm CBM}$, as discussed in Section III.5.1, therefore more α-nuclei are ingested into the central burning zone. Thus, during late core helium burning, when the ^{12}C+α is dominant, more ^{12}C is turned into ^{16}O. The second point is related to the timing of the convective helium core growth (see Fig. (III.12)). Whilst in the 15 $M_\odot$ models with $f_{\rm CBM} \leq 0.022$ the core growth is roughly linear in time, in the models with $f_{\rm CBM} = 0.035$ or 0.05 core growth occurs mainly during the initial phase of core helium burning, i.e. when $X_c(^4\text{He}) \geq 0.8$, and the core growth is relatively

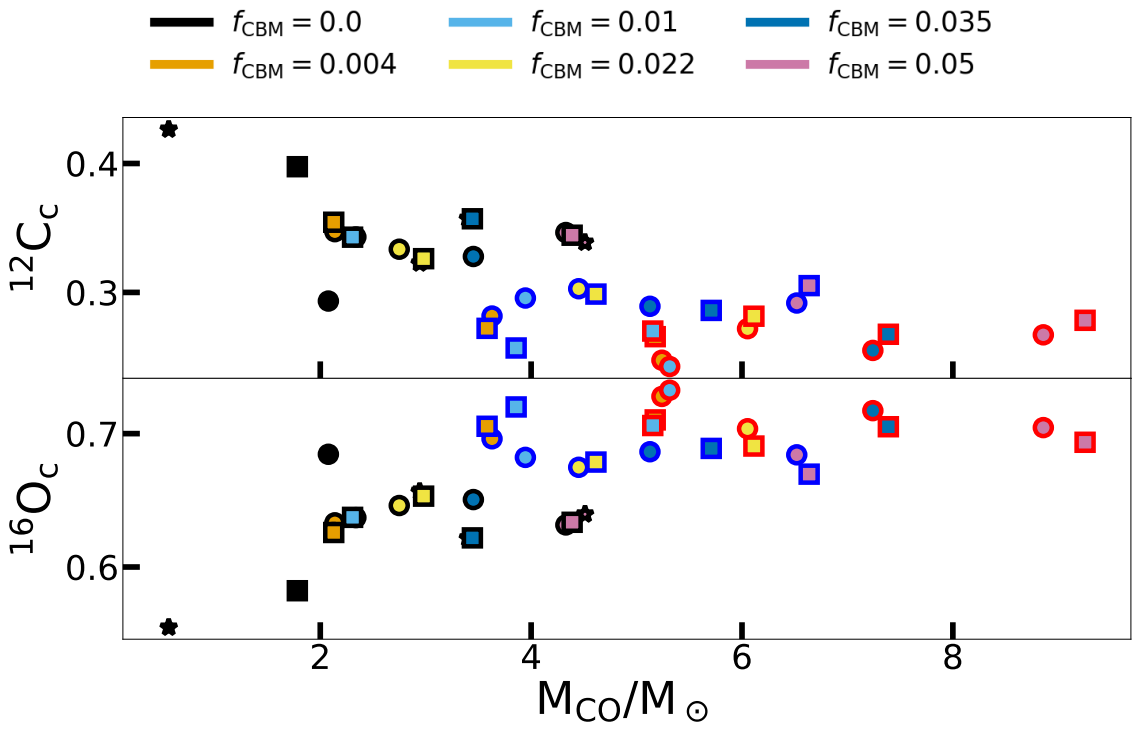

Figure III.13: The ^{12}C, top, and ^{16}O, bottom, mass fractions in the centre as a function of the carbon-oxygen core mass at core helium depletion. Plotted are the values for the 15 (black edge) 20 (blue edge) and 25 $M_\odot$ (red edge) models. The Schwarzschild boundary criterion is indicated by a circle and Ledoux criterion with a star ($\alpha_{sc} = 0.004$) or a square ($\alpha_{sc} = 0.4$), respectively. The colour scheme shows the value of f_{CBM}.

slower thereafter. Therefore, there is less α entrained during the late burning phase, when the ^{12}C+α reaction is dominant, resulting in a slightly higher ^{12}C and lower ^{16}O mass fraction in these models. The Schwarzschild model with $f_{CBM} = 0.035$ has a convective core growth more similar to the models with lower amounts of convective boundary mixing. This is also reflected in its lower ^{12}C and higher ^{16}O compared to the rest of the models with large amounts of convective boundary mixing.

Fig. (III.13) also depicts that with the semiconvective efficiencies used in this work, semiconvection has almost no influence on the carbon and oxygen mass fraction at the end of core helium burning. The only models where there is an impact are the ones with no convective boundary mixing, where a higher semiconvective efficiency leads to a larger convective core shown in Fig. (III.12). Consequently, there is more fuel available during the late burning phase, resulting in the lower ^{12}C and higher ^{16}O mass fraction.

The 15 $M_\odot$ Schwarzschild model with no convective boundary mixing does not follow this trend. This model has a much higher ^{16}O to ^{12}C ratio in the centre than any other of the 15 $M_\odot$ simulations. This is because of the sharp increase of the convective core described in Section III.5.1, which transports fuel into the convective region during late core helium burning. This brings a lot of fresh α into the core and more carbon is synthesised into oxygen.

Fig. (III.13) clearly shows a higher ^{16}O to ^{12}C ratio with increasing initial mass. This is expected due

to the temperature dependence of the ^{12}C+α reaction, hence, more massive stars synthesise more ^{16}O and less ^{12}C during core helium burning (e.g. Prantzos et al., 1990).

The central ^{12}C and ^{16}O mass fractions in the 20 and 25 $M_\odot$ models with different amounts of convective boundary mixing appear to be constant around $X_c(^{12}C)\sim 0.3$, $X_c(^{16}O)\sim 0.68$ and $X_c(^{12}C)\sim 0.22$, $X_c(^{16}O)\sim 0.7$, respectively. Contrary to the 15 $M_\odot$ models the ^{12}C+α reaction seems to be saturated under the conditions in these models. This is a result of the higher central temperatures in the models with the same initial mass but larger amounts of convective boundary mixing, which leads other reactions to activate, such as $^{16}O(\alpha,\gamma)^{20}Ne$ (e.g. Arnett & Thielemann, 1985). The models with values of $f_{\rm CBM} \leq 0.01$ have a lower ^{12}C and higher ^{16}O mass fraction. This behaviour is a consequence of the *core breathing pulses*, which occur during the late stages of core helium burning and affect the size of the convective core - see discussions in Sections III.5.1 and III.7. These events ingest more fuel into the burning region. Therefore the final ^{16}O mass fraction is increased and the ^{12}C mass fraction is decreased. Since the *core breathing pulses* are more extreme with less convective boundary mixing, the ^{16}O to ^{12}C ratio is slightly higher with less convective boundary mixing.

Comparing the different initial masses it is obvious that depending on the amount of convective boundary mixing lower mass models can have a similar ^{16}O to ^{12}C ratio at the end of core helium burning to higher mass models with less convective boundary mixing. This is striking because this ratio is crucial in determining the evolution of the advanced burning phases, in particular the convective history (see discussions in Sukhbold & Woosley, 2014; Chieffi & Limongi, 2019). Therefore, the amount of convective boundary mixing not only directly affects these convective regions by enhancing the convectively mixed region but also indirectly by setting the ^{16}O to ^{12}C ratio at the end of core helium burning.

The carbon to oxygen ratio at core helium depletion is very uncertain, especially due to the uncertainty in the reaction rate (e.g. Woosley et al., 2002). I show here that the amount of convective boundary mixing introduces another uncertainty in this ratio. The convective boundary criterion seem to affect the ratio less when comparing the different models with the same initial mass but varying $f_{\rm CBM}$ in Fig. (III.13). Nevertheless, the importance of this uncertainty needs to be determined in the absence of *core breathing pulses* which are thought to be numerical artefacts (Constantino et al., 2016) but see discussion in Section III.7.

The weak s-process in massive stars depends on the efficiency of the neutron source reaction ^{22}Ne(α,n)^{25}Mg, which determines the neutron density in the helium core. The efficiency of the neutron source reaction depends on (i) the nuclear abundances of ^{22}Ne and ^{4}He and (ii) the central conditions such as temperature and density. At solar metallicity, most of the metals are CNO elements, which are mostly turned into ^{14}N during hydrogen burning. Hence, the ^{22}Ne abundance before the activation of the ^{22}Ne+α reaction during core helium burning is directly related to the initial metal abundance in all my calculations ($X(^{22}Ne) \approx \frac{22}{14}\cdot X^{\rm CNO}_{ini}$). The amount of α available, on the other hand, depends on

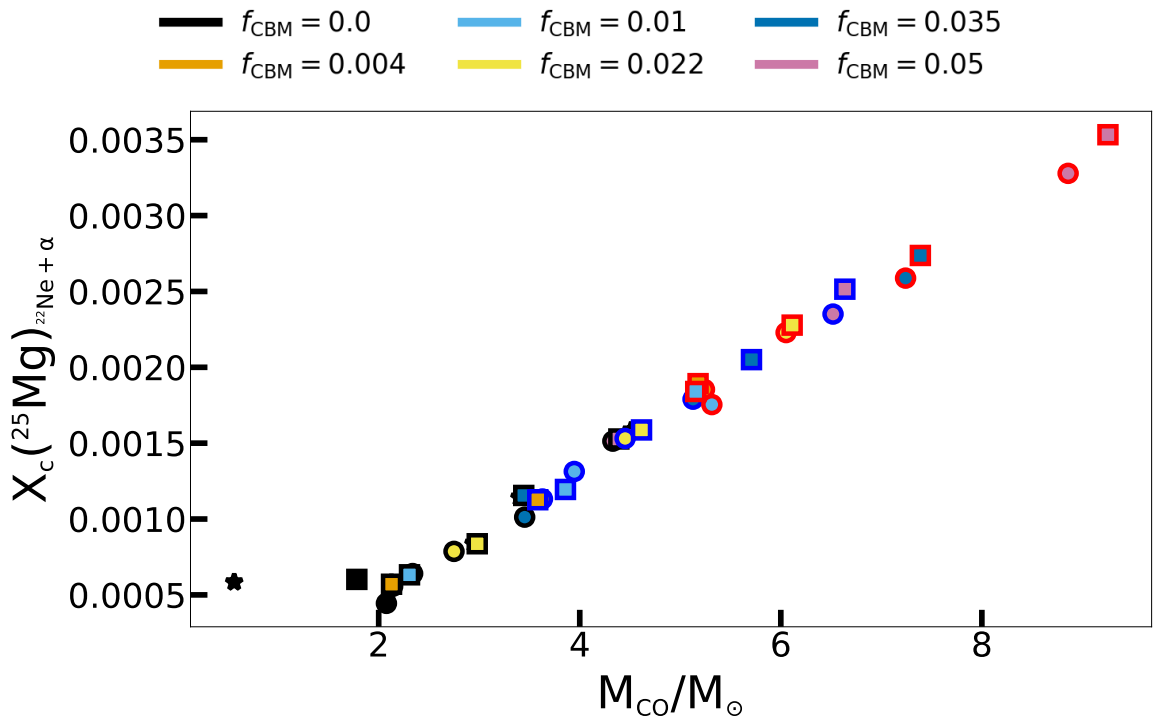

Figure III.14: The ^{25}Mg mass fraction produced at the centre by the neutron source reaction during core helium burning as a function of the carbon-oxygen core mass at core helium depletion. Plotted are the values for the 15 (black edge) 20 (blue edge) and 25 $M_\odot$ (red edge) models. A circle indicates the *Schwarzschild* criterion, a star the *Ledoux* criterion with $\alpha_{sc} = 0.004$ and a square the *Ledoux* criterion with $\alpha_{sc} = 0.4$. The colour scheme shows the value of f_{CBM}.

the size of the convective core and on the amount of fuel entrained at the top of the convective core. The differences in the central thermodynamic condition between the models depend on the different amounts of convective boundary mixing as well.

Fig. (III.14) presents the ^{25}Mg mass fraction produced at the centre by the neutron source reaction ^{22}Ne(α,n)^{25}Mg during core helium burning as a function of the carbon-oxygen core mass for the three initial masses. The number of neutrons released by the neutron source reaction is equal to the number of ^{25}Mg produced in Fig. (III.14), thus, it indicates the neutron flux and with it the activity of the weak s-process.

Fig. (III.14) shows a clear trend of an increasing ^{25}Mg production with increasing f_{CBM} for all initial masses. This is because (i) more fuel is entrained into the convective zone with an increasing amount of convective boundary mixing and (ii) the models with more convective boundary mixing have larger core masses, hence they burn helium in the centre at a slightly higher temperature and lower density compared to models with less convective boundary mixing. Moreover, the convective boundary criterion leads to different convective core sizes (Fig. (III.12)) which leads to different activity of the neutron source reaction. The shift of $X_c(^{25}Mg)$ to higher values with larger initial mass results from the fact that these models have larger core masses and burn helium at higher temperatures.

Fig. (III.14) depicts that the different semiconvective efficiencies do not change the amount of ^{25}Mg

produced by the ^{22}Ne+α reaction, which is a result of the reduced occurrence of semiconvection with increasing amount of convective boundary mixing. Therefore, the semiconvective efficiency does not affect the weak s-process efficiency during core helium burning.

Again, it is interesting to see in Fig. (III.14) that models with a large amount of convective boundary mixing behave like models of a larger initial mass but less convective boundary mixing in terms of carbon-oxygen core mass and s-process activity.

I want to stress here that the $X_c(^{25}Mg)$ in Fig. (III.14) is not equal to the ^{25}Mg abundance at core helium depletion. Indeed, $X_c(^{25}Mg)$ corresponds to the production at the very centre, whereas the final ^{25}Mg abundance is determined by the conditions throughout the convective core. Additionally, some of the ^{25}Mg is further processed by burning.

The difference in s-process activity during core helium burning can shift the final weak s-process production between iron and strontium. Furthermore, more ^{22}Ne+α consumption during core helium burning leads to higher s-process yields (Pignatari et al., 2010).

The changes in nucleosynthesis due to the f_0 parameter is linear. A larger f_0 implies slightly less convective boundary mixing, thus, smaller amount of fuel available in the late core helium burning. Therefore, the abundances of ^{12}C and ^{22}Ne are higher and the abundances of ^{16}O and ^{25}Mg are lower than shown in Figs. (III.13) and (III.14). The differences of the nucleosynthesis during core helium burning due to semiconvection are slim as can be seen in Figs. (III.13) and (III.14) and mainly affect the simulations with no convective boundary mixing.

6 Blue versus Red Supergiant Evolution

The different behaviour in depth and duration of the intermediate convective zone discussed in Section III.4 has an important impact on the surface evolution of the model, which in turn influences the later stellar structure and evolution.

Fig. (III.15), left panel, shows the Hertzsprung-Russell diagram for the 15 $M_\odot$ models. The main-sequence tracks in the Hertzsprung-Russell diagram are discussed in Sections I.2 and III.3. The models leave the main sequence via the *Henyey hook* where the first difference between the two boundary criteria arises. The tracks of the Ledoux models form a loop (top left of the tracks) before they start crossing towards the cooler, red side of the Hertzsprung-Russell diagram, whereas the Schwarzschild models evolve via a hook. With increasing amount of convective boundary mixing, the latter show loops as well. This contrast arises from the different location of the intermediate convective zone, which becomes more similar with increasing $f_{\rm CBM}$ (see Figs. (III.8) and (III.9)).

The Ledoux models with no convective boundary mixing (black dotted and dashdotted lines in Fig. (III.15)) show the most different tracks when crossing to the red supergiant branch on the cool

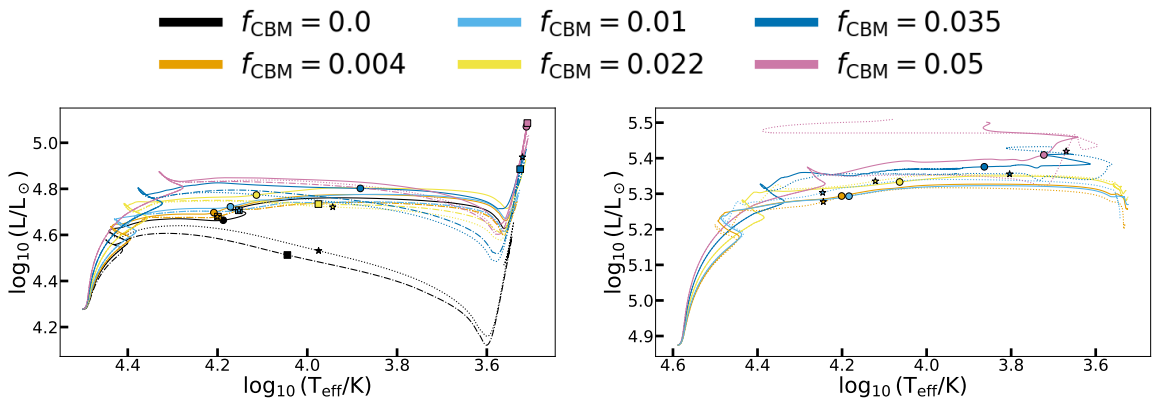

(a) $15\,M_\odot$ (b) $25\,M_\odot$

Figure III.15: The Herzsprung-Russell diagram for various calculations of models with initial masses of 15 and $25\,M_\odot$, both with $f_0 = 0.002$. The solid lines indicate Schwarzschild models and all the others are Ledoux models with either $\alpha_{sc} = 0.4$ (dotted line) or $\alpha_{sc} = 0.004$ (dash-dotted line). The colour scheme indicates the amount of convective boundary mixing. The markers show the location where helium burning is ignited in the core, i.e. when 0.3% of the helium left after core hydrogen depletion is burnt. The different marker styles indicate the different boundary criteria used in the calculation, where circles indicate the *Schwarzschild* criterion and the others are Ledoux models with $\alpha_{sc} = 0.004$ (square) or $\alpha_{sc} = 0.4$ (star).

side of the Hertzsprung-Russell diagram by decreasing their surface luminosity. Fig. (III.16) (left panel) which presents the evolution of the surface temperature as a function of the central helium mass fraction sheds light on what happens in the interior of these models. The two Ledoux models, after the *Henyey hook* in the upper left corner, drop their surface temperature before they consume any significant amount of helium in their interior. Hence, they directly cross the *Hertzsprung gap* to the cool side of the Herztsprung-Russell diagram before they fully ignite helium in their core, despite the fact that Fig. (III.15) suggests that they start burning helium at $\log T_{eff} \approx 4.0$. The fast red-ward evolution results in a primarily adiabatic expansion of the envelope, thus a decrease in surface luminosity. The Schwarzschild model with no convective boundary mixing (the black solid line in Fig. (III.15)) on the other hand, ignites helium in its core at around $\log T_{eff} \approx 4.2$. Fig. (III.16) reveals that the model consumes $\sim 80\%$ of its central ^{4}He in the hotter, blue side of the Hertzsprung-Russell diagram, before it moves to the cool, red side. The crossing of the *Hertzsprung gap* in this simulation occurs with a nearly constant surface luminosity, which is due to a quasi-hydrostatic contraction/expansion. The short loop-like structure at $\log T_{eff} \approx 4.2$ in the Schwarzschild model is because of a strong, boosted hydrogen shell, which stops the expansion of the envelope by supporting the core.

These two scenarios, either spending the whole of the core helium burning phase as a red supergiant or spending most of core helium burning as a blue supergiant, are a consequence of the different intermediate convective zone and the activity of the hydrogen shell described in Section III.4.

These extreme differences of red- or blue-ward evolution with either the *Ledoux* or the *Schwarzschild* criterion in the $15\,M_\odot$ models decrease with increasing amount of convective boundary mixing (see

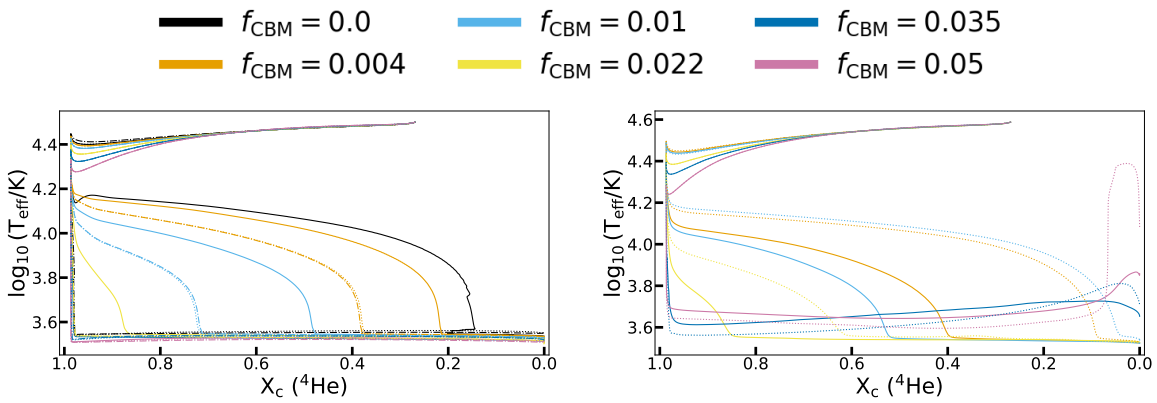

(a) 15 $M_\odot$ (b) 25 $M_\odot$

Figure III.16: Evolution of the effective temperature as a function of the central ^{4}He mass fraction. Shown are the 15 and 25 $M_\odot$ models, all with $f_0 = 0.002$. The solid lines indicate Schwarzschild models and all the other are Ledoux models with either $\alpha_{sc} = 0.4$ (dotted line) or $\alpha_{sc} = 0.004$ (dash-dotted line). The colour scheme indicates the amount of convective boundary mixing.

Figs. (III.15) and (III.16)). However, crucial variations arise with the choice of f_{CBM}. When a small amount of convective boundary mixing is applied, i.e. $f_{CBM} = 0.004$, the erasing of the chemical stratification at the lower convective boundary of the intermediate convective zone in the Ledoux models dominates - see discussion in Section III.4. As a result, both, the Ledoux and the Schwarzschild models, predict an overlap of the intermediate convective zone and the hydrogen burning shell. Consequently, these models experience a more "*Schwarzschild*-like" evolution where the star consumes $\sim 50\%$ of its central helium before they evolve red-ward. The blue supergiant lifetime is shorter in these models compared to the Schwarzschild model with no convective boundary mixing (compare in Table III.1) because of the shorter duration of the intermediate convective zone (Fig. (III.10)). These three models exhibit a vertex at $\log T_{eff} \approx 4.2$ which is due to the boost of the hydrogen shell. When higher amounts of convective boundary mixing are used, $f_{CBM} = 0.01$, 0.022 and additionally 0.035 in the Schwarzschild case, the effect of faster energy regulation dominates - see Section III.4. This results in a shorter duration of the intermediate convective zone and a weaker hydrogen shell. As a consequence, the models evolve more "*Ledoux*-like", meaning they evolve red-ward faster and spend most of their core helium burning phase as red supergiants. The loop-like structure around $\log T_{eff} \approx 4.2$ in Fig. (III.15) flattens and the point of central helium ignition is shifted to slightly cooler values of the surface temperature. For even more convective boundary mixing, $f_{CBM} = 0.05$ and 0.035 for the Ledoux models, the intermediate convective zone does not overlap with the hydrogen burning shell anymore, even less than in the Ledoux models with no convective boundary mixing. Therefore, the energy generation of hydrogen burning decreases fast and the shell moves outwards due to the lack of fuel at the shell location - see Section III.4. Consequently, the model moves very fast to the cooler part of the Hertzsprung-Russell diagram as shown in Fig. (III.16) and Table III.1. Moreover, core helium burning only ignites once the model has ascended the red supergiant branch. This is in fact

the result from an even faster red-ward evolution than the other models. The Ledoux models with no convective boundary mixing and with $f_{\rm CBM} = 0.022$ and the Schwarzschild model with $f_{\rm CBM} = 0.035$ reach the red supergiant branch after they have consumed $\sim 80\%$ of their $X_c(^4\mathrm{He})$. On the contrary, the Ledoux models with $f_{\rm CBM} = 0.035$ reach the red supergiant branch with having less helium consumed and the models with $f_{\rm CBM} = 0.05$ do not consume any notable amount of helium before they start ascending the red supergiant branch. Since these models do not have a strong hydrogen shell to support the core against contraction, more gravitational energy is released, of which part leads to a more extreme expansion and relatively high mass-loss rate before helium is ignited in the centre. The effect of this transition, from "*Schwarzschild*-like" to "*Ledoux*-like", is nicely presented in Fig. (III.16) and is a function of $f_{\rm CBM}$.

The generally larger intermediate convective zone in the 20 and $25\,\mathrm{M}_\odot$ models leads to a slower red-ward evolution and these models generally consume more helium in their cores as blue supergiants, as shown in Figs. (III.15) and (III.16) for the $25\,\mathrm{M}_\odot$ models. The location of helium ignition in Fig. (III.15), however, does not greatly change with higher initial mass and seems to be more dependent on the amount of convective boundary mixing.

Interestingly, the central evolution presented in Fig. (III.16) reveals important qualitative differences. The Ledoux models with $f_{\rm CBM} = 0.004$ and 0.01 both spend nearly their whole core helium burning phase as blue supergiants, $\sim 90\%$ and $\sim 75\%$, respectively (see Table III.1), whereas their Schwarzschild counterparts only spend $\sim 64\%$ and $\sim 30\%$, respectively, of their core helium burning phase as blue supergiants. Furthermore, the Ledoux models with $f_{\rm CBM} = 0.004$ and 0.01 behave more similarly during this stage than the respective Schwarzschild model with the same $f_{\rm CBM}$ and vice-versa. Hence, the stability criterion introduces a larger uncertainty in these models with medium and low amounts of convective boundary mixing during this stage. This occurs for both initial masses, 20 and $25\,\mathrm{M}_\odot$.

Another interesting feature appearing in Figs. (III.15) and (III.16) is that the models with large amount of convective boundary mixing, $f_{\rm CBM} = 0.035$ and 0.05, start to move back to the hot side of the Hertzsprung-Russell diagram towards the end of helium depletion. This is a consequence of the fast red-ward evolution after the main sequence of these models and the resulting relatively large mass loss (see Fig. (III.17)) which erodes most of the hydrogen rich envelopes of these stars - also compare $\mathrm{M_{tot}}$ and M_α in Table III.1. Indeed, the $25\,\mathrm{M}_\odot$ models with $f_{\rm CBM} = 0.05$ lose enough mass to evolve blue-wards with the Ledoux model ending in the Wolf-Rayet phase, defined in our models as $X_{\rm surf}(^1\mathrm{H}) < 0.4$ and $\log_{10} T_{\rm eff} > 4.0$. As expected, this behaviour is more dominant in the $25\,\mathrm{M}_\odot$ models than in the $20\,\mathrm{M}_\odot$ models.

The effect of the *convective fingers* on the intermediate convective zone in the models with $f_{\rm CBM} = 0.022$ - as discussed in Section III.3 - is also apparent. In the $20\,\mathrm{M}_\odot$ Ledoux model the duration

of the intermediate convective zone is shorter due to the influence of the *convective fingers* and it crosses nearly directly to the cool part of the Hertzsprung-Russell diagram, whereas its Schwarzschild counterpart stays for some time in the hot part. In the $25\,M_\odot$ Ledoux models with $f_{\rm CBM} = 0.022$, on the other hand, the intermediate convective zone is larger due to the interference of the *convective fingers* and it experiences a slower red-ward evolution than its Schwarzschild counterpart.

Table III.1 includes the ratio of the blue supergiant to core helium burning lifetimes. This shows once more that the simulations with a larger and longer intermediate convective zone stay longer in the hot part of the Hertzsprung-Russell diagram. Vice versa, a smaller intermediate convective zone leads to a faster red-ward evolution. Furthermore, the Schwarzschild models predict constant or slightly decreasing blue supergiant lifetimes with increasing initial mass whereas the Ledoux models predict first an increase and then a decrease for the two largest values of $f_{\rm CBM}$. This difference is due to the initial location of the intermediate convective zone.

Some of the models spend more than half of their core helium burning lifetime as blue supergiants. This is partly in contradiction with Davies & Dessart (2018) who found a transition from fast to slow red-ward evolution around 15 - $25\,M_\odot$. Moreover, Davies & Dessart (2018) state that the location of helium ignition impacts the way the star crosses the Hertzsprung-Russell diagram. I, however, do not see a clear indication of this in my mass range because all of the models with $f_{\rm CBM} \lesssim 0.022$ ignite helium burning in their cores at around $\log_{10} T_{\rm eff} \approx 4.2 - 4.1$ with the exceptions being the models with large amount of convective boundary mixing. So the location of helium ignition in my models only shows whether a low and intermediate $f_{\rm CBM}$ or a large $f_{\rm CBM}$ is used. The main impact I find, as stated by Davies & Dessart (2018) as well, is the location and duration of the intermediate convective zone.

These two different evolutionary paths, core helium burning as a blue or red supergiant, or a combination thereof, have an important impact on the structure of the star and its further evolution, in particular (i) the mass loss rates, (ii) the shape of the surface convective zone and surface enrichment, (iii) the central evolution (Section III.5) and (iv) the star type at the end of core helium burning, either red supergiant, blue supergiant or Wolf-Rayet star.

Fig. (III.17) presents the mass loss rates, $\dot{M}$, as a function of the central helium mass fraction, starting at core hydrogen depletion, at the bottom left. $\dot{M}$ shows similar low values in all models at the end of their main-sequence evolution. Thereafter the mass loss rates evolution exhibits quite a contrast. The mass loss rates depend crucially on the time when the model enters the red supergiant phase. During the time a model evolves as a blue supergiant, its mass loss rates stay relatively low, following the mass loss prescription from Vink et al. (2000, 2001) - see Section B.1.6. However, once the model evolves red-ward it experiences a drastic increase in its mass loss rate. This is around $\log_{10} T_{\rm eff} = 4.0$ when the stellar evolution code switches from the mass loss prescription for O-stars to the empirical

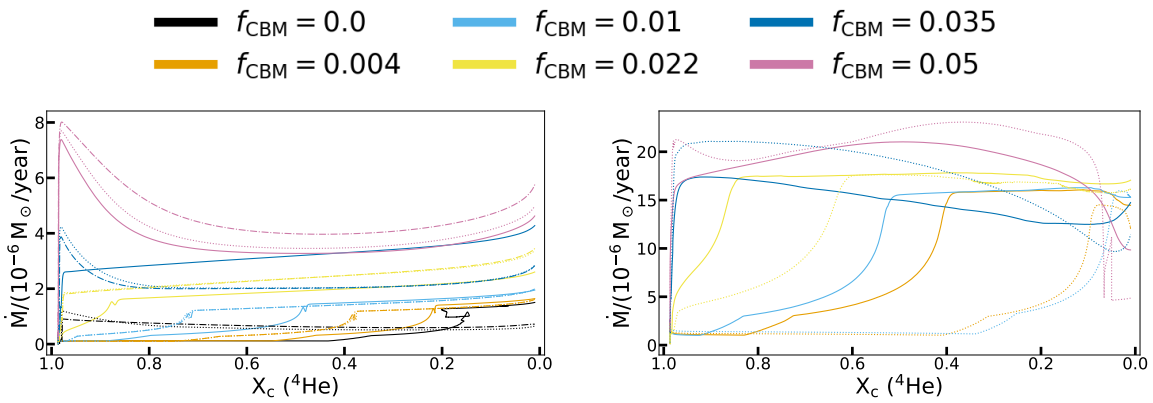

(a) $15\,M_\odot$ (b) $25\,M_\odot$

Figure III.17: The mass-loss rate per year as a function of the central helium mass fraction. The tracks begin at central hydrogen depletion and go up to central helium depletion. Shown are the tracks for the 15 and $25\,M_\odot$ models, left and right respectively, all with $f_0 = 0.002$. The solid lines indicate Schwarzschild models and all the other lines are Ledoux models with either $\alpha_{sc} = 0.4$ (dotted line) or $\alpha_{sc} = 0.004$ (dash-dotted line). The colour scheme shows the amount of convective boundary mixing.

mass loss rates by de Jager et al. (1988). The different dependency on the surface temperature and luminosity leads to the drastic increase of the mass loss rates - see Section B.1.6.

As previously discussed, the time a model spends as a blue supergiant depends on the duration, location and size of the intermediate convective zone, which itself depends on the stability criterion used and the amount of convective boundary mixing applied. In general, models with a larger f_{CBM} parameter experience a faster red-ward evolution, hence, they experience an increased $\dot{M}$ earlier. Additionally, there is a difference between the *Ledoux* and the *Schwarzschild* criterion models, in that the latter experience a later and less intense increase in $\dot{M}$, which is present for all f_{CBM}-values used in this work. This is a result from the differences in the intermediate convective zone.

The simulations with no convective boundary mixing (the black lines in Fig. (III.17)) defy this general trend, because the Schwarzschild model has the longest blue supergiant lifetime whereas the Ledoux models the shortest. Furthermore, the models with $f_{CBM} = 0.05$ and the Ledoux models with $f_{CBM} = 0.035$ experience a relatively high $\dot{M}$ which is reduced by about half in the subsequent evolution. This is due to the drop of the total luminosity (see Fig. (III.10)). The high luminosity after core hydrogen depletion in these models is due to the more extreme central contraction without a strong support from the hydrogen shell, as discussed in Section III.4.

The 20 and $25\,M_\odot$ models generally have higher mass-loss rates with increasing f_{CBM} and hence a smaller total mass at core helium depletion (Table III.1). There are, however, some exceptions. The Ledoux and Schwarzschild models, each with $f_{CBM} = 0.004$ and 0.01, show more similar mass loss rates than their counterparts with the same f_{CBM} but different stability criterion. This is a consequence of the more similar intermediate convective zone previously discussed.

The changes in mass-loss rates seen in Fig. (III.17) are due to the different phases the models are in, as discussed above. The variation due to the uncertainty of convective boundary mixing leads to a wide range of total masses at core helium depletion (see Table III.2). The most extreme cases are the models with an initial mass of $25\,M_\odot$ where the final mass ranges from 21.59 $M_\odot$ down to 12.57 $M_\odot$. The depth and strength of the intermediate convective zone further affects the appearance of the surface convective zone. A less energetic hydrogen shell favours core contraction, thus expansion of the envelope, which in turn cools down and the opacity in the envelope increases. As a consequence, a surface convective zone develops, which penetrates deep into the star - see Figs. (III.8) and (III.9) where some panels show a convective zone in the upper right side - and enriches the surface with previously synthesised material from the interior. A stronger hydrogen shell, on the other hand, delays the formation of the surface convective zone and the surface enrichment occurs later (see discussion in e.g. Georgy et al., 2014). Therefore, the surface composition and composition of winds will be affected.

In Section III.4 I have shown that the f_0 parameter has an important effect on the intermediate convective zone when small values of $f_{\rm CBM}$ are used, especially in the Ledoux models. Following the discussion, this affects the red-ward evolution (Table III.1) and with it the mass loss rates. Therefore, this parameter should not be overlooked in discussions.

7 Discussion

One of the main goals of this work is to show the relative importance of convective boundary mixing uncertainties and which quantities of stellar evolution are mostly affected. In Table III.2 I list the variation of the core masses and the total mass at core helium depletion and in Table III.3 the variation of the lifetime of some stellar stages. The two tables show for each initial mass the maximum difference in the predicted values of my simulations and the relative variation with respect to a reference model. The reference model for all initial masses is the Ledoux model with $f_{\rm CBM} = 0.035$ and $\alpha_{\rm sc} = 0.4$, which is, in the $15\,M_\odot$ case, the closest setting to the calibration of Brott et al. (2011).

The two largest relative deviations in Table III.2 are the total mass of the star and the carbon-oxygen core mass, which are both above 50%. For the two higher initial masses, the uncertainty of the total star mass dominates, with $\sim 65\%$ and $\sim 75\%$ respectively for the 20 and $25\,M_\odot$ models, whereas in the $15\,M_\odot$ models the relative variation of the carbon-oxygen core is the largest with $\sim 70\%$. The absolute deviation of the total mass is about $9\,M_\odot$. This large uncertainty is a result of the models spending different amounts of time as blue or red supergiants, where different mass loss prescriptions apply. This is a consequence of both, the boundary criterion and the amount of convective boundary mixing which influence the location, shape and duration of the intermediate convective zone - see Sec-

tion III.4. The core masses, with the exception of the carbon-oxygen core mass in the $15\,M_\odot$ models, show smaller but still non-negligible deviations. The helium core masses have differences up to $4\,M_\odot$ and relative variations of $\sim 35-45\%$. The absolute difference is larger for the higher initial masses, a consequence of the size difference of these models, but the relative variation is smaller because of the larger M_{He} of the reference model. The uncertainty of helium core mass is dominated by the amount of convective boundary mixing and the choice of the boundary criterion only gives maximal differences up to $0.5\,M_\odot$ (see Table III.1). The carbon oxygen-core masses follow the same trend but with larger absolute and relative variations, i.e. $\sim 2.5-4.1\,M_\odot$ and $\sim 50-70\%$, respectively. These differences are mainly influenced by the choice of f_{CBM} and the choice of the boundary criterion is less important than for M_{He} in most cases. The boundary criterion mainly influences the timing when the convective helium core grows but has less impact on its maximal extent. M_{CO} shows a slightly higher absolute variation because the variations from the previous stellar phases cumulate. Thus, the relative uncertainty of the core masses increases as stellar evolution proceeds and might be even higher for the further evolution (see e.g. Davis et al., 2019). The uncertainty of the mixing assumptions also influences convective shell interactions during the later evolutionary stages (e.g. Clarkson & Herwig, 2020).

I want to stress here, that some of the core masses in the $15\,M_\odot$ models with larger values of f_{CBM} are as large as the same core mass in the $20\,M_\odot$ models with moderate values of f_{CBM}. The same applies for the 20 and $25\,M_\odot$ models. These models with large amounts of convective boundary mixing would therefore have an evolution after core helium burning that is more similar to models with a higher mass but less convective boundary mixing. This would change the "*zero-age main sequence - supernova progenitor*" relation and the final fate of massive stars as a function of their initial mass. Furthermore, the core masses are often used to relate to the pre-supernovae compactness and explodability of a star (e.g. O'Connor & Ott, 2011; Müller et al., 2016; Ertl et al., 2016; Sukhbold et al., 2018; Chieffi & Limongi, 2019). Relative uncertainties of $\gtrsim 40-70\%$ make these predictions unreliable and more dependent on the parameter choices than the actual physics. Moreover, these uncertainties will impact 3D hydrodynamics simulations for which 1D stellar evolution models are used as input model. The core hydrogen and core helium burning lifetimes in Table III.3 show a decreasing variation, relative and absolute, with initial mass. Convective boundary mixing mainly influences the burning lifetimes by extending the convective core and providing more fuel for the burning phase. The models with higher initial masses consume their fuel faster, hence the smaller variation in lifetimes with increasing initial mass. The differences of the core hydrogen burning lifetimes are nearly completely due to the choice of f_{CBM} and only the models with no convective boundary mixing show a dependence on the boundary criterion. The relative variation of the helium burning lifetimes is more than twice the relative variation of the hydrogen burning lifetimes. Similar to hydrogen burning, these differences

in the helium burning lifetimes are mainly determined by the amount of convective boundary mixing but there is also a small dependence on the boundary criterion. The variation in the blue supergiant lifetimes is extreme but this is to be expected considering the uncertainty connected with this phase. This huge variation translates into the uncertainty of the total mass in Table III.2.
The blue values in brackets in Tables III.2 and III.3 represent the same variations but they include the $15\,M_\odot$ models with no convective boundary mixing. These variations are larger, mainly because of the pure Ledoux model with slow semiconvection, which has much smaller cores (see Table III.1).

In Sections III.3 and III.5 I have shown that the helium and carbon-oxygen core masses increase with increasing amount of convective boundary mixing. Furthermore, convective boundary mixing enhances the main-sequence width and prevents the occurrence of *convective fingers*. Also, models with more convective boundary mixing have longer main-sequence and core helium burning lifetimes as shown in Table III.1 and experience more mass loss (see Fig. (III.17)). These are effects which are generated by rotation as well (e.g. Heger et al., 2000; Meynet & Maeder, 2000, and Chapter IV). Therefore, some solutions of stellar models might not be singular and care has to be taken when trying to fit 1D stellar evolution models to observations. In this Chapter I studied non-rotating stellar models in order to investigate the effects of convective boundary mixing without blurring of rotation-driven mixing. In reality, both processes occur and influence each other (e.g. Brun et al., 2017; Korre et al., 2019) but it is still an open question how convection and rotation interact with each other - see also Chapter IV.

Gabriel et al. (2014) discuss the important issue of discontinuities at convective boundaries and how to choose the "right" convective boundary location in the framework of the mixing-length theory. They argue that the convective boundary is determined by either $\mathbf{F}_{\rm rad} = \mathbf{F}_{\rm tot}$, $v_{\rm conv} = 0$ or, following Biermann (1932), $\nabla_{\rm rad} = \nabla_{\rm ad}$, all taken on the convective side of the boundary. On the radiative side of the boundary, the condition $\nabla_{\rm rad} \leq \nabla_{\rm ad}$ must hold: (i) equality if there is no discontinuity in the chemical composition, since all other variables T, P, ρ, and L are continuous and (ii) inequality if there is a discontinuity of the chemical composition, resulting in the density and opacity to be discontinuous, which is generally the case. In many present-day stellar evolution codes, including `MESA` which was used for this work, the boundary location is determined as the position where the discriminant $y = \nabla_{\rm rad} - \nabla_{\rm ad}$ or $y = \nabla_{\rm rad} - \nabla_{\rm ad} + B$, respectively, changes sign - see Section B.1.3.2. Therefore, the codes include points in the radiative region to identify the convective boundary, contrary to the argument above. If y is continuous at the convective boundary interface, this method works as well. However, if discontinuities are present, this procedure can lead to an incorrect positioning of the boundary as shown by Gabriel et al. (2014). For both, the Ledoux and the Schwarzschild criterion, y

is discontinuous if the chemical composition profile is discontinuous. In addition, y is discontinuous if there is a μ-gradient in an adjacent layer of the boundary and the Ledoux criterion is used. Furthermore, in order to find the boundary location between cell k and $k+1$ the codes interpolate in order to find the exact location where y cancels. However, interpolation over an interval is mathematically not allowed, which may have important consequences on the positioning of the boundary (see Gabriel et al., 2014, for more details).

Similar issues arise in the calculations with no convective boundary mixing, especially with the *Ledoux* criterion. Convective boundary mixing removes possible discontinuities at the convective boundary. Therefore, the problem with a discontinuity in the chemical composition or its gradient at the convective boundary is reduced, depending on the degree of convective boundary mixing and amount of resolution at the boundary. In thin convective layers such as the *convective fingers* the problems still arise. However, these convective regions might be a relic of 1D stellar evolution and might not occur in reality - see discussion further down. Nevertheless, in most of the 1D stellar evolution codes the convective boundary is determined before convective boundary mixing is applied, as discussed in Section B.1.3. Hence, this problem is not solved but rather avoided in my models.

The *convective fingers* discussed in Section III.3 do not influence the simulation significantly, except if they are able to connect with the convective hydrogen core or if they persist until the intermediate convective zone appears. Especially the first event can lead to significant changes of, e.g., the helium core mass and hydrogen burning lifetime. I demonstrated that there is a limiting amount of convective boundary mixing above which no *convective fingers* appear. This limit, however, increases with increasing initial mass. On the other hand observations suggest, that the required amount of convective boundary mixing during the main-sequence evolution is above the $f_{\rm CBM}$ limits for *convective fingers*. Therefore, they might not occur at all. If they do occur, there are other issues, such as the high diffusion coefficient and convective velocity predicted by the mixing-length theory, which seem unrealistic for thin convective layers. Furthermore, if some sort of mixing above the convective hydrogen core takes place, its nature needs to be determined, i.e. whether it has a finger-like structure as found by, e.g., Langer et al. (1985) and discussed in my work or whether it is more a slow constant mixing as suggested by Schwarzschild & Härm (1958) and implemented in the MESA code (Paxton et al., 2019). Another possibility could be to limit the mixing efficiency in thin convective layers by the distance to the convective boundary, as shown in Section B.2.2. However, *convective fingers* might be a relic of 1D stellar evolution and finite timestepping, that introduce discontinuities at the location of the convective boundary of the retreating hydrogen core at a certain timestep. Moreover, 3D simulations cleary show that the convective boundary is dynamic and fluctuates (e.g. Cristini et al., 2017; Jones et al., 2017), which affects the chemical composition profile that is left behind the retreating hydrogen

core. Furthermore, 3D simulations clearly show that at the interface of the convective and radiative region internal gravity waves are generated, that propagate to the surface (Cristini et al., 2017; Edelmann et al., 2019). How much these waves mix the composition needs to be determined but they definitely affect the radiative region above the convective core.

Some of the convective helium cores in Fig. (III.12) show core breathing pulses (Castellani et al., 1985). There is evidence that these *core breathing pulses* might be of a theoretical or numerical nature (Constantino et al., 2016; Farmer et al., 2016). We note that the core breathing pulses that occur in some of our models always appear after the intermediate convective zone disappeared and the energy generation of the hydrogen shell drops (compare Figs. (III.8) and (III.10)). At this point the convective core experiences an increase in pressure and readjusts itself. This process, however, is dynamic and time dependent. The pulses of the convective core could therefore be a result of the 1D mixing prescription (e.g. Renzini & Fusi Pecci, 1988), hence, they could be the issue of idealised physics rather than a numerical problem. Moreover, we note that when the convective boundary mixing zone is large enough, this scenario does not occur, i.e. $f_{\rm CBM} \geq 0.022$ (Constantino et al. (2017) found a similar dependence and proposed an entrainment rate for the convective helium core). Therefore, it could be that *core breathing pulses* occur when the envelope to core ratio is above a critical value, where the envelope exerts enough pressure on the core once the hydrogen shell disappears to introduce contraction. On the other hand, if the ratio is below the critical value the envelope is not massive enough to introduce a contraction of the core after the disappearance of the hydrogen shell and no *core breathing pulses* occur.

A complete understanding of the blue versus red evolution after the main sequence is still missing. Several ideas have been suggested (e.g. Renzini et al., 1992; Sugimoto & Fujimoto, 2000; Stancliffe et al., 2009) but there is no general accepted solution. Nevertheless, it is known that the blue to red supergiant ratio depends strongly on internal mixing processes (e.g. Langer & Maeder, 1995; Georgy et al., 2014; Schootemeijer et al., 2019). There are two possible ways massive stars evolve into the blue supergiant region. Either they evolve from the main sequence to the blue supergiant region, type I, or they evolve directly from the main sequence to the red supergiant region and then back towards the blue region, type II. Ekström et al. (2012) find in their evolutionary grid that blue supergiant type II occurs in massive stars of about 20 $M_\odot$ or higher; this limit depends on the mass loss rates that are assumed during the red supergiant phase (e.g. Georgy, 2012). The two types of blue supergiants have a different mass, structure and surface abundances. Furthermore, their following evolution and supernova type will differ (e.g. Georgy et al., 2012; Yoon et al., 2012; Eldridge et al., 2013).

In Section III.4 I discussed that blue supergiants in my grid are either type I, with small and intermediate values of $f_{\rm CBM}$, or possibly type II, when large values of $f_{\rm CBM}$ are used, depending on the initial mass. This is due to the impact of the intermediate convective zone on the evolution of the star. The type I blue supergiant models move to the red supergiant region as soon as the intermediate convective zone disappears and the hydrogen shell weakens. Nonetheless, some models spend more than half, or nearly all, of their core helium burning phase as blue supergiants depending on the convective boundary criterion and the amount of convective boundary mixing (see Table III.1). The type II blue supergiant phase only occurs in the $25\,{\rm M}_{\odot}$ models with large amounts of convective boundary mixing and the star only spends a short fraction of core helium burning as this type. Nevertheless, this model becomes a Wolf-Rayet star at the end of core helium burning, which will change its further evolution and final fate. Moreover, we find that semiconvection with the efficiencies tested has no remarkable impact on the blue to red supergiant ratio. Recently, Schootemeijer et al. (2019) compared a grid of stellar models with varying amounts of internal mixing to observation of massive stars in the Small Magellanic Cloud and conclude that a medium amount of convective boundary mixing - they use the penetrative 'overshoot' with $0.22 \lesssim \alpha_{\rm ov} \lesssim 0.33$, and efficient semiconvection, $\alpha_{\rm sc} \gtrsim 1$ - is needed to match observations. Furthermore, they find that inefficient semiconvection, $\alpha_{\rm sc} \lesssim 1$, can be ruled out because not enough blue supergiants are created. I agree with Schootemeijer et al. (2019) that in general less convective boundary mixing favours blue supergiants but a straight comparison is not possible due to the different initial metallicity (at a lower initial metallicity, more blue supergiants are expected, e.g. Georgy et al., 2013). Nevertheless, I seem to contradict Schootemeijer et al. (2019) in my claim that the relative importance of semiconvective mixing decreases with increasing amount of convective boundary mixing. The simple explanation is the fact that Schootemeijer et al. (2019) only apply convective boundary mixing at the convective hydrogen core whereas I include it at all convective boundaries. This leads to a different behaviour of the intermediate convective zone, hence, red-ward evolution - see Sections III.4 and III.6. Furthermore, Schootemeijer et al. (2019) apply the penetrative convective boundary mixing scheme, "step-overshoot", which creates a discontinuity in the chemical composition at the boundary. I conclude that in my simulations a more efficient semiconvection of $\alpha_{\rm sc} > 1$ might only affect the outcome in the calculation with no or a small amount of convective boundary mixing.

Another important impact on possible blue loops is the amount of mass loss during the red supergiant phase, especially at solar metallicity. This might strip the star of its envelope and move it back to the blue supergiant region. Indeed, if I enhance the mass loss rates due to dust formation during the red supergiant phase following the prescription of van Loon et al. (2005), the models with a fast red-ward evolution go back into the blue region. The models that stay in the blue region right after the main sequence do not experience enough mass loss once they enter the red supergiant phase to do a blue

loop. However, the mass loss rates during the red supergiant branch are very uncertain and it is not sure which mass loss prescription is the correct one, if any. Saio et al. (2013) suggest to distinguish between the two blue supergiant types with radial pulsations (e.g. Bowman et al., 2019) in addition to the CNO surface enrichment, i.e. blue supergiants type II exhibit radial pulsations. Observed number ratios of blue supergiant type I or II to red supergiant would help to constrain the internal mixing process of, e.g., the intermediate convective zone, the boundary criterion (e.g. Georgy et al., 2021) and the mass-loss rates.

Vink et al. (2010) find a steep drop in the rotation rates of B supergiants and propose two possible explanations for their nature. I want to discuss the possibility that this could be a consequence of the intermediate convective zone. As discussed in Section III.6, if a massive star has a strong intermediate convective zone it can spend $75-90\%$ of its helium burning phase as a blue supergiant right after the main sequence. On the other hand, rotation tends to smooth the structure above the convective hydrogen core, which reduces the intermediate convective zone and leads to a faster red-ward evolution (Maeder & Meynet, 2001, and Chapter IV). Thus, it is much less probable for these stars to be observed during the crossing to the red supergiant branch. Therefore, the observed blue supergiants after the main sequence are most probably the ones with a strong intermediate convective zone, hence, no or a slow rotation. If this is indeed the case, such observations could be used to constrain the mixing of the intermediate convective zone.

Smartt et al. (2009) found a lack of supernovae originating from red supergiants above $\sim 17\,M_\odot$ in contrast to theoretical predictions, which they labelled as "*red supergiant problem*" - see Section I.3.1 for more details. Recently, Dorn-Wallenstein et al. (2020) found pulsating yellow supergiants which they identify as post red supergiant stars and they estimate their mass to be in the "*problematic*" region. This indicates that the "*missing red supergiants*" above $\sim 17\,M_\odot$ are indeed missing because these stars evolved away from the red supergiant branch and that the traditional theoretical predicted fate of stars in this mass range could be wrong. In fact, the post-main-sequence evolution of massive stars is blurred by many uncertainties and parametrisations. Therefore, the details of such an evolutionary scenario is still unclear. Some authors argue that pre-supernova outbursts shortly before the collapse could be responsible (Fuller, 2017; Leung & Fuller, 2020). An other solution could be binarity. The more massive stars expand to larger radii during the red supergiant phase, hence, they are able to fill the Roche lobe more easily and will lose more mass via mass transfer. The stripped star will evolve away from the red supergiant phase, becoming a blue or yellow supergiant or a Wolf-Rayet star. Also, the red supergiant mass-loss rates are a major uncertainty in stellar evolution calculations, see discussion in Section I.2.2. Depending on the mass-loss rates, massive stars above $\sim 20\,M_\odot$ can lose enough mass to evolve back to the blueor yellow supergiant branch or even become Wolf-Rayet stars. Here, I want to point out that a proper treatment of the convective boundary could play a crucial role

Table III.2: The absolute and relative variation of the total mass, M_{tot}, the helium core mass, M_α, and the carbon-oxygen core mass, M_{CO}. The individual values of each model are shown in Table III.1. The values include Ledoux and Schwarzschild models.

	$\Delta M_{tot}/M_\odot$	δM_{tot}	$\Delta M_\alpha/M_\odot$	δM_α	$\Delta M_{CO}/M_\odot$	δM_{CO}
$15\,M_\odot$	3.38 (3.45)	27.72% (27.80%)	2.30 (2.74)	43.07% (51.31%)	2.40 (3.94)	69.77% (114.53%)
$20\,M_\odot$	8.60	74.35%	2.94	36.70%	2.94	51.49%
$30\,M_\odot$	9.02	65.84%	3.96	40.08%	4.1	55.48%

Notes: The variation for a quantity Q is calculated as

$$\delta Q = \frac{\Delta Q}{Q_{ref}} \equiv \frac{Q_{max} - Q_{min}}{Q_{ref}} \times 100, \tag{III.1}$$

where Q_{max} and Q_{min} are the maximal and minimal value of the quantity for the initial mass and Q_{ref} the value of the reference model (see text).

* The blue values in brackets include the models with no convective boundary mixing.

Table III.3: The absolute and relative variation of the main-sequence lifetime, τ_H, the core helium burning lifetime, τ_{He} and the blue supergiant lifetime, τ_{BSG}. The individual values of each model are shown in Tables III.1. The values include both, the Ledoux and Schwarzschild models.

	$\Delta\tau_H$/Myrs	$\delta\tau_H$	$\Delta\tau_{He}$/Myrs	$\delta\tau_{He}$	$\Delta\tau_{BSG}$/Myrs	$\delta\tau_{BSG}$
$15\,M_\odot$	3.35 (4.13)	24.38% (30.06%)	0.69 (0.69)	73.40% (73.40%)	1.16 (1.16)	5800.0% (5800.0%)
$20\,M_\odot$	1.88	19.87%	0.36	50.00%	0.88	4400.0%
$25\,M_\odot$	1.25	16.82%	0.25	40.98%	0.54	2702.5%

Notes: See Table III.2 for the calculation of ΔQ and δQ.

* The blue values in brackets include the models with no CBM.

in particular due to the impact of the intermediate convective zone. Fig.(III.15) illustrates that all the 15 $M_\odot$ models are red supergiants at the end of core helium burning, however, the 25 $M_\odot$ models with large f_{CBM} naturally evolve away from the red supergiant branch at the end of core helium burning, becoming blue supergiants or Wolf-Rayet stars (see also Table III.1). Therefore, the inclusion of convective boundary mixing might partly help to solve the "*red supergiant problem*". It is important to note, that I do not claim that the red supergiants become yellow supergiants, or any other star type, but that the prediction of traditional stellar evolution models are blurred by the uncertainties of stellar evolution. Consequently, the model predict a fate that is not observed. However, considering the uncertainties, it is possible that massive stars above $\sim 17\,M_\odot$ evolve away from the red supergiant branch, towards the blue or yellow supergiant phase or the Wolf-Rayet phase. The details of this evolutionary scenario and its fate depends on many input physics and their uncertainties and needs further investigation.

For simplicity, I use the same f_{CBM} at all convective boundaries in all evolutionary stages, core and shell convective zones and all initial masses in my simulations. However, the amount of convective boundary mixing depends on the stiffness of the boundary (e.g. bulk Richardson number, Cristini et al., 2019) and different f_{CBM}-values might be needed for different stellar stages, resulting in different evolutionary paths. It is an ongoing effort to create a convective boundary mixing prescription which depends on the physics of the boundary rather than the parametrisation (e.g. Pratt et al., 2017; Arnett et al., 2018, 2019).

In Section III.2 I mentioned the use of `MESA`s `MLT++` in models that experience envelope inflation. Only models with large amounts of convective boundary mixing experience density and gas-pressure inversions in their outer layers. Recent efforts to constrain internal mixing in massive stars with observations (e.g. Brott et al., 2011; Castro et al., 2014; Schootemeijer et al., 2019; Higgins & Vink, 2019) indicate that stars in the mass range studied here have larger amounts of convective boundary mixing than often assumed in "*traditional state-of-the-art*" stellar evolution models. Therefore, models in the mass range 15-25 $M_\odot$ might experience inflated envelopes. However, the stability and treatment of such radiation-dominated envelopes is still an open question (e.g. Joss et al., 1973; Maeder, 1987b; Langer, 1997; Bisnovatyi-Kogan & Dorodnitsyn, 1999; Maeder, 2009; Suárez-Madrigal et al., 2013)

8 Conclusions

I calculated two grids of stellar models, one with the *Ledoux* and the other one with the *Schwarzschild* convective boundary criterion, for three initial masses 15, 20 and 25 $M_\odot$, in order to investigate

the impact of some convective boundary mixing uncertainties. In each grid I varied the amount of convective boundary mixing between $(0.004, 0.01, 0.022, 0.035, 0.05)$ and, in the *Ledoux* case, the semiconvective efficiency. In Sections III.3, III.4 and III.5 I presented the impact of the uncertainties on the stellar structure. The key findings are the following:

1. During the main-sequence evolution the difference of the convective core size due to the two convective stability criteria converges in all models when convective boundary mixing is included. Furthermore, the region above the core converges with more convective boundary mixing. I find that the minimum amount of convective boundary mixing, above which no *convective fingers* are present increases with initial mass. This indicates that *convective fingers* might be a relic of 1D stellar evolution since observations suggest larger amounts of convective boundary mixing during the main-sequence evolution in massive stars.

2. The width of the main sequence broadens significantly with increasing amount of convective boundary mixing and with the largest f_{CBM} values the terminal-age main sequence bends to cooler effective temperatures with increasing initial mass, which is more in agreement with recent observations (e.g. Castro et al., 2014; McEvoy et al., 2015). The width of the main sequence is nearly independent of the convective boundary criterion and semiconvective efficiency.

3. The initial location of the intermediate convective zone strongly depends on the stability criterion, regardless of the amount of convective boundary mixing. When using the *Schwarzschild* criterion there is an overlap with the hydrogen burning shell, whereas there is no overlap when using the *Ledoux* criterion. The further evolution of the intermediate convective zone is largely determined by the amount of convective boundary mixing. More mixing shortens the lifetime of the intermediate convective zone and leads to an overlap with the hydrogen burning shell in the Ledoux models. An overlap between the two boosts the latter, leading to crucial differences in the further central and surface evolution of the model.

4. The relative importance of semiconvection drastically decreases with an increasing amount of convective boundary mixing.

5. Generally, more convective boundary mixing leads to larger core masses and longer lifetimes. The larger convective hydrogen cores are supported by asteroseismic observations of eclipsing binaries (e.g. Tkachenko et al., 2020). Models with large amounts of convective boundary mixing behave more like models of a higher initial mass but less convective boundary mixing in terms of core masses, core helium burning lifetimes and nucleosynthesis. This would lead to a different further evolution, supernova progenitor structure and explodability than currently presented in the literature.

In Section III.5.2, I showed the impact of the convective boundary mixing uncertainties on the nucleosynthesis during central helium burning. In the $15\,M_\odot$ models the ^{12}C to ^{16}O ratio decreases as f_{CBM} increases due to the larger amount of fuel available during the late stage of this burning phase. The ^{12}C to ^{16}O ratio is naturally saturated in the models with higher initial masses due to the activation of other particle capture reactions. Furthermore, I find an increase of the weak s-process activity in the simulations with larger amounts of convective boundary mixing. This might affect the peak production of the weak s-process and will be subject of further studies.

In Section III.6 the impact of the intermediate convective zone on the surface evolution of the star was discussed. The simulations that predict a strong intermediate convective zone remain in the blue supergiant region until the convective shell recedes, whereas models with a short intermediate convective region evolve directly to the red supergiant branch. As a result, some models spend nearly their whole core helium burning lifetime as blue supergiants, depending on the strength of the intermediate convective zone. On the other hand, some of the more massive models very quickly enter the red supergiant phase after the main sequence and become blue supergiants, and later on Wolf-Rayet stars, at the end of core helium burning due to strong mass-loss. This not only affects the blue to red supergiant ratio but also the total mass at core helium depletion, the further evolution, the pre-supernova structure and explodability of these models.

In Tables III.2 and III.3 the absolute and relative variations of the total mass, the core masses and the stellar life times are presented to show which part of stellar evolution is mostly affected by the uncertainties of convective boundary mixing. The most affected values are the blue supergiant lifetimes and, correlated, the mass loss rates. The importance of the latter increases with initial mass. The core masses show an uncertainty of $\sim 40\%$ for the helium core mass and $\sim 50-70\%$ for the carbon-oxygen core mass. The lifetimes show a relative variation of $\sim 15-25\%$ for the hydrogen burning phase and $\sim 40-70\%$ for the helium burning lifetime. The biggest uncertainty for all phases comes from the amount of convective boundary mixing. The choice of the boundary criterion, either *Ledoux* or *Schwarzschild*, mainly influences the intermediate convective zone, by determining its initial location, and the growth of the convective helium core. The convective cores, however, grow to similar maximal sizes and the difference introduced by the boundary criterion is small. Therefore, the choice of the boundary criterion has nearly no impact on the main-sequence evolution but it crucially affects the surface evolution.

This work shows the need to improve the treatment of convective boundaries in 1D stellar evolution codes in order to have more reliable predictions of the evolution of massive stars. The intermediate convective zone, for example, should be investigated in multi-dimensional simulations to constrain the amount of mixing at the convective boundary and to test the two boundary criteria. Furthermore, observations of the ratio of the two blue supergiant types (i.e. a blue supergiant right after the main

sequence or after the red supergiant phase, e.g. Saio et al., 2013) and red supergiants would help to constrain the internal mixing processes and the boundary criterion. Also, asteroseismic observations may help in constraining the amount of extra mixing at the convective boundary (see e.g. Fig.(III.7b)). However, constraining the amount of mixing is only a first step. In order to have more reliable predictions ultimately a non-parametrised but physical theory is sought, which is work in progress by many teams.

Chapter IV

The Uncertainty in Angular Momentum Transport

Transport of angular momentum is one of the big open questions of stellar evolution theory. Current stellar models fail to predict the rotation rates of the compact objects left at the end of a star's evolution and to reproduce the observed internal rotation profile of stars. New theoretical prescriptions for the missing angular momentum transport are suggested, however, none is accepted as the general solution to the problem. Recently, Fuller et al. (2019) published a modification to the Tayler-Spruit magnetic dynamo, claiming that it largely reproduces observations but there is some controversy. In this Chapter, I present `MESA` stellar evolution models, using three different angular momentum transport mechanisms, transport by hydrodynamic instabilities, the Tayler-Spruit dynamo and the Fuller-modified version thereof. In these models, I study the differences in angular momentum transport and changes in the evolution of rotation. Additionally, I investigate several uncertainties in the implementation of the magnetic dynamos. I find the three transport processes predict distinct ranges of core rotation at the end of their evolution, mostly independent of the uncertainties investigated. However, the evolution of rotation and the angular momentum distribution vary, depending on the transport mechanism and the uncertainty. This not only implies different rotation rates at a certain stage of the star's life, influenced by the numerical choices, but also affects the structure of the star and its subsequent evolutionary path, nucleosynthesis and timescales, which will be discussed in future work.

1 Introduction

Rotation is often considered as a secondary process of stellar evolution. However, rotation is present throughout the entire evolution of a star, influencing the evolutionary path, the timescales and the nucleosynthesis. Rotation-induced instabilities drive internal mixing processes that mix the chemical composition and rotation can enhance the mass-loss rates - see Sections I.4 and II.2. The internal transport processes also allow for a redistribution of angular momentum in the star. Thus, the rotational velocities of a star evolve over time. Recent work (Marigo et al., 2001; Meynet & Maeder, 2002; Hirschi, 2007; Ekström et al., 2008; Frischknecht et al., 2016; Chieffi & Limongi, 2020; Rizzuti et al., 2021) even suggest that at low metallicity rotation plays a dominant role in the evolution and nucleosynthesis. Therefore, the rotational effects are a crucial ingredient to model the life of a star and enable to explain observations - see Section I.4.

Rotating liquid bodies at constant density have been studied for a long time, starting with the works by McLaurin, Jacobi, Poincaré and K. Schwarzschild. Kippenhahn & Thomas (1970) presented a method to numerically treat rotation in stellar evolution models which was simulated in a simple model for angular momentum transport by Kippenhahn et al. (1970). In their pioneering work, Endal & Sofia (1978) include several rotation-induced instabilities in their simulations of rotating stars. They derived *order-of-magnitude* estimates for the diffusive efficiency of the rotational mixing processes and carried out time-dependent stellar evolution calculations. Pinsonneault et al. (1989) introduced the parametrisation discussed in Section B.1.4 for a more accurate estimate of the rotational mixing efficiencies and constrained the parameters to solar models. Chaboyer & Zahn (1992); Zahn (1992) showed, while the rotation-induced mixing of matter can be treated as a diffusive process the angular momentum transport by the large scale meridional flows has to be simulated as an advective process. This led to a split in the treatment of angular momentum transport in stellar evolution codes, those that treat angular momentum transport as a purely diffusive process (e.g. Heger et al., 2000; Petrovic et al., 2005; Paxton et al., 2013) and those that compute transport of angular momentum with an advective-diffusive scheme (e.g. Ekström et al., 2012; Potter et al., 2012a; Chieffi & Limongi, 2013).

Stellar models that transport angular momentum by hydrodynamic instabilities only are known to predict faster core rotation rates of white dwarfs, neutron stars and black holes than observed (Heger et al., 2000; Suijs et al., 2008; Eggenberger et al., 2012; Mosser et al., 2012; Cantiello et al., 2014), implying that an additional mechanism, or several mechanisms, operate. Possible candidates are a magnetic dynamo, where magnetic field lines generated by the dynamo action create a torque between differentially rotating layers and slow it down - see Section II.3 - or gravity waves (Talon & Charbonnel, 2005; Belyaev et al., 2013; Fuller et al., 2015b; Edelmann et al., 2019). The true nature of the missing transport mechanism is still under debate and in the following I will focus on magnetic

dynamos.

A magnetic dynamo action in the convective regions of a star is likely to exist (Parker, 1979; Charbonneau & MacGregor, 2001; Brun et al., 2005), however, it is currently not clear if these generated fields can reach the surface and how deep they penetrate the radiative region. Since the turbulent flow in the convective regions transports angular momentum very effectively, an additional magnetic dynamo would have little influence on the angular momentum distribution. Spruit (1999, 2002) showed that, in a differentially rotating star, a magnetic dynamo can be active in the radiative regions of the star, depending on the gradient of the rotation rate. The torque created by this Tayler-Spruit dynamo can effectively reduce the differential rotation between layers, leading to near-solid body rotation. However, the existence of the Tayler-Spruit dynamo is strongly debated - see discussion in Section II.3.2. Moreover, while the Tayler-Spruit dynamo allows to reduce the angular momentum of the cores, it fails to predict the observed rotation rates of white dwarfs, neutron stars and black holes (Heger et al., 2005; Suijs et al., 2008). Alternative magnetic dynamos based on other magnetic instabilities have been proposed, such as the magnetorotational instability (Velikhov, 1959; Wheeler et al., 2015), the α-Ω dynamo (e.g. Brandenburg, 2001; Potter et al., 2012c) or other theoretical prescriptions for dynamos in magnetic rotating stars (e.g. Fuller et al., 2019; Takahashi & Langer, 2020). The incoherency of the different angular transport mechanisms leads to a uncertain prediction of the evolution of rotation and consequently the structure and evolutionary path of rotating stars. On top of the various magnetic dynamos, each dynamo is differently implemented in the stellar evolution codes and includes different numerical aides such as smoothing, dependence on chemical stratification and free parameters. Consequently, angular momentum transport in stars is subject to large uncertainties and prediction of rotating stars, for example the core rotation rate of massive stars at the pre-supernova stage, are highly unreliable.

In this Chapter, I present a grid of stellar evolution models of massive stars using different flavours of angular momentum transport, in order to investigate the difference between the transport mechanisms and asses the uncertainty on the evolution of rotation. In particular, I compare models with no magnetic fields, with the Tayler-Spruit dynamo of Spruit (2002) and with the Fuller-modified Tayler-Spruit dynamo of Fuller et al. (2019). Moreover, I study the influence of spatial and temporal smoothing processes, the dependence of the angular momentum transport on the inhibiting effect of chemical stratification, a possible interaction between the shear created by the turbulent motion at the convective boundary and the magnetic dynamo and the dependence of angular momentum transport on the metallicity and the initial rotation rate. In the current Chapter, I focus the discussion mainly on the aspect of angular momentum transport and how the rotation rate evolves over time. The impact on the structure, evolution and fate of the rotating stars will be discussed in future work.

2 Stellar Models - Physical Ingredients

In order to study the uncertainty introduced by the transport of angular momentum in models of massive stars, I computed a set of rotating stellar models with initial masses of 15, 25, 30 and 60 $M_\odot$. The simulations were carried out using the `MESA` stellar evolution code (Paxton et al., 2011, 2013, 2015, 2018), revision 10108 - see also Appendix B. The set up of the models is similar to Chapter III. Here, I only discuss the different physics used and refer the reader to Section III.2 for a complete overview of the modelling ingredients.

The thermonuclear reactions were accounted for with `MESA`'s `approx21` network. This is a 21 isotope reaction network, which is capable of efficiently generating reasonably accurate nuclear energy generation rates from hydrogen through silicon burning. It incorporates an "*electron-dump*" isotope from the iron group with the task to fake the electron captures that occur during the late phases of the evolution. It includes pp-I reactions (the simplest pp-chain reaction - see Section I.2.1.1) and steady-state CNO-cycles for hydrogen burning, standard α-chains, heavy ion-reactions, aspects of photodisintegration into ^{54}Fe and neutron-proton conversion (Paxton et al., 2011). The `approx21` reaction network reduces the computational cost immensely and allows to compute models on a faster timescale, however, some key quantities are subject to uncertainty due to the small network (Farmer et al., 2016).

The same physics for mass loss by stellar winds was used as in Section III.2, but the wind scaling factor, $\eta_{\rm wind}$, is set to 1.0 contrary to $\eta_{\rm wind} = 0.85$ used in Chapter III. Maeder & Meynet (2001) introduced this reduction factor to scale empirical mass-loss rates to observations (see their Section 2.2 for details). Theoretical mass-loss rates such as the one from Vink et al. (2000, 2001), however, do not need to be scaled to observations, justifying $\eta_{\rm wind} = 1.0$. This wind-scaling parameter is multiplied to all the mass-loss recipes in the `MESA`'s `Dutch` scheme, including the empirical mass-loss rates by de Jager et al. (1988) - see Section B.1.6. However, the latter is subject to large uncertainties, which reduces the relative impact of the different scaling factor. This is a point to improve in the future.

Contrarily to the models in Chapter III, the treatment of `MLT++` is used in all the models to deal with density and pressure inversions in the envelope.

I modelled convection using the *Henyey* flavour (Henyey et al., 1965) of the mixing-length theory (Vitense, 1953; Böhm-Vitense, 1958) - see Section B.1.3.1. The mixing-length $\ell_{\rm MLT}$ was set to $1.67\,H_P$, in accordance with Arnett et al. (2018). The convective boundary was determined with the *Schwarzschild* criterion for stability, which is justified by 3D hydrodynamic simulations (Arnett et al., 2019). Convective boundary mixing was accounted for with the exponential decaying diffusive model of Freytag et al. (1996) - see Section B.1.3.2 for more details. I further modified the diffusion coefficient and convective velocity following Jones et al. (2017) to mimic the spherically averaged

radial diffusion and velocity profiles from their 3D simulations. The implementation of this scheme is outlined in Section B.2.2. Jones et al. (2017) suggest to use $f_{\rm CBM} = f_0 = 0.03$, based on the results from their oxygen shell simulation. In this Chapter, however, I use $f_{\rm CBM} = f_0 = 0.05$ for all models. A larger $f_{\rm CBM}$ is supported for 15 to 25 $\rm M_\odot$ by the main-sequence width which increases with mass (see for example Fig.(III.7a)) and the size convective boundary mixing region predicted by the entrainment law during the main sequence (Scott et al., 2021). This value for the parameter is derived from non-rotating models and rotating models might have a smaller value of ~ 0.04 (J. Klencki, priv.comm.), however, it is still an open question. Furthermore, higher mass models might predict a different amount of convective boundary mixing, which is another open question. Therefore, the value of 0.05 was chosen for all models for comparison reasons.

The models are computed until the pre-supernova stage, defined as the point when the infall velocity reaches $v_{\rm infall} = 10^8\,\rm cm\,s^{-1}$ in any zone. The radial velocity flag is activated when the electron mass fraction, Y_e, drops below 0.47, which is shortly after core silicon depletion or right before it. Before this point, the radial velocity is always zero.

Rotation is initiated once the star approaches the zero-age main sequence, determined by $\frac{\rm L_{nuc}}{\rm L_{tot}} = 0.99$. This avoids problems with the convergence during the pre-main-sequence contraction. At this point, the angular rotation velocity, Ω, is set to 0.4 of the critical angular rotation velocity, $\Omega_{\rm crit} = \sqrt{\frac{GM}{R^2}}$. The rotation velocity is adjusted to the desired velocity over timesteps via a relaxation method. As part of the relaxation method the nuclear burning is ignored, i.e. the thermonuclear evolution is frozen. This allows the model to fully adjust to the imposed rotation before it resumes with its evolution.

In all models I included the Eddington-Sweet circulation and the secular shear instabilities and their respective scaling factors in Eq.(B.40) are all set to unity. The other rotation-induced hydrodynamical instabilities are excluded for the reasons outlined in Section B.1.4. The factor f_c, which is multiplied to the sum of the diffusion coefficient of all rotation-induced instabilities, is set to 0.0228 following the calibration of Brott et al. (2011). The *default* models apply $f_\mu = 0.1$, according to Yoon et al. (2006), in order to reduce the inhibiting effect on mixing by the chemical stratification - see also Section B.1.4. In Section IV.3.5, different values for f_μ in the range of $[0.0, 0.0001, 0.001, 0.01, 0.1]$ are discussed, in order to investigate the impact of the chemical stratification on angular momentum transport. In all models, the convective zones are treated as layers with solid body rotation.

The smoothing schemes for rotational mixing is outlined in Appendix B.1.5.1.1. In the *default* models, only the diffusion coefficient and the turbulent viscosity generated by the Tayler-Spruit dynamo is spatially smoothed, including two neighbouring cells on each side. Temporal smoothing in the *default* models is also only applied to the Tayler-Spruit dynamo, using $f_r = 0.001$ and $f_t = 0.2$. The *default* implementation of the Fuller-modified Tayler-Spruit dynamo is explained in Section B.2.1.

I used the same resolution, at which my models seem to converge, in all simulations. The settings are chosen to properly resolve gradients, focussing around convective boundary and nuclear burning regions, and appropriate timestepping, especially during the advanced stellar evolution. The details can be found in the inlist in Appendix B.3.

In order to investigate the uncertainty in angular momentum transport, I computed three *default* models for each initial mass, (i) one without magnetic fields, (ii) one with the Tayler-Spruit dynamo and (iii) one with the Fuller-modified Tayler-Spruit dynamo. Additionally, I computed models that investigate (iv) different amounts of smoothing, (v) a reduced inhibiting effects of the chemical stratification on the rotational mixing, (vi) the interaction between the magnetic field and the convective boundary mixing, (vii) the change of angular momentum transport at lower metallicity and (viii) the impact of the initial rotation rate.

3 Angular Momentum Transport with Different Mechanisms

3.1 $15\,M_\odot$ models

Fig.(IV.2) presents the rotation profile of the $15\,M_\odot$ models at various stellar stages using the three different angular momentum transport mechanisms; only hydrodynamic and no magnetic fields, the Tayler-Spruit dynamo and the Fuller-modified Tayler-Spruit dynamo. All three models begin with the same rotation rate, $\frac{\Omega}{\Omega_{\rm crit}} = 0.4$, however, the evolution of the rotation rate depends strongly on the angular momentum transport mechanism.

The rotation profile of the model where angular momentum is only transported by hydrodynamical instabilities is shown in Fig.(IV.2a). The angular rotation velocity, Ω, which is assumed to be constant throughout the star at the zero-age main sequence, increases in the central region of the star during its evolution whereas it decreases in the envelope. On the other hand, the specific angular momentum is roughly similar in the core with a modest decrease as evolution proceeds and a slightly larger reduction in the envelope. This is a result from the inefficient angular momentum transport of the hydrodynamical instabilities discussed in Section II.2. Therefore, most of the angular momentum present at the zero-age main sequence remains in the core, which spins up when the star contracts during the subsequent evolution due to angular momentum conservation. This results in a fast spinning core. Similarly, the expanding envelope spins down. The location of the split between contraction and expansion is related to the hydrogen burning shell, i.e. the mirror-principle - see discussion in Chapter

III. The step-like features in Ω and the spikes in j, which are more present during the advanced stellar evolution phases, result from the occurrence of convective zones. The turbulent convective motion is very efficient at transporting angular momentum. Therefore, in this Chapter convective zones are assumed to rotate as solid bodies (this is an assumption often made in stellar evolution models). Hence, the Ω profile is flat and $j = r^2\Omega$ increases outwards in the convective zone. At the bottom boundary location there is a drop in both profiles due to the efficient transport of angular momentum in the convectively mixed regions. Also, it is apparent that stellar winds, even though relatively weak in these models, remove mass and angular momentum from the surface of the star.

Fig.(IV.2b) displays the $15\,M_\odot$ model with the Tayler-Spruit dynamo, as discussed in Sections II.3.1.2 and B.1.5.1. The dynamo action couples the differentially rotating layers if the shear exceeds a minimal shear, Eq.(II.52). This introduces angular momentum transport that can efficiently extract angular momentum from the core. Indeed, the rotation rate of the core at silicon depletion in Fig.(IV.2b) is about two orders of magnitude slower compared to the non-magnetic model in Fig.(IV.2a). Comparing the angular momentum transport during the main-sequence evolution, i.e. the difference between the black solid and the orange dashed curves, reveals that no angular momentum is transported out of the core. The envelope, on the other hand, shows a flatter Ω profile in the magnetic model due to the coupling of the differentially rotating layers. This is also apparent in the j profile where there is a drop in the specific angular momentum at the bottom of the envelope. The absence of angular momentum transport, followed by an abrupt drop which indicates transport to occur is a consequence of the fact that the magnetic dynamo is ignored in the convective boundary mixing region - see Section B.1.5.1. This introduces a bottleneck for the transport of angular momentum during the main sequence. During the post-main-sequence evolution, i.e. between the orange dashed and the cyan solid line, the evolution of rotation in the envelope is similar in both, the magnetic and the non-magnetic case. The reason is the dominating effect of the envelope expansion which results in a decrease of Ω. Furthermore, the dominant redistribution of angular momentum in both models occurs from the surface convective zone that appears shortly before core helium ignition, indicated by the very flat Ω profile and the dip in the j profile around $\sim 6\,M_\odot$. The magnetic dynamo is active in the envelope of the Tayler-Spruit model but its impact is overshadowed by the other two processes. In the core, however, a drastic difference between the two models occurs. The rotation rate in the whole core of the magnetic model is reduced, despite the post-main-sequence contraction. At the same time, the specific angular momentum in this region is strongly reduced, signalling an efficient transport of angular momentum from the core to the envelope, which is due to the magnetic coupling. Nevertheless, the coupling is not strong enough to sustain solid body rotation and a difference in Ω of several orders of magnitude between the core and the envelope develops. During the subsequent evolutionary phases, some angular momentum is removed from the core, visualised by the reduction of

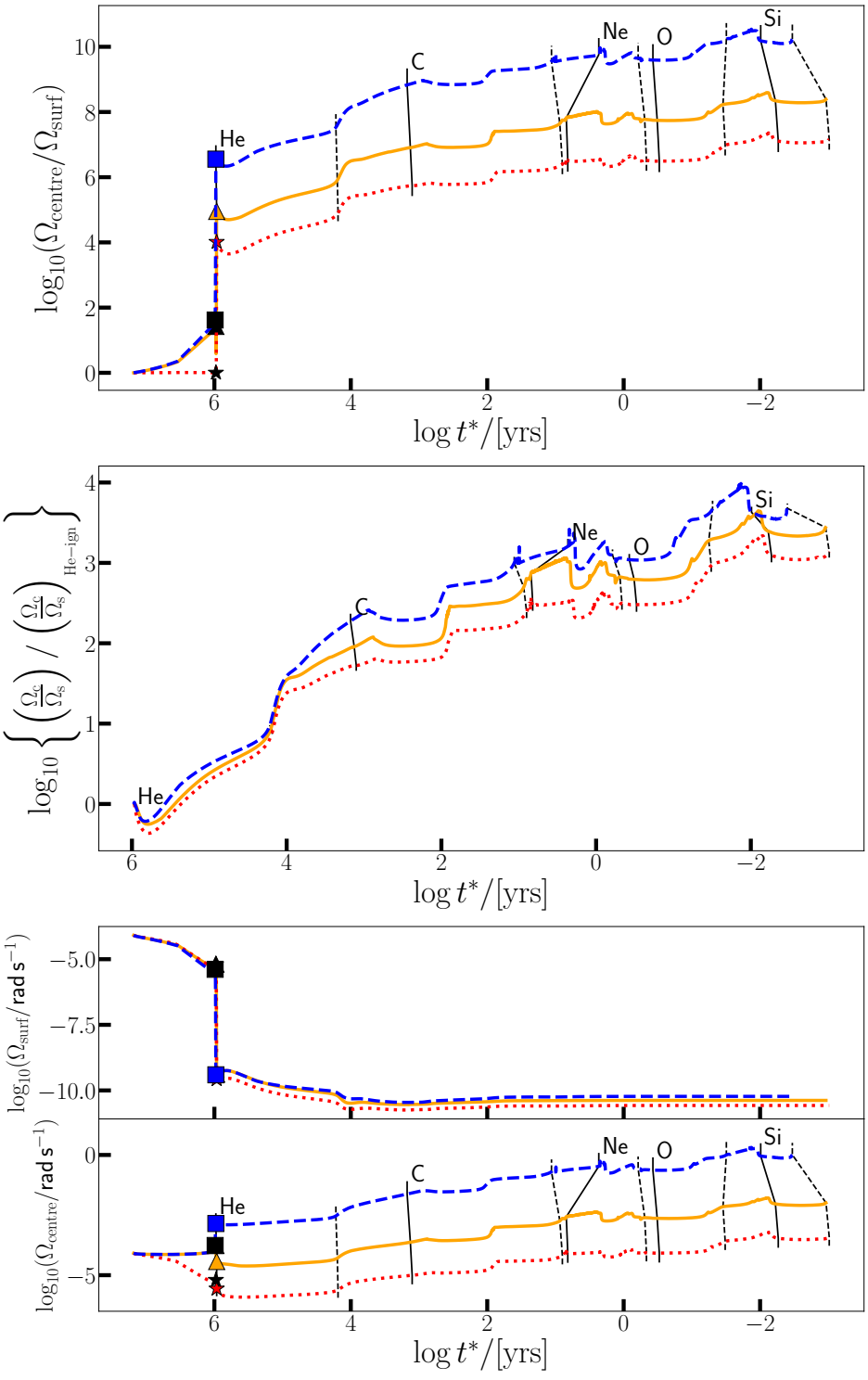

Figure IV.1: The evolution of the angular rotation velocity in the 15 $M_\odot$ models with the default angular momentum transport mechanisms, non-magnetic (blue dashed line), Tayler-Spruit dynamo (orange solid line) and Fuller-modified Tayler-Spruit dynamo (red dotted line), as a function of the time left until core collapse. The *top panel* shows the evolution of the ratio of the rotation rate in the centre to the one at the surface from the zero-age main sequence up to silicon depletion. The *middle panel* presents the same as in the top panel but limited between core helium ignition and silicon depletion and the curves have been normalised to the values at core helium ignition. The *bottom panel* plots the central and surface rotation rate separately. The ignition of the various burning stages are indicated by a solid, labelled line and the depletion is marked by a consecutive dashed line. Helium ignition is pointed out by a marker, with a blue square representing the non-magnetic, an orange triangle the Tayler-Spruit dynamo and a red star the Fuller-modified Tayler-Spruit model, respectively. Hydrogen depletion is designated with the same marker shape but black color.

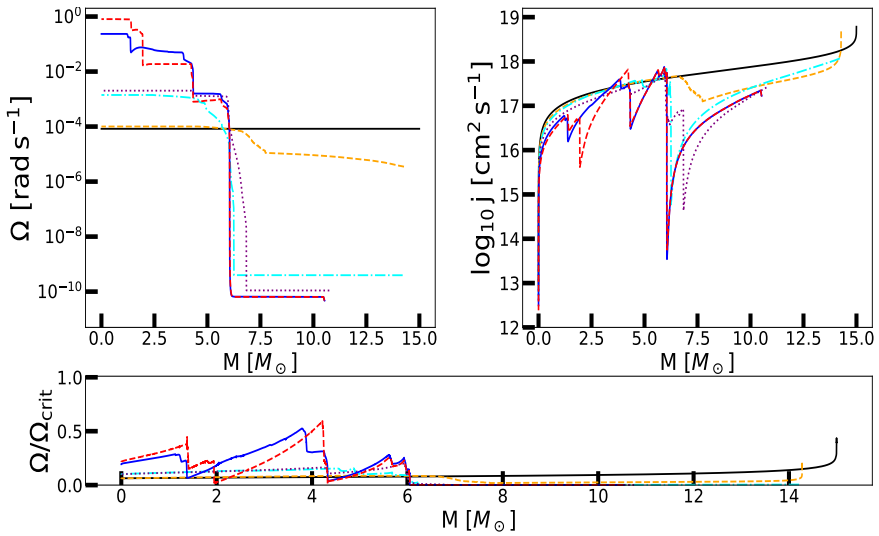

(a) no magnetic fields

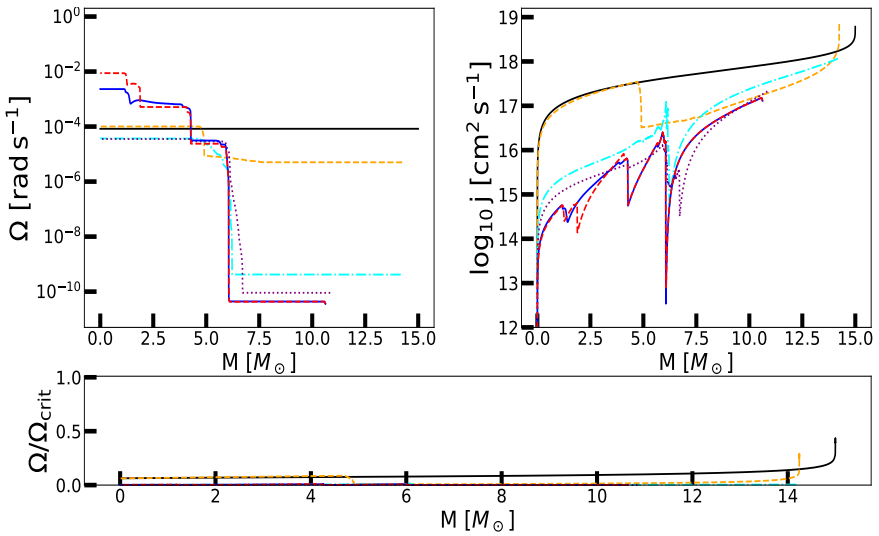

(b) Taylor-Spruit dynamo

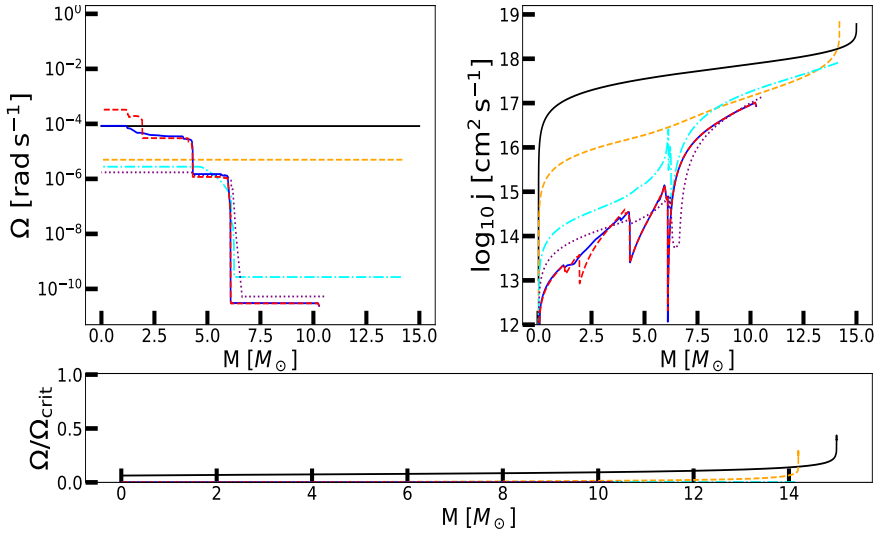

(c) Fuller-modified Taylor-Spruit dynamo

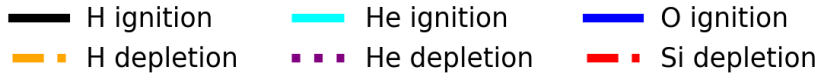

Figure IV.2: The rotation profile of the 15 $M_\odot$ models for the different angular momentum transport mechanisms, showing on the top left panel the angular rotation velocity, Ω, on the top right panel the specific angular momentum, j, and on the bottom panel the ratio of the angular rotation velocity to the critical angular rotation velocity. Each line presents the profile at a different evolutionary stage indicated by the colour and linestyle. To enable a better comparison, the axis of each thematic subplot group has been scaled to the same values. The ignition of a burning phase is defined as when 0.3% of the mass fraction of the fuel is burnt and depletion when the fuel drops below 1%. The latter is early enough to avoid a spinning up of the core due to contraction after the burning phase ends.

j, however, Ω increases due to contraction of the core. The latter dominates the evolution of rotation during the advanced stellar stages because of the shorter evolutionary timescale. At the same time, Ω decreases in the envelope because of expansion and a small portion of angular momentum is lost through stellar winds. Therefore, the phase between core hydrogen depletion and helium ignition is key in slowing down the spinning core with the Tayler-Spruit dynamo.

Fig.(IV.2c) shows the $15\,M_{\odot}$ model with the Fuller-modified Tayler Spruit dynamo, discussed in Sections II.3.1.3 and B.2.1. This version of the magnetic dynamo operates on a shorter timescale and has a higher saturation level, creating a stronger magnetic torque. Therefore, the model including the Fuller-modified Tayler-Spruit dynamo experiences an efficient spin down of its core. This can be seen in Fig.(IV.2c), where the core rotation rate at silicon depletion is about two orders of magnitude slower than the one predicted by the Tayler-Spruit dynamo. Comparing Figs.(IV.2b) and (IV.2c) it can be seen that the evolution of angular momentum during the post-main-sequence evolution is similar with a slightly higher angular momentum transport in the core during the advanced phases in the model with the Fuller-modified dynamo. However, during the main sequence the Fuller-modified dynamo is able to maintain a solid body rotation and j drops significantly throughout the star, indicating a strong transport of angular momentum from the core to the envelope. This efficient spinning down during the main sequence finally leads to the much slower spinning core at core collapse.

Fig.(IV.1) shows the evolution of the angular rotation velocity in the $15\,M_{\odot}$ models throughout the star's life. The ratio of the angular velocity in the centre to the surface in the top panel confirms several points:

1) During the main sequence, from the very left of the plot up to the black markers, the models without magnetic fields and with the Tayler-Spruit dynamo develop a similar differential rotation between the centre and the surface. This indicates that the magnetic coupling between core and envelope during the main-sequence evolution is very inefficient in the *default* Tayler-Spruit model. The reason is the strong chemical stratification above the receding hydrogen core that suppresses the rotation-induced instabilities and reduces the magnetic dynamo - see discussion in Section IV.3.5. Furthermore, the Tayler-Spruit dynamo is ignored in the convective boundary mixing region - see Section IV.3.6. For these reasons, a bottleneck for the transport of angular momentum as well as for the chemical mixing arises in the region above the convective core (see Fig.(IV.3)). Therefore, the star cannot maintain the solid body rotation which is imposed at the zero-age main sequence and the core begins to spin up towards the end of the main sequence. On the other hand, the Fuller-modified Tayler-Spruit dynamo is able to maintain a constant ratio between the angular rotation velocity in the centre and the surface. This is a result from several factors: (a) this dynamo version generates stronger torques and operates on a shorter timescale, hence, it is more efficient at coupling differentially rotating layers, (b) the implementation of the Fuller-modified dynamo

includes the full convective region, including the boundary region and (c) the chemical stratification is taken differently into account, i.e. the Tayler-Spruit dynamo uses a patching formula with $\nu_{\rm TS} \propto \left(\frac{\Omega}{\rm N_\mu}\right)^4$ whereas the Fuller-modified version uses $\nu_{\rm TSF} \propto \left(\frac{\Omega}{\rm N_{eff}}\right)^2$. Therefore, the magnetic dynamo action creates a strong torque that efficiently couples the differentially rotating layers. The resulting viscosity generated by the Fuller-modified dynamo can locally exceed the viscosity of the Tayler-Spruit dynamo by several orders of magnitude as shown in Fig.(IV.3). Therefore, the Fuller-modified Tayler-Spruit dynamo maintains a near solid-body rotation. It should be noted, that the difference in the ratio between the three models seen in Fig.(IV.1, top panel), is due to the removal of angular momentum from the core. The bottom panel in Fig.(IV.2) clearly shows that the surface rotation rate is roughly decreasing by the same amount in the models during the main-sequence evolution. In the centre, the Fuller-modified Tayler-Spruit dynamo slows down the core rotation, whereas the pure hydrodynamic and the Tayler-Spruit model have a nearly constant $\Omega_{\rm centre}$ throughout the main sequence, indicating no angular momentum transport out of the core.

2) All three models with different efficiencies in angular momentum transport experience a drastic increase in differential rotation during the post-main-sequence phase. In all models, the difference between the surface and the central rotation rate increases by more than two orders of magnitude. This similarity, however, is misleading and is a result from the rapid expansion of the star which in all models drastically reduces the surface rotation speed. At the same time, the core in the hydrodynamic model spins up because of the contraction and the rotation-induced hydrodynamical instabilities do not transport angular momentum efficiently enough to prevent this spin up - see also Figs.(IV.2a) and (IV.4a). On the other hand, in both magnetic models the core first spins up until the shear between the core and envelope is strong enough for the activation of the magnetic dynamo, leading to a spin-down of the rotating core. Interestingly, during this short post-main-sequence phase the Tayler-Spruit dynamo is able to spin down the core by a larger amount than the Fuller-modified version (compare also Fig.(IV.2)). The reason for this is that the viscosity generated by the Tayler-Spruit dynamo is large throughout the star during this phase ($\log \nu_{\rm TS} \gtrsim 10$ in Fig.(IV.4b)), whereas the viscosity generated by the Fuller-modified version shows a drop to lower values in the intermediate region of the star (see Fig.(IV.4c)). Therefore, the Tayler-Spruit dynamo is able to efficiently diffuse angular momentum from the core, despite the jaggy viscosity profile. In the model with the Tayler-Spruit-Fuller dynamo, angular momentum is less efficiently diffused from the core due to the drop of $\nu_{\rm TSF}$ in the intermediate region[1]. Therefore, the core rotation is

[1]This drop results from numerical smoothing - see Section B.2.1. The issue is that the smoothing equation, Eq.(B.76), is implemented in two steps. First, if a region is not convective, $\log \nu_{\rm TSF}$ is divided by $2n+1$, where n is the number of zones included in the smoothing. Second, if the region is radiative, convective, a convective boundary region or semiconvective, $\log \nu_{\rm TSF}$ is unchanged in this cell after the first step, otherwise it is the sum following Eq.(B.76). Theoretically, this should not pose an issue, since the dynamo is not active in radiative regions without rotation because there is no differential rotation. However, the intermediate region shown in Fig.(IV.4c) is marked as radiative despite having a gradient in Ω. In general, the mixing type in a cell is set to "`rotation_mixing`" if the diffusion coefficient for mixing, $D_{\rm mix}$, is larger than zero and if the cell is not mixed otherwise, i.e. if the mixing type is "`no_mixing`". However,

less reduced in the Fuller-modified dynamo than in the Tayler-Spruit version. Nevertheless, both models massively spin down their cores during the short phase between core hydrogen depletion and core helium ignition.

3) The top panel in Fig.(IV.2) indicates that the evolution of the ratio $\Omega_{\rm centre}/\Omega_{\rm surf}$ is similar after core helium ignition. The middle panel presents the same ratio but limited to the evolution between core helium ignition and core silicon depletion and normalised to the ratio at core helium ignition. Indeed, the curves evolve very similarly during core helium burning and the star's advanced stages. There are some small differences, the main one arising after core helium depletion where the contracting core generates a rotational shear, which allows the magnetic dynamos to be active. The similarity of the angular rotation velocity ratio between the three models is due to two reasons. First, the evolutionary timescale becomes shorter as the evolution proceeds - see Section I.2. Thus, there is less time to diffuse angular momentum and restore solid-body rotation. Therefore, despite the strong magnetic viscosity generated in the models (see for example Fig.(IV.5)) not much more angular momentum is transported from the core than in the non-magnetic models. This behaviour becomes more dominant for the later phases due to the shorter timescales, which can also be observed in Fig.(IV.2), where there is nearly no difference in j between oxygen ignition and silicon depletion in the core. Second, a strong chemical stratification arises at the boundaries of convective regions due to the interface of the newly synthesised and the unburnt material. For example, in Fig.(IV.5) there are layers with a strong ∇_μ which are generated by the boundary regions of the convective helium core, the hydrogen shell and bottom of the surface convective zone. In these zones, the rotation-induced mixing is suppressed. In fact, below each layer with a strong chemical stratification there is a faster rotating layer in Fig.(IV.5), showing that these layers create a bottleneck for the transport of angular momentum (and rotation-induced chemical mixing).

   In summary, the largest differences between the three different treatments of angular momentum transport occur during the main-sequence evolution and the short post-main-sequence phase before core helium ignition.

In order to discuss the qualitative difference in angular momentum transport during the main sequence, Fig.(IV.3) presents the profiles of the turbulent viscosities in the $15\,{\rm M}_\odot$ models when the hydrogen mass fraction drops below 0.3. The rotation-induced angular momentum transport in the non-magnetic model (Fig.(IV.3a)) is clearly dominated by the Eddington-Sweet circulation throughout the envelope of the star, except for the region of the retreating hydrogen core. There, a strong chemical stratification suppresses the mixing by the Eddington-Sweet circulation. In this region, the

$D_{\rm mix}$ drops to zero in the intermediate region due to the strong chemical stratification where rotation-induced mixing is suppressed. (In contrast, in the Tayler-Spruit model, $D_{\rm mix}$ is never zero because there is mixing due to the magnetic dynamo and the jaggy ∇_μ profile allows for some zones to be mixed by the Eddington-Sweet circulation.) Therefore, $\log \nu_{\rm TSF}$ is reduced by a factor $\frac{1}{5}$.

retreating convective core left behind a jaggy chemical composition gradient, leading to thin layers where the circulation is active. The lack of an efficient angular momentum transport leads to an increase of the rotational shear between the core and the envelope, giving rise to the secular shear instability which is confined to thin layers where the chemical stratification does not suppress it. In the convective boundary region, the secular shear instability is not active, because convection efficiently redistributes angular momentum and a rotational shear only develops at the outer part of the boundary region. Simultaneously, the gradient in chemical composition, which is low throughout the convective core, increases towards the outer boundary of the convective boundary mixing region. Therefore, the Eddington-Sweet circulation arises in the inner part of the convective boundary but is suppressed further out by the chemical stratification. This prediction needs to be considered with care due to the limitations of 1D modelling - see Sections II and B - i.e. should a slow large-scale fluid motion develop due to thermal imbalance in the convective boundary mixing layer that is well mixed?[2] Nevertheless, the total viscosity, $\nu_{\rm AM} = \nu_{\rm AM,rot} + \nu_{\rm AM,non-rot}$, is smaller in the convective boundary mixing than in the neighbouring convective zone. Additionally, the bottleneck in $\nu_{\rm AM}$ at the outer part of the convective boundary mixing region maintains a separation between the turbulent viscosity in the core and the envelope, hence, this modelling inconsistency does not affect the large-scale angular momentum transport.

The non-magnetic hydrodynamic instabilities in the model with the Tayler-Spruit dynamo in Fig.(IV.3b) predict similar turbulent viscosities, with the exception in the transition region between the convective core and the radiative envelope. Additionally, the torque by the magnetic dynamo generates an strong viscosity, leading to a near solid-body rotation. The sharp cut-off of $\nu_{\rm TS}$ outside of the convective boundary mixing region is due to the numerical suppression of the dynamo action in convective and convective boundary regions. Therefore, the rotation rate increases inside of the convective boundary mixing region, contrarily to the non-magnetic model where it begins to increase at the point where the top boundary of the convective hydrogen core was located at the zero-age main sequence. In the magnetic model, there is therefore a thin layer in the outer convective boundary mixing region where the secular shear instability is active.

Fig.(IV.3b) nicely presents the bottleneck of angular momentum transport between the core and envelope, with a small gap between convective core and radiative envelope where nearly no angular momentum is transported through[3]. This creates the rotational shear between core and envelope previously discussed. In the region between the convective core and the envelope, the jaggy profile of the chemical composition gradient is flatter. Consequently the Eddington-Sweet circulation is present over larger layers and is present down to where it overlaps with the outer layer of the convective boundary

[2]It should be remembered that the implementation of convective boundary mixing only considers the mixing of chemical elements but ignores the mixing of entropy. Therefore, a thermal imbalance develops in this chemically well-mixed layer.

[3]A tiny amount is transported by the convective boundary mixing but this is negligible.

mixing zone. The reason for this different behaviour is the chemical mixing by the magnetic dynamo. Even though it is weaker than the viscosity generated by the magnetic dynamo, the derived diffusion coefficient in the envelope still has values around $\log D_{\rm TS} \sim 8$, hence, this process contributes to the reduction of the chemical stratification.

The turbulent viscosities of the hydrodynamical mixing processes are very similar in the model with the Fuller-modified Tayler-Spruit dynamo in Fig.(IV.3c), however, the rotation-induced instabilities are not present in the intermediate region. There, a strong chemical stratification with a smooth profile suppresses any rotation-induced chemical mixing. The reason for the smooth ∇_μ in the intermediate region is the fact that the Fuller-modified dynamo efficiently couples any differentially rotating layers, leading to a near solid-body rotation. Hence, the shear is not strong enough for the secular shear instability to be activated. In addition, the implementation of the Fuller-modified magnetic dynamo does not consider any chemical mixing. Therefore there is no rotation-induced chemical mixing that reduces the chemical stratification as in the other two models. The Fuller-modified Tayler-Spruit dynamo is only active in distinct layers, where in most layers the viscosity generated by the magnetic torque, $\nu_{\rm TSF}$, is slightly smaller than in the model with the Tayler-Spruit dynamo. The reason for this is that the model rotates close to solid body, hence, there is nearly no shear present - compare the range of Ω in Fig.(IV.3). This is the result of the Fuller-modified dynamo that efficiently couples differentially rotating layers in the first place. The numerous peaks in the magnetic viscosity seen in Fig.(IV.3c) are in fact layers where a weak differential rotation is present and the dynamo acts to restore solid-body rotation. If the shear is large, as for example at the bottom of the region with the Eddington-Sweet circulation, a strong viscosity is generated, which efficiently couples the rotating core and the envelope. The peak between the convective and the convective boundary mixing region is numerically suppressed towards the convective core, because there is no dynamo for $N^2 \leq 0$. In the intermediate zone, however, a shear resides but the transport of angular momentum is reduced due to the strong chemical stratification, $\nu_{\rm TSF} \sim N_\mu^{-2}$.

Similar to Fig.(IV.3), Fig.(IV.4) presents the turbulent viscosity but during the phase when the model has left the main sequence and is evolving towards the red supergiant branch. The impact of the profiles has already been discussed above. In the non-magnetic-model, the Eddington-Sweet circulation is the dominant hydrodynamic process to transport angular momentum throughout the star because convective regions are mostly absent during this evolutionary stage. In the mass region $2 - 4\,{\rm M}_\odot$ and in the envelope, the secular shear instability activates due to the development of a strong shear. However, $\nu_{\rm AM}$ is not strongly affected by this instability because in those regions the Eddington-Sweet circulation is active as well. The jaggy viscosity profile in the intermediate region is a result from ∇_μ in these regions, which developed during the main-sequence evolution. The zigzag pattern is elongated because of the narrow layers of the intermediate convective zone and secular shear mixing. In the

Tayler-Spruit dynamo, the turbulent viscosity is dominated by the dynamo action in the entire star, which efficiently couples the differentially rotating layers. In the intermediate region, there are two layers where the viscosity is dominated by the convective motions generated by the intermediate convective zone. The Eddington-Sweet circulation is active in the core and envelope of this model but its contribution to angular momentum transport is negligible compared to the magnetic viscosity. In the intermediate region, the circulation is only active in narrowly confined layers because it is suppressed by the chemical stratification otherwise. The latter is also the reason for the jaggy $\nu_{\rm TS}$ profile. Due to the weaker shear the secular shear instability is almost absent in this model with the exception of the intermediate region. There, however, the instability is often suppressed by the chemical stratification. As a result of the strong turbulent viscosity throughout the star, the Tayler-Spruit model, which had a similar rotation rate profile to the non-magnetic model during the main-sequence evolution, slows down the core spin during this phase. Nevertheless, this phase is not long enough to spin down the core to the same magnitude as the model with the Fuller-modified dynamo. The Fuller-modified Tayler-Spruit dynamo predicts a strong magnetic viscosity in the evelope and core, but in the intermediate region it drops to lower values due to the numerical smoothing routine, as discussed above. Consequently, a rotational shear begins to build up in this region, however, the secular shear instability is not activated due to the strong chemical stratification. Therefore, the smoothing routine creates a bottleneck for the angular momentum transport in the current implementation of the Fuller-modified magnetic dynamo as published in Fuller et al. (2019). It could potentially underestimate the angular momentum transport, see discussion in Section IV.3.4, and could reduce the core rotation of massive stars more than anticipated (e.g. Fuller & Ma, 2019; Ma & Fuller, 2019).

Fig.(IV.5) presents the profile of the turbulent viscosity during core helium burning. In each subplot, the large turbulent viscosity from non-rotating fluid instabilities on the left hand side is due to the convective helium core and on the right hand side from the surface convective region. These two convective zones sandwich a radiative region with an outward moving hydrogen burning shell. In this intermediate layer, only rotation-induced mixing processes take place. In the non-magnetic model, the Eddington-Sweet circulation is the dominant angular momentum transport process and it is able to maintain a nearly constant Ω in the regions it is active. However, there are two layers where a strong chemical composition gradient is present: at the boundary of the convective core and at the location of the hydrogen shell. There, any rotational mixing is suppressed and this bottleneck in angular momentum transport leads to a further increase in the shear between the slowly rotating envelope and the core region. At the boundary of these regions and below the surface convective zone, where the rotational shear is stronger, the secular shear instability is active but it is limited to narrow layers due to the strong chemical stratification and does not change the angular momentum distribution significantly. In the Tayler-Spruit dynamo, the hydrodynamic instabilities, rotating and

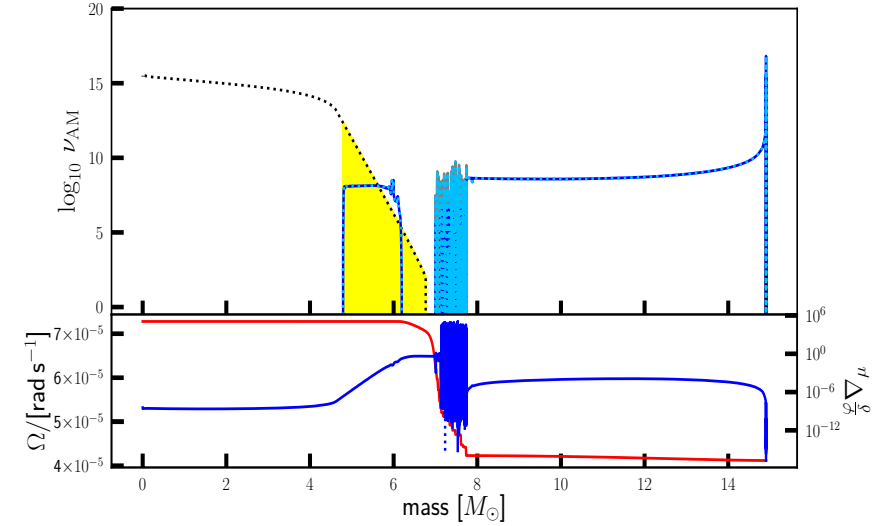

(a) non-magnetic

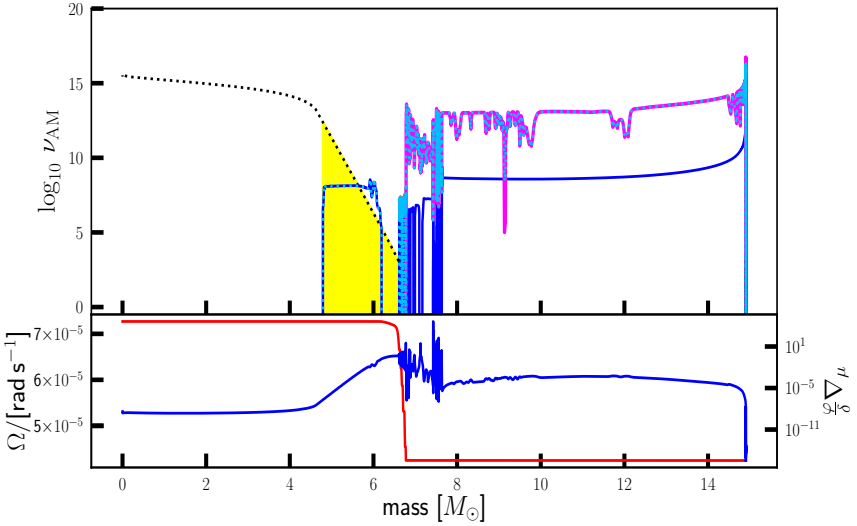

(b) Taylor-Spruit dynamo

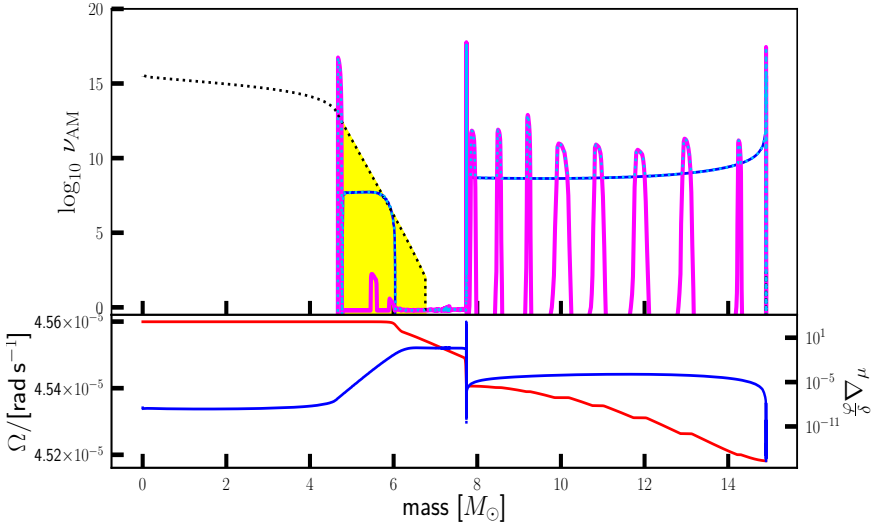

(c) Fuller-modified Taylor-Spruit dynamo

Figure IV.3: The profile of the turbulent viscosity in 15 $\mathrm{M}_\odot$ models with different angular momentum transport mechanisms during core hydrogen burning when the hydrogen mass fraction drops below 0.3. Each top panel shows the total turbulent viscosity generated by non-rotating sources such as convection (black dotted line) and the turbulent viscosity generated by rotation-induced instabilities (sky-blue dotted line). Additionally shown are the turbulent viscosities generated by each rotation-induced instability, the viscosity produced by the Eddington-Sweet circulation (dark-blue solid line), the secular shear instability (grey solid line) and the magnetic dynamo (magenta solid line). The yellow shaded region indicates the location of convective boundary mixing regions. The bottom panel depicts the rotation rate (red) and the gradient in the chemical composition (blue). It should be noted that the range of the axis in the bottom panel varies between the figures.

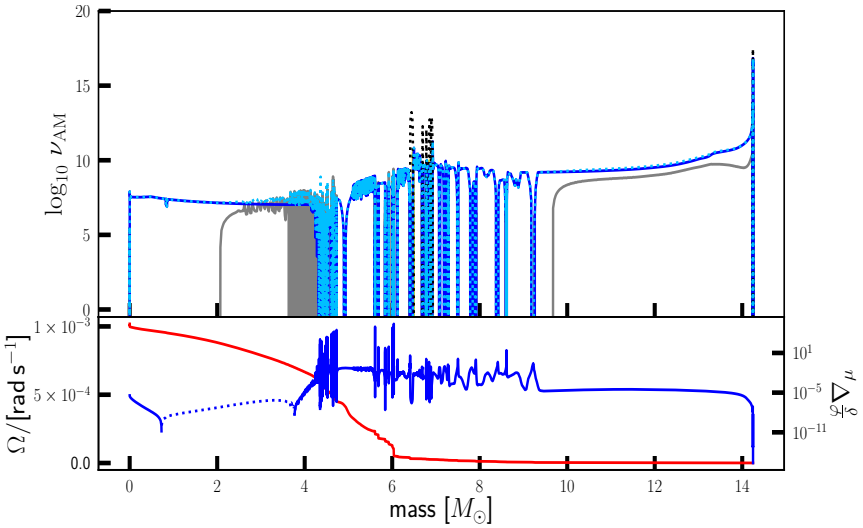

(a) non-magnetic

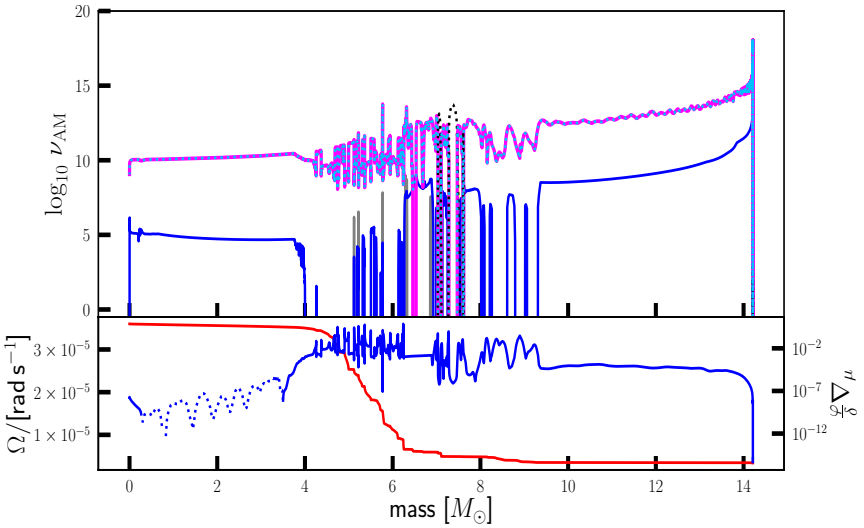

(b) Taylor-Spruit dynamo

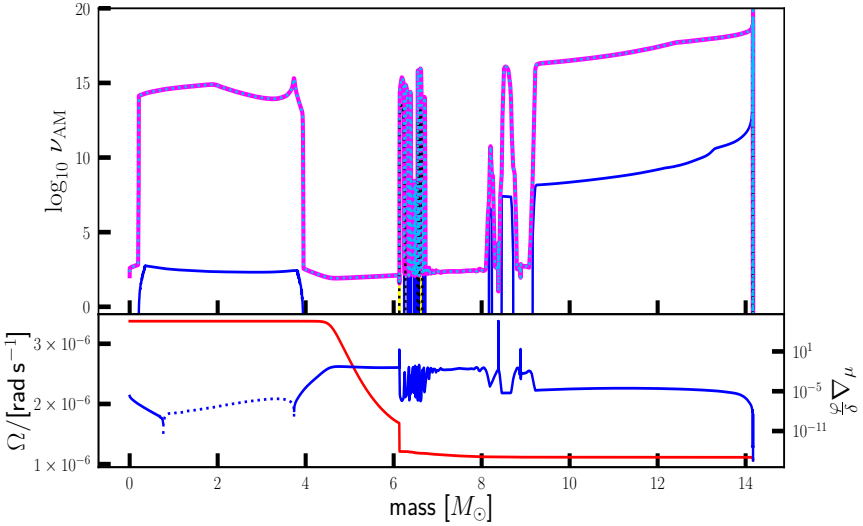

(c) Fuller-modified Taylor-Spruit dynamo

Figure IV.4: The same as in Fig.IV.3 but during the post-main-sequence evolution, exactly between hydrogen depletion and helium ignition. A dotted line in $\frac{\varphi}{\delta}\nabla_\mu$ indicates negative values.

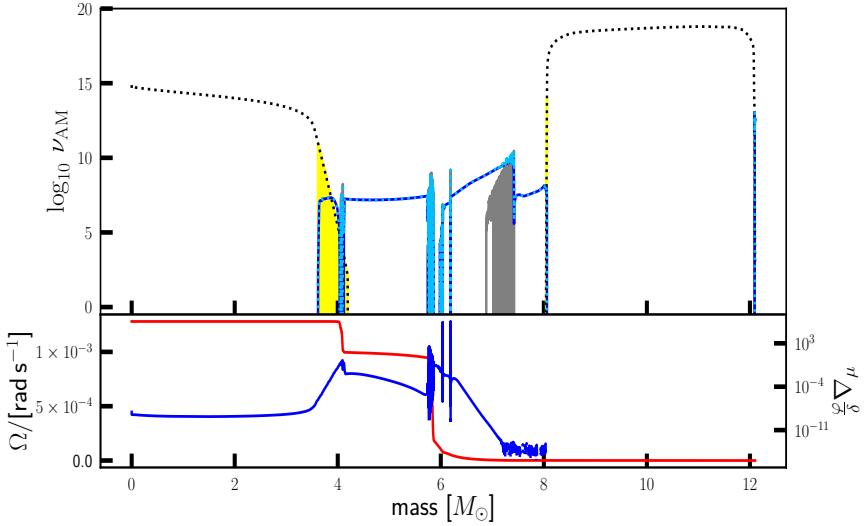

(a) non-magnetic

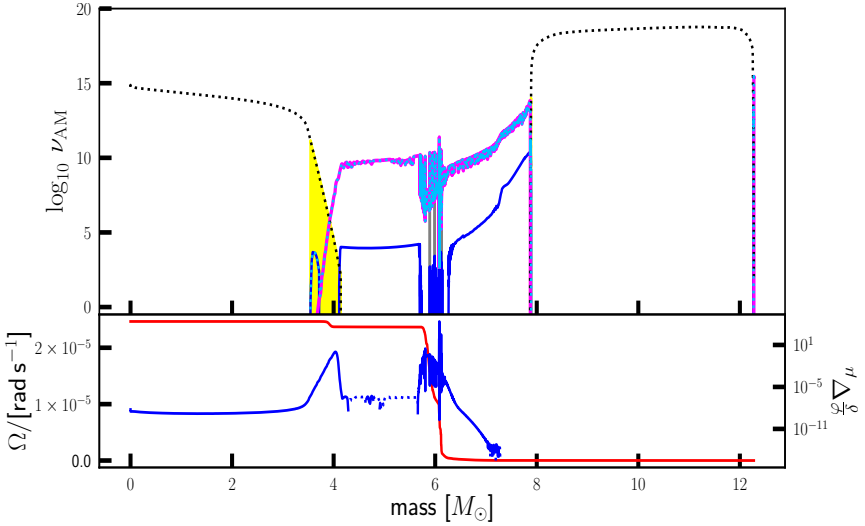

(b) Taylor-Spruit dynamo

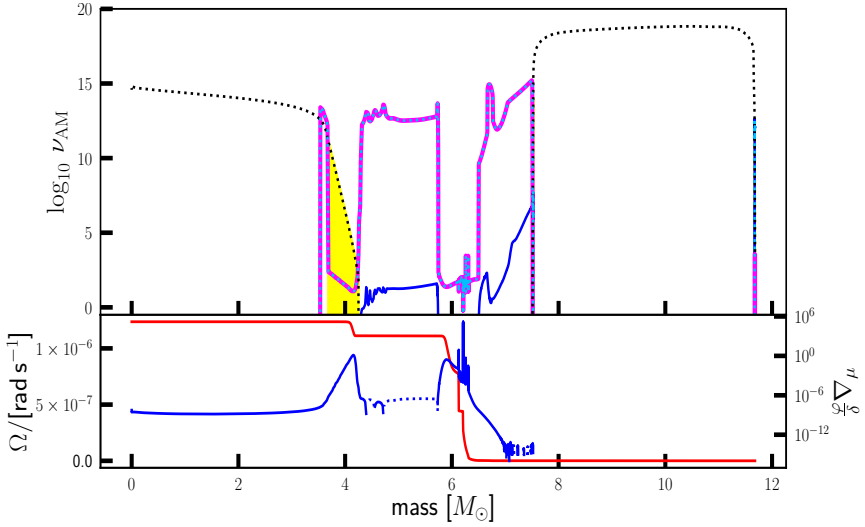

(c) Fuller-modified Taylor-Spruit dynamo

Figure IV.5: The same as in Fig.IV.3 but during the core helium burning when the mass fraction ^{4}He in the core drops below 0.4. A dotted line in $\frac{\varphi}{\delta}\nabla_\mu$ indicates negative values.

non-rotating, generate a similar viscosity as in the non-magnetic model but their viscosities are weaker on average by about two orders of magnitude. This is because of the different gradient in chemical composition and the different rotation profile, i.e. Ω is roughly constant and has a drop at the location of the hydrogen shell, which is weaker in the magnetic model due to the slower rotating core. Indeed, rotation in the radiative layer is mainly coupled by the magnetic torque, which is only interrupted at the hydrogen shell due to the dependence of ν_{TS} on N_μ^2 - see Section II.3.1.2. Similarly to the non-magnetic model, this interruption of $\nu_{\rm TS}$ creates a bottleneck in angular momentum transport and further increases the rotational shear between the core and the envelope. The magnetic viscosity in the model with the Fuller-modified Tayler-Spruit dynamo is also active throughout the radiative region, with a magnitude larger than the one predicted by the Tayler-Spruit dynamo. However in some regions the viscosity drops to a fifth of the value. This is a result of the smoothing routine as previously discussed.

A careful reader might notice that in Fig.(IV.5b) the Tayler-Spruit dynamo generates a magnetic viscosity in the convective boundary mixing region despite the claim in Section B.1.5.1 that it is excluded from this zone. However, the magnetic dynamo is not computed in this layer. The magnetic viscosity in the convective boundary region seen in Fig.(IV.5b) is a result of numerical smoothing, where $\nu_{\rm TS}$ is smoothed into the boundary region of the growing convective core - see also discussion in Section IV.3.4.

The key points discussed in the context of Fig.(IV.5) are also applicable to the further evolutionary stages, where the structure of the turbulent viscosity between convective and radiative regions looks qualitatively similar. There, the angular momentum transport in the radiative regions between convective zones is limited by the chemical stratification. Furthermore, the evolutionary timescale becomes shorter with each burning stage, giving less time for the redistribution of angular momentum. Therefore, the core region spins up (see Fig.(IV.2)). The separation between the fast spinning core and the slow rotating envelope at the location of the hydrogen shell remains for the rest of the evolution.

3.2 25 and 30 $\mathrm{M}_\odot$ models

In Section I.4.2 I explained that the evolutionary path of rotating stars at solar metallicity can roughly be separated into two groups, stars with $M \lesssim 30\,\mathrm{M}_\odot$ where rotation-induced mixing dominates and stars with $M \gtrsim 30\,\mathrm{M}_\odot$ where the rotation-enhanced mass loss dominates. Indeed, the models with an initial mass of 25 and $30\,\mathrm{M}_\odot$ predict a similar angular momentum distribution as the $15\,\mathrm{M}_\odot$ models at the various stellar stages in the core region and hence a similar core spin at collapse (see Fig.(IV.6)). However, due to the higher initial mass the model predicts higher mass-loss rates which remove nearly the entire hydrogen-rich envelope - in some cases even the entire envelope (see Table V.1). The removal

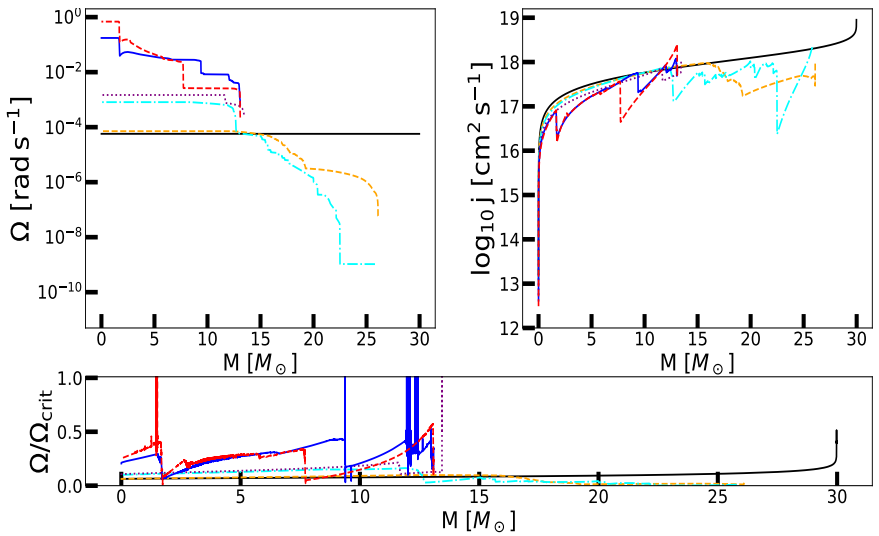

(a) no magnetic fields

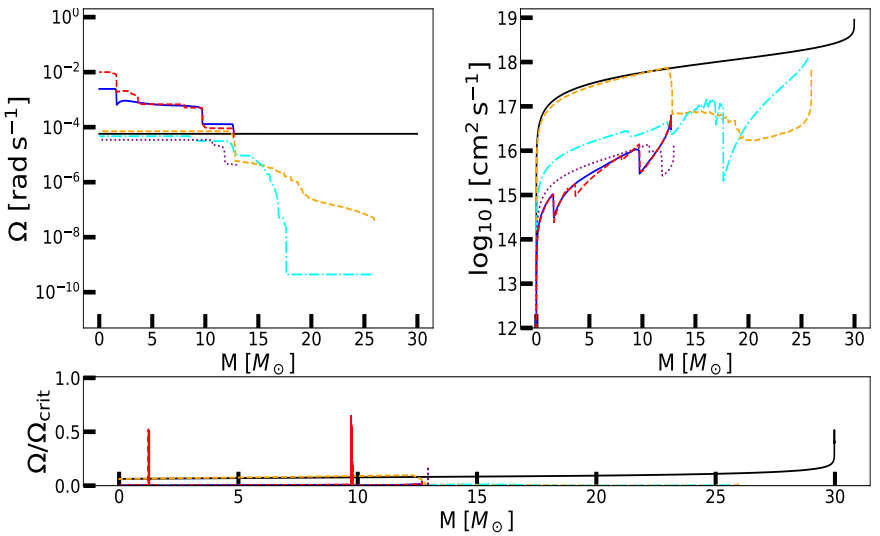

(b) Taylor-Spruit dynamo

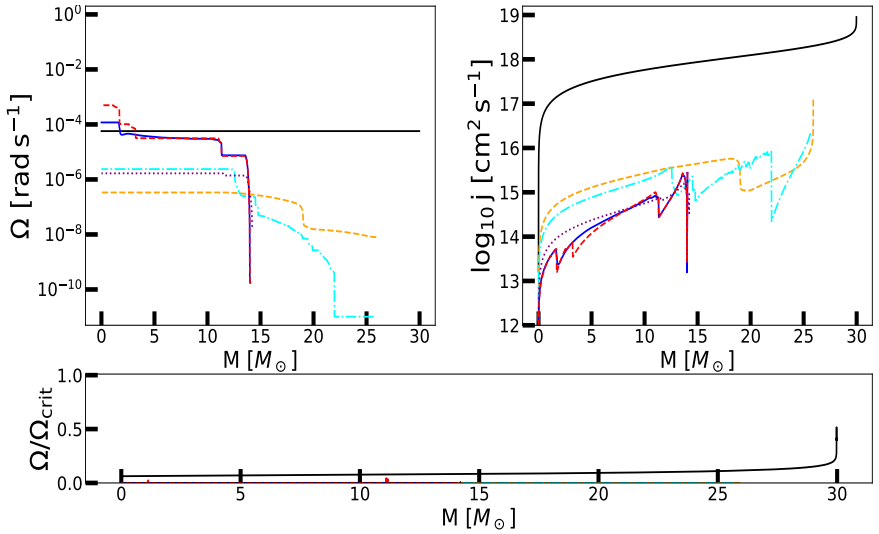

(c) Fuller-modified Taylor-Spruit dynamo

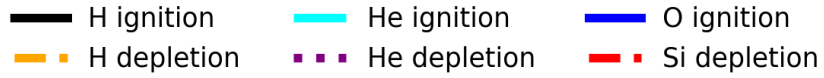

Figure IV.6: The rotation profile of the 30 $M_\odot$ models for the different angular momentum transport mechanisms, showing on the top left panel the angular rotation velocity, Ω, on the top right panel the specific angular momentum, j, and on the bottom panel the ratio of the angular rotation velocity to the critical angular rotation velocity. Each line presents the profile at a different evolutionary stage indicated by the colour and linestyle. For comparison reasons, the axis of each thematic subplot group have been scaled to the same values. The ignition of a burning phase is defined as when 0.3% of the fuel is burnt and depletion when the fuel drops below 1%.

of the envelope by winds does not influence the angular momentum distribution in the core because it occurs during core helium burning, whereas most of the angular momentum transport happens between core hydrogen exhaustion and core helium ignition. Consequently, the rotation rate in the core increases during the advanced stellar phases because of contraction but the angular momentum distribution remains roughly the same and thus is similar to the prediction of the $15\,M_\odot$ models. Fig.(IV.6c) suggests that the Fuller-modified Tayler-Spruit dynamo transports more angular momentum during the main-sequence and less during the post-main-sequence phase compared to the $15\,M_\odot$ model in Fig.(IV.2c). This, however, is misleading because at $X_c(^4He) = 0.1$ the angular momentum profiles are similar. The difference seen between Figs.(IV.2c) and (IV.6c) results from the fact that the more massive cores begin to contract earlier, which builds up a stronger shear, allowing more angular momentum to be transported before hydrogen depletes completely in the core. This results in a weaker shear during the post-main-sequence evolution, hence, less angular momentum transport and finally a similar core spin at helium ignition as in the $15\,M_\odot$ model.

3.3 $60\,M_\odot$ models

Contrarily to the massive stars discussed above, the $60\,M_\odot$ models at solar metalicity already lose more than $10\,M_\odot$ during their main-sequence evolution via stellar winds. This allows the star to lose a substantial amount of angular momentum from its surface. This can be seen in Fig.(IV.7a), showing the rotation profile of the non-magnetic $60\,M_\odot$ model. Earlier, I showed that the hydrodynamic instabilities alone are not able to reduce the rotation rate in the core during the main sequence (see Fig.(IV.2a)). However, Fig.(IV.7a) depicts that there is a reduction of angular momentum and the angular velocity during hydrogen burning - the latter only by a small amount. This is because at the beginning of the main-sequence evolution, when there is no strong chemical stratification present, the Eddington-Sweet circulation generates a viscosity of $\log \nu_{AM} \gtrsim 9.5$ throughout the radiative envelope[4]. Therefore, angular momentum is evenly redistributed to replenish the removed angular momentum at the surface of the star. Indeed, the reduction of j and Ω in the central region occurs during the beginning of the main sequence, when $X_c(^4He) > 0.4$. Thereafter, the chemical stratification above the receding hydrogen core prevents transport of angular momentum from the core to the surface. Thus, stellar winds still slow down the envelope rotation but do not affect the core rotation after a chemical stratification has built up above the receding convective hydrogen core. There is also a reduction of angular momentum during core helium burning, where stellar winds remove the entire envelope and part of the helium core including its angular momentum. Thereafter, the evolutionary

[4]The viscosity generated by the Eddington-Sweet circulation is stronger in more massive stars due to its local luminosity and temperature gradient dependence (see Eq.(II.25))

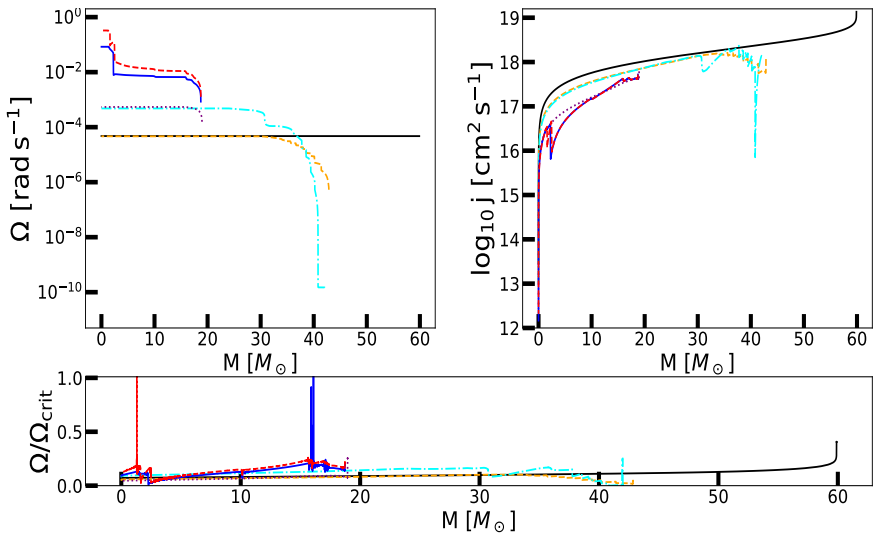

(a) no magnetic fields

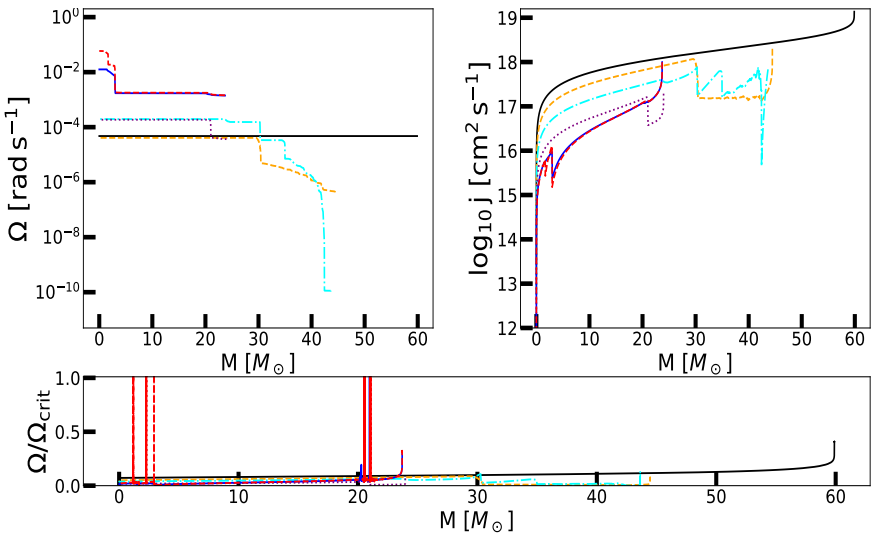

(b) Taylor-Spruit dynamo

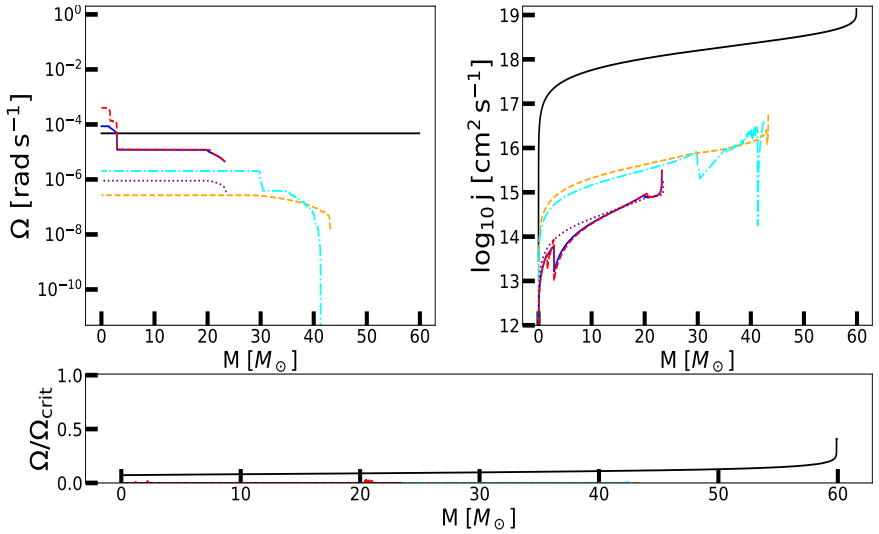

(c) Fuller-modified Taylor-Spruit dynamo

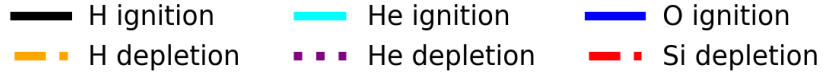

Figure IV.7: The same as in Fig.(IV.6) but for models with an initial mass of 60 $M_\odot$.

timescale speeds up and mass loss is not fast enough to remove a substantial amount of matter and angular momentum from the surface of the star. The rotating core contracts and spins up during the advanced stages, predicting a slightly slower rotating core than the lower mass models discussed earlier. A similar main-sequence scenario is predicted by the $60\,M_\odot$ model with the Tayler-Spruit dynamo, leading to a reduction of Ω and j (see Fig.(IV.7b)), similar to the non-magnetic case. Contrarily to the $15\,M_\odot$ Tayler-Spruit model, where the dynamo strongly couples the differentially rotating layers during the post-main-sequence phase and reduces the angular momentum in the core (see Fig.(IV.2b)), the $60\,M_\odot$ model with the Tayler-Spruit model transports only a small amount of angular momentum. This is because the convective core never disappears entirely after hydrogen depletes and maintains a size of $\sim 15\,M_\odot$. Therefore, the Tayler-Spruit dynamo is only active in confined regions between the convective core and the intermediate convective zone and in the envelope. As a result, the transport of angular momentum transport is "disconnected" into regions, leading to an overall inefficient transport - see discussions in Sections IV.3.5 and IV.3.6. The reduction of angular momentum during the core helium burning phase is mainly due to strong stellar winds that erode away the envelope and part of the convective core, similarly to the non-magnetic case. During the advanced stages the angular momentum does not change significantly and the predicted rotation rate at silicon depletion is larger than in the $15\,M_\odot$ model. The evolution of the rotation in the $60\,M_\odot$ model with the Fuller-modified Tayler-Spruit dynamo, shown in Fig.(IV.7c), is very similar to the $30\,M_\odot$ model but additional removal of angular momentum takes place due to stellar winds. The rotation rate at silicon depletion, however, is very similar to the lower mass models because the contraction during the advanced phases dominates the evolution of the angular rotation velocity.

3.4 Smoothing of the Tayler-Spruit and the Fuller-modified Tayler-Spruit dynamo

In Section B.1.5.1 I discussed the option to spatially and temporally smooth the diffusion coefficient and the turbulent viscosity generated by the Tayler-Spruit dynamo. The amount of angular momentum transported by the Tayler-Spruit dynamo depends strongly on the smoothing process. Fig.(IV.8a) presents the Tayler-Spruit model with no smoothing, i.e. spatial and temporal smoothing are switched off. Indeed, the rotation profile of this model looks very similar to the non-magnetic model in Fig.(IV.2a), hence, if no smoothing is included the magnetic dynamo is not able to transport a significant amount of angular momentum. This is because the dynamo is only allowed to be active in confined regions where $q > q_{\rm min}$ - see Section II.3.1.2 - leading to a jagged profile of the magnetic viscosity shown in Fig.(IV.9a). The layers with $q < q_{\rm min}$ prevent an efficient transport of angular momentum. The spatial smoothing routine does not increase the amount of angular momentum

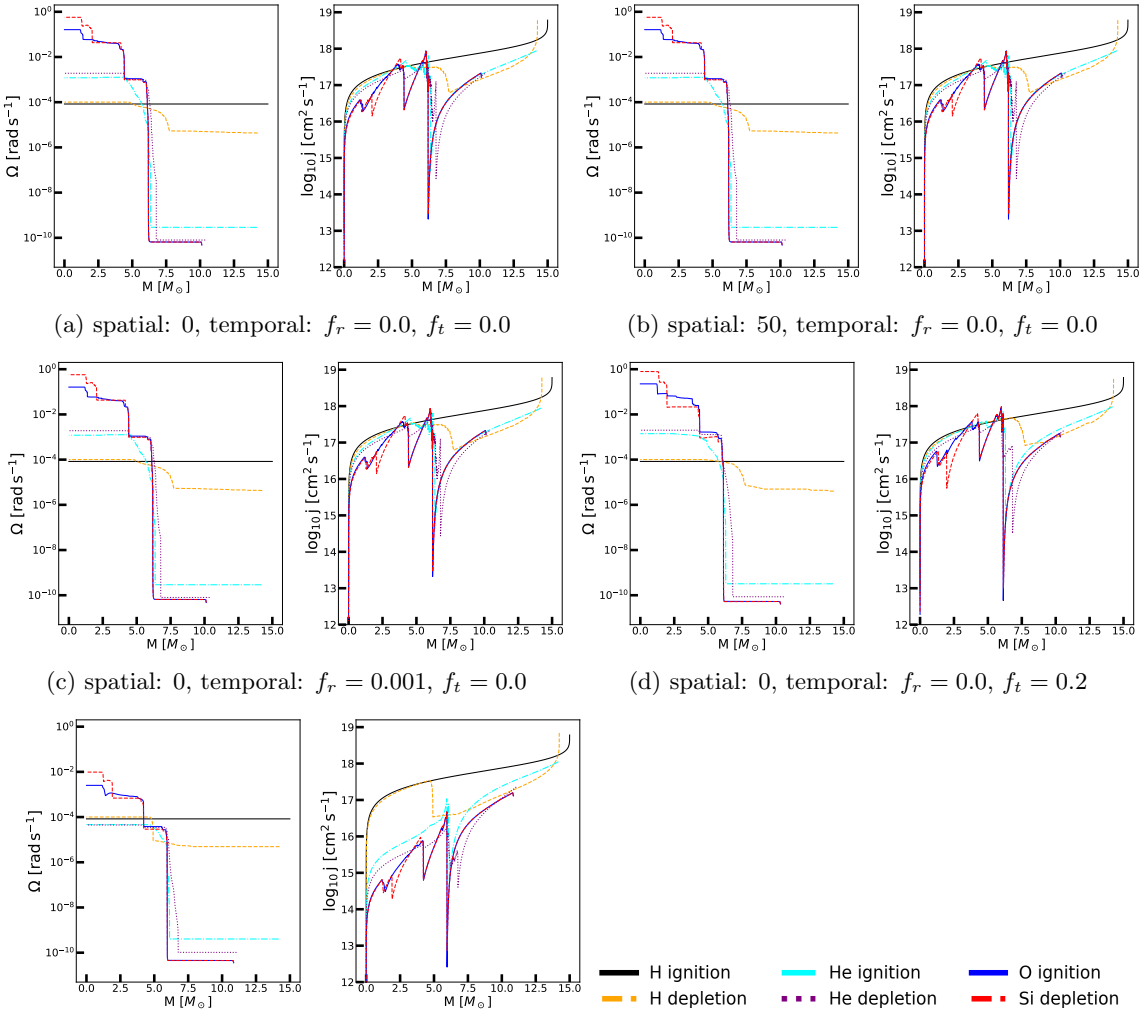

(a) spatial: 0, temporal: $f_r = 0.0$, $f_t = 0.0$

(b) spatial: 50, temporal: $f_r = 0.0$, $f_t = 0.0$

(c) spatial: 0, temporal: $f_r = 0.001$, $f_t = 0.0$

(d) spatial: 0, temporal: $f_r = 0.0$, $f_t = 0.2$

(e) spatial: 0, temporal: $f_r = 0.001$, $f_t = 0.2$

Figure IV.8: The Ω- and j-profiles as a function of the mass coordinate at different evolutionary stages in the $15\,M_\odot$ models applying the Tayler-Spruit dynamo with different smoothing coefficients. The three coefficients for each model are indicated in the caption of each subfigure - see Section B.51 for more details on the coefficients. The colour indicates the evolutionary stage.

transported by the dynamo, even for a large number of cells included in the smoothing process as can be seen in Fig.(IV.8b). It can be seen in Fig.(IV.9b) that $\nu_{\rm TS}$ is continuously large over a wider range and only drops to zero in the middle of the radiative envelope and in the region close to the core, which finally prevents an efficient rotational coupling of the whole envelope. However, Fig.(IV.9b) reveals a troublesome feature: the magnetic dynamo is active in regions with $q < q_{\rm min}$. This is a result of the smoothing process, where $\nu_{\rm TS}$ is smoothed into the "*forbidden*" region. The consequence is the rugged $\nu_{\rm TS}$ connecting layers with active and inactive magnetic dynamo. Therefore, it is important to use small numbers of cells for the smoothing process to avoid an oversmoothing of the "*forbidden*" region, hence the default value of 2 for the spatial smoothing process in this work. The temporal smoothing routine can lead to a considerable amount of angular momentum as it is shown in Fig.(IV.8), however, it depends on the two parameters, f_r and f_t (see Eq.(B.51)). If $f_t = 0.0$ the smoothing is not

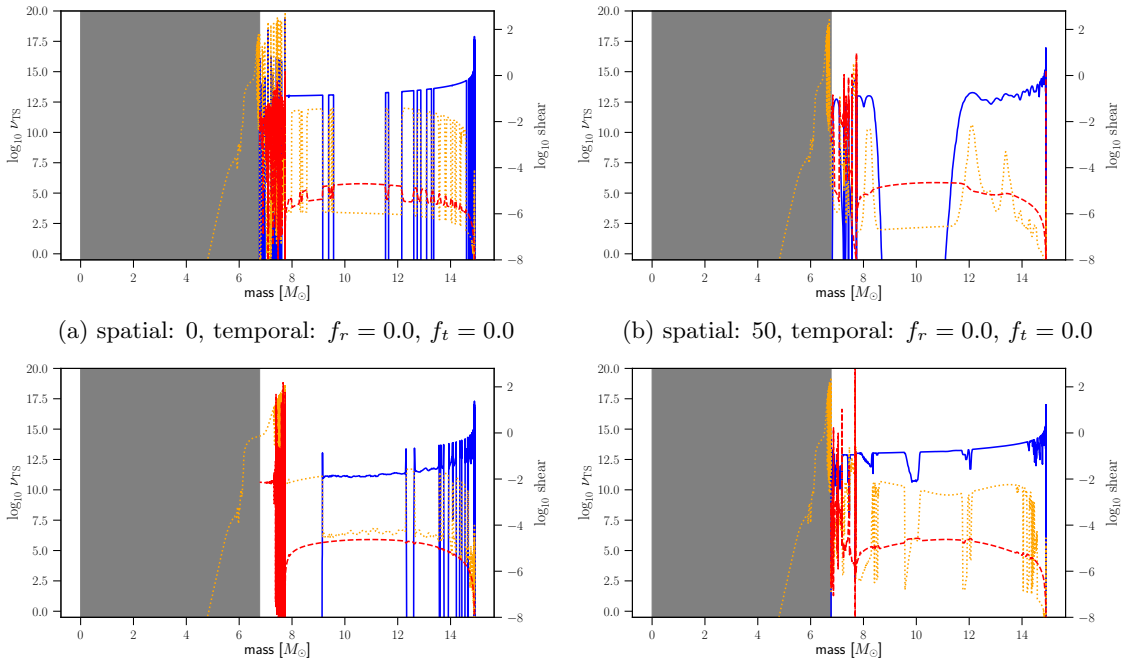

(a) spatial: 0, temporal: $f_r = 0.0$, $f_t = 0.0$

(b) spatial: 50, temporal: $f_r = 0.0$, $f_t = 0.0$

(c) spatial: 0, temporal: $f_r = 0.0$, $f_t = 0.2$

(d) spatial: 0, temporal: $f_r = 0.001$, $f_t = 0.2$

Figure IV.9: The magnetic viscosity $\nu_{\rm TS}$ (solid blue), the rotational shear (dotted orange) and the minimum shear $q_{\rm min}$ (dashed red) (see Eq.(II.52)) as a function of the mass coordinate in the $15\,{\rm M}_\odot$ models applying the Tayler-Spruit dynamo. The profile is during the main sequence when the hydrogen mass fraction in the core drops below 0.3. The grey shaded area on the left represents the convective core including the convective boundary mixing region.

applied, unaffected by the value of f_r. Therefore, the rotation profile in Fig.(IV.8c) is the same as in the model without numerical smoothing of the Tayler-Spruit dynamo. If $f_r \geq 0.0$ and $f_t > 0.0$, the temporal smoothing is used as shown in Eq.(B.51), trying to limit the change of the magnetic viscosity within a certain range of the value from the previous time step. For very large values of f_r and f_t, the smoothing routine neglects the value from the previous time step and the value from the current time step is used. This can lead to an "*on-off*" behaviour of the magnetic dynamo in a layer due to the condition $q > q_{\rm min}$ for the dynamo to be active and its dependence on the transport of angular momentum. Therefore, intermediate values for f_r and f_t are needed for smoothing. Nevertheless, the temporal smoothing routine also leads to problems. Fig.(IV.9c) presents the magnetic viscosity, shear and $q_{\rm min}$ for the model where no spatial smoothing is included but temporal smoothing is used with $f_r = 0.0$ and $f_t = 0.2$. The subfigure shows that $\nu_{\rm TS}$ is suppressed by the smoothing process in regions where $q \gg q_{\rm min}$. Consequently, this model transports even less angular momentum during the main-sequence evolution than the model with no smoothing. Finally, if $f_r = 0.001$ and $f_t = 0.2$, the model seems to predict a more constant magnetic viscosity throughout the radiative envelope of the star. However, again the dynamo is active in "*forbidden*" region. Including both, spatial smoothing and temporal smoothing leads to a similar profile with an active dynamo in the "forbidden" region. This problem seems to be limited by the current implementation of the Tayler-Spruit dynamo in the `MESA`

stellar evolution code. Possibly a general formulation of the dynamo, instead of a patching formula as described in Eq.(II.56) could improve the situation but this is future work. For now, it is important to be aware of the limitations of the Tayler-Spruit dynamo and its dependence on smoothing processes.

Earlier, I discussed that there is an inconsistency in the routine which numerically smooths the magnetic viscosity of the Fuller-modified Tayler-Spruit dynamo. In detail, the smoothing proceeds via two sequential *if-conditions*. The first condition prepares the array containing the unsmoothed values of $\log \nu_{\rm TSF}$ by dividing them by the number of cells included in the smoothing routine, i.e. $2n+1$ where n is the number of cells on one side that are included in the smoothing. However, if the cell is mixed by convection it is excluded from this step. The second condition adds the values of the $2n$ neighbouring cells to the new $\log \nu_{\rm TSF}$, if the cell is not convective, semiconvective, a convective boundary mixing cell or is labelled as radiative, i.e. no rotational mixing occurs. Otherwise, the zone is excluded from the sum. This avoids smoothing the convective diffusivity into non-convective zones but introduces two inconsistencies. (i) Excluding a summand in the second step artificially reduces the magnetic viscosity close to cells which are convective, semiconvective, convective boundary mixing or radiative because in the first step the values are divided by $2n+1$ in all cells but convective ones. (ii) In `MESA`, a non-convective, non-semiconvective or non-convective boundary cell is marked with "`rotation_mixing`" if it contains a non-zero diffusion coefficient. Otherwise it is radiative. However, in regions with a strong chemical stratification the rotation-induced chemical mixing is suppressed (see Figs.(IV.3), (IV.4) and (IV.5)). Therefore, it is marked as radiative despite containing differentially rotating layers where the magnetic dynamo action could operate. Consequently, the second *if-condition* of the smoothing routine excludes these cells from the smoothing sum, which artificially reduces the magnetic viscosity - see discussion above.

In order to test the problematic behaviour of the smoothing routine outlined in the previous paragraph, I compute a $15\,{\rm M}_\odot$ model with the Fuller-modified Tayler-Spruit dynamo but exclude any smoothing of $\log \nu_{\rm TSF}$ and $\log \nu_\Omega$. Fig.(IV.10) shows that the low values of the magnetic viscosity disappear in the radiative regions as expected. Therefore, $\log \nu_{\rm TSF}$ is large throughout the star during the post-main sequence evolution but there is a small reduction in the intermediate region due to the dependence of the magnetic viscosity on the chemical stratification through N^2_μ. Consequently, a modest shear develops in this layer, with a sharp drop at the hydrogen shell. Similarly, the magnetic viscosity profile during core helium burning does not have the deep dips from the smoothing but at the locations with a strong chemical stratification there is a reduction of angular momentum transport due to the chemical stratification. As a result, the Ω profile has a drop at each location where there is an increased ∇_μ. Most important is the hydrogen shell, where the chemical stratification leads to a local minimum of $\log \nu_{\rm TSF}$ and prevents angular momentum transport from the core to the envelope.

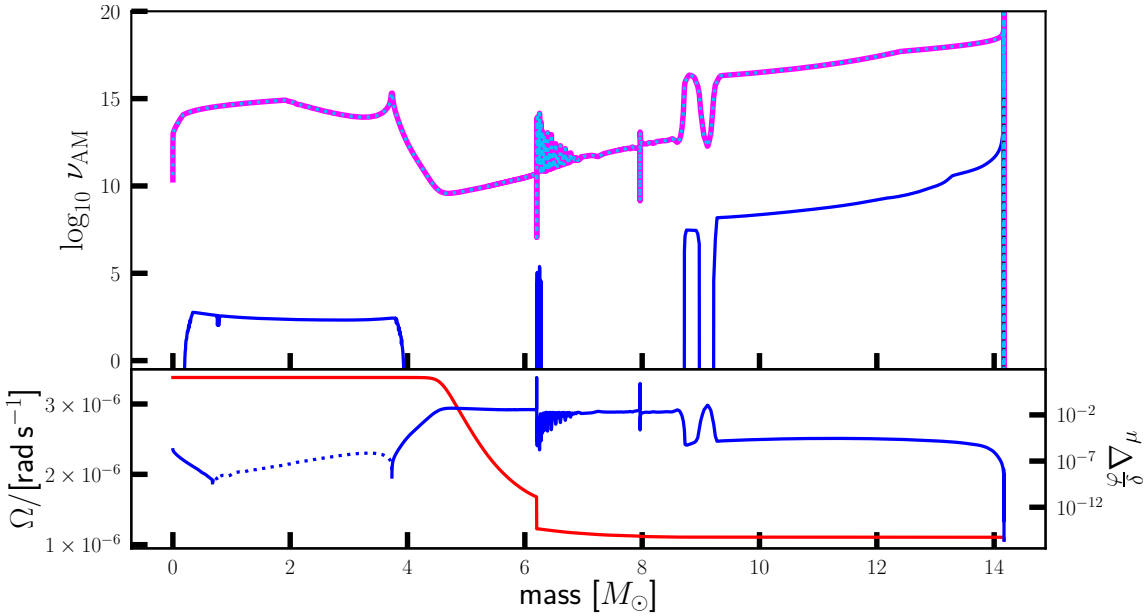

(a) post main sequence

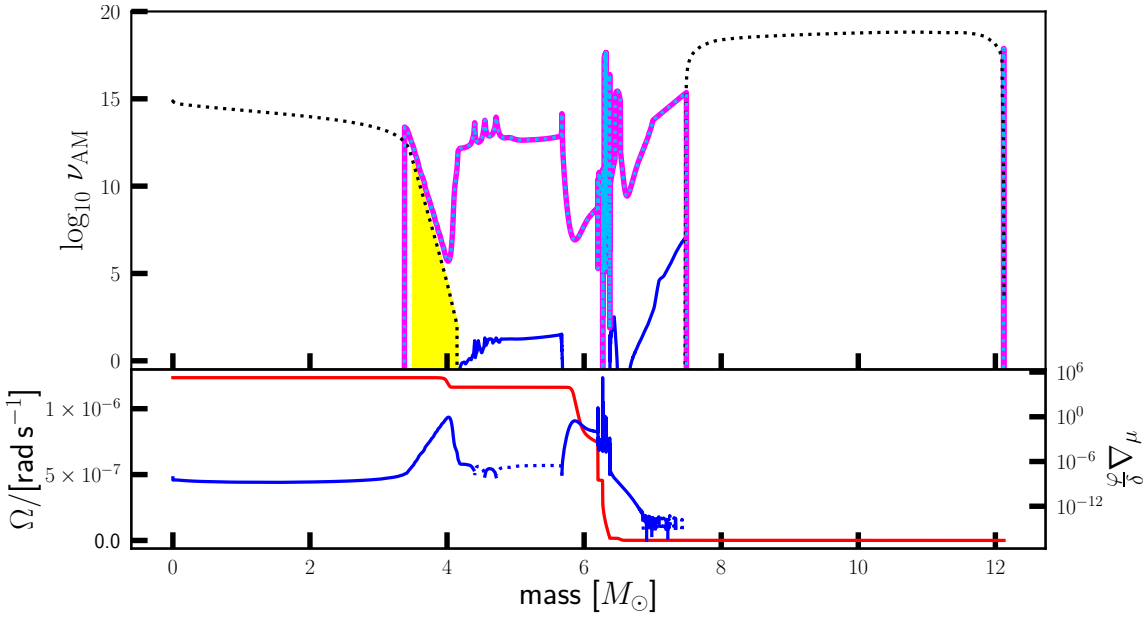

(b) core helium burning

Figure IV.10: The profile of the turbulent viscosity in the 15 $M_\odot$ model applying the Fuller-modified Tayler-Spruit dynamo but excluding the smoothing of the magnetic viscosity (a) between the main sequence and core helium burning as in Fig.(IV.4) and (b) during core helium burning, when the helium mass fraction drops below 0.4, compare to Fig.(IV.5). The figure is organised as those two figures.

Accordingly, a shear between envelope and core develops similarly to the model with the smoothed Fuller-modified dynamo. Thus, while the smoothing routine can change the local profile of log $\nu_{\rm TSF}$, the bottleneck in angular momentum transport at the hydrogen shell, and other chemically stratified layers, is not much influenced, leading to a very similar Ω-profile in the Fuller-modified Tayler-Spruit models with and without smoothing.

The Fuller-modified Tayler-Spruit dynamo is controversial and some scientists argue that the increased amount of angular momentum transport generated by the dynamo action in the `MESA` code is a result of the smoothing routine (e.g. P. Eggenberger, private communication). Comparing Figs.(IV.10), (IV.4c) and (IV.5c) shows that the magnetic viscosity is of the same magnitude for both, the smoothed and unsmoothed dynamo, except in the regions discussed in the previous paragraph. Therefore, the magnitude of the viscosity generated by the Fuller-modified dynamo does not depend on the smoothing process.

3.5 The Parameters f_μ and f_c

In Section B.1.4, the two parameters f_c and f_μ were introduced in order to calibrate the uncertain order-of-magnitude estimates for the rotation-induced mixing processes in the diffusive framework of the Heger et al. (2000) implementation. The diffusion coefficients generated by the rotational instabilities (see Eq.(B.40)), are multiplied by f_c. ∇_μ, on the other hand, is multiplied by f_μ in order to reduce the sensitivity of the rotation-induced instabilities to the chemical stratification[5]. Heger et al. (2000) calibrated f_c and f_μ to match the surface enrichment of nitrogen in observed stars in the mass range 10-20 $\rm M_\odot$ and the helium enrichment in 60 $\rm M_\odot$ stars and stars below 20 $\rm M_\odot$. They find the best match with $f_c = \frac{1}{30}$[6] and $f_\mu = 0.05$. Yoon et al. (2006) concluded that when the chemical mixing by the magnetic dynamo is used, $f_\mu = 0.1$ should be used. Brott et al. (2011) calibrate the mixing efficiency, f_c, to observations of B-stars. For their 13 $\rm M_\odot$ model they conclude that $f_c = 0.0228$ with $f_\mu = 0.05$ matches the observations best[7]. In this work, the values $f_c = 0.0228$ and $f_\mu = 0.1$ are the default choices for the two parameters.

In order to asses the uncertainty in angular momentum transport, the dependence of the rotation-induced instabilities on f_c and f_μ needs to be determined. It could be argued that the two values are calibrated to observations and there is no need to asses their uncertainty. However, the models

[5]It is crucial to notice that f_μ is only multiplied to ∇_μ but not to $N_\mu = \frac{g\varphi}{H_P}\nabla_\mu$. Hence, the chemical stratification is only reduced in the stability criterion in the dynamical and secular shear instability and in the "*breaking velocity*" of the Eddington-Sweet circulation and the Goldreich-Schubert-Fricke instability. In all the other instabilities, where the chemical stratification is taken into account through N_μ, it is not reduced.

[6]There seems to be some confusion in the literature concerning the factor f_c and the work of Chaboyer & Zahn (1992). Heger et al. (2000) state that Chaboyer & Zahn (1992) find a similar f_c value based on a theoretical approach. Moreover, Brott et al. (2011) discuss that Heger et al. (2000) adopted f_c from the work by Chaboyer & Zahn (1992). However, Chaboyer & Zahn (1992) do not introduce such a scaling factor and the numerical term in their Eq.(16), which only affects one term and not the sum of the diffusion coefficients, is not comparable with a fully diffusive prescription since the meridional circulation is treated in a different manner.

[7]They exclude chemical mixing from the Taylor-Spruit dynamo due to its controversy.

were calibrated with one set of values for all initial masses, metallicity and initial rotation velocity, whereas they could vary with initial mass for example. In addition, the values are calibrated to the surface enrichment of helium and nitrogen, hence, the observations account for the rotational chemical mixing processes but do not cover the angular momentum transport processes. Moreover, the same value for f_c multiplies all diffusion coefficients and the same dependence on the chemical stratification is assumed. Lastly, different implementations of the diffusive scheme for rotational mixing might need different values for f_c and f_μ. Therefore, the two parameters in the Heger-implementation of rotational mixing are still uncertain and their impact on angular momentum transport needs to be discussed.

In this work, I keep $f_c = 0.0228$ and only investigate different values for f_μ. The reason for this is that f_c is multiplied to the rotational diffusion coefficient for chemical mixing but not to the viscosities for angular momentum transport. Therefore, the parameter f_c influences angular momentum transport only indirectly through the mixing of chemical elements, i.e. by reducing the chemical stratification where rotation-induced mixing is active. However, as discussed above, the bottlenecks for angular momentum transport are layers with a strong chemical stratification where chemical mixing is suppressed. Consequently, different choices of f_c do not greatly affect the overall distribution of angular momentum such as the fast rotating core. In contrast, different values for f_μ can allow for mixing in the regions with strong chemical stratification, hence, it crucially impacts the rotational chemical mixing and transport of angular momentum.

Fig.(IV.11) shows the rotation profile of the $15\,M_\odot$ models with the Tayler-Spruit dynamo and different values of f_μ. The comparison between this figure and Fig.(IV.2b) shows that a smaller f_μ, leads to a reduction of Ω and j in the core during the main-sequence evolution, hence, angular momentum is transported out of the core. The angular momentum transport becomes more efficient for lower values of f_μ. This is because f_μ reduces ∇_μ enough so that rotation-induced mixing is not suppressed anymore. Consequently, the angular momentum is transported more efficiently through the bottleneck layers. Additionally, the chemical composition is mixed throughout the envelope, leading to a much weaker chemical stratification and in turn more efficient rotational mixing. Indeed, comparing Figs.(IV.3b), (IV.12a) and (IV.12b) illustrates that a smaller f_μ is able to overcome the chemical stratification above the convective core that forms a bottleneck for chemical mixing and angular momentum transport. While for $f_\mu = 0.01$, the stratification is only partly overpowered, the radiative and convective boundary is fully mixed by the Eddington-Sweet circulation in the model with $f_\mu = 0.0001$ and $\log \nu_{\rm TSF}$ is smooth throughout the radiative envelope. The chemical mixing results in a smooth ∇_μ profile and a much weaker chemical stratification, because the model evolved closer to homogeneous - see discussion in Section I.4.2. In addition to the chemical mixing, the reduction of the chemical stratification also allows for more angular momentum to be removed from the core,

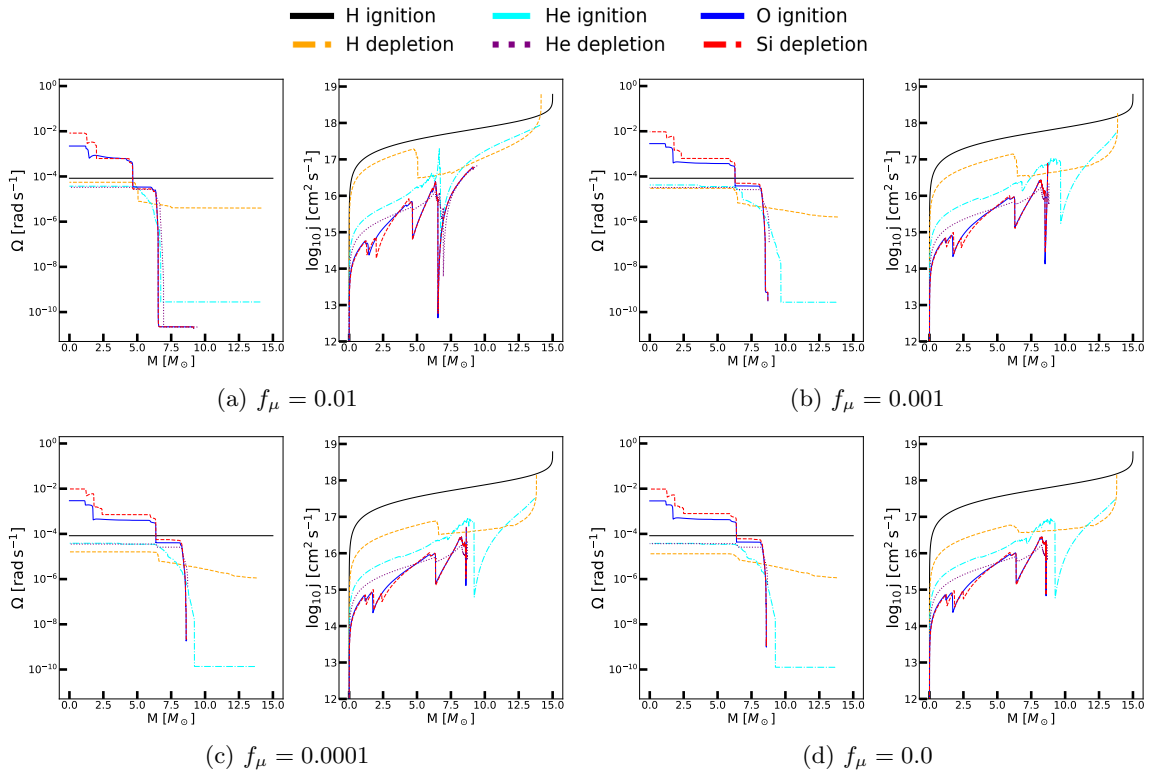

(a) $f_\mu = 0.01$ (b) $f_\mu = 0.001$

(c) $f_\mu = 0.0001$ (d) $f_\mu = 0.0$

Figure IV.11: The rotation profile of the 15 $M_\odot$ Tayler-Spruit model with different values of f_μ, showing for each subfigure the angular rotation velocity, Ω, on the left and the specific angular momentum, j, on the right. Each line represents the profile at a different evolutionary stage, indicated by the colour and the linestyle. For comparison reasons, the axes of each thematic subplot are scaled to the same values in this and in Fig.(IV.2).

as discussed above, due to the constant magnetic viscosity and the Eddington-Sweet circulation that is continuous in the radiative and convective boundary mixing region. However, as can be seen in Fig.(IV.12b), the largest difference in Ω remains in the convective boundary mixing zone, where the Tayler-Spruit dynamo is artificially suppressed. Therefore, the 15 $M_\odot$ model with the Tayler-Spruit dynamo and $f_\mu = 0.0001$ still has a faster core rotation at the end of the main sequence than the model with the Fuller-modified dynamo - but see discussion in Section IV.3.6. Nevertheless, the sharp rise in Ω between the interface of the convective core and the radiative envelope is spread out over a larger region. Therefore, the shear in each zone in this layer is weaker and in the model with $f_\mu = 0.0001$ the secular shear instability does not occur anymore.

Fig.(IV.2b) and Fig.(IV.11) both predict a similar rotation rate and angular momentum profile at core helium ignition, suggesting that during the post-main-sequence evolution the Tayler-Spruit models with a larger value for the f_μ parameter transport more angular momentum away from the core. The cause for this behaviour is the receding convective hydrogen core at the end of the main-sequence. In all models, the convective zone begins to recede and the core starts to contract due to the diminishing nuclear energy generation. The gravitational contraction of the core leads to an increase in the angular rotation rate due to conservation of angular momentum. In the default Tayler-Spruit model

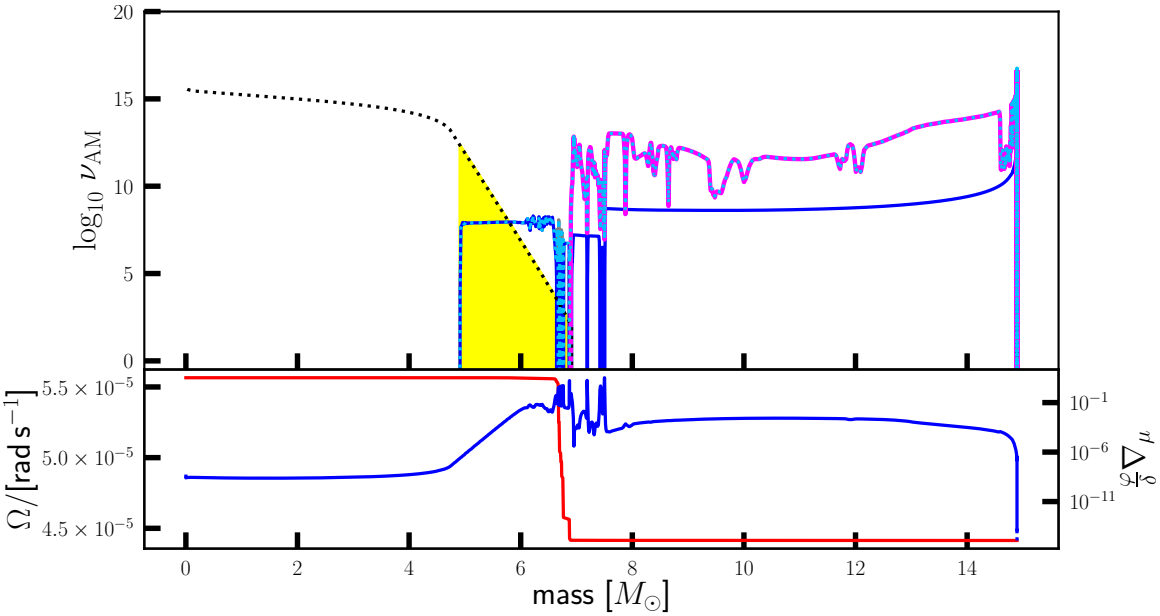

(a) $f_\mu = 0.01$

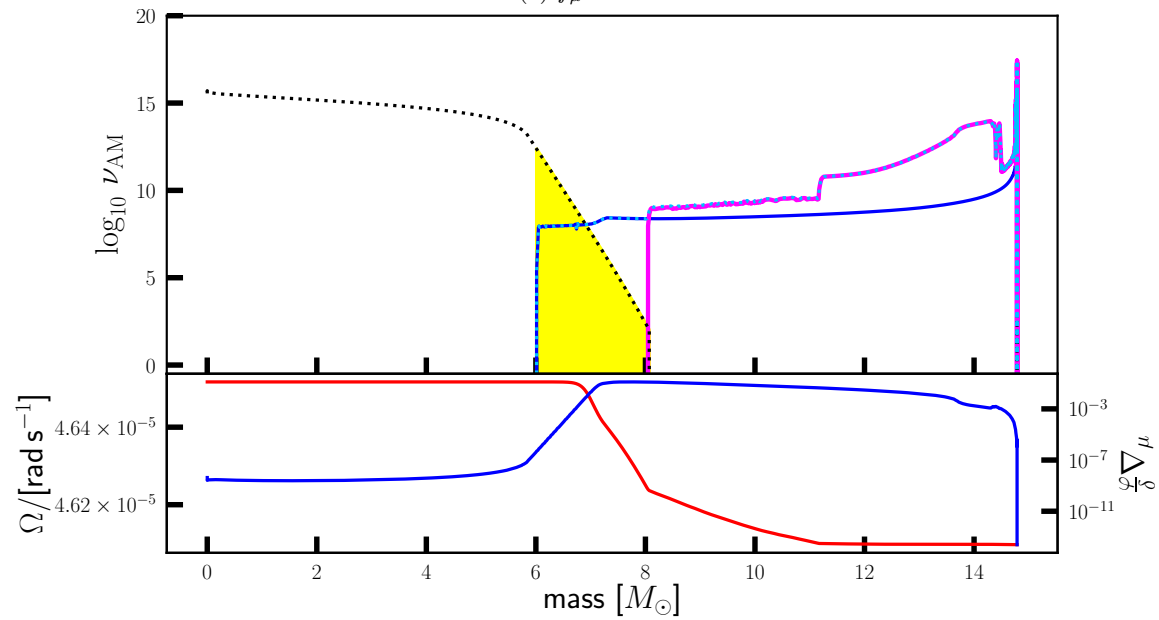

(b) $f_\mu = 0.0001$

Figure IV.12: The profile of the turbulent viscosity in the 15 $\mathrm{M}_\odot$ Tayler-Spruit model with different values of f_μ during the main-sequence evolution, when the central hydrogen mass fraction drops below 0.3. The colour and linestyle are the same as in Fig.(IV.3).

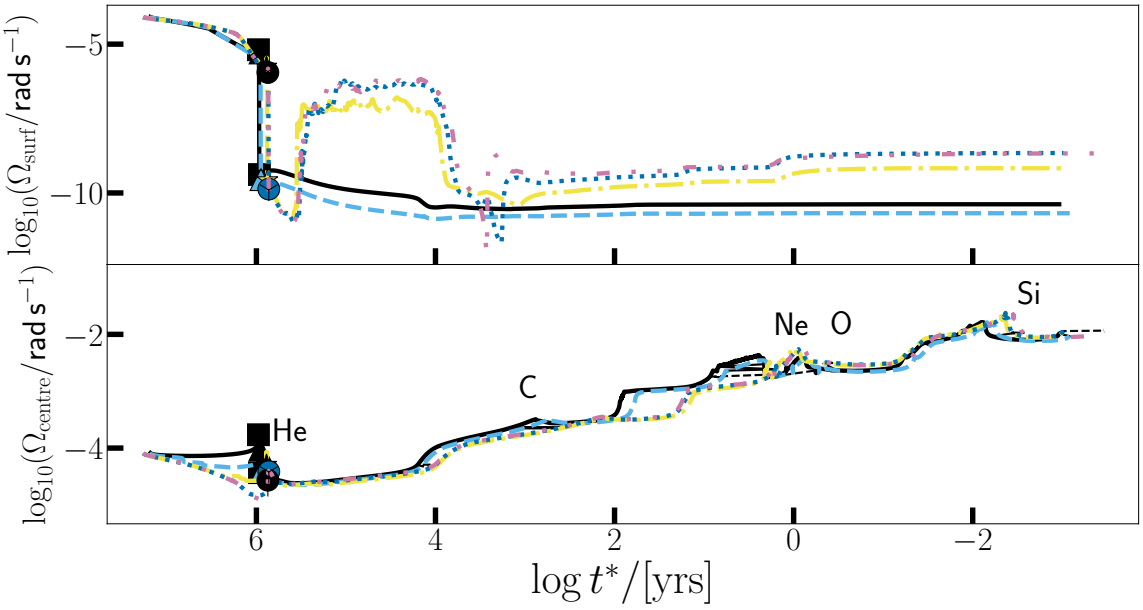

Figure IV.13: The evolution of the angular rotation velocity at the surface (top) and in the core (bottom) in the $15\,\mathrm{M}_\odot$ models with the Tayler-Spruit dynamo and different values for f_μ: 0.1 (black solid line), 0.01 (light blue dashed line), 0.001 (yellow dash-dotted line), 0.0001 (dark blue dotted line) and 0.0 (pink dashed-dotted-dotted line). The various overlapping markers indicate where hydrogen depletes (black) and where helium is ignited (coloured). The start of the various burning phases is labelled.

and the one with $f_\mu = 0.01$, the receding convective core experiences two minor growth phases on a short timescale (small compared to the time the convective core receedes), accompanied by a local expansion, before it completely vanishes. Therefore, Ω in the core region is redistributed, leading to a lower value in the inner core but a flatter profile up to the outer location of the minor core growth. After the convective core entirely disappeared, the core region contracts until helium burning is ignited and the angular rotation rate increases in all models. On the contrary, the convective core in models with $f_\mu \leq 0.001$ recedes smoothly without any disturbance, leading to an increase of Ω in the core. Consequently, the rotation rate at core helium ignition in all the Tayler-Spruit models with different f_μ is very similar despite the difference at core hydrogen depletion. Whether the behaviour of the receding convective core is physical or numerical is an open question and the investigation is beyond the scope of this thesis. It should be noted that this is a very sensitive phase, where the superadiabaticity $\nabla_{\rm rad} - \nabla_{\rm ad}$ is close to zero, hence, a small perturbation, numerical or physical, can lead to convection. Also, if rotational mixing ingests hydrogen into the receding convective core it can temporarily reignite the burning. On the other hand, if f_μ is small, rotational instabilities mixed the radiative region, thus, the hydrogen content above the convective core is much lower and it is harder to ingest fuel into the convective region.

Fig.(IV.2b) and Fig.(IV.11) show that the profiles of Ω and j during core helium burning and onward do not depend on the value of f_μ. Indeed, the rotation rate in the core evolves nearly independently of

f_μ (see Fig.(IV.13)) and the small differences are mainly due to the longer burning phase, hence a later contraction of the core thereafter. It might be expected that more angular momentum is transported from the core because (a) the chemical stratification in the radiative regions between the convective zones suppresses the transport instabilities less with lower f_μ and (b) the strength of the rotational diffusion coefficients is not sustainably changed. However, because the evolutionary timescale becomes shorter with each stage, the large scale rotation-induced transport processes, which operate on slower timescales, are not fast enough to diffuse angular momentum from the core. Therefore, the many convective shells become the dominant process for angular momentum transport during the advanced phases. On the contrary, the surface rotation rate in Fig.(IV.13) shows quite a different evolution. This, however, is not a result of angular momentum transport but a matter of the compactness of the envelope. While the models with $f_\mu \geq 0.01$ evolve directly to the red supergiant branch, where the envelope expands by several orders of magnitude, the models with $f_\mu \leq 0.001$ experience a quasi chemical-homogeneous evolution during core hydrogen burning. Consequently, they evolve into Wolf-Rayet stars shortly after the main sequence, which have a more compact envelope. The changes of the envelope between expansion and contraction lead to the change in $\Omega_{\rm surf}$ seen in Fig.(IV.13).
A similar behaviour is found in the non-magnetic and the Fuller-modified Tayler-Spruit models with smaller f_μ values, however, the conclusion for the total angular momentum transported is different due to the different nature of the models. In the *default* non-magnetic model with $f_\mu = 0.1$, nearly no angular momentum is transported from the core (see Fig.(IV.2a)) because of the prohibiting chemical stratification. Therefore, lowering the importance of the limiting stratification allows angular momentum to be transported from the core. Consequently, there is a significant reduction of angular momentum in the core during the main sequence. During the further evolution, the non-magnetic rotational instabilities are not fast enough to redistribute a significant amount of angular momentum - see discussion above - independent of f_μ. As a result, the core rotation in non-magnetic models is slower with a lower f_μ, contrary to the Tayler-Spruit dynamo. In the Fuller-modified Tayler-Spruit model, a lower f_μ allows for the Eddington-Sweet circulation to be active throughout the entire radiative envelope, which reduced the chemical stratification above the receding convective hydrogen core. This in turn reduces the chemical term of the Brunt-Väisälä frequency, N^2_μ, leading to a stronger magnetic coupling and more angular momentum transport during the main-sequence evolution. Therefore, the models with lower f_μ have a slower core rotation at the end of the main sequence, similar to the Tayler-Spruit dynamo. During the post-main-sequence phase, the Fuller-modified Tayler-Spruit model with the default f_μ value has a larger Ω in the core than the models with lower f_μ values. Consequently, the core contraction generates a higher angular rotation velocity and the rotation-induced instabilities, in particular the magnetic dynamo, produce stronger angular momentum transport in the core. As a result, the model with default f_μ predicts a similar Ω-profile in the core region at core helium ignition

as the models with lower values of f_μ. In the Fuller-modified Tayler-Spruit models, this occurs without the odd behaviour of the receding convective hydrogen core seen in the Tayler-Spruit models. In the envelope, the rotation profile differs due to the different structure, i.e. the models with $f_\mu \leq 0.001$ experience a quasi chemical-homogeneous evolution. However, the angular rotation velocity of the envelope is tiny in all models and the differences are negligible. In both the non-magnetic and the Fuller-modified Tayler-Spruit models the angular momentum transport during the advanced phases of stellar evolution is negligible due to the faster evolutionary timescale.

In summary, the different f_μ values influence when angular momentum is transported. While this leads to a different rotation rate in the non-magnetic models, the models including a magnetic dynamo do converge to roughly the same core rotation rate at helium ignition, nearly independently of f_μ. However, the structure of the stars is different due to the more efficient mixing during the main sequence - see Section V.2. Also, the Tayler-Spruit dynamo and the Fuller-modified Tayler-Spruit dynamo predict different amounts of angular momentum transport even if the impact of the chemical stratification is reduced. This is because the latter has a higher saturation level, generating a stronger magnetic torque and it operates on a shorter timescale.

3.6 The Taylor-Spruit Dynamo and Convective Boundary Mixing

In Section B.1.5.1, I discussed the fact that the implementation of the Tayler-Spruit dynamo is ignored in convective zones, in particular in convective boundary mixing regions, where $\nu_{\rm TS}$ is artificially set to zero. The result can be seen in Fig.(IV.3b) where the magnetic viscosity drops sharply at the outer edge of the convective zone. This creates a one-zone layer with inefficient angular momentum transport between the convective core, where transport occurs by turbulent motion, and the radiative envelope, where the magnetic dynamo operates. The theory of the Tayler-Spruit dynamo has been developed for the radiative zones of the star, where differential rotation winds up the magnetic field lines. It is therefore not applicable in the convective regions of the star where other magnetic dynamos can operate (see e.g. Spruit, 1999; Charbonneau, 2005, and citations therein for alternative theories). The magnetohydrodynamical coupling between a convective and radiative zone is still an open question (e.g. Wood & Brummell, 2018; Korre et al., 2021). The evolution of the large-scale magnetic fields not only depends on the interaction with the mean fluid flow but also on the fluctuation-induced electromotive force and the evolution of the flow depends on Reynolds and Lorentz stresses. In radiative zones these terms are likely negligible. However, at the interface between a radiative and a convective region they are expected to influence the evolution of the large-scale magnetic fields and flows due to convective boundary mixing. Therefore, the magnetohydrodynamical coupling between

a convective and radiative region will be a combination of interaction between large-scale fields and flows and small-scale fields and flows. Some of the fields can be produced by a dynamo action in the convective or radiative zone but part of the fields are also generated locally by the interaction of the convective boundary mixing motion with the large-scale magnetic field from the radiative layers. Up to date, there is no complete theory that allows to make predictions on the magnetic coupling between radiative and convective zones.

In order to investigate the possible impact of a magnetic dynamo in the convective boundary mixing region, I computed a $15\,M_{\odot}$ model where the Tayler-Spruit dynamo is computed in the convective boundary mixing region. I only include the dynamo action in the convective boundary mixing region because this is where the convective core generates shear, whereas the assumption of solid-body rotation in convective zones suppresses any shear in the rest of the convective core. The dynamo action in the convective boundary mixing layer is simulated in the same way as in the radiative layers. While this is a very crude, and most probably wrong approach, it nevertheless gives insight on how a possible magnetic dynamo, or another possible angular momentum transport mechanism, might affect the angular momentum distribution if it is able to operate in the bottleneck region. Fig.(IV.14a) shows the turbulent viscosity in the $15\,M_{\odot}$ model, which includes the Tayler-Spruit dynamo in the convective boundary mixing region. It can be seen that the magnetic dynamo operates in the convective boundary mixing zone, represented by the yellow shaded region, generating a magnetic viscosity, depicted by the solid magenta line. The dynamo action is only active in the very outer layers of the convective boundary region and is inert in the region closer to the convective zone. This is a result of the exponentially decaying mixing efficiency of the boundary mixing scheme, leading to a less efficient angular momentum transport further away from the Schwarzschild boundary which creates a gradient in the Ω profile, hence, shear. In the inner region, however, angular momentum is redistributed well enough to keep a constant angular rotation speed.

In the context of 3D hydrodynamic simulations of turbulent convective boundaries, this could be thought of in the following way. The region after the mixing-length boundary - the turning region in Section II.1.3 - is fully mixed and angular momentum is equally distributed, depending on the rotation law for convective bodies. In the region further out, where the flow turns around - the shear region in Section II.1.3 - the radial velocity is going to zero and the horizontal velocity dominates. This could produce a gradient in the angular momentum distribution, similar to the sigmoid-shape seen for the chemical species in 3D hydrodynamic simulations. Furthermore, the horizontal velocity introduces convective shear which could generate a dynamo action, or give rise to another instability, that transports angular momentum. Therefore, it is possible that there could be a dynamo active at the edge of the convective zone. However, the interaction between the convective and rotation-induced shear and possible magnetic fields is still an open question.

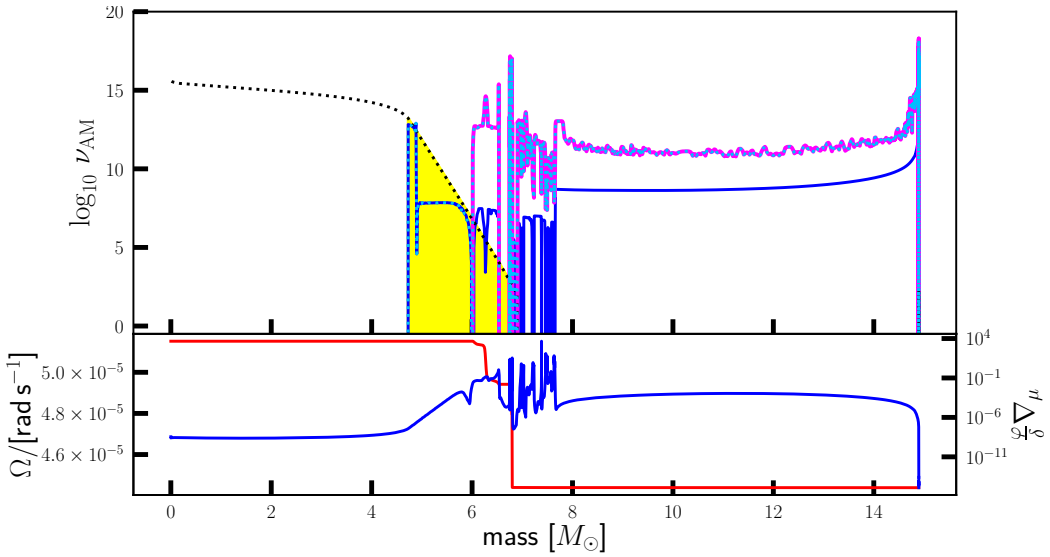

(a)

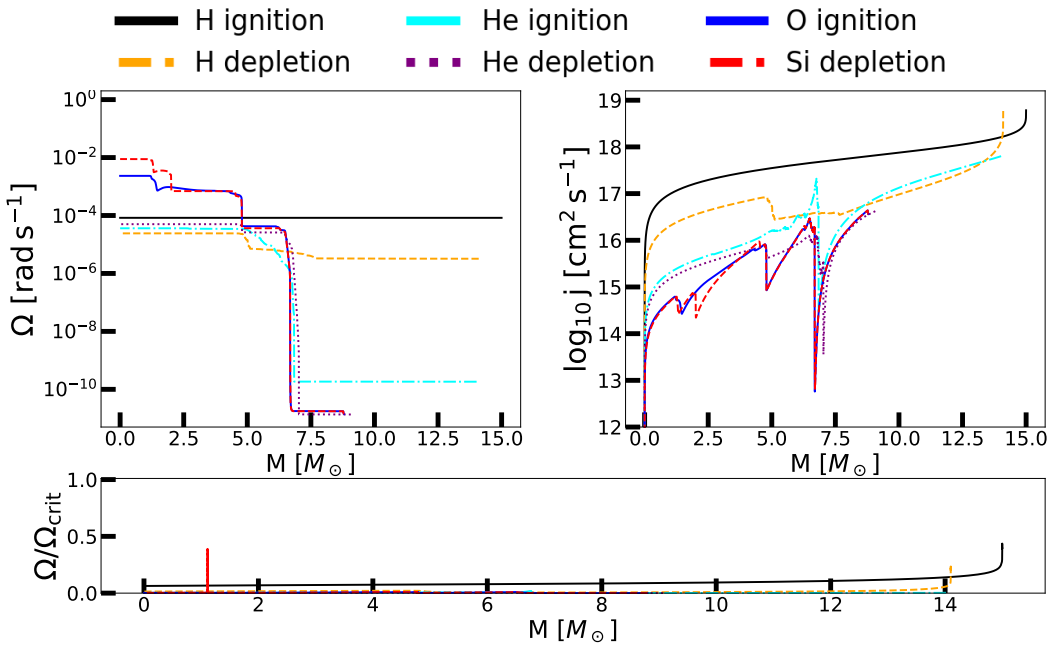

(b)

Figure IV.14: (a) The turbulent viscosity in the 15 $M_\odot$ model applying the Tayler-Spruit dynamo, including in the convective boundary mixing region. The figure is organised as Fig (IV.3). (b) The rotation profile of the 15 $M_\odot$ Talyer-Spruit model, including the dynamo in the convective boundary layer, showing on the top left panel the angular rotation velocity, Ω, on the top right panel the specific angular momentum, j, and on the bottom panel the ratio of the angular rotation velocity to the critical angular rotation velocity. Each line presents the profile at a different evolutionary stage indicated by the colour and linestyle. For comparison reasons, the axes of each thematic subplot group have been scaled to the same values. The ignition of a burning phase is defined as when 0.3% of the fuel is burnt and depletion when the fuel drops below 1%. The latter is early enough to avoid a spinning up of the core due to contraction after the burning phase ends.

Fig.(IV.14b) presents the evolution of the rotation profile in the $15\,M_\odot$ model with the Tayler-Spruit dynamo, including the magnetic dynamo in the convective boundary mixing region. Indeed, including the dynamo into the convective boundary mixing region allows the model to overcome the angular momentum transport bottleneck during the main sequence, reducing the angular momentum content of the core and slowing it down. The chemical stratification above the receding convective core limits the dynamo action which leads to a slower rotating envelope already during the main sequence. During the post-main-sequence evolution, the angular momentum in the core is further reduced, however, the core spins up due to contraction. Consequently, the model predicts a similar angular rotation profile as the default Tayler-Spruit model. Furthermore, during the advanced evolution, the evolutionary timescale is too short for the dynamo to effectively operate and there is no significant difference between the two models (compare Figs.(IV.2b) and (IV.14b)).

3.7 Convergence between the Magnetic Dynamos?

In the previous Sections, I first discussed the *default* version of the $15\,M_\odot$ model with the Tayler-Spruit model, pointing out the bottleneck in regions with a strong chemical composition gradient and the convective boundary mixing zone. This prevents the magnetic dynamo to transport any angular momentum between the core and envelope during the main-sequence evolution. Following this discussion, I investigated two options to overcome the bottleneck of angular momentum transport: a reduced impact of the chemical stratification by lowering the artificial parameter f_μ and allowing the Tayler-Spruit dynamo to be active in the convective boundary mixing region. Indeed, both options are able to reduce the specific angular momentum during the main sequence. This leads to the question whether the Tayler-Spruit dynamo is able to reduce the core spin to a similar extent as the Fuller-modified dynamo. Fig.(IV.15) presents the surface angular velocity, $\Omega_{\rm surf}$, and the angular velocity in the centre, $\Omega_{\rm centre}$, of the various models with a magnetic dynamo discussed in the previous Sections. The bottom plot clearly illustrates that during the main-sequence evolution the model with the default Tayler-Spruit dynamo maintains a nearly constant, slightly increasing $\Omega_{\rm centre}$, whereas the model with the default Fuller-modified Tayler-Spruit dynamo experiences a slowdown of $\Omega_{\rm centre}$. As expected, all the models that include a variation of the Tayler-Spruit dynamo to overcome the bottleneck of angular momentum transport reduce their $\Omega_{\rm centre}$ during the main sequence. Fig.(IV.15) includes (i) a Tayler-Spruit model where the dynamo action is included in the convective boundary mixing region - see Section IV.3.6 - (ii) a Tayler-Spruit model where the dependence of the rotation-induced instabilities on the chemical stratification is reduced, i.e. $f_\mu = 0.0001$[8] - see Section IV.3.5 - and (iii) a model that includes the first and second case. The three Tayler-Spruit variations evolve similarly during the main sequence regarding the core rotation. In the first half of main sequence

[8] I chose the model with $f_\mu = 0.0001$ because it represents the most optimistic case.

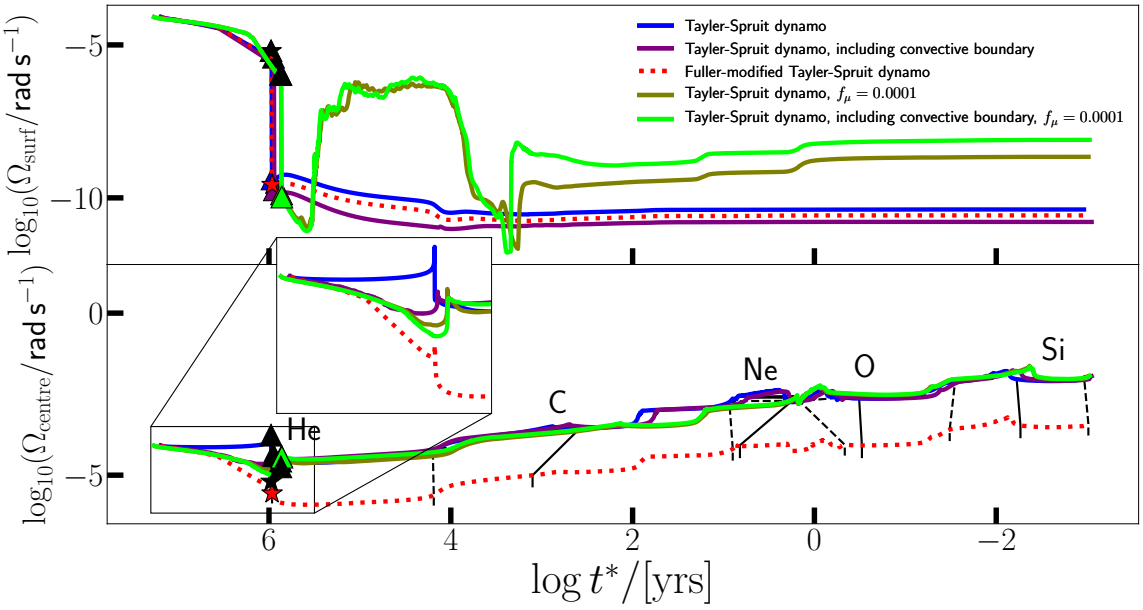

Figure IV.15: The evolution of the angular rotation velocity on the surface, top, and in the centre, bottom, in various 15 $M_\odot$ models with a magnetic dynamo as a function of the time left until the core collapses. The models include different versions of the magnetic dynamos discussed in the previous Sections, see the legend for details. The black marker indicate the depletion of hydrogen in the centre and the colored marker the ignition of helium in the core. The different burning stages are labeled. The inset window presents an enlarged view on the main-sequence and post-main-sequence evolution.

they have a similar reduction of $\Omega_{\rm centre}$ as the Fuller-modified dynamo. This is the result of angular momentum being transported through the region above the convective hydrogen core, which is restricted in the default Tayler-Spruit dynamo. However, beginning at the middle of the main-sequence lifetime the Fuller-modified Tayler-Spruit model shows a faster reduction of $\Omega_{\rm centre}$ compared to the variations of the Tayler-Spruit models, which all continue to slow down the core at the same rate. The difference arises from the amplitude of the coupling: in the model with Fuller-modified Tayler-Spruit model the dynamo creates a strong viscosity of the order of $\log \nu_{\rm TSF} \sim 15$ in layers with strong shear (see Fig.(IV.3c)) whereas in the models with the different versions of the Tayler-Spruit dynamo the magnetic viscosity is of the order of $\log \nu_{\rm TSF} \sim 10$ (see Figs.(IV.12b) and (IV.14a)). Consequently, the angular momentum distribution in the Fuller-modified model remains close to solid body rotation whereas in the different Tayler-Spruit models shear between core and envelope develops. The difference in $\Omega_{\rm centre}$ at the end of the main sequence between the Taylor-Spruit models results from the different efficiencies of angular momentum transport through the bottleneck region above the convective core. The model that includes the dynamo in the convective boundary mixing region and ignores the chemical stratification predicts the slowest core rotation at the end of the main sequence. During the post-main-sequence evolution the cores in the modified Tayler-Spruit models spin up, as explained in Sections IV.3.5 and IV.3.6, and they predict a similar angular rotation rate of the core during the further evolution as the default Tayler-Spruit model. Thus, in terms of final rotation rate

predicted by the models, there is no convergence between the Fuller-modified Tayler-Spruit dynamo and optimistic versions of the Talyor-Spruit dynamo, but between the different versions of the Taylor-Spruit dynamo. However, the different efficient coupling during the main-sequence evolution in the Taylor-Spruit model leads to slightly different evolution of the rotation rate. For example, the bottom plot in Fig.(IV.15) reveals that the contraction at the end of the advanced burning stages occurs at different times, indicating different burning lifetimes. Also, the surface rotation rate, $\Omega_{\rm surf}$, increases during core helium burning in the models with $f_\mu = 0.0001$, pointing out a contraction and expansion of the envelope. These differences will affect the evolution of the model.

Fig.(IV.15) shows that the chemically stratified region above the convective hydrogen core is one of the big problems in terms on angular momentum transport and a proper treatment of the chemical stratification and its impact on the rotation-induced angular momentum transport and chemical mixing would help in reducing the uncertainty of angular momentum transport by a magnetic dynamo.

4 Angular Momentum Transport at Lower Metallicities

In Section IV.3, I discussed how the evolution of the angular momentum distribution in higher mass stars at solar metallicity is influenced by strong mass loss. The question that naturally arises is how the angular momentum transport behaves at lower metallicities. In order to test the impact of lower initial metallicities on the distribution of angular momentum, I calculated the models presented in Section IV.3 at metallicities of $Z = 0.002$ and 0.0004. In terms on angular momentum transport, the main impact from the lower initial metallicity are the weaker stellar winds. In fact, the $15\,\mathrm{M}_\odot$ models at $Z = 0.0004$ show a very similar evolution of the angular momentum distribution to the $15\,\mathrm{M}_\odot$ models at solar metallicity. Since the mass-loss rates increase gradually with initial mass, I only discuss the change in angular momentum transport at lower metallicities in the $60\,\mathrm{M}_\odot$ models. The lower mass models in the sample show gradually reduced differences on the angular momentum distribution when changing the initial metallicity.

Fig.(IV.18) presents the evolution of the Ω and j in the $60\,\mathrm{M}_\odot$ models at $Z = 0.0004$ for the models with the three *default* angular momentum transport mechanisms. The shape of the rotation rate and the specific angular momentum profile in the non-magnetic model (see Fig.(IV.18a)) are more similar to the $15\,\mathrm{M}_\odot$ models because it does not lose angular momentum through stellar winds. Hence, the redistribution mainly occurs by rotation-induced hydrodynamic instabilities, which are not very efficient as discussed in the earlier Sections. The biggest difference in Ω is in the envelope, where in the low metallicity models the rotation rate does not drop as much. This is because the initial composition

contains less metals and therefore the opacity is lower - see Appendix B.1.2.0.1. Consequently, the envelope expands less, thus, Ω does not drop to the same low values. This difference exists for all the initial masses studied here. If the metallicity is increased to $Z = 0.002$, the mass loss is not negligible and a small amount of angular momentum is removed from the core. Also, the envelope expands more, leading to a slower surface rotation, before it is stripped away by stellar winds. It should be noted that at both lower metallicities the model reaches critical rotation in the envelope towards the end of their evolution, which drives strong rotation-induced mass loss.

The angular rotation rate and specific angular momentum distribution in the $60\,M_\odot$ models with the Tayler-Spruit dynamo at $Z = 0.002$ and 0.0004 evolve very similar to the respective model at solar metallicity. The main difference is that the model at solar metallicity loses more mass during core hydrogen burning. However, both lower metallicity models lose a substantial part of their mass during core helium burnin g. The reason for the high mass-loss rates at low metallicity is the formulation and implementation of the mass-loss rates for red supergiants - see also Appendix B.1.6: when the effective temperature drops below $\log T_{\rm eff} < 4.08$ the `MESA` code smoothly switches to the red supergiant mass-loss rates given by Eq.(B.59), which is fully active for $\log T_{\rm eff} < 3.9$. Furthermore, the mass-loss recipe for red supergiants by de Jager et al. (1988) does not include a metallicity dependence, hence, it predicts the rates on mass and luminosity alone, see Eq.(B.59). The low metallicity $60\,M_\odot$ models with the Tayler-Spruit dynamo both evolve to $\log T_{\rm eff} < 3.9$ after the main sequence, where they ignite helium burning and do not return back to effective temperatures of $\log T_{\rm eff} > 4.08$. This is because they have a short and weak intermediate convective zone, see discussion in Chapter III and Section V.2. Therefore, they experience a strong red supergiant mass loss, despite not being on the red supergiant branch, showing the need for a revision of the mass-loss recipes in the region $\log T_{\rm eff} < 4.1$. In this case, an overestimation of the stellar winds leads to a wrong prediction of the angular momentum transport during the evolution of massive stars at low metallicity and could affect predictions of low-metallicity black hole spins.

The $60\,M_\odot$ models with the Fuller-modified Tayler-Spruit dynamo at $Z = 0.002$ predict a very similar evolution of the angular rotation velocity and specific angular momentum distribution compared to the solar metallicity model but less mass loss. The same could be said for the model at $Z = 0.00004$, but there the angular momentum profile is higher at the end of core hydrogen burning. This, however, is a result of the timing when contraction at the end of the main sequence begins and the shear between core and envelope increases, similar to the $30\,M_\odot$ models. Indeed, once central helium burning ignites, the angular momentum profiles are similar once again until the end of silicon burning. In the envelope, the angular rotation velocity profile remains mostly flat until the helium burning phase because of the reduced expansion of the envelope at lower metallicity. This allows for more angular momentum transport by the Eddington-Sweet circulation, $\nu_{\rm ES} \propto \Omega^2$, but reduces the strength of the magnetic

dynamo which depends on the shear.

In summary, at lower metallicity where the stellar wind are weaker, the angular momentum transport is dominated by rotation-induced instabilities in massive stars, contrary to solar metallicity where mass loss has a crucial impact on the rotation rate. However, due to the formulation and implementation of stellar winds in the stellar evolution code, some of the low metallicity models still experience a modest mass loss, which blurs this picture.

The points discussed above lead to different predictions of the rotation rate at silicon depletion and finally the spin of the final compact object. Generally, the models at lower metallicity have a faster rotation rate and more angular momentum in the core. The exception is the Tayler-Spruit model at $Z = 0.0004$ which predicts a slower rotating core due to the behaviour of the stellar wind mentioned above. If the mass-loss rates in the region $\log T_{\rm eff} < 4.1$ would include a metallicity dependence, this model would most probably follow the same trend as the other models. Therefore, the $60\,M_\odot$ models predict faster rotating cores at lower metallicities, hence, faster spinning compact objects at the end of their life. This discrepancy with metallicity disappears with decreasing initial mass.

5 Dependence of Angular Momentum Transport on the Initial Rotation Speed

Stars are observed to rotate at different speeds on the main sequence with typical rotation rates between $0 - 250\,\mathrm{km\,s^{-1}}$ (e.g. Huang & Gies, 2006a; Hunter et al., 2008; Dufton et al., 2013). It is therefore of interest to know how the evolution of different initial rotation rates is affected by the three angular momentum transport mechanisms discussed in the earlier Sections and what the predicted pre-supernova spin is.

Fig.(IV.16) presents the specific angular momentum at hydrogen, helium and silicon depletion in $32\,M_\odot$ model at the metalicity $Z = 0.002$ for the three angular momentum transport mechanisms. These models are published in Belczynski et al. (2020a). Fig.(IV.16a) shows that at the end of the main sequence the angular momentum distribution in the models depends on the initial rotation rate and the angular momentum transport mechanism, with no strong trend. However, the angular momentum distribution in the inner part of the star after the core helium burning phase, presented in Fig.(IV.16b), clearly depends on the transport mechanism and is mostly independent of the initial rotation. This convergence of the rotation rate for a given angular momentum transport mechanism is a result of the dependence of (a) the rotation-induced instabilities on the rotation rate and the shear, which becomes stronger in faster rotating models, and (b) the rotation-enhanced winds on the initial rotation rate. In fact, a faster initial rotation leads to enhanced mass-loss rates during

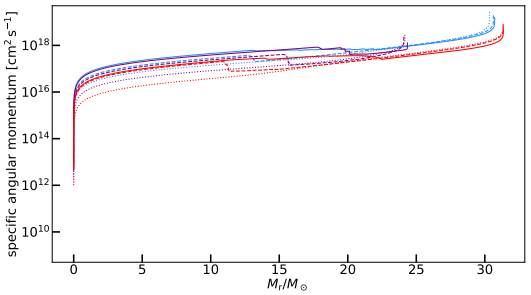

(a) hydrogen depletion

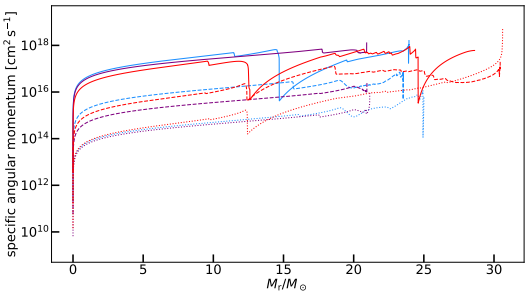

(b) helium depletion

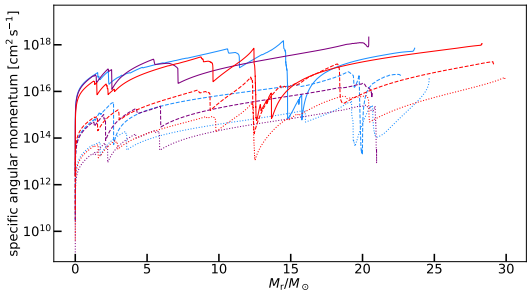

(c) silicon depletion

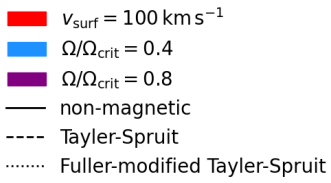

Figure IV.16: The profile of the specific angular momentum in the 32 $M_\odot$ models of the three angular momentum transport processes with different initial rotation rates. Each plot presents the profile at a different stellar stage. The dominant transport mechanism is indicated by the linestyle and the initial rotation by the colour scheme.

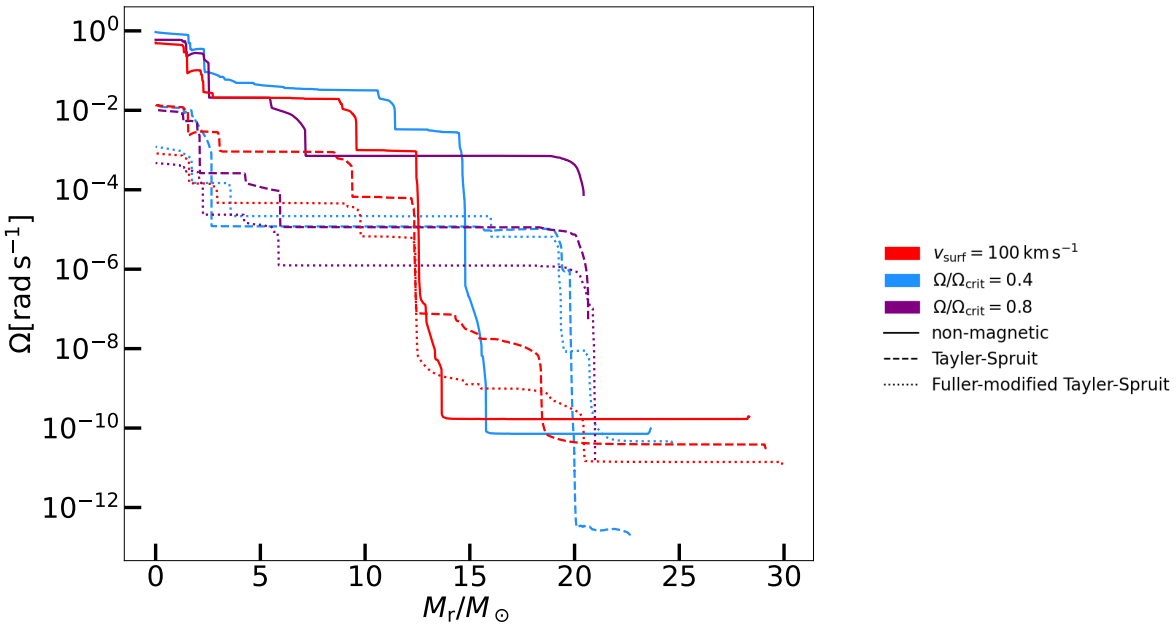

Figure IV.17: The profile of the angular rotation rate in the 32 $M_\odot$ models for three *default* angular momentum transport processes with different initial rotation rates at silicon depletion. The linestyle depicts the dominant angular momentum transport mechanism and the colour scheme indicates the initial rotation rate.

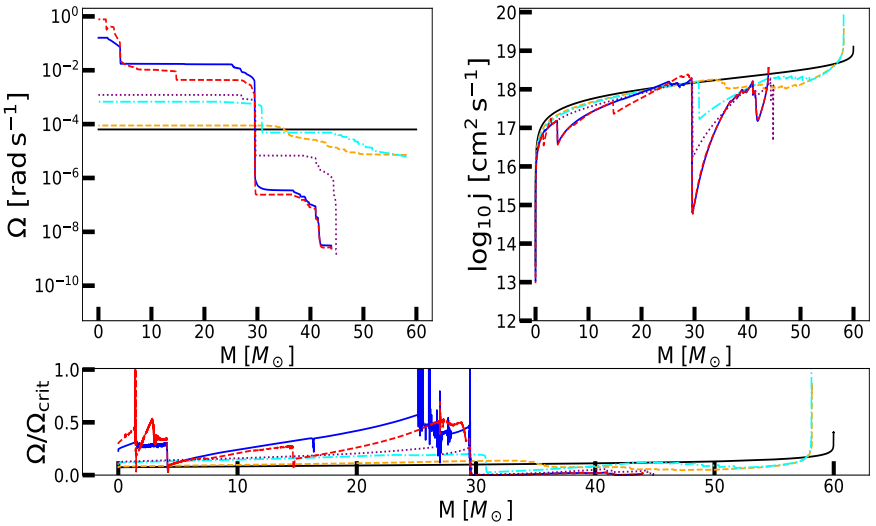

(a) no magnetic fields

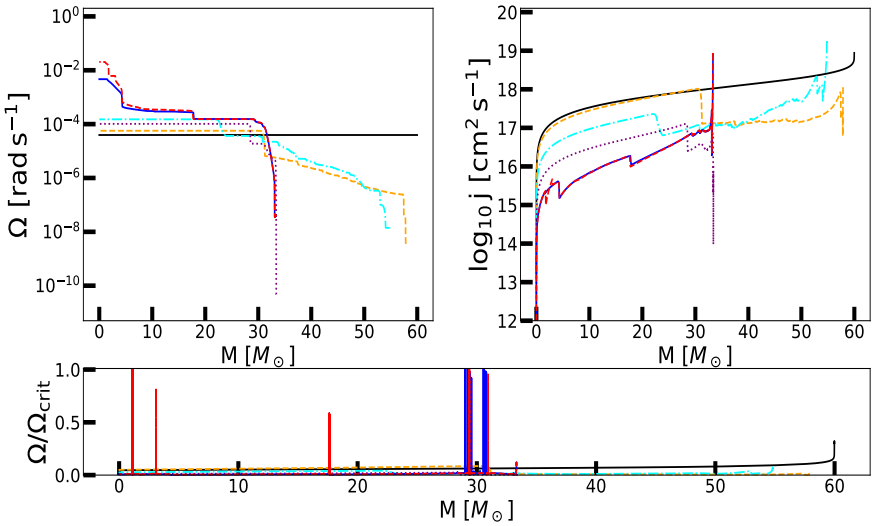

(b) Taylor-Spruit dynamo

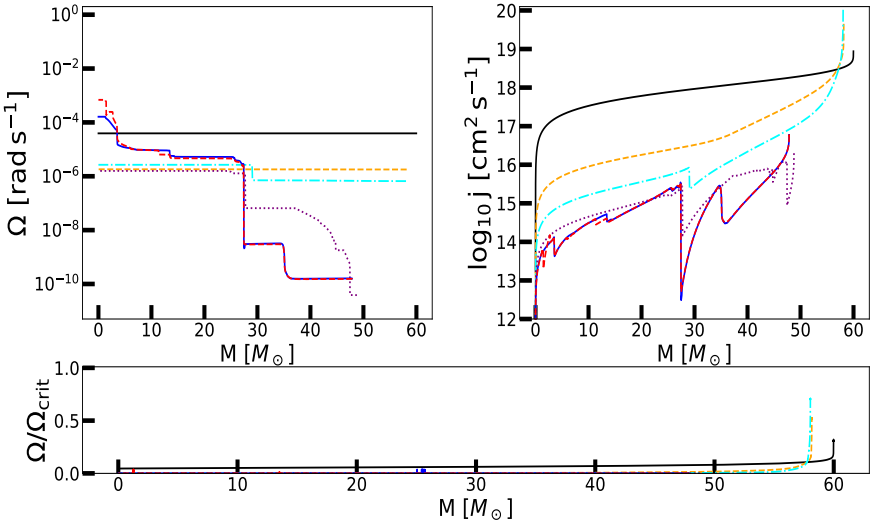

(c) Fuller-modified Taylor-Spruit dynamo

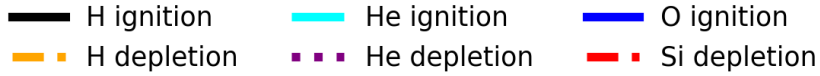

Figure IV.18: The rotation profile of the 60 $M_\odot$ models at a metallicity of $Z = 0.0004$ for the different angular momentum transport mechanisms, showing on the top left panel the angular rotation velocity, Ω, on the top right panel the specific angular momentum, j, and on the bottom panel the ratio of the rotation rate to the critical rotation rate. Each line presents the profile at a different evolutionary stage indicated by the colour and linestyle. For comparison reasons, the axes of each thematic subplot group have been scaled to the same values. The ignition of a burning phase is defined as when 0.3% of the fuel is burnt and depletion when the fuel drops below 1%.

also Section V.2.

6 Conclusion and Discussion

In this Chapter, I presented rotating stellar models of different initial masses, each of which was computed with three different angular momentum transport mechanisms, in order to study the uncertainty of the angular momentum distribution during the evolution of massive stars. The three transport mechanisms are (1) hydrodynamic instabilities, (2) hydrodynamic instabilities and the Tayler-Spruit dynamo and (3) hydrodynamic instabilities and the Fuller-modified version of the Tayler-Spruit dynamo. In this Chapter I focussed the discussion on the angular momentum distribution and evolution of rotation. The impact of the uncertainties in the different transport mechanisms on the structure and evolutionary path of massive stars will be investigated in future work.
The behaviour of the *default* models can be summarised as follows:

1. The default versions of the three angular momentum transport mechanisms predict three distinct core spins at the end of their evolution when they begin to collapse. The model with the purely hydrodynamic angular momentum transport predicts the fastest core rotation, whereas the Tayler-Spruit dynamo estimates a medium value and the Fuller-modified Tayler-Spruit dynamo the slowest.

2. In general, most of the angular momentum transport occurs before core helium depletion. Thereafter, the evolutionary timescales become much faster and large-scale angular momentum transport becomes negligible. During the advanced stellar phases, the core spins up by several orders of magnitude due to contraction and conservation of angular momentum.

3. The default implementations of the three mechanisms transport angular momentum during different stages. The hydrodynamic instabilities alone do not efficiently transport angular momentum and the initial angular momentum content of the core is only slightly reduced. The Talyer-Spruit dynamo transports a large amount of angular momentum during the post-main-sequence evolution, before helium ignites in the centre, and a small amount during all the subsequent phases up to core oxygen ignition. It removes about three orders of magnitude of angular momentum from the core, reducing the spin of the core by about two orders of magnitude compared to the non-magnetic models. However, this magnetic dynamo is not able to extract angular momentum from the core during the main-sequence evolution because of (a) the inhibiting chemical stratification above the convective core and (b) the convective boundary mixing region where the magnetic dynamo is ignored. The Fuller-modified Tayler-Spruit dynamo efficiently removes angular momentum from the core during the main-sequence and

post-main-sequence evolutionuntil helium ignites in the core and smaller amounts in the ensuing phases up to core oxygen ignition. It is able to reduce j in the core by more than four orders of magnitude. The efficient transport of angular momentum maintains a near-solid body rotation during the main-sequence phase and a comparatively low Ω during the further phases. The final core spin is more than three orders of magnitude lower compared to the model with hydrodynamic instabilities only.

4. The core spin at collapse of a model with a given angular momentum transport mechanism is nearly independent of the initial rotation. However, the models experience different amounts of spin-down during their evolution, hence, the distribution of angular momentum during these phases differs. This affects the structure of the star.

5. The initial metallicity of the stellar models mainly influences rotation through the strength of stellar winds, which remove angular momentum from the surface. The impact is dominant in the $60\,M_\odot$ models and becomes gradually weaker for the lower initial masses.

Angular momentum transport in massive stars depends strongly on the treatment of the chemical stratification that develops above the convective core during the main sequence. This layer, plus the fact that the magnetic dynamo is ignored in the convective boundary mixing zone, creates a bottleneck in angular momentum transport that leads to the separation between core and envelope rotation. Indeed, I find that if the inhibiting effect of the stratification is reduced, implemented by a lower f_μ parameter, the Tayler-Spruit dynamo in combination with the rotation-induced hydrodynamic instabilities is able to transport a substantial amount of angular momentum during the main-sequence stage. Similarly, including the Tayler-Spruit dynamo into the convective boundary mixing region - a crude estimate to couple the differential rotation introduced by this region and the magnetic dynamo - leads to a reduction of more than an order of magnitude in j. Interestingly enough, a more efficient angular momentum transport during the main sequence reduces the shear developing during the post-main-sequence phase. Therefore, the magnetic dynamo is relatively weaker during this phase. Consequently, the modified models with the Tayler-Spruit dynamo predict a similar angular momentum content and rotation rate of the core as the *default* model with the Tayler-Spruit dynamo. Therefore, for a given initial mass, each angular momentum transport flavour predicts a distinct range of spins of the core at collapse, only weakly varying with the uncertainties studied in this Chapter. However, the evolutionary path of the star depends on the uncertainties, as angular momentum is transported during different phases.

This Chapter shows that the treatment and prediction of rotation in stellar evolution codes is highly uncertain and much effort is needed to improve it. One needed improvement is the dependence of the

rotation-induced mixing on the chemical stratification. First, the Heger et al. (2000) implementation of some rotational-induced instabilities accounts for the limiting effect of the chemical stratification via a "braking velocity" - see Section II.2. This overestimates its inhibiting effect, creating the bottleneck in angular momentum transport above the convective hydrogen core seen in this Chapter. Second, the chemical composition gradient is multiplied by a factor f_μ in some rotation-induced instabilities in order to reduce its limiting effect - see Section II.2 for more details. The choice of this free parameter influences the amount of mixing that occurs in chemically stratified regions. It is therefore crucial to constrain its value or replace it with a physical formulation. In addition, if the chemical composition gradient is considered through the Brunt-Väisälä frequency, $N^2 = \frac{g\delta}{H_P}\left(\nabla_{\rm ad} - \nabla_{\rm rad} + \frac{\varphi}{\delta}\nabla_\mu\right)$, the ∇_μ is not multiplied by f_μ. Therefore, the limitation of the chemical stratification is not taken into account consistently in the various rotation-induced instabilities - a fact that should be improved. There are theories and implementations of rotational instabilities that consider the gradients in chemical composition as physical effects (see e.g. Chaboyer & Zahn, 1992; Zahn, 1992; Maeder & Zahn, 1998)[9], hence, an update of the Heger et al. (2000) implementation in the `MESA` code is needed.

Another uncertainty in the rotation scheme implemented in `MESA` is the free parameter f_c, which is multiplied to the sum of the diffusion coefficients generated by rotational instabilities. This parameter is introduced, as well as f_μ, to account for the *order-of-magnitude* estimates of the rotation-induced mixing efficiencies (see Eq.(B.40)). Introducing non-physical parameters is tricky, because they can be used to do anything. There are several publications that try to constrain f_c and f_μ (e.g. Pinsonneault et al., 1989; Heger et al., 2000; Yoon et al., 2006; Brott et al., 2011; Chieffi & Limongi, 2013). However, calibration is difficult because the observed effects used are also dependent on other uncertain physics, for example convective boundary mixing, and a solution might not be unique. Furthermore, calibration of the two parameters with a certain observation does not necessarily reproduce other observations nor does it have to be true for other initial conditions such as mass or metallicity or evolutionary stages. Additionally, one parameter, f_c, is used to correct the sum of all diffusion coefficients for rotation-induced chemical mixing, despite the fact that some need different scaling and some do not need rescaling at all. For example, the diffusion coefficient for chemical mixing generated by the Tayler-Spruit dynamo, $D_{\rm TS}$ in Eq.(II.59), is computed within a factor of unity (§3.2 Spruit, 2002) and does not need to be rescaled.

Both the magnetic dynamos studied in this Chapter use numerical smoothing - see Sections B.1.7 and B.2.1. In the case of the Tayler-Spruit dynamo, numerical smoothing is needed to obtain a large-scale angular momentum transport by the dynamo action. On the other hand, too much smoothing leads to the dynamo being active in "*forbidden*" regions - see Section IV.3.4. The dependence of the implementation of the dynamo on numerical smoothing indicates the theory itself needs revision. A first

[9]Note that the implementations in the named publications are for the advective-diffusive scheme.

step could be to implement a general description of the Tayler-Spruit dynamo (as for example done by Maeder & Meynet, 2004, 2005) rather than the inaccurate formulation in `MESA`, which patches together two different regimes - see Section II.3.1.2.1. The Fuller-modified Taylor-Spruit dynamo also includes a numerical smoothing routine. In this case, the *default* implementation leads to a non-physical reduction of the magnetic viscosity in some layers - see discussion in Section IV.3.4. Excluding the smoothing process in the simulation removes this behaviour but introduces thin layers with a very strong dynamo action, which might not be physical either. The problem with the simulation of a magnetic dynamo in a stellar evolution code is the fact that the magnetic fields themselves, and their effects such as the torque, are not directly simulated. Instead, only the resulting magnetic viscosity and diffusion coefficient are computed in a region where the shear exceeds a minimum shear for the dynamo to be active. Consequently, the transport process needs to be smoothed over the other cells in order to generate a large-scale transport, otherwise the dynamo action is not able to generate an efficient angular momentum transport.

6.1 The role of $q_{\rm min}$ in the Fuller-modified Tayler-Spruit dynamo

The theory of the Fuller-modified Tayler-Spruit dynamo only allows for an active magnetic dynamo when the shear, q, is larger than a minimum shear, $q_{\rm min}$ (see Eq.(II.68)). In Section B.2.1 I explained that the current implementation does not check for this condition (see Fuller et al., 2019, Appendix D1)[10]. Therefore, the magnetic dynamo can be active in regions where the shear is not sufficiently strong. This could lead to an overestimation of the angular momentum transport by the Fuller-modified Tayler-Spruit dynamo. In the following, I present a short discussion on a model that includes the condition of $q > q_{\rm min}$ for the Fuller-modified Tayler-Spruit dynamo to be active. Note that this study is preliminary and further work is needed.

Fig.(IV.20) presents the profile of the turbulent viscosity in the models applying the Fuller-modified Tayler-Spruit dynamo, which includes the $q_{\rm min}$ condition and excludes numerical smoothing - for the latter see Section IV.3.4. The profile is shown at three different stellar phases, during core hydrogen burning, during the post-main-sequence evolution and when the star burns helium in the core. The $q_{\rm min}$ condition prevents the magnetic dynamo from being active in regions where the shear is not strong enough to generate a dynamo action, i.e. no magnetic dynamo where $q < q_{\rm min}$. Comparing Fig.(IV.20) to Figs.(IV.3c), (IV.4c) and (IV.5c) reveals that the magnetic dynamo is not always active if the $q_{\rm min}$ condition is considered. For example, during core hydrogen burning the Fuller-modified dynamo is only active in a thin layer below the large-scale Eddington-Sweet circulation in the envelope.

[10] All subsequent papers that use this implementation will have the same issue.

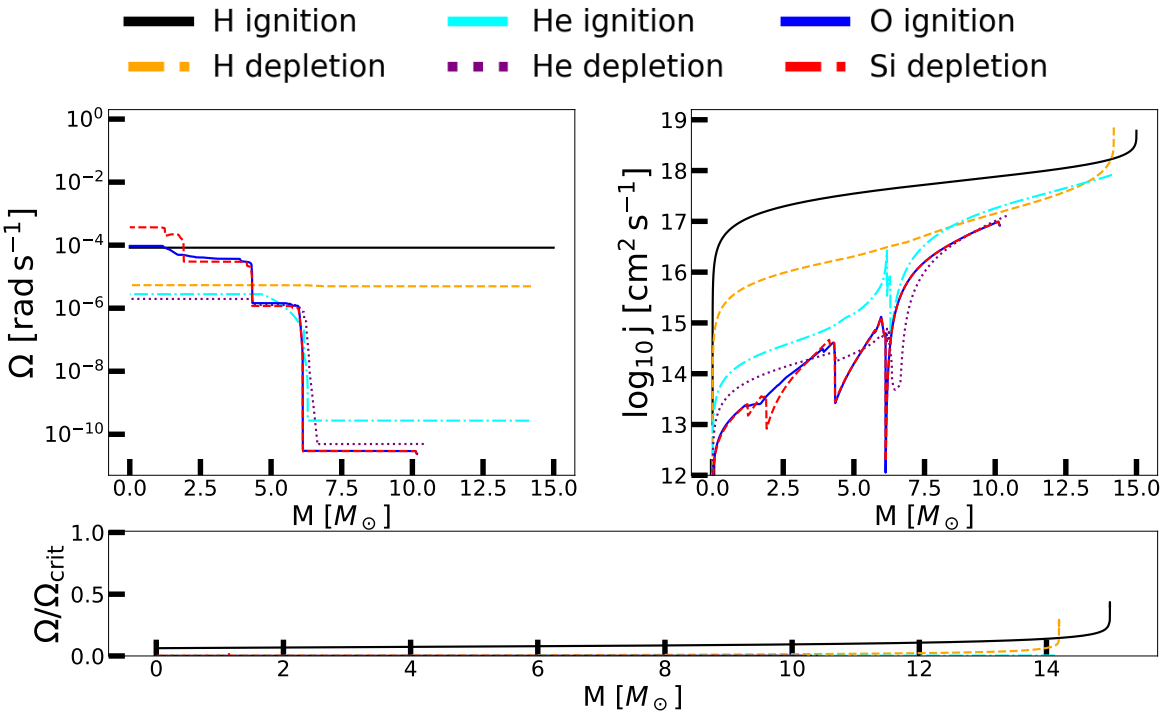

Figure IV.19: The rotation profile of the 15 $M_\odot$ model with the Fuller-modified Tayler-Spruit dynamo that includes the $q_{\min}$ condition and excludes numerical smoothing. The top left panel shows the angular rotation velocity, Ω, the top right panel the specific angular momentum, j, and on the bottom panel the ratio of the angular rotation velocity to the critical angular rotation velocity. Each line presents the profile at a different evolutionary stage indicated by the colour and linestyle. The ignition of a burning phase is defined as when 0.3% of the fuel is burnt and depletion when the fuel drops below 1%.

This is the only location where the gradient in the rotation profile is strong enough to trigger the dynamo action. In the envelope, Ω experiences a tiny gradient but is close to solid-body rotation due to the Eddington-Sweet circulation. Similarly, the core rotates close to solid-body due to the convective motion that efficiently redistributes angular momentum. Therefore, the region where the shear rises above the minimal shear during the main sequence is in the intermediate region. As soon as the criterion $q > q_{\min}$ is satisfied, a strong viscosity is generated with log $\nu_{\rm TSF} > 16$ which keeps the layer between the core and the envelope close to solid-body rotation. In between core hydrogen and core helium burning, the $q_{\min}$ condition is met throughout the entire star and the magnetic dynamo generates strong viscosity throughout the star, transporting a similar amount of angular momentum as in Fig.(IV.10a). During core helium burning, the $q_{\min}$ condition is satisfied in nearly all of the radiative zone between the convective core and envelope, with the exception of a few narrow layers. At these locations, the chemical stratification leads to a reduction of $\nu_{\rm TSF}$ (see Fig.(IV.10b)). Consequently, the resulting transport of angular momentum during core helium burning is very similar in the models with and without the $q_{\min}$ condition. A similar behaviour occurs during the subsequent phases of stellar evolution in terms of magnetic dynamo and angular momentum transport. Therefore, the $q_{\min}$ condition can affect the local strength of $\nu_{\rm TSF}$, however, the difference for $\nu_{\rm AM}$ is not strong enough

and the overall rotation rates do not change significantly, as can be seen by comparing Figs.(IV.2c) and (IV.19). Nevertheless, even if excluding the $q_{\rm min}$ condition does result in the similar outcome does not mean it is justified to do so. The stellar model should simulate the physics correctly and in the derivation of the magnetic dynamo it was assumed that the dynamo action is only active in regions where $q > q_{\rm min}$. Consequently, it is essential to include the $q_{\rm min}$ condition in the computation of magnetic stellar models.

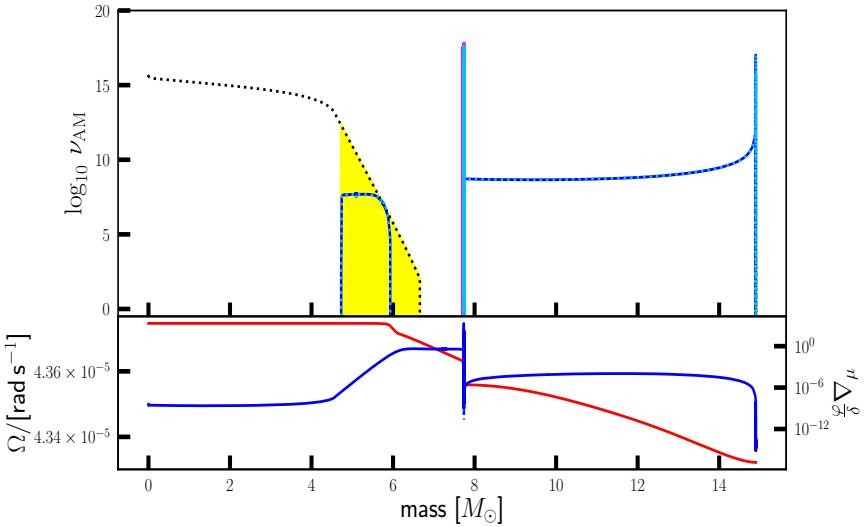

(a) core hydrogen burning

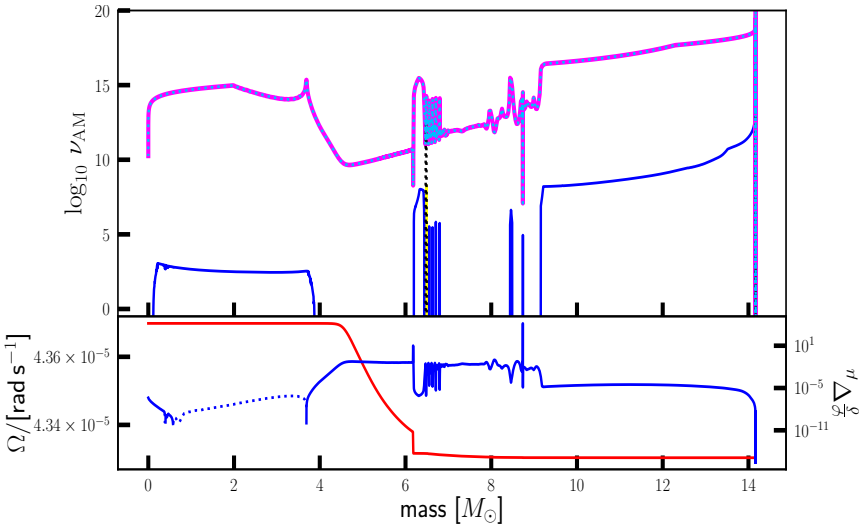

(b) post-main sequence

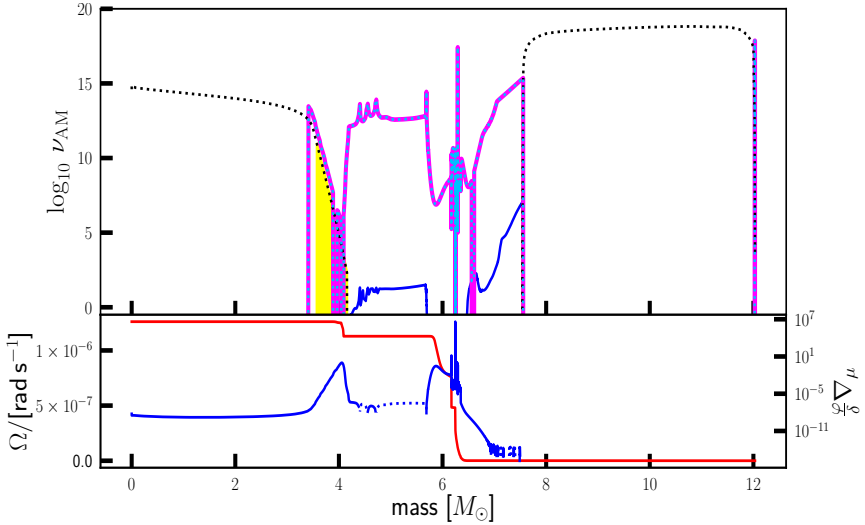

(c) core helium burning

Figure IV.20: The profile of the turbulent viscosity in the 15 $M_\odot$ model with the Fuller-modified Tayler-Spruit dynamo that includes the $q_{\min}$ condition and excludes numerical smoothing. $\nu_{\rm AM}$ is shown (a) during core hydrogen burning when the hydrogen mass fraction drops below 0.3, (b) during the post-main-sequence evolution and (c) during core helium burning when the hydrogen mass fraction drops below 0.4. Each top panel shows the total turbulent viscosity generated by non-rotating sources such as convection (black dotted line) and the turbulent viscosity generated by rotation-induced instabilities (sky-blue dotted line). Additionally shown are the turbulent viscosities generated by each rotation-induced instability, the viscosity produced by the Eddington-Sweet circulation (dark-blue solid line), the secular shear instability (grey solid line) and the magnetic dynamo (magenta solid line). The yellow shaded region indicates the location of convective boundary mixing regions. The bottom panel depicts the rotation rate and the gradient in the chemical composition. A dotted line for $\frac{\varphi}{\delta}\nabla_\mu$ stands for negative values. It should be noted that the range of the axis in the bottom panel varies between the figures.

Chapter V

Conclusion and Outlook

In this Thesis, I investigated two groups of internal mixing processes in massive stars: convection and rotation. I focussed the study on convective boundary mixing and angular momentum transport by rotation-induced instabilities, exploring their uncertainty and impact on stellar evolution. I examined the two physical processes separately, in order to study them without interference between the two.

Convective boundary mixing is discussed in Chapter III. I investigated how the location of the convective boundary and different amounts of convective boundary mixing affect the structure and evolution of massive stars. I found that while the boundary location converges during core hydrogen burning with more convective boundary mixing, there is a divergence in the subsequent evolution. Moreover, the behaviour of the intermediate convective zone and how it interacts with the hydrogen burning shell is a crucial phase for the further evolution of the star. In total, the core masses experience an uncertainty of up to $\sim$ 70% at core helium depletion. Furthermore, the surface evolution of stars, such as the main-sequence width and blue versus red supergiant evolution, depend critically on the mixing choices. Hence, these uncertainties affect the lifetimes in regimes with different surface temperatures and star radii. Since the mass-loss rates depend strongly on the location in the Herzsprung-Russell diagram, the mixing choice further affects these observables through mass-loss. Comparison between model predictions and spectroscopic observations of the main-sequence width and asteroseismic observations of convective core masses suggest that models require larger amounts of convective boundary mixing during their main-sequence evolution than currently adopted in the literature. Therefore, studies focusing on the later stages or the final fate of massive stars need to be revised to have a more accurate understanding of massive star evolution.

In Chapter IV, I investigated rotation-induced instabilities and how related theoretical and implementation uncertainties affect the transport of angular momentum. I limited this study to hydrodynamical instabilities and two magnetic dynamos, the Tayler-Spruit dynamo (Spruit, 2002) and the Fuller-modified Tayler-Spruit dynamo (Fuller et al., 2019). The three transport processes predict dis-

tinct ranges of the core rotation rate at core collapse. However, the timing and strength of angular momentum transport during the evolution of the star depends strongly on the transport mechanism and its uncertainty. Generally, the main transport of angular momentum occurs before core helium ignition and no angular momentum is transported after core oxygen ignition.

This work presents the uncertainty of stellar evolution models and their predictions, generated by the uncertainties of convective boundary mixing and rotation-induced mixing. It is clear that the evolution of massive stars is strongly influenced by the uncertain implementation of these physical processes, be it either the simplification of 3D processes into 1D, parametrisation of physical processes, numerical issues such as smoothing, missing processes or knowledge. It shows that more work is needed to provide reliable predictions for stellar evolution.

1 Future Work

In an ideal world of modelling, it would be possible to simulate the structure of a star in 3D over the whole stellar lifetime, including collapse and the ensuing explosion phase. Moreover, it would be possible to run these models in a reasonable time, allowing to study a large parameter space of initial mass, metallicity, rotation rate and distribution of binary companions. This would allow us to explain in more detail the status of the Universe observed today. In reality, numerical models of stars are far from ideal. The study of stellar evolution is limited to 1D due to the computational cost and the short timesteps needed in 3D simulations, for example to resolve turbulence, imposing simplifications and uncertainties.

In the following, I discuss a few points to improve upon, based on the content of the earlier Chapters.

1.1 Convective Boundary Mixing

- The need to include convective boundary mixing in stellar evolution calculation is generally accepted, but questions like "*how*" and "*how much*" are still under debate. The exponentially decaying convective boundary mixing scheme, for example, is based on multi-D simulations and its free parameter is constrained for certain initial masses and stages. This prescription allows to reproduce the radially decaying velocity profile and the sigmoid-shape of the chemical composition at the convective boundary seen in multi-D simulations. However, mixing is only applied to matter but not entropy. A next step is therefore to include a treatment for energy transport in the convective boundary region which allows a better prediction of this region (see Michielsen et al., 2019) and provide a physical reason for the amount of mixing rather than a free parameter. Scott et al. (2021) implemented an entrainment law which mixes an amount of matter at the convective boundary depending on its structure. Therefore, it would be interesting to study the evolution of massive

stars up to core collapse with the entrainment law. However, due to the cumulative nature of the entrainment law it is difficult to implement for the advanced burning stages. Alternatively, the instantaneous entrainment could be used (Staritsin, 2013).

- Meakin & Arnett (2007) show that the boundary location in 3D hydrodynamical simulations agrees on average more with the Schwarzschild solution. This, however, is an initial value problem. The convective boundary of the growing instability starts at the location determined by the Ledoux criterion. It is the intermittency and fluctuations at the convective boundary which erase the chemical stratification near the boundary and move the location to the Schwarzschild solution on a finite timescale. While this is less of an issue for convective zones with a long lifetime, such as the convective hydrogen core, it is crucial for short-living convective layers such as the intermediate convective zone. The behaviour of the intermediate convective zone depends strongly on the choice of the boundary location, which then influences the evolutionary path of the star - see Chapter III. Therefore, the timescale on which the boundary changes from the Ledoux to the Schwarzschild criterion, on average, should be investigated with 3D hydrodynamic simulations. Additionally, it is advisable to study the behaviour of the intermediate convective zone in 3D as it crucially impacts the later evolution of the star. Alternatively, it would also be interesting to explore this evolutionary phase using the entrainment law implementation - see previous point.
- There are two types of blue supergiants, the ones that evolved directly from the main sequence and those that were red supergiants before. The latter generates radial pulsations, which allow us to distinguish between the two types (e.g. Saio et al., 2013). Since the evolution during the post-main-sequence phase is crucially dependent on the intermediate convective zone, such observations would constrain its mixing. However, the analysis would not be straightforward as the evolution also depends on other processes such as rotation and mass-loss rates.

1.2 Rotation-Induced Mixing and Magnetic Fields

- The implementation of the Fuller-modified Tayler-Spruit dynamo still has some issues that need to be sorted out and its impact needs to be further investigated.
  - At the end of Chapter IV, I presented preliminary models of the Fuller-modified Tayler-Spruit dynamo using the $q_{\rm min}$ condition. This needs a more in depth examination. Also, its implementation can be improved. For example, there could be a smooth transition between the on-off behaviour, introduced by the *if-condition* in the implementation, of the dynamo action.
  - The smoothing process in the current implementation leads to an artificial reduction of the magnetic viscosity. In this Thesis I simply switched off the smoothing routine to test the impact of the magnetic dynamo without such a reduction. In the future, a better smoothing routine should be implemented and tested.

- In Section B.2.1 I discussed that an analytical solution for the equation determining $N^2_{\rm eff}$ requires a difficult root-finding problem. The short-term solution used in the implementation suggested by Fuller et al. (2019) (a) applies the Tayler-instability timescale of a non-rotating star (which can be justified only for slowly rotating stars) and (b) initially calculates $\omega_{\rm A}$ with N^2 instead of $N^2_{\rm eff}$. This simplification should be improved or at least it should be verified that is does not lead to a drastically wrong $N^2_{\rm eff}$ in all the scenarios it is used.
- The dynamo action and the viscosity it generates have to be revised in the close proximity of convective regions. In these layers, the magnetic torque can approach infinity because $N^2_{\rm eff}$ approaches zero. In order to prevent this scenario, Fuller et al. (2019) computes the viscosity as $\nu_{\rm TSF} = q\Omega r^2$ if $N^2_{\rm eff} < 2q^2\Omega^2$. The limit is arbitrary and could be chosen differently (Fuller, priv. comm.). Also, the formulation of the viscosity does not represent the physics occurring in the convective boundary mixing layer and its neighbouring region. This problem is similar to the issue with the Tayler-Spruit dynamo, where the convective boundary mixing region is ignored - see Section IV.3.6.

- Angular momentum transport by the Eddington-Sweet circulation is implemented as a diffusive process in `MESA`. An analogous implementation of this large-scale fluid motion, the meridional circulation, is described as an advective-diffusive process. Strictly speaking, the treatment of the circulation as an advective-diffusive process is physically correct, because it is the fluid motions, which arise from a thermal imbalance, that transport angular momentum. Therefore, angular momentum is transported inwards and outwards, depending on the location in the star (see Fig.(I.5b)). This is contrary to the implementation of the Eddington-Sweet circulation in `MESA`, where angular momentum is only diffused to a lower concentration. Consequently, even if the Eddington-Sweet circulation predicts a similar magnitude of angular momentum transport as the meridional circulation, it might transport it into the wrong direction, hence, it fails at reproducing the local rotation profile. Therefore, a stellar evolution code would use ideally the advective-diffusive scheme. However, in Chapter IV, I have shown that the angular momentum transport in magnetic models is dominated by the dynamo action. It would be useful to investigate if the diffusive versus advective-diffusive treatment matters in the presence of a magnetic dynamo or if the difference is overshadowed by the much more efficient angular momentum transport by magnetic fields. Furthermore, the interaction between magnetic fields and the slow large-scale mixing is an open question. It may be that the circulation is suppressed in presence of strong magnetic fields, hence, this would avoid the issue of diffusive versus advective-diffusive.
- The implementation of rotation-induced mixing and angular momentum transport in `MESA` (and other stellar evolution codes) is based on "*order-of-magnitude*" estimates (Endal & Sofia, 1978; Heger et al., 2000), multiplied with free parameters in order to scale their impact (Pinsonneault

et al., 1989). This approach leads to many uncertainties and it is time to include more accurate prescriptions, that include physics rather than "*order-of-magnitude*" estimates multiplied with scaling parameters. For example, I (in collaboration with Z. Keszthelyi, G. Meynet, R. Hirschi, P. Eggenberger) implemented the meridional circulation for chemical mixing, following the `GENEC` implementation, into the `MESA` code. However, the complication is that this is only applicable for chemical mixing and not angular momentum transport due to the advective-diffusive prescription in `GENEC`. This is still work in progress.

- In Chapter IV, I showed that the rotation-induced transport of angular momentum and mixing of chemical elements depends strongly on the treatment of the chemical stratification. The Eddington-Sweet circulation and the Goldreich-Schubert-Fricke instability consider the chemical stratification as a "*braking velocity*", which overestimates its inhibiting effect. Including the gradient of chemical composition in the derivation of the Eddington-Sweet circulation (see e.g. Maeder & Zahn, 1998, their Section 4; beware this is for the advective-diffusive case) would reduce this uncertainty. Also, the impact of the chemical stratification is scaled with the f_μ parameter, but it is not done consistently. The parameter is only multiplying ∇_μ if this term is used directly in the formula for the instability. However, if the chemical stratification is considered via the Brunt-Väisälä frequency, $N^2 = \frac{g\delta}{H_P}\left(\nabla_{\rm ad} - \nabla_{\rm rad} + \frac{\varphi}{\delta}\nabla_\mu\right)$, it is not scaled. In order to have a consistent prescription, it is recommended to scale the impact of the chemical stratification for rotational instabilities the same way. Thus, including f_μ also in the computation of N^2 where it is used to compute rotation-induced instabilities.
- The Tayler-Spruit dynamo in `MESA` is implemented following the formula suggested by Spruit (2002). This prescription computes the magnetic viscosity and diffusion coefficient for chemical mixing in two extreme cases: (a) when the chemical stratification dominates over the thermal gradient and (b) when there is no gradient in the chemical composition. In the intermediate case, the viscosity and diffusion coefficient are patched together from the two cases. The solution is therefore an estimate rather than an exact solution. It would be desirable to implement a general equation for the magnetic dynamo as, e.g., suggested by Maeder & Meynet (2004, 2005).
- In stellar models, the total diffusion coefficient is often considered to be the sum of the diffusion coefficients from the rotation-induced and non-rotating instabilities. However, in reality the different instabilities cannot be taken into account separately as they interact with each other. Maeder et al. (2013) propose a treatment to simultaneously consider various instabilities and their interaction. This general description has not been implemented into a stellar evolution code yet, mainly because a non-linear second-order equation needs to be solved. Nevertheless, in the future the interaction of the different instabilities should be considered to get the physics correct, for example by following Maeder et al. (2013).

- In this work, I only investigated the "*traditional*" hydrodynamic instabilities and two magnetic dynamos. There are other possibilities that could transport angular momentum and it would be interesting to investigate them, possibly in combination with the two magnetic dynamos. For example, the magnetorotational instability is more active during the late phase of stellar evolution (Wheeler et al., 2015). Therefore it could provide the missing angular momentum transport in the model with the Tayler-Spruit dynamo. Also other instabilities, such as internal gravity waves (Talon & Charbonnel, 2005; Belyaev et al., 2013; Edelmann et al., 2019) and how they interact with possible magnetic dynamos, should be considered in future work.

The analysis in Chapter IV is limited to the evolution of rotation and angular momentum distribution. Rotation also changes the structure and evolution of stars, which in turn depends on the uncertainties discussed in Chapter IV. An in depth study to assess the impact of these uncertainties on the stellar structure, evolution and fate of massive stars will be done in the future. Some preliminary results are presented in Section V.2. Also, the nucleosynthesis in the models presented in Chapter IV can be examined by post-processing the models. I have saved the necessary output files from all the rotating models to do so. This would allow to investigate the production and yields of rotating models with improved physics such as the mixing prescription and magnetic dynamo. Vice versa, studying observables such as the surface enrichment could help in constraining some of the uncertainties.

2 Preliminary Results

Rotation changes the evolutionary path of a star by mixing regions that would otherwise remain unchanged. Rotational mixing can transport fuel into an active burning region, which changes the nucleosynthesis, prolongs the burning timescale and increases the core size. Vice versa, the end products of the thermonuclear reactions can be transported into the envelope of massive stars. Furthermore, mixing of matter in the envelope of massive stars changes the opacity profile and surface composition. Hence, rotating stars will follow a different evolutionary path, for example they are more likely to form Wolf-Rayet stars, and therefore have a different observational signature. In Chapter IV, I discussed three different angular momentum transport processes and how they affect the angular momentum distribution and evolution of rotation. The distribution of angular momentum affects the presence and strength of rotation-induced mixing processes, which in turn change the structure of the star and the way it evolves. Here, I present some preliminary results, investigating the structure of rotating massive stars and their predicted neutron star spin period. The full analysis will be published in the future.

2.1 The Structure of Rotating Massive Stars

The core mass is defined as the location where the abundance of the main element drops below a certain value, in my case 0.01, and where the main fuel of the previous burning phase rises above a threshold, here 0.1. The core mass depends strongly on the extent of the convective zone accompanying the burning layer and additional mixing above it. In non-rotating models, the only mixing occurring is thermally-driven, dominantly turbulent convection. Consequently, core masses are tightly correlated to the upper location of convective regions. For example, the helium core mass at the end of the main-sequence phase coincides with the location of the convective core before it recedes. Similarly, the helium core mass after core helium depletion is located above the hydrogen burning shell. Rotation mainly influences the structure through mixing of matter in the radiative zones of the star. This provides the convective region with unburnt fuel, reflected by, e.g., the longer hydrogen burning lifetimes in Table V.1, and transports away synthesised products, changing the composition in the radiative envelope. This results in larger core masses, because the main product of the current burning is transported further out. Indeed, all the rotating 15 and 25 $M_\odot$ models in this thesis have a larger helium core mass at core helium depletion compared to the non-rotation model, as shown in Table V.1. Likewise, the carbon-oxygen core mass is larger at core helium depletion in the rotating models. However, in the *default* rotating models the difference for each respective core mass is modest because the rotation-induced mixing above the convective zones is limited by the chemical stratification, similarly to the angular momentum transport discussed in Section IV.3.

The small differences in M_α and $M_{\rm CO}$ in Table V.1 between the rotating models result from small differences in the diffusion profile in the radiative layers. For example, the helium core mass depends on the interface of the radial helium and hydrogen abundance profiles above the hydrogen burning layer. First, the profiles are used to determine the mass location of the helium core. Second, the hydrogen abundance profile in the radiative zone determines the behaviour of the ensuing hydrogen burning shell. A shallow profile forces the burning zone to move outwards faster, resulting in a more massive helium core mass according to its definition. On the other hand, a high hydrogen abundance in a layer keeps the hydrogen burning shell longer at that location, leading to a less massive helium core.

In the non-rotating model, the outward receding helium profile and the outwards increasing hydrogen profile are both very smooth, a result from the "*new*" convective mixing scheme - see Appendix B.2.2 - and well resolved physics. In the rotating model with hydrodynamic instabilities only, the same resolution and convective mixing is used. There, however, the secular shear instability generates a very jaggy mixing profile at the boundary between convective and radiative layers. As a result, both the radial hydrogen and helium abundance profiles are not smooth anymore but are step-like. This

Table V.1: Properties of the models at core helium depletion, when the central helium mass fraction drops below 0.01%.

model	rotation features	M_{tot} [$M_\odot$]	M_α [$M_\odot$]	M_{CO} [$M_\odot$]	τ_H [Myrs]	τ_{He} [Myrs]	$\log_{10} T_{eff,min}^{MS}$ [K]
		$Z = 0.014$					
$12\,M_\odot$,	$f_\mu = 0.1$, no B-field	9.38	4.59	2.88	20.18	1.28	4.27
Schwarzschild,	$f_\mu = 0.1$, TS	9.44	4.54	2.87	20.18	1.24	4.27
$f_{CBM} = 0.05$	$f_\mu = 0.0001$, TS	7.02	6.34	4.38	25.20	0.93	4.33
$\frac{\Omega}{\Omega_{crit}} = 0.4$							
$15\,M_\odot$,	non-rotating	11.38	5.77	3.65	14.04	0.91	4.29
Schwarzschild,	$f_\mu = 0.1$, no B-field	10.68	5.91	3.69	14.30	0.94	4.30
$f_{CBM} = 0.05$	$f_\mu = 0.1$, TS	10.78	5.86	3.74	14.31	0.91	4.29
$\frac{\Omega}{\Omega_{crit}} = 0.4$	$f_\mu = 0.1$, TS (include CBM)	8.96	6.43	4.23	14.74	0.86	4.27
	$f_\mu = 0.1$, TSF	10.43	5.91	3.77	14.27	0.91	4.29
	$f_\mu = 0.1$, TSF (no-smooth)	10.24	5.95	3.81	14.27	0.91	4.29
	$f_\mu = 0.1$, TSF (q_{min})	10.32	5.93	3.79	14.27	0.91	4.29
	$f_\mu = 0.01$, TS	9.33	6.30	4.10	14.69	0.88	4.29
	$f_\mu = 0.001$, TS	8.77	8.15	5.71	17.51	0.74	4.37
	$f_\mu = 0.0001$, TS	8.68	8.21	5.79	17.63	0.72	4.36
	$f_\mu = 0.0001$, TS (include CBM)	8.67	8.23	5.80	17.65	0.71	4.36
	$f_\mu = 0.0$, TS	8.65	8.22	5.80	17.64	0.72	4.36
$15\,M_\odot$,	$f_\mu = 0.1$, no B-field	11.30	5.82	3.89	14.05	0.91	4.30
Schwarzschild,	$f_\mu = 0.1$, TS	10.81	5.96	4.07	14.05	0.90	4.30
$f_{CBM} = 0.05$	$f_\mu = 0.0001$, TS	9.81	6.26	4.36	14.31	0.88	4.29
$\frac{\Omega}{\Omega_{crit}} = 0.1$							
$25\,M_\odot$,	non-rotating	11.84	10.69	7.99	7.54	0.57	4.26
Schwarzschild,	$f_\mu = 0.1$, no B-field	12.16	11.21	8.32	7.67	0.58	4.26
$f_{CBM} = 0.05$	$f_\mu = 0.1$, TS	11.90	11.00	8.29	7.67	0.56	4.25
$\frac{\Omega}{\Omega_{crit}} = 0.4$	$f_\mu = 0.1$, TS (include CBM)	···	11.51	8.55	7.89	0.52	4.19
	$f_\mu = 0.1$, TSF	11.89	10.96	8.24	7.62	0.57	4.25
	$f_\mu = 1.0$, no B-field	11.84	10.73	7.92	7.64	0.59	4.29
	$f_\mu = 1.0$, TS	11.76	10.84	8.12	7.65	0.57	4.28
	$f_\mu = 1.0$, TSF	11.86	10.80	8.10	7.64	0.57	4.28
	$f_\mu = 0.05$, no B-field	12.23	11.27	8.37	7.72	0.57	4.24
	$f_\mu = 0.05$, TS	12.13	11.33	8.62	7.72	0.55	4.24
	$f_\mu = 0.0001$, no B-field	···	10.98	8.16	8.85	0.50	4.34
	$f_\mu = 0.0001$, TS	···	11.79	8.80	8.77	0.50	4.33
	$f_\mu = 0.0001$, TS (include CBM)	···	11.65	8.74	8.78	0.50	4.33
$30\,M_\odot$,	non-rotating	···	12.85	9.81	6.32	0.48	4.19
Schwarzschild,	$f_\mu = 0.1$, no B-field	···	13.24	9.97	6.44	0.51	4.20
$f_{CBM} = 0.05$	$f_\mu = 0.1$, TS	···	12.80	9.79	6.44	0.49	4.19
$\frac{\Omega}{\Omega_{crit}} = 0.4$	$f_\mu = 0.1$, TSF	14.12	13.59	10.67	6.40	0.49	4.20
$60\,M_\odot$,	non-rotating	···	18.92	15.35	3.88	0.36	4.22
Schwarzschild,	$f_\mu = 0.1$, no B-field	···	18.82	15.22	3.89	0.36	4.54
$f_{CBM} = 0.05$	$f_\mu = 0.1$, TS	···	23.80	19.50	3.88	0.34	4.45
$\frac{\Omega}{\Omega_{crit}} = 0.4$	$f_\mu = 0.1$, TSF	···	23.32	19.39	3.86	0.34	4.50
		$Z = 0.002$					
$60\,M_\odot$,	non-rotating	···	31.66	27.03	3.95	0.33	3.93
Schwarzschild,	$f_\mu = 0.1$, no B-field	···	29.52	24.84	4.04	0.34	3.67
$f_{CBM} = 0.05$	$f_\mu = 0.1$, TS	···	31.31	26.61	4.03	0.33	4.02
$\frac{\Omega}{\Omega_{crit}} = 0.4$	$f_\mu = 0.1$, TSF	···	32.61	27.90	4.01	0.33	3.89
		$Z = 0.0004$					
$60\,M_\odot$,	non-rotating	44.30	30.01	25.50	3.93	0.32	4.37
Schwarzschild,	$f_\mu = 0.1$, no B-field	44.36	29.52	24.63	4.03	0.34	4.46
$f_{CBM} = 0.05$	$f_\mu = 0.1$, TS	33.37	30.92	26.81	4.02	0.33	3.87
$\frac{\Omega}{\Omega_{crit}} = 0.4$	$f_\mu = 0.1$, TSF	48.20	27.66	23.31	4.02	0.33	4.28

Notes: Shown are the total star mass, M_{tot}, the helium core mass, M_α, the carbon-oxygen core mass, M_{CO} and the minimum effective temperature reached during the main-sequence evolution, $\log_{10} T_{eff,min}^{MS}$. The core mass is defined as the location where the abundance of the main fuel in the burning process, which creates the main end product of the burning phase, is below 0.1 and the abundance of the end product is above 0.01. The main-sequence phase is defined to start when 0.3% of hydrogen has burnt and ends when the central hydrogen mass fraction drops below 10^{-5}. There is no entry for M_{tot} if the star has lost its entire hydrogen envelope, either through stellar winds or rotation-induced mixing.

scenario is even more pronounced in the model with the Tayler-Spruit dynamo. There, the dynamo action provides an additional chemical mixing with a strongly jaggy profile. Consequently, the step-like features in the radial hydrogen and helium abundance profiles are more prominent. In contrast, the model with the Fuller-modified Tayler-Spruit dynamo does not include chemical mixing by the magnetic dynamo nor is the secular shear instability active at the interface between convective and radiative regions - see Section IV.3. Therefore, this model predicts smooth radial abundance profiles of hydrogen and helium similar to the non-rotating model. These differences create the small differences in the core masses in Table V.1. It should be noted that the step-like abundance profiles can lead to a slightly arbitrary variation of the predicted core mass. This is an issue that needs to be considered with all rotating stellar models throughout the literature.

The impact of rotation-induced mixing on the core masses can also be seen in the models with a reduced inhibiting effect of the chemical stratification in Table V.1. If f_μ is lowered, the core mass increases. This is mainly because a weaker limiting restriction by the chemical stratification allows for more mixing in the radiative layer above the convective zone - see Section IV.3.5. Additionally, in models with $f_\mu \leq 0.001$ the convective hydrogen core initially grows during the main-sequence evolution before it recedes. Recalling from Section II.1.1, a convective zone is defined as the region where $\nabla_{\rm rad} > \nabla_{\rm ad}$ when the Schwarzschild criterion is used. The adiabatic temperature gradient is roughly constant in the interior of the star and very similar in the models with the same initial mass. On the other hand, $\nabla_{\rm rad} \propto \kappa \ell_{\rm rad} P$. In Section III.3 I discussed the reason why the convective core in non-rotating stars recedes during the main-sequence evolution. The rotating models with the *default* values of f_μ experience no rotation-induced mixing in the chemically stratified layer above the receding convective hydrogen core. Therefore, $\nabla_{\rm rad}$ behaves roughly similar in this region. However, for values of $f_\mu \leq 0.001$, the stratification is overcome and the layer is fully mixed (see Fig(IV.12b)). Therefore, (i) the opacity is lower because more helium is mixed into this region and (ii) the local luminosity is higher due to the higher energy generation from the more abundant fuel. Consequently, the condition $\nabla_{\rm rad} < \nabla_{\rm ad}$ is met further out and the convective core actually grows during the beginning of the main-sequence evolution before it recedes. This leads to much larger core masses as can be seen in Table V.1. The model with $f_\mu = 0.01$ is in the transition, where rotational mixing partly overcomes the stratification but not enough to generate a growing convective hydrogen core.

At solar metallicity, models with initial masses $M \gtrsim 25\,{\rm M}_\odot$ experience strong stellar winds that remove the entire hydrogen envelope and part of the helium core mass before helium depletion in the centre. The changes in the helium core mass further influence the structure of the subsequent burning stages. Consequently, the structure of these stars is not only influenced by rotation-induced mixing and rotation-enhanced mass-loss rates but also by how the surface evolution of the star proceeds. For example, a chemically homogeneous evolution will form more massive cores and a star that moves

below log $T_{\rm eff} \sim 4$ will experience the stronger red supergiant mass-loss rates, hence, it is more likely to end up with smaller core masses.

2.2 Rotation Rate of Compact Objects

One of the arguments in favour of a missing angular momentum transport process is the fact that the model predictions of massive rotating stars are not able to match the observed spin period of young neutron stars (e.g. Heger et al., 2000, 2005; Petrovic et al., 2005; Hirschi et al., 2005b; Wheeler et al., 2015). However, Ma & Fuller (2019) suggest that they match the observed slow rotation rates of neutron stars when including the Fuller-modified Tayler-Spruit dynamo. Fig.(V.1) presents the estimated neutron star period as a function of the gravitation mass[1], $M_{\rm grav,NS}$, for the 15 $M_\odot$ models at solar metallicity with different angular momentum transport assumptions and for a few 12 and 60 $M_\odot$ models presented in Table V.1 - see the legend for details. The spin period and the gravitational mass are computed following Heger et al. (2005), their Section 3.4. Additionally, Fig.(V.1) shows observed spin periods of young neutron stars. A few neutron stars have fast natal spin periods of 11 ms (Marshall et al., 1998) or 20 ms (Muslimov & Page, 1996; Kaspi & Helfand, 2002) but the majority rotate slower with a spin period of $50 - 100$ ms (Muslimov & Page, 1996; Faucher-Giguère & Kaspi, 2006; Popov et al., 2010; Popov & Turolla, 2012). There are also a few very slowly rotating neutron stars with a natal spin of up to 400 ms (Gotthelf et al., 2013). The comparison between the model predictions and observations reveals several points. First, the three different angular momentum transport mechanisms predict three distinct ranges for the spin period of neutron stars. Also, the period is mostly independent of the various related uncertainties in angular momentum transport investigated in Chapter IV. However, $M_{\rm grav,NS}$ does show a dependence on the uncertainty, mainly due to the amount of chemical mixing occuring during the stellar evolution. Second, the non-magnetic models fail to predict the observed rotation rate of neutron stars because of missing angular momentum transport. Considering the critical rotation rate for stars, $\Omega_{\rm crit} = \left(\frac{GM}{R^2}\right)^{1/2}$, a simple estimate for the minimum rotation period of a stable configuration can be obtained, $P > \frac{2\pi}{\Omega_{\rm crit}} = 2\pi \left(\frac{GM}{R^2}\right)^{-1/2}$. Thus, for a typical neutron star mass of 1.4 $M_\odot$ with a radius of 10;km the minimum stable rotation period is $P > 0.46$ milliseconds. Therefore, the rotation rate of he non-magnetic models predict unstable neutron star configurations, see for example discussion in Heger et al. (2000). Third, the two magnetic dynamos predict spin periods that are in the range of observations. However, the estimate

[1] A proto-neutron star with a baryonic mass $M_{\rm bary}$ loses binding energy due to neutrino emission. The gravitational mass is the baryonic mass corrected for neutrino losses, $M_{\rm grav} = M_{\rm bary} - f \times M_{\rm grav}$. The baryonic mass is the mass below the mass cut in a supernova explosion, which typically occurs at the location where the entropy drops below a value of $4 \times k_B$ (Janka, 2004), where k_B is the Boltzmann constant. The factor to correct for the neutrino losses is estimated as $f = \frac{0.6\times\beta}{1-\frac{1}{2}\beta}$ with $\beta = \frac{GM_{\rm grav}}{R_{\rm NS}c^2}$ (Lattimer & Prakash, 2001). Here, G is the gravitational constant, c the speed of light and $R_{\rm NS}$ the radius of the neutron star assuming a Newtonian polytrope, $R_{\rm NS} = 15.12 \times \left(\frac{M_{\rm bary}}{M_\odot}\right)^{-\frac{1}{3}}$ (Shapiro & Teukolsky, 1983).

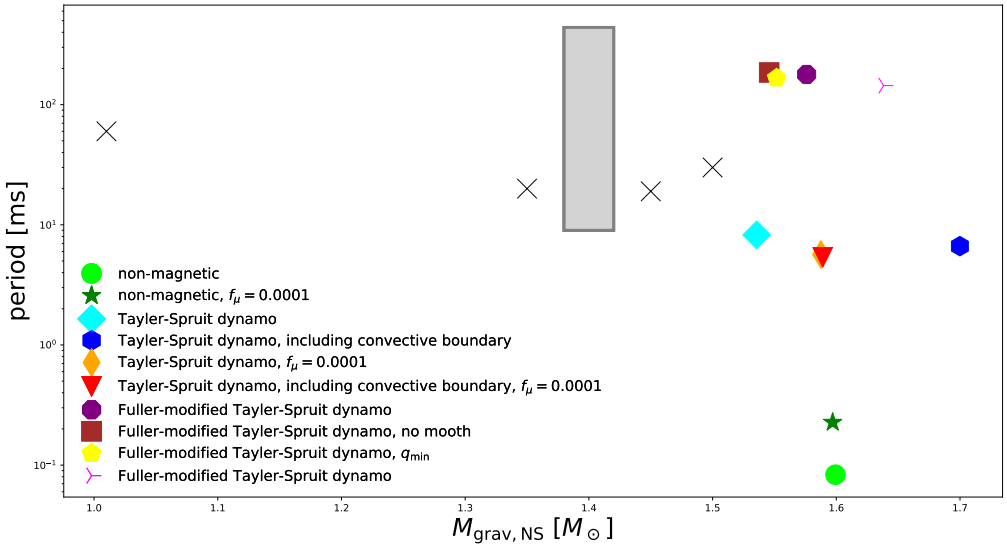

(a)

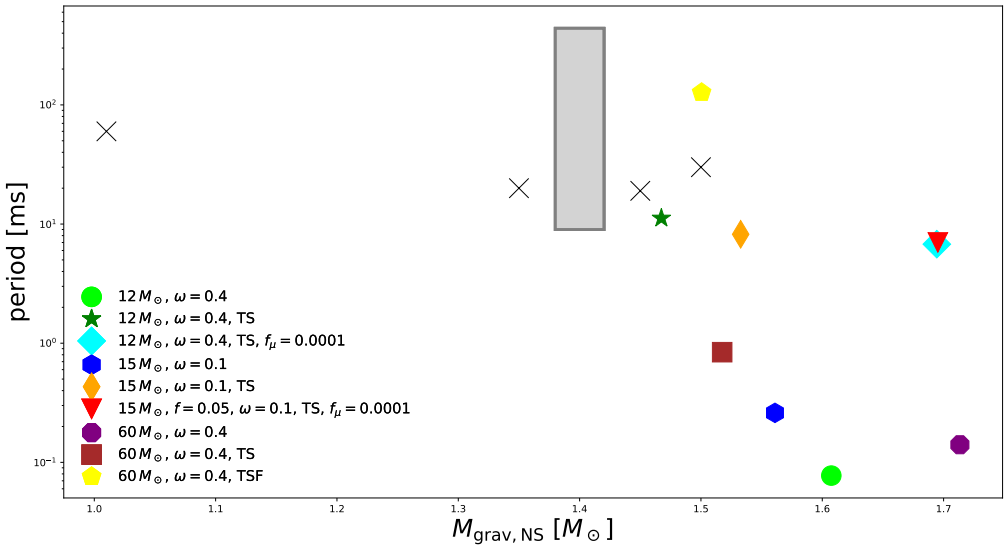

(b)

Figure V.1: Observed and estimated neutron star spin period as a function of the gravitational mass for (a) the $15\,\mathrm{M}_\odot$ models presented in Chapter IV and (b) the $12\,\mathrm{M}_\odot$ and $60\,\mathrm{M}_\odot$ models presented in Table V.1 and the $15\,\mathrm{M}_\odot$ models shown in (a) but with a slower initial rotation rate. The coloured markers present estimates based on the models and the black crosses show observed neutron star spins by Muslimov & Page (1996) and Faucher-Giguère & Kaspi (2006). The grey rectangle depicts an observed range of neutron star spins (Marshall et al., 1998; Kaspi & Helfand, 2002; Faucher-Giguère & Kaspi, 2006; Popov et al., 2010; Popov & Turolla, 2012; Gotthelf et al., 2013) with an assumed neutron star mass of $1.4\,\mathrm{M}_\odot$.

of the models with the Tayler-Spruit dynamo only covers the very fast rotating neutron stars, whereas the prediction by the models with the Fuller-modified Tayler-Spruit dynamo agrees with the slower rotating neutron stars in the sample. None of the models manages to predict the majority of natal neutron star spin periods. Therefore, while the Tayler-Spruit dynamo does not transport enough angular momentum, the Fuller-modified version slows down the rotation cores too much. It should be noted, that Fig.(V.1) only shows three different initial masses and two different initial rotation rates. A range of initial masses, initial rotation rates and metallicities may produce a broader range. However, Subfig.(V.1b) indicates that changing the initial mass and initial rotation rate reproduces the trend discussed for the $15\,M_{\odot}$ models. Thus, the question of the missing angular momentum transport mechanism is still open.

Bibliography

Abbott B. P., et al., 2016, Phys. Rev. Lett., 116, 061102

Abbott R., et al., 2020a, PhRvL, 125, 101102

Abbott R., et al., 2020b, ApJL, 900, L13

Aerts C., Van Reeth T., Tkachenko A., 2017, ApJL, 847, L7

Aerts C., Mathis S., Rogers T. M., 2019, ARA&A, 57, 35

Akiyama S., Wheeler J. C., Meier D. L., Lichtenstadt I., 2003, ApJ, 584, 954

Angulo C., et al., 1999, NuPhA, 656, 3

Arcavi I., et al., 2017, Nature, 551, 64

Arnett W. D., 1972, ApJ, 173, 393

Arnett W. D., 1974, ApJ, 193, 169

Arnett W. D., Meakin C., 2010, in Cunha K., Spite M., Barbuy B., eds, IAU Symposium Vol. 265, Chemical Abundances in the Universe: Connecting First Stars to Planets. pp 106–110 (arXiv:0912.2978), doi:10.1017/S174392131000030X

Arnett W. D., Moravveji E., 2017, The Astrophysical Journal Letters, 836, L19

Arnett W. D., Thielemann F.-K., 1985, ApJ, 295, 589

Arnett W. D., Meakin C., Viallet M., Campbell S. W., Lattanzio J. C., Mocák M., 2015, ApJ, 809, 30

Arnett W. D., et al., 2018, arXiv e-prints, p. arXiv:1810.04659

Arnett W. D., et al., 2019, ApJ, 882, 18

Arnould M., Goriely S., 2003, PhR, 384, 1

Arnould M., Mowlavi N., 1993, in Weiss W. W., Baglin A., eds, Astronomical Society of the Pacific Conference Series Vol. 40, IAU Colloq. 137: Inside the Stars. pp 310–323

Asplund M., Nordlund Å., Trampedach R., Stein R. F., 1999, A&A, 346, L17

Asplund M., Grevesse N., Sauval A. J., Scott P., 2009, ARA&A, 47, 481

Baade W., Zwicky F., 1934, Proceedings of the National Academy of Science, 20, 254

Badnell N. R., Bautista M. A., Butler K., Delahaye F., Mendoza C., Palmeri P., Zeippen C. J., Seaton M. J., 2005, MNRAS, 360, 458

Banerjee P., Heger A., Qian Y.-Z., 2019, arXiv e-prints, p. arXiv:1906.07335

Barkat Z., Rakavy G., Sack N., 1967, PhRvL, 18, 379

Beasor E. R., Davies B., Smith N., van Loon J. T., Gehrz R. D., Figer D. F., 2020, MNRAS, 492, 5994

Beaudet G., Petrosian V., Salpeter E. E., 1967, ApJ, 150, 979

Beck P. G., et al., 2011, Science, 332, 205

Beck P. G., et al., 2014, A&A, 564, A36

Belczynski K., et al., 2020a, A&A, 636, A104

Belczynski K., et al., 2020b, ApJ, 890, 113

Belyaev M. A., Rafikov R. R., Stone J. M., 2013, ApJ, 770, 67

Bertelli G., Bressan A. G., Chiosi C., 1984, A&A, 130, 279

Bestenlehner J. M., 2020, MNRAS, 493, 3938

Bestenlehner J. M., et al., 2014, A&A, 570, A38

Bethe H. A., 1990, Reviews of Modern Physics, 62, 801

Bethe H. A., Wilson J. R., 1985, ApJ, 295, 14

Bethe H. A., Brown G. E., Applegate J., Lattimer J. M., 1979, NuPhA, 324, 487

Biermann L., 1932, ZA, 5, 117

Bisnovatyi-Kogan G. S., Dorodnitsyn A. V., 1999, A&A, 344, 647

Bloecker T., 1995, A&A, 297, 727

Blondin J. M., Mezzacappa A., DeMarino C., 2003, ApJ, 584, 971

Bodansky D., Clayton D. D., Fowler W. A., 1968, ApJS, 16, 299

Bohm K. H., Cassinelli J., 1971, A&A, 12, 21

Böhm-Vitense E., 1958, ZA, 46, 108

Bond J. R., Arnett W. D., Carr B. J., 1984, ApJ, 280, 825

Bouret J.-C., Martins F., Hillier D. J., Marcolino W., Rocha-Pinto H., Georgy C., Lanz T., Hubeny I., 2021, arXiv e-prints, p. arXiv:2101.09269

Bowman D. M., et al., 2019, Nature Astronomy, 3, 760

Braithwaite J., Nordlund Å., 2006, A&A, 450, 1077

Braithwaite J., Spruit H. C., 2004, Nature, 431, 819

Brandenburg A., 2001, ApJ, 550, 824

Bromm V., Larson R. B., 2004, ARA&A, 42, 79

Brott I., et al., 2011, A&A, 530, A115

Brown T. M., Christensen-Dalsgaard J., Dziembowski W. A., Goode P., Gough D. O., Morrow C. A., 1989, ApJ, 343, 526

Browning M. K., Brun A. S., Toomre J., 2004, ApJ, 601, 512

Bruenn S. W., et al., 2016, ApJ, 818, 123

Brüggen M., Hillebrandt W., 2001, MNRAS, 320, 73

Brun A. S., Palacios A., 2009, ApJ, 702, 1078

Brun A. S., Browning M. K., Toomre J., 2005, ApJ, 629, 461

Brun A. S., et al., 2017, ApJ, 836, 192

Buchler J. R., Yueh W. R., 1976, ApJ, 210, 440

Buchmann L., 1996, ApJL, 468, L127

Burbidge E. M., Burbidge G. R., Fowler W. A., Hoyle F., 1957, Reviews of Modern Physics, 29, 547

Burrows A., Goshy J., 1993, ApJL, 416, L75

Burrows A., Vartanyan D., 2020, arXiv e-prints, p. arXiv:2009.14157

Burrows A., Hayes J., Fryxell B. A., 1995, ApJ, 450, 830

Burrows A., Vartanyan D., Dolence J. C., Skinner M. A., Radice D., 2018, SSRv, 214, 33

Cai T., 2020, ApJ, 888, 46

Caleo A., Balbus S. A., Tognelli E., 2016, MNRAS, 460, 338

Cameron A. G. W., 1959, ApJ, 130, 895

Cameron A. G. W., 1960, AJ, 65, 485

Cantiello M., Mankovich C., Bildsten L., Christensen-Dalsgaard J., Paxton B., 2014, ApJ, 788, 93

Cantiello M., Fuller J., Bildsten L., 2016, ApJ, 824, 14

Canuto V. M., 1998, ApJ, 508, L103

Canuto V. M., 1999, ApJ, 524, 311

Canuto V. M., 2011, A&A, 528, A76

Carneiro L. P., Puls J., Hoffmann T. L., Holgado G., Simón-Díaz S., 2019, A&A, 623, A3

Cassisi S., Potekhin A. Y., Pietrinferni A., Catelan M., Salaris M., 2007, ApJ, 661, 1094

Castellani V., Chieffi A., Tornambe A., Pulone L., 1985, ApJ, 296, 204

Castor J. I., Abbott D. C., Klein R. I., 1975, ApJ, 195, 157

Castro N., Fossati L., Langer N., Simón-Díaz S., Schneider F. R. N., Izzard R. G., 2014, A&A, 570, L13

Caughlan G. R., Fowler W. A., 1988, Atomic Data and Nuclear Data Tables, 40, 283

Chaboyer B., Zahn J. P., 1992, A&A, 253, 173

Chandrasekhar S., 1961, Hydrodynamic and Hydromagnetic Stability. Dover Edition

Charbonneau P., 2005, Living Reviews in Solar Physics, 2, 2

Charbonneau P., MacGregor K. B., 2001, ApJ, 559, 1094

Charbonneau P., Michaud G., Proffitt C. R., 1989, ApJ, 347, 821

Chatzopoulos E., Wheeler J. C., 2012, ApJ, 748, 42

Chiappini C., Frischknecht U., Meynet G., Hirschi R., Barbuy B., Pignatari M., Decressin T., Maeder A., 2011, Nature, 472, 454

Chieffi A., Limongi M., 2013, ApJ, 764, 21

Chieffi A., Limongi M., 2019, arXiv e-prints, p. arXiv:1911.08988

Chieffi A., Limongi M., 2020, ApJ, 890, 43

Chiu H.-Y., Morrison P., 1960, PhRvL, 5, 573

Choi J., Dotter A., Conroy C., Cantiello M., Paxton B., Johnson B. D., 2016, ApJ, 823, 102

Choplin A., Hirschi R., Meynet G., Ekström S., Chiappini C., Laird A., 2018, A&A, 618, A133

Claret A., Torres G., 2017, ApJ, 849, 18

Claret A., Torres G., 2018, ApJ, 859, 100

Clarkson O., Herwig F., 2020, arXiv e-prints, p. arXiv:2005.07748

Colgate S. A., Grasberger W. H., White R. H., 1961, AJ, 70, 280

Collins G. W. I., 1978, The virial theorem in stellar astrophysics. Pachart Pub. House

Constantino T., Campbell S. W., Lattanzio J. C., van Duijneveldt A., 2016, MNRAS, 456, 3866

Constantino T., Campbell S. W., Lattanzio J. C., 2017, MNRAS, 472, 4900

Costa V., Pumo M. L., Bonanno A., Zappalà R. A., 2006, A&A, 447, 641

Costa G., Girardi L., Bressan A., Marigo P., Rodrigues T. S., Chen Y., Lanza A., Goudfrooij P., 2019, MNRAS, 485, 4641

Côté B., et al., 2018, ApJ, 855, 99

Côté B., et al., 2019, ApJ, 875, 106

Couch R. G., Schmiedekamp A. B., Arnett W. D., 1974, ApJ, 190, 95

Couch S. M., Chatzopoulos E., Arnett W. D., Timmes F. X., 2015, ApJL, 808, L21

Cox J. P., Giuli R. T., 1968, Principles of stellar structure. Cambridge Scientific Publishers

Cristini A., Meakin C., Hirschi R., Arnett D., Georgy C., Viallet M., Walkington I., 2017, MNRAS, 471, 279

Cristini A., Hirschi R., Meakin C., Arnett D., Georgy C., Walkington I., 2019, MNRAS, 484, 4645

Crowther P. A., 2007, ARA&A, 45, 177

Cyburt R. H., et al., 2010, The Astrophysical Journal Supplement Series, 189, 240

Davies B., 2017, Philosophical Transactions of the Royal Society of London Series A, 375, 20160270

Davies B., Beasor E. R., 2020a, MNRAS, 493, 468

Davies B., Beasor E. R., 2020b, MNRAS, 496, L142

Davies B., Dessart L., 2018, preprint, (arXiv:1811.04087)

Davies B., et al., 2013, The Astrophysical Journal, 767, 3

Davis A., Jones S., Herwig F., 2019, MNRAS, 484, 3921

Deheuvels S., et al., 2014, A&A, 564, A27

Deng L., Xiong D. R., Chan K. L., 2006, ApJ, 643, 426

Denissenkov P. A., Pinsonneault M., 2007, ApJ, 655, 1157

Denissenkov P. A., Ivanova N. S., Weiss A., 1999, A&A, 341, 181

Denissenkov P. A., Herwig F., Woodward P., Andrassy R., Pignatari M., Jones S., 2019, MNRAS, 488, 4258

Donati J. F., Landstreet J. D., 2009, ARA&A, 47, 333

Dorn-Wallenstein T. Z., Levesque E. M., Neugent K. F., Davenport J. R. A., Morris B. M., Gootkin K., 2020, ApJ, 902, 24

Dufton P. L., Ryans R. S. I., Simón-Díaz S., Trundle C., Lennon D. J., 2006, A&A, 451, 603

Dufton P. L., et al., 2013, A&A, 550, A109

Ebinger K., et al., 2017, in Kubono S., Kajino T., Nishimura S., Isobe T., Nagataki S., Shima T., Takeda Y., eds, 14th International Symposium on Nuclei in the Cosmos (NIC2016). p. 020611 (arXiv:1610.05629), doi:10.7566/JPSCP.14.020611

Ebinger K., Curtis S., Fröhlich C., Hempel M., Perego A., Liebendörfer M., Thielemann F.-K., 2019, ApJ, 870, 1

Eddington A. S., 1925, The Observatory, 48, 73

Eddington A. S., 1929, MNRAS, 90, 54

Edelmann P. V. F., Röpke F. K., Hirschi R., Georgy C., Jones S., 2017, A&A, 604, A25

Edelmann P. V. F., Ratnasingam R. P., Pedersen M. G., Bowman D. M., Prat V., Rogers T. M., 2019, ApJ, 876, 4

Eggenberger P., Maeder A., Meynet G., 2005, A&A, 440, L9

Eggenberger P., Meynet G., Maeder A., Hirschi R., Charbonnel C., Talon S., Ekström S., 2008, Ap&SS, 316, 43

Eggenberger P., Montalbán J., Miglio A., 2012, A&A, 544, L4

Eggenberger P., et al., 2019a, A&A, 621, A66

Eggenberger P., Buldgen G., Salmon S. J. A. J., 2019b, A&A, 626, L1

Eggenberger P., den Hartogh J. W., Buldgen G., Meynet G., Salmon S. J. A. J., Deheuvels S., 2019c, A&A, 631, L6

Eggleton P. P., 1971, MNRAS, 151, 351

Eggleton P. P., 1972, MNRAS, 156, 361

Ekström S., Meynet G., Chiappini C., Hirschi R., Maeder A., 2008, A&A, 489, 685

Ekström S., et al., 2012, A&A, 537, A146

El Eid M. F., Fricke K. J., Ober W. W., 1983, A&A, 119, 54

Eldridge J. J., Tout C. A., 2004, MNRAS, 353, 87

Eldridge J. J., Vink J. S., 2006, A&A, 452, 295

Eldridge J. J., Izzard R. G., Tout C. A., 2008, MNRAS, 384, 1109

Eldridge J. J., Fraser M., Smartt S. J., Maund J. R., Crockett R. M., 2013, MNRAS, 436, 774

Endal A. S., Sofia S., 1976, ApJ, 210, 184

Endal A. S., Sofia S., 1978, ApJ, 220, 279

Ertl T., Janka H.-T., Woosley S. E., Sukhbold T., Ugliano M., 2016, ApJ, 818, 124

Falk S. W., Arnett W. D., 1973, ApJL, 180, L65

Farmer R., Fields C. E., Petermann I., Dessart L., Cantiello M., Paxton B., Timmes F. X., 2016, ApJS, 227, 22

Farmer R., Renzo M., de Mink S. E., Marchant P., Justham S., 2019, ApJ, 887, 53

Farouqi K., Hallmann O., Kratz K. L., Ott U., 2010, in Nuclei in the Cosmos. p. 81

Farrell E. J., Groh J. H., Hirschi R., Murphy L., Kaiser E., Ekström S., Georgy C., Meynet G., 2020, MNRAS,

Faucher-Giguère C.-A., Kaspi V. M., 2006, ApJ, 643, 332

Ferguson J. W., Alexander D. R., Allard F., Barman T., Bodnarik J. G., Hauschildt P. H., Heffner-Wong A., Tamanai A., 2005, ApJ, 623, 585

Ferrario L., 2018, Contributions of the Astronomical Observatory Skalnate Pleso, 48, 15

Fewell M. P., 1995, American Journal of Physics, 63, 653

Fields C. E., Timmes F. X., Farmer R., Petermann I., Wolf W. M., Couch S. M., 2018, ApJS, 234, 19

Filippenko A. V., 1997, ARA&A, 35, 309

Fossati L., et al., 2015, A&A, 582, A45

Fowler W. A., Hoyle F., 1964, ApJS, 9, 201

Fraley G. S., 1968, Ap&SS, 2, 96

Frebel A., Beers T. C., 2018, Physics Today, 71, 30

Freedman R. S., Marley M. S., Lodders K., 2008, ApJS, 174, 504

Freytag B., Ludwig H. G., Steffen M., 1996, A&A, 313, 497

Freytag B., Liljegren S., Höfner S., 2017, A&A, 600, A137

Fricke K., 1968, ZA, 68, 317

Frischknecht U., Hirschi R., Thielemann F. K., 2012, A&A, 538, L2

Frischknecht U., et al., 2016, MNRAS, 456, 1803

Fröhlich C., Martínez-Pinedo G., Liebendörfer M., Thielemann F. K., Bravo E., Hix W. R., Langanke K., Zinner N. T., 2006, PhRvL, 96, 142502

Fryer C. L., 1999, ApJ, 522, 413

Fryer C. L., Heger A., 2000, ApJ, 541, 1033

Fryer C. L., Kalogera V., 2001, ApJ, 554, 548

Fryer C. L., Woosley S. E., Heger A., 2001, The Astrophysical Journal, 550, 372

Fuller J., 2017, MNRAS, 470, 1642

Fuller J., Ma L., 2019, ApJL, 881, L1

Fuller G. M., Fowler W. A., Newman M. J., 1985, ApJ, 293, 1

Fuller J., Cantiello M., Stello D., Garcia R. A., Bildsten L., 2015a, Science, 350, 423

Fuller J., Cantiello M., Lecoanet D., Quataert E., 2015b, ApJ, 810, 101

Fuller J., Piro A. L., Jermyn A. S., 2019, MNRAS, 485, 3661

Fynbo H. O. U., et al., 2005, Nature, 433, 136

Gabriel M., Belkacem K., 2018, A&A, 612, A21

Gabriel M., Noels A., Montalbán J., Miglio A., 2014, A&A, 569, A63

Gagnier D., Rieutord M., Charbonnel C., Putigny B., Espinosa Lara F., 2019, A&A, 625, A88

Georgy C., 2010, PhD thesis, Geneva Observatory, Geneva University

Georgy C., 2012, A&A, 538, L8

Georgy C., Meynet G., Walder R., Folini D., Maeder A., 2009, A&A, 502, 611

Georgy C., Meynet G., Maeder A., 2011, A&A, 527, A52

Georgy C., Ekström S., Meynet G., Massey P., Levesque E. M., Hirschi R., Eggenberger P., Maeder A., 2012, A&A, 542, A29

Georgy C., Ekström S., Saio H., Meynet G., Groh J., Granada A., 2013, in Kervella P., Le Bertre T., Perrin G., eds, EAS Publications Series Vol. 60, EAS Publications Series. pp 43–50 (arXiv:1301.2978), doi:10.1051/eas/1360004

Georgy C., Saio H., Meynet G., 2014, MNRAS, 439, L6

Georgy C., Saio H., Meynet G., 2021, arXiv e-prints, p. arXiv:2104.06278

Getman K. V., Feigelson E. D., Luhman K. L., Sicilia-Aguilar A., Wang J., Garmire G. P., 2009, ApJ, 699, 1454

Gies D. R., Lambert D. L., 1992, ApJ, 387, 673

Gilmer M. S., Kozyreva A., Hirschi R., Fröhlich C., Yusof N., 2017, ApJ, 846, 100

Glebbeek E., Gaburov E., de Mink S. E., Pols O. R., Portegies Zwart S. F., 2009, A&A, 497, 255

Goldreich P., Schubert G., 1967, ApJ, 150, 571

Görres J., Arlandini C., Giesen U., Heil M., Käppeler F., Leiste H., Stech E., Wiescher M., 2000, PhRvC, 62, 055801

Gotthelf E. V., Halpern J. P., Alford J., 2013, ApJ, 765, 58

Gräfener G., Hamann W. R., 2008, A&A, 482, 945

Gräfener G., Vink J. S., de Koter A., Langer N., 2011, A&A, 535, A56

Greiner W., Neise L., Stöcker H., 1993, Thermodynamik und Statistische Mechanik, second edition edn. Theoretische Physik Vol. 9, VerlagHarri Deutsch

Heger A., Langer N., 2000, ApJ, 544, 1016

Heger A., Woosley S. E., 2002, ApJ, 567, 532

Heger A., Langer N., Woosley S. E., 2000, ApJ, 528, 368

Heger A., Fryer C. L., Woosley S. E., Langer N., Hartmann D. H., 2003, ApJ, 591, 288

Heger A., Woosley S. E., Spruit H. C., 2005, ApJ, 626, 350

Henyey L., Vardya M. S., Bodenheimer P., 1965, ApJ, 142, 841

Herwig F., 2000, A&A, 360, 952

Herwig F., Bloecker T., Schoenberner D., El Eid M., 1997, A&A, 324, L81

Herwig F., Freytag B., Hueckstaedt R. M., Timmes F. X., 2006, ApJ, 642, 1057

Herwig F., Freytag B., Fuchs T., Hansen J. P., Hueckstaedt R. M., Porter D. H., Timmes F. X., Woodward P. R., 2007, in Kerschbaum F., Charbonnel C., Wing R. F., eds, Astronomical Society of the Pacific Conference Series Vol. 378, Why Galaxies Care About AGB Stars: Their Importance as Actors and Probes. p. 43 (arXiv:0709.0197)

Higgins E. R., Vink J. S., 2019, A&A, 622, A50

Hirschi R., 2007, A&A, 461, 571

Hirschi R., Maeder A., 2010, A&A, 519, A16

Hirschi R., Meynet G., Maeder A., 2004, A&A, 425, 649

Hirschi R., Meynet G., Maeder A., 2005a, A&A, 433, 1013

Hirschi R., Meynet G., Maeder A., 2005b, A&A, 443, 581

Hix W. R., Thielemann F.-K., 1996, ApJ, 460, 869

Hix W. R., Thielemann F.-K., 1999, ApJ, 511, 862

Hix W. R., et al., 2016, Acta Physica Polonica B, 47, 645

Huang W., Gies D. R., 2006a, ApJ, 648, 580

Huang W., Gies D. R., 2006b, ApJ, 648, 591

Hubbard W. B., Lampe M., 1969, ApJS, 18, 297

Humphreys R. M., Davidson K., 1994, PASP, 106, 1025

Hunter I., Lennon D. J., Dufton P. L., Trundle C., Simón-Díaz S., Smartt S. J., Ryans R. S. I., Evans C. J., 2008, A&A, 479, 541

Iben I. J., 1975, ApJ, 196, 525

Iglesias C. A., Rogers F. J., 1993, ApJ, 412, 752

Iglesias C. A., Rogers F. J., 1996, ApJ, 464, 943

Imbriani G., et al., 2005, European Physical Journal A, 25, 455

Itoh N., Hayashi H., Nishikawa A., Kohyama Y., 1996, ApJS, 102, 411

Janka H. T., 2001, A&A, 368, 527

Janka H.-T., 2004, Neutron Star Formation and Birth Properties, doi:10.48550/ARXIV.ASTRO-PH/0402200, https://arxiv.org/abs/astro-ph/0402200

Janka H.-T., 2012, Annual Review of Nuclear and Particle Science, 62, 407

Janka H. T., Buras R., Kitaura Joyanes F. S., Marek A., Rampp M., Scheck L., 2005, NuPhA, 758, 19

Janka H. T., Langanke K., Marek A., Martínez-Pinedo G., Müller B., 2007, PhR, 442, 38

Janka H.-T., Melson T., Summa A., 2016, Annual Review of Nuclear and Particle Science, 66, 341

Jermyn A. S., Tout C. A., Chitre S. M., 2018, MNRAS, 480, 5427

Jones S., et al., 2013, ApJ, 772, 150

Jones S., Hirschi R., Pignatari M., Heger A., Georgy C., Nishimura N., Fryer C., Herwig F., 2015, MNRAS, 447, 3115

Jones S., Röpke F. K., Pakmor R., Seitenzahl I. R., Ohlmann S. T., Edelmann P. V. F., 2016, A&A, 593, A72

Jones S., Andrassy R., Sandalski S., Davis A., Woodward P., Herwig F., 2017, MNRAS, 465, 2991

Jones S., et al., 2019, A&A, 622, A74

Joss P. C., Salpeter E. E., Ostriker J. P., 1973, ApJ, 181, 429

Kaeppeler F., et al., 1994, ApJ, 437, 396

Kaiser E. A., Hirschi R., Arnett W. D., Georgy C., Scott L. J. A., Cristini A., 2020, MNRAS, 496, 1967

Kasen D., Woosley S. E., 2009, ApJ, 703, 2205

Kasen D., Woosley S. E., Heger A., 2011, ApJ, 734, 102

Kasen D., Metzger B., Barnes J., Quataert E., Ramirez-Ruiz E., 2017, Nature, 551, 80

Kaspi V. M., Helfand D. J., 2002, in Slane P. O., Gaensler B. M., eds, Astronomical Society of the Pacific Conference Series Vol. 271, Neutron Stars in Supernova Remnants. p. 3 (arXiv:astro-ph/0201183)

Kato S., 1966, PASJ, 18, 374

Kazeroni R., Abdikamalov E., 2020, MNRAS, 494, 5360

Keszthelyi Z., Meynet G., Georgy C., Wade G. A., Petit V., David-Uraz A., 2019, MNRAS, 485, 5843

Kippenhahn R., 1974, in Tayler R. J., Hesser J. E., eds, IAU Symposium Vol. 66, Late Stages of Stellar Evolution. p. 20

Kippenhahn R., Moellenhoff C., 1974, Ap&SS, 31, 117

Kippenhahn R., Thomas H. C., 1970, in Slettebak A., ed., IAU Colloq. 4: Stellar Rotation. p. 20

Kippenhahn R., Weigert A., 1994, Stellar Structure and Evolution. Springer-Verlag

Kippenhahn R., Meyer-Hofmeister E., Thomas H. C., 1970, A&A, 5, 155

Knobloch E., Spruit H. C., 1983, A&A, 125, 59

Kochanek C. S., 2020, MNRAS, 493, 4945

Köhler K., et al., 2015, A&A, 573, A71

Korre L., Garaud P., Brummell N. H., 2019, MNRAS, 484, 1220

Korre L., Brummell N. H., Garaud P., Guervilly C., 2021, MNRAS,

Kozyreva A., et al., 2017, MNRAS, 464, 2854

Kudritzki R.-P., Puls J., 2000, ARA&A, 38, 613

Kudritzki R. P., Pauldrach A., Puls J., Abbott D. C., 1989, A&A, 219, 205

Kunz R., Fey M., Jaeger M., Mayer A., Hammer J. W., Staudt G., Harissopulos S., Paradellis T., 2002, ApJ, 567, 643

Kurucz R. L., 1979, ApJS, 40, 1

Landau L., Lifschitz E. M., 1966, Hydrodynamik. Course of Theoretical Phyiscs Vol. 6, Akademie-Verlag Berlin

Langanke K., et al., 2003, PhRvL, 90, 241102

Langer N., 1997, in Nota A., Lamers H., eds, Astronomical Society of the Pacific Conference Series Vol. 120, Luminous Blue Variables: Massive Stars in Transition. p. 83

Langer N., 1998, A&A, 329, 551

Langer N., 2012, ARA&A, 50, 107

Langer N., Maeder A., 1995, A&A, 295, 685

Langer N., Fricke K. J., Sugimoto D., 1983, A&A, 126, 207

Langer N., El Eid M. F., Fricke K. J., 1985, A&A, 145, 179

Langer N., Kiriakidis M., El Eid M. F., Fricke K. J., Weiss A., 1988, A&A, 192, 177

Langer N., Norman C. A., de Koter A., Vink J. S., Cantiello M., Yoon S. C., 2007, A&A, 475, L19

Laplace E., Justham S., Renzo M., Götberg Y., Farmer R., Vartanyan D., de Mink S. E., 2021, arXiv e-prints, p. arXiv:2102.05036

Lattimer J. M., Prakash M., 2001, ApJ, 550, 426

Leung S.-C., Fuller J., 2020, ApJ, 900, 99

Leung S.-C., Nomoto K., Blinnikov S., 2019, ApJ, 887, 72

Levesque E. M., 2010, PhD thesis, University of Hawai'I at Manoa

Liebendörfer M., Mezzacappa A., Thielemann F.-K., Messer O. E., Hix W. R., Bruenn S. W., 2001, PhRvD, 63, 103004

Liebendörfer M., Mezzacappa A., Messer O. E. B., Martinez-Pinedo G., Hix W. R., Thielemann F. K., 2003, NuPhA, 719, C144

Limongi M., Chieffi A., 2018, ApJS, 237, 13

Lucy L. B., Solomon P. M., 1970, ApJ, 159, 879

Ludwig H.-G., Freytag B., Steffen M., 1999, A&A, 346, 111

Lyutikov M., Blackman E. G., 2001, MNRAS, 321, 177

Ma L., Fuller J., 2019, MNRAS, 488, 4338

Maeder A., 1975, A&A, 43, 61

Maeder A., 1987a, A&A, 173, 247

Maeder A., 1987b, A&A, 178, 159

Maeder A., 1997, A&A, 321, 134

Maeder A., 2003, A&A, 399, 263

Maeder A., 2009, Physics, Formation and Evolution of Rotating Stars. Springer, doi:10.1007/978-3-540-76949-1

Maeder A., Meynet G., 2000a, ARA&A, 38, 143

Maeder A., Meynet G., 2000b, A&A, 361, 159

Maeder A., Meynet G., 2001, A&A, 373, 555

Maeder A., Meynet G., 2004, A&A, 422, 225

Maeder A., Meynet G., 2005, A&A, 440, 1041

Maeder A., Meynet G., 2012, Reviews of Modern Physics, 84, 25

Maeder A., Zahn J.-P., 1998, A&A, 334, 1000

Maeder A., Meynet G., Lagarde N., Charbonnel C., 2013, A&A, 553, A1

Magic Z., Collet R., Asplund M., Trampedach R., Hayek W., Chiavassa A., Stein R. F., Nordlund Å., 2013, A&A, 557, A26

Magill J., Pfennig G., Galy J., 2006, Karlsruher Nuklidkarte

Mandel I., de Mink S. E., 2016, MNRAS, 458, 2634

Marigo P., Girardi L., Chiosi C., Wood P. R., 2001, A&A, 371, 152

Markova N., Puls J., Langer N., 2018, A&A, 613, A12

Marshall F. E., Gotthelf E. V., Zhang W., Middleditch J., Wang Q. D., 1998, ApJL, 499, L179

Martínez-Pinedo G., Fischer T., Lohs A., Huther L., 2012, PhRvL, 109, 251104

Martins F., Depagne E., Russeil D., Mahy L., 2013, A&A, 554, A23

Massey P., 2013, NewAR, 57, 14

Mathis S., Palacios A., Zahn J. P., 2004, A&A, 425, 243

Mathys G., 2012, in Shibahashi H., Takata M., Lynas-Gray A. E., eds, Astronomical Society of the Pacific Conference Series Vol. 462, Progress in Solar/Stellar Physics with Helio- and Asteroseismology. p. 295

Mauron N., Josselin E., 2011, A&A, 526, A156

McEvoy C. M., et al., 2015, A&A, 575, A70

Meakin C. A., Arnett D., 2007, ApJ, 667, 448

Mestel L., 1953, MNRAS, 113, 716

Meynet G., Maeder A., 1997, A&A, 321, 465

Meynet G., Maeder A., 2000, A&A, 361, 101

Meynet G., Maeder A., 2002, A&A, 390, 561

Meynet G., Maeder A., 2003, A&A, 404, 975

Meynet G., Maeder A., 2005, A&A, 429, 581

Meynet G., Eggenberger P., Mowlavi N., Maeder A., 2009, in Mamajek E. E., Soderblom D. R., Wyse R. F. G., eds, IAU Symposium Vol. 258, The Ages of Stars. pp 177–188 (arXiv:0811.2339), doi:10.1017/S1743921309031834

Meynet G., et al., 2015, A&A, 575, A60

Michielsen M., Pedersen M. G., Augustson K. C., Mathis S., Aerts C., 2019, Astronomy and Astrophysics, 628, A76

Mihalas D., 1978, Stellar atmospheres. W.H.Freeman & Co Ltd

Miyaji S., Nomoto K., Yokoi K., Sugimoto D., 1980, PASJ, 32, 303

Mocák M., Meakin C., Campbell S. W., Arnett W. D., 2018, MNRAS, 481, 2918

Modjaz M., et al., 2008, AJ, 135, 1136

Mokiem M. R., et al., 2006, A&A, 456, 1131

Mokiem M. R., et al., 2007, A&A, 473, 603

Moravveji E., Aerts C., Pápics P. I., Triana S. A., Vandoren B., 2015, Astronomy and Astrophysics, 580, A27

Moravveji E., Townsend R. H. D., Aerts C., Mathis S., 2016, The Astrophysical Journal, 823, 130

Mosser B., et al., 2012, A&A, 548, A10

Müller B., 2020, Living Reviews in Computational Astrophysics, 6, 3

Müller P. E., Vink J. S., 2014, A&A, 564, A57

Müller B., Heger A., Liptai D., Cameron J. B., 2016, MNRAS, 460, 742

Müller B., Melson T., Heger A., Janka H.-T., 2017, MNRAS, 472, 491

Muslimov A., Page D., 1996, ApJ, 458, 347

Myra E. S., Bludman S. A., 1989, ApJ, 340, 384

Nakamura K., Takiwaki T., Kuroda T., Kotake K., 2015, PASJ, 67, 107

Neilson H. R., Lester J. B., 2008, ApJ, 684, 569

Nieuwenhuijzen H., de Jager C., 1990, A&A, 231, 134

Nieva M. F., Przybilla N., 2012, A&A, 539, A143

Noels A., Montalban J., Miglio A., Godart M., Ventura P., 2010, Ap&SS, 328, 227

Nomoto K., 1984, ApJ, 277, 791

Nomoto K., 1987, ApJ, 322, 206

Nugis T., Lamers H. J. G. L. M., 2000, A&A, 360, 227

O'Connor E., Ott C. D., 2011, ApJ, 730, 70

Oda T., Hino M., Muto K., Takahara M., Sato K., 1994, Atomic Data and Nuclear Data Tables, 56, 231

Owocki S. P., Puls J., 2002, ApJ, 568, 965

Owocki S. P., Gayley K. G., Shaviv N. J., 2004, ApJ, 616, 525

Paczyński B., 1969, AcA, 19, 1

Paczynski B., Proszynski M., 1986, ApJ, 302, 519

Parker E. N., 1979, Cosmical magnetic fields. Their origin and their activity. The International Series of Monographs on Physics, Oxford: Clarendon Press

Parsons S. B., 1971, MNRAS, 152, 121

Paxton B., Bildsten L., Dotter A., Herwig F., Lesaffre P., Timmes F., 2011, ApJS, 192, 3

Paxton B., et al., 2013, ApJS, 208, 4

Paxton B., et al., 2015, ApJS, 220, 15

Paxton B., et al., 2018, ApJS, 234, 34

Paxton B., et al., 2019, ApJS, 243, 10

Petrovic J., Langer N., Yoon S. C., Heger A., 2005, A&A, 435, 247

Pian E., et al., 2017, Nature, 551, 67

Pignatari M., Gallino R., Heil M., Wiescher M., Käppeler F., Herwig F., Bisterzo S., 2010, ApJ, 710, 1557

Pignatari M., et al., 2016, ApJS, 225, 24

Pinçon C., Belkacem K., Goupil M. J., Marques J. P., 2017, A&A, 605, A31

Pinsonneault M. H., Kawaler S. D., Sofia S., Demarque P., 1989, ApJ, 338, 424

Piro A. L., Ott C. D., 2011, ApJ, 736, 108

Pitts E., Tayler R. J., 1985, MNRAS, 216, 139

Podsiadlowski P., Joss P. C., Hsu J. J. L., 1992, ApJ, 391, 246

Pope S. B., 2000, Turbulent Flows. Cambridge University Press, doi:10.1017/CBO9780511840531

Popov S. B., Turolla R., 2012, Ap&SS, 341, 457

Popov S. B., Pons J. A., Miralles J. A., Boldin P. A., Posselt B., 2010, MNRAS, 401, 2675

Potekhin A. Y., Chabrier G., 2010, Contributions to Plasma Physics, 50, 82

Potter A. T., Tout C. A., Eldridge J. J., 2012a, MNRAS, 419, 748

Potter A. T., Tout C. A., Brott I., 2012b, MNRAS, 423, 1221

Potter A. T., Chitre S. M., Tout C. A., 2012c, MNRAS, 424, 2358

Povh B., Rith K., Scholz C., Zetsche F., 2009, Teilchen und Kerne. Physics and astronomy online library, Springer Berlin Heidelberg, https://books.google.co.uk/books?id=aSWr16XxDc8C

Powell J., Müller B., Heger A., 2021, arXiv e-prints, p. arXiv:2101.06889

Prantzos N., Boissier S., 2003, A&A, 406, 259

Prantzos N., Hashimoto M., Nomoto K., 1990, A&A, 234, 211

Pratt J., Baraffe I., Goffrey T., Constantino T., Viallet M., Popov M. V., Walder R., Folini D., 2017, Astronomy and Astrophysics, 604, A125

Preibisch T., Zinnecker H., 2007, in Elmegreen B. G., Palous J., eds, IAU Symposiom Vol. 237, Triggered Star Formation in a Turbulent ISM. pp 270–277 (arXiv:astro-ph/0610826), doi:10.1017/S1743921307001597

Prialnik D., Kovetz A., 1995, ApJ, 445, 789

Przybilla N., Nieva M. F., Irrgang A., Butler K., 2013, in Alecian G., Lebreton Y., Richard O., Vauclair G., eds, EAS Publications Series Vol. 63, New Advances in Stellar Physics: From Microscopic to Macroscopic Processes. pp 13–23, doi:10.1051/eas/1363002

Puls J., Vink J. S., Najarro F., 2008, A&A Rv, 16, 209

Puls J., Sundqvist J. O., Markova N., 2015, in Meynet G., Georgy C., Groh J., Stee P., eds, IAU Symposium Vol. 307, New Windows on Massive Stars. pp 25–36 (arXiv:1409.3582), doi:10.1017/S174392131400622X

Raiteri C. M., Busso M., Gallino R., Picchio G., Pulone L., 1991a, ApJ, 367, 228

Raiteri C. M., Busso M., Gallino R., Picchio G., 1991b, ApJ, 371, 665

Rakavy G., Shaviv G., 1967, ApJ, 148, 803

Ramírez-Agudelo O. H., et al., 2013, A&A, 560, A29

Rapagnani D., et al., 2017, Nuclear Instruments and Methods in Physics Research B, 407, 217

Rauscher T., 2010, in Nuclei in the Cosmos. p. 59

Rauscher T., Heger A., Hoffman R. D., Woosley S. E., 2002, ApJ, 576, 323

Rauscher T., Nishimura N., Hirschi R., Cescutti G., Murphy A. S. J., Heger A., 2016, MNRAS, 463, 4153

Reimers D., 1975, Memoires of the Societe Royale des Sciences de Liege, 8, 369

Renzini A., 1987, A&A, 188, 49

Renzini A., Fusi Pecci F., 1988, ARA&A, 26, 199

Renzini A., Greggio L., Ritossa C., Ferrario L., 1992, ApJ, 400, 280

Renzo M., Ott C. D., Shore S. N., de Mink S. E., 2017, A&A, 603, A118

Renzo M., Farmer R. J., Justham S., de Mink S. E., Götberg Y., Marchant P., 2020, MNRAS, 493, 4333

Ritter C., Herwig F., Jones S., Pignatari M., Fryer C., Hirschi R., 2018, MNRAS, 480, 538

Rizzuti F., Cescutti G., Matteucci F., Chieffi A., Hirschi R., Limongi M., Saro A., 2021, MNRAS, 502, 2495

Roberts L. F., Reddy S., Shen G., 2012, PhRvC, 86, 065803

Rogers T. M., McElwaine J. N., 2017, The Astrophysical Journal, 848, L1

Rogers F. J., Nayfonov A., 2002, ApJ, 576, 1064

Rüdiger G., Kitchatinov L. L., Elstner D., 2012, MNRAS, 425, 2267

Saio H., Georgy C., Meynet G., 2013, MNRAS, 433, 1246

Salpeter E. E., 1953, Annual Review of Nuclear and Particle Science, 2, 41

Sana H., et al., 2012, Science, 337, 444

Sander A., Hamann W. R., Todt H., 2012, A&A, 540, A144

Sanyal D., Grassitelli L., Langer N., Bestenlehner J. M., 2015, A&A, 580, A20

Sanyal D., Langer N., Szécsi D., -C Yoon S., Grassitelli L., 2017, A&A, 597, A71

Saumon D., Chabrier G., van Horn H. M., 1995, ApJS, 99, 713

Scheck L., Plewa T., Janka H. T., Kifonidis K., Müller E., 2004, PhRvL, 92, 011103

Schneider F. R. N., Ohlmann S. T., Podsiadlowski P., Röpke F. K., Balbus S. A., Pakmor R., 2020, MNRAS, 495, 2796

Schneider F. R. N., Podsiadlowski P., Müller B., 2021, A&A, 645, A5

Schootemeijer A., Langer N., Grin N. J., Wang C., 2019, A&A, 625, A132

Schwab J., Quataert E., Bildsten L., 2015, MNRAS, 453, 1910

Schwarzschild M., Härm R., 1958, ApJ, 128, 348

Scott L. J. A., Hirschi R., Georgy C., Arnett W. D., Meakin C., Kaiser E. A., Ekström S., Yusof N., 2021, MNRAS, 503, 4208

Seaton M. J., 2005, MNRAS, 362, L1

Shapiro S. L., Teukolsky S. A., 1983, Black holes, white dwarfs, and neutron stars : the physics of compact objects

Shaviv G., Salpeter E. E., 1973, ApJ, 184, 191

Shibagaki S., Kajino T., Mathews G. J., Chiba S., Nishimura S., Lorusso G., 2016, The Astrophysical Journal, 816, 79

Smartt S. J., 2009, ARA&A, 47, 63

Smartt S. J., 2015, PASA, 32, e016

Smartt S. J., Eldridge J. J., Crockett R. M., Maund J. R., 2009, MNRAS, 395, 1409

Smartt S. J., et al., 2017, Nature, 551, 75

Smith N., 2014, ARA&A, 52, 487

Sobral D., Matthee J., Darvish B., Schaerer D., Mobasher B., Röttgering H. J. A., Santos S., Hemmati S., 2015, ApJ, 808, 139

Song H., Wang J., Song F., Zhang R., Li Z., Peng W., Zhan Q., Jing J., 2018, ApJ, 859, 43

Spada F., Gellert M., Arlt R., Deheuvels S., 2016, A&A, 589, A23

Spiegel E. A., Zahn J. P., 1992, A&A, 265, 106

Spruit H. C., 1992, A&A, 253, 131

Spruit H. C., 1999, A&A, 349, 189

Spruit H. C., 2002, A&A, 381, 923

Spruit H. C., Knobloch E., Roxburgh I. W., 1983, Nature, 304, 520

Stancliffe R. J., Chieffi A., Lattanzio J. C., Church R. P., 2009, PASA, 26, 203

Stancliffe R. J., Fossati L., Passy J. C., Schneider F. R. N., 2016, A&A, 586, A119

Staritsin E. I., 2013, Astronomy Reports, 57, 380

Straka C. W., Demarque P., Guenther D. B., 2005, ApJ, 629, 1075

Suárez-Madrigal A., Krumholz M., Ramirez-Ruiz E., 2013, arXiv e-prints, p. arXiv:1304.2317

Sugimoto D., Fujimoto M. Y., 2000, ApJ, 538, 837

Sugimoto D., Nomoto K., Eriguchi Y., 1981, Progress of Theoretical Physics Supplement, 70, 115

Suijs M. P. L., Langer N., Poelarends A. J., Yoon S. C., Heger A., Herwig F., 2008, A&A, 481, L87

Sukhbold T., Woosley S. E., 2014, ApJ, 783, 10

Sukhbold T., Ertl T., Woosley S. E., Brown J. M., Janka H. T., 2016, ApJ, 821, 38

Sukhbold T., Woosley S. E., Heger A., 2018, ApJ, 860, 93

Summa A., Janka H.-T., Melson T., Marek A., 2018, ApJ, 852, 28

Sweet P. A., 1950, MNRAS, 110, 548

Szécsi D., Langer N., Yoon S.-C., Sanyal D., de Mink S., Evans C. J., Dermine T., 2015, A&A, 581, A15

Takahashi K., Langer N., 2020, arXiv e-prints, p. arXiv:2010.13909

Takahashi K., Witti J., Janka H. T., 1994, A&A, 286, 857

Takahashi K., Yoshida T., Umeda H., 2013, ApJ, 771, 28

Talon S., Charbonnel C., 2005, A&A, 440, 981

Talon S., Zahn J. P., 1997, A&A, 317, 749

Tauris T. M., Langer N., Kramer M., 2011, MNRAS, 416, 2130

Tayler R. J., 1973, MNRAS, 161, 365

Tennekes H., Lumley J. L., 1972, First Course in Turbulence. MIT press

The L.-S., El Eid M. F., Meyer B. S., 2007, ApJ, 655, 1058

Thielemann F. K., Arnett W. D., 1985, ApJ, 295, 604

Thielemann F.-K., Nomoto K., Hashimoto M.-A., 1996, ApJ, 460, 408

Thielemann F. K., Hirschi R., Liebendörfer M., Diehl R., 2011, Massive Stars and Their Supernovae. Berlin Springer Verlag, pp 153–232

Thielemann F.-K., Eichler M., Panov I., Pignatari M., Wehmeyer B., 2017a, Making the Heaviest Elements in a Rare Class of Supernovae. Springer International Publishing AG, p. 1843, doi:10.1007/978-3-319-21846-5˙81

Thielemann F. K., Eichler M., Panov I. V., Wehmeyer B., 2017b, Annual Review of Nuclear and Particle Science, 67, 253

Timmes F. X., Swesty F. D., 2000, ApJS, 126, 501

Tkachenko A., et al., 2020, A&A, 637, A60

Trampedach R., Stein R. F., Christensen-Dalsgaard J., Nordlund Å., Asplund M., 2014, MNRAS, 445, 4366

Turatto M., 2003, Classification of Supernovae. Springer Verlag, pp 21–36, doi:10.1007/3-540-45863-8˙3

Turner J., 1973, Buoyancy effects in fluids, 1st edn. Cambridge University Press

Turolla R., Zane S., Watts A. L., 2015, Reports on Progress in Physics, 78, 116901

Ugliano M., Janka H.-T., Marek A., Arcones A., 2012, ApJ, 757, 69

Ulmer A., Fitzpatrick E. L., 1998, ApJ, 504, 200

Umeda H., Nomoto K., 2002, ApJ, 565, 385

Umeda H., Yoshida T., Nagele C., Takahashi K., 2020, ApJL, 905, L21

Varma V., Müller B., 2021, arXiv e-prints, p. arXiv:2101.00213

Velikhov E., 1959, J. Exptl. Theoret. Phys (USSR), 36, 1398

Vink J. S., 2008, NewAR, 52, 419

Vink J. S., 2011, Ap&SS, 336, 163

Vink J. S., 2012, Astrophysics and Space Science Library, p. 221–247

Vink J. S., 2015, Mass-Loss Rates of Very Massive Stars. Springer International Publishing, p. 77, doi:10.1007/978-3-319-09596-7˙4

Vink J. S., 2018, A&A, 619, A54

Vink J. S., de Koter A., Lamers H. J. G. L. M., 2000, A&A, 362, 295

Vink J. S., de Koter A., Lamers H. J. G. L. M., 2001, A&A, 369, 574

Vink J. S., Brott I., Gräfener G., Langer N., de Koter A., Lennon D. J., 2010, A&A, 512, L7

Vink J. S., Muijres L. E., Anthonisse B., de Koter A., Gräfener G., Langer N., 2011, A&A, 531, A132

Vitense E., 1953, ZA, 32, 135

Wagle G. A., Ray A., Dev A., Raghu A., 2019, ApJ, 886, 27

Walborn N. R., Morrell N. I., Howarth I. D., Crowther P. A., Lennon D. J., Massey P., Arias J. I., 2004, ApJ, 608, 1028

Walder R., Folini D., Meynet G., 2012, SSRv, 166, 145

Waldman R., 2008, ApJ, 685, 1103

Walmswell J. J., Eldridge J. J., 2012, Monthly Notices of the Royal Astronomical Society, 419, 2054

Wanajo S., Ishimaru Y., 2005, in Hill V., Francois P., Primas F., eds, IAU Symposium Vol. 228, From Lithium to Uranium: Elemental Tracers of Early Cosmic Evolution. pp 435–438, doi:10.1017/S1743921305006174

Warhaft Z., 2002, Proceedings of the National Academy of Sciences, 99, 2481

Wasiutynski J., 1946, Astrophysica Norvegica, 4, 1

Weaver T. A., Woosley S. E., 1993, PhR, 227, 65

Weaver T. A., Zimmerman G. B., Woosley S. E., 1978, ApJ, 225, 1021

Weis K., Bomans D. J., 2020, Galaxies, 8, 20

West C., Heger A., Austin S. M., 2013, ApJ, 769, 2

Wheeler J. C., Kagan D., Chatzopoulos E., 2015, ApJ, 799, 85

Winteler C., Käppeli R., Perego A., Arcones A., Vasset N., Nishimura N., Liebendörfer M., Thielemann F. K., 2012, ApJL, 750, L22

Wood T. S., Brummell N. H., 2018, ApJ, 853, 97

Woodward P. R., Herwig F., Lin P.-H., 2015, The Astrophysical Journal, 798, 49

Woosley S. E., 1993, ApJ, 405, 273

Woosley S. E., 2017, ApJ, 836, 244

Woosley S. E., 2019, ApJ, 878, 49

Woosley S. E., Bloom J. S., 2006, ARA&A, 44, 507

Woosley S. E., Heger A., 2006, ApJ, 637, 914

Woosley S. E., Hoffman R. D., 1992, in American Astronomical Society Meeting Abstracts. p. 107.03

Woosley S., Janka T., 2005, Nature Physics, 1, 147

Woosley S. E., Weaver T. A., 1995, ApJS, 101, 181

Woosley S. E., Arnett W. D., Clayton D. D., 1972, ApJ, 175, 731

Woosley S. E., Arnett W. D., Clayton D. D., 1973, ApJS, 26, 231

Woosley S. E., Langer N., Weaver T. A., 1993, ApJ, 411, 823

Woosley S. E., Wilson J. R., Mathews G. J., Hoffman R. D., Meyer B. S., 1994, ApJ, 433, 229

Woosley S. E., Heger A., Weaver T. A., 2002, Reviews of Modern Physics, 74, 1015

Woosley S. E., Blinnikov S., Heger A., 2007, Nature, 450, 390

Wright G. A. E., 1973, MNRAS, 162, 339

Xiong D. R., Cheng Q. L., Deng L., 1997, ApJS, 108, 529

Xu Y., Takahashi K., Goriely S., Arnould M., Ohta M., Utsunomiya H., 2013, NuPhA, 918, 61

Yadav N., Müller B., Janka H. T., Melson T., Heger A., 2020, ApJ, 890, 94

Yakovlev D. G., Urpin V. A., 1980, Soviet Ast., 24, 303

Yoon S.-C., Cantiello M., 2010, The Astrophysical Journal, 717, L62

Yoon S. C., Langer N., 2005, A&A, 443, 643

Yoon S. C., Langer N., Norman C., 2006, A&A, 460, 199

Yoon S. C., Woosley S. E., Langer N., 2010, ApJ, 725, 940

Yoon S. C., Dierks A., Langer N., 2012, A&A, 542, A113

Yoshida T., Umeda H., Maeda K., Ishii T., 2016, MNRAS, 457, 351

Young T. R., 2004, ApJ, 617, 1233

Yusof N., et al., 2013, MNRAS, 433, 1114

Zahn J. P., 1974, in Ledoux P., Noels A., Rodgers A. W., eds, IAU Symposium Vol. 59, Stellar Instability and Evolution. p. 185

Zahn J. P., 1991, A&A, 252, 179

Zahn J. P., 1992, A&A, 265, 115

Zahn J. P., Brun A. S., Mathis S., 2007, A&A, 474, 145

Zapartas E., de Mink S. E., Justham S., Smith N., Renzo M., de Koter A., 2021, A&A, 645, A6

Zinnecker H., Yorke H. W., 2007, ARA&A, 45, 481

de Jager C., Nieuwenhuijzen H., van der Hucht K. A., 1988, Astronomy and Astrophysics Supplement Series, 72, 259

de Koter A., Heap S. R., Hubeny I., 1997, ApJ, 477, 792

de Mink S. E., Cantiello M., Langer N., Pols O. R., Brott I., Yoon S. C., 2009, A&A, 497, 243

deBoer R. J., et al., 2017, Reviews of Modern Physics, 89, 035007

den Hartogh J. W., Eggenberger P., Hirschi R., 2019, A&A, 622, A187

den Hartogh J. W., Eggenberger P., Deheuvels S., 2020, A&A, 634, L16

van Loon J. T., Cioni M. R. L., Zijlstra A. A., Loup C., 2005, A&A, 438, 273

von Zeipel H., 1924a, MNRAS, 84, 665

von Zeipel H., 1924b, MNRAS, 84, 684

Appendix A

Publications

1 Publications in Peer-Reviewed Scientific Journals

- Scott, L.J.A., Hirschi, R., Georgy, C., Arnett, W.D., Meakin, C., **Kaiser, E.A.**, Ekström, S., Yusof, N., **Convective core entrainment in 1D main sequence stellar models**, 2021, MNRAS, 503, 4208
- Farrell, E., Groh, J.H., Hirschi, R., Murphy, L., **Kaiser, E.**, Ekström, S., Georgy, C., Meynet, G., **Is GW190521 the merger of black holes from the first stellar generations?**, 2021, MNRAS, 502, L40
- **Kaiser, E. A.**, Hirschi, R., Arnett, W. D., Georgy, C., Scott, L.J.A., Cristini, A., **Relative importance of convective uncertainties in massive stars**, 2020, MNRAS, 496, 1967
- Belczynski, K., Klencki, J., Fields, C.E., Olejak, A., Berti, E., Meynet, G., Fryer, C.L., Holz, D.E., O'Shaughnessy, R., Brown, D.A., Bulik, T., Leung, S.C., Nomoto, K., Madau, P., Hirschi, R., **Kaiser, E.**, Jones, S., Mondal, S., Chruslinska, M., Drozda, P., Gerosa, D., Doctor, Z., Giersz, M., Ekstrom, S., Georgy, C., Askar, A., Baibhav, V., Wysocki, D., Natan, T., Farr, W.M., Wiktorowicz, G., Coleman Miller, M., Farr, B., Lasota, J. -P., 2020, **Evolutionary roads leading to low effective spins, high black hole masses, and O1/O2 rates for LIGO/Virgo binary black holes**, A&A, 636, A104
- Belczynski, K., Hirschi, R., **Kaiser, E.A.**, Liu, J., Casares, J., Lu, Y., O'Shaughnessy, R., Heger, A., Justham, S., Soria, R., **The Formation of a 70 $M_\odot$ Black Hole at High Metallicity**, 2020, ApJ, 890, 113
- Arnett, W.D., Meakin, C., Hirschi, R., Cristini, A., Georgy, C., Campbell, S., Scott, L.J.A., **Kaiser, E.A.**, Viallet, M., Mocák, M., **3D Simulations and MLT. I. Renzini's Critique**, 2019, ApJ, 882, 18

2 Peer-Reviewed Conference Proceedings

- **Kaiser, E.A.**, Hirschi, R., Arnett, W.D., Cristini, A., Georgy, C., Scott, L.J.A., **Relative Importance of Convective Uncertainties**, 2019, NICXV
- Hampton, C.V., Lugaro, M., Papakonstantinou, P., Isar, P.G., Nordström, B., Özkan, N., Aliotta, M., Ćiprijanović, A. Curtis, S., Di Criscienzo, M., den Hartogh, J., Font, A.S., Kankainen, A., Kobayashi, C., Lederer-Woods, C., Niemczura, E., Rauscher, T., Spyrou, A., Van Eck, S., Yavahchova, M., Chantereau, W., de Mink, S.E., **Kaiser, E.A.**, Thielemann, F.-K., Travaglio, C., Venkatesan, A., Collet, R., **Women Scientists Who Made Nuclear Astrophysics**, 2019, NICXV

3 Submitted Publications

- Arnett, W.D., Hirschi, R., Campbell, S., Mocák, M., Georgy, C., Meakin, C., Cristini, A., Scott, L.J.A., **Kaiser, E.A.**, Viallet, M., 2018, arXiv

Appendix B

Software Tools

In this Appendix, the stellar evolution code used for this thesis is introduced and the numerical methods of the key physics are outlined. In the last Section, two code extensions, which are used in later Chapters, are explained and the lists with the input physics are presented.

Stellar evolution is a theory that includes a broad range of physics, some of which was introduced in Chapter I. Therefore, in order to explain the life of a star, a variety of physical processes have to be included into a mathematical model. In the past, the model was solved by hand. Nowadays it can easily be solved with computers, allowing to evolve a star through its entire life in a relatively short timescale, depending on the scenario. A software tool that solves the mathematical model is called a stellar evolution code. This Chapter introduces the methodology to perform detailed numerical simulations of stars and describes the methods and tools that were used to produce the results presented later in this thesis.

1 Stellar Evolution Code - `MESA`

The stellar evolution code *Modules for Experiments in Stellar Astrophysics* (or `MESA` in short - Paxton et al., 2011, 2013, 2015, 2018, 2019) is a software instrument. `MESA` is a suite of open source libraries for a wide range of applications in computational stellar astrophysics, made of independent modules for physics and numerical algorithms. It is constructed in a way that each of the individual modules is usable on its own, encouraging new computational experiments in astrophysics (Paxton et al., 2011). The code includes comprehensive microphysics and is being maintained and developed since its first

release in 2007 by a dedicated code development team[1]. MESA is publicly available[2].

MESA/star solves the equations of stellar structure and the composition equations, presented in Section B.1.2, simultaneously in a fully coupled manner (structure, burning and mixing, Paxton et al., 2011, 2013). This is advantageous for the accuracy of the converged solution at each time step because there is feedback between these three main sets of equations. MESA/star uses an adaptive spatial resolution refinement at each timestep - see Section B.1.7.2 - sophisticated timestep control - see Section B.1.7.1 - and supports "thread-safe" shared memory parallelism based on the OpenMP[3]. Also, it is possible to extend MESA by making use of the so-called *hooks*, which are provided in the source code - see Section B.2. There, extra physics can be included into the computations and easily shared with the community, instead of altering the source code. Users are encouraged to share all information needed for others to recreate their results, which are made available on the MESA market and zenodo.

The MESA code is applicable to a wide range of stellar evolution scenarios[4], covering the evolution of low-mass stars from the pre-main-sequence to a cooling white dwarf, intermediate-mass stars through the thermal pulses during the asymptotic giant branch phase, the complete evolution of massive stars from the pre-main-sequence to the onset of core-collapse and the evolution of giant planets. MESA also allows to compute more specific scenarios, such as pulsation in stars, binary evolution and the explosive phase of massive stars. More detailed information can be found in the instrument papers (Paxton et al., 2011, 2013, 2015, 2018, 2019) or on http://mesa.sourceforge.net.

The stellar evolution models presented in this thesis have been calculated with MESA revision 10398, which was released in March 2018. There exist newer releases but I kept using the same revision throughout my PhD work. This avoids the testing needed when updating to a later version and allows direct comparison between models in the various Chapters.

In this Chapter, the numerical method of the physics used in this work and some other key features are presented. First, the equations of stellar structure are introduced which are the core of the stellar evolution code. In the following Subsections, the implementation of the thermally-driven and rotation-induced mixing is described, in particular the parametrisations and input parameters are highlighted. Also, the reason for inclusion or exclusion of certain processes is debated. At the end, some of the code alterations are discussed.

1.1 Numerical Method

MESA includes several modules that provide numerical methods, each for a different aspect of physics or numerics. MESA/star is a full-featured stellar structure and evolution library which utilises these

[1] mesa.sourceforge.net/index.html
[2] How to obtain the latest MESA revision.
[3] https://www.openmp.org
[4] The broad applicability of MESA is visible in the list of published results, which can be found on the MESA market.

modules to provide a coupled solution of the structure and composition equations with automatic mesh and timestep refinement and analytic Jacobian matrices. At the start of a simulation, `MESA/star` reads all the input files and initialises the physics modules, which accesses the opacity and equation of state tables - see Section B.1.2.0.1 - and creates the nuclear reaction network (see Eq.(B.9)). Afterwards, the specified starting model is prepared. `MESA` offers two ways to begin a new evolutionary sequence (see Paxton et al. (2011)). The first option is to load a model, which is called "photo" in the `MESA` community[5], created from a previous run. Additionally, each `MESA` distribution includes a variety of saved models. It is also possible to relax a model of a certain mass to a new mass with a specified mass gain or loss. The second option is to construct a pre-main-sequence model, based on a user-chosen mass, uniform composition, luminosity and central temperature - the latter has to be low enough so that thermonuclear burning is insignificant, i.e. the default is $T_c = 9 \times 10^5$ K. Based on this, an initial guess for ρ_c is made by assuming a polytrope with $n = 1.5$ - see Section I.2.1. This is an appropriate choice for a fully convective star, however, in the subsequent search for a converged pre-main-sequence model `MESA` uses the mixing-length module, the equation of state module and a Newton solver to find a ρ_c satisfying the desired mass. Once the starting model is loaded, the computation enters the evolution loop, consisting of four components for each timestep:

(i) The new timestep is prepared by remeshing the model where necessary - see Section B.1.7.2. Also, a backup of the current state is created to allow for another attempt if the timestepping fails.

(ii) The model is adjusted to possible mass loss or mass gain. The variables for the model are evaluated, reflecting the changes made by remeshing and changing mass, including the Brunt-Väisälä frequency and the diffusion coefficient for mixing of the composition. Rotation is set, if it is enabled in the model.

(iii) The model is solved for its new structure and composition through repeated Newton iterations. `MESA/star` uses the previous modified model - see steps above - as the initial trial solution and converges to a final solution by iterating through the Newton-Raphson solver. A solution is accepted when the corrections and residuals meet a specified set of convergence criteria. Non-convergence causes the loop to return to the beginning, indicating a failure which leads to a retry. Convergence, on the other hand, is followed by a call for a routine that adjust the total angular momentum via a diffusion equation.

(iv) Finally, output files for the new model are generated.

After succeeding this evolution loop, the model has evolved one timestep and re-enters the loop until a stopping condition is met or an error in one of the four components occurs - for more details see Paxton et al. (2011) and Paxton et al. (2013), Appendix B.

[5] a binary file containing the complete state of the current model.

`MESA/star` discretises the star into cells. The number of cells depends on the complexity of nuclear burning, gradient of state variables, composition and various user-defined tolerances. For each cell, `MESA/star` simultaneously solves the full set of coupled equations that describe the structure of the star using a Newton method, a N-dimensional root find, to solve a system of N non-linear differential-algebraic equations. N is the number of basic variables in each zone times the number of zones in the current model. The equations are written in a relation $\mathcal{F}(\text{basic variables}) = 0$, with $\mathcal{F}$ being the vector-valued function of the residuals. While the solution never reaches $\mathcal{F} = 0$, a solution is accepted depending on the magnitude of $\mathcal{F}$ and the relative size of the adjustments to the basic variables (see Paxton et al., 2011, for more details).

Each cell of the star contains variables that are defined at the outer boundary of the cell (extensive variables) or that are mass-averaged over the cell (intensive variables). The latter are variables that describe matter, such as thermodynamic or composition variables. This separation of the definition is a consequence of finite volume, flux conservation formulation of the equations and improves stability and efficiency of the simulation (Sugimoto et al., 1981). All variables are evaluated at the same time $t + \delta t$.

In the following Subsections, the key structure and evolution equations are presented. Many of these equations are reformulated in `MESA` to enhance numerical stability of the linear algebra and minimise round-off errors.

1.2 Equations of Stellar Structure

Models of the stellar structure describe the interior profile of a star and allow to make predictions on how a star evolves. In order to describe the structure of a star, one needs to consider the mass distribution, motions due to forces, energy generation and loss, the transport of energy and the change of the nuclear abundance. Quantifying these physical procedures gives a full set of five equations - the equations of stellar structure (see Eqs.(B.1)-(B.5)). A solution of those fully coupled, non-linear partial differential equations for a time t and given boundary conditions is called a stellar model.

In a non-rotating, single star without strong magnetic fields the dominant forces are pressure and gravity, which are isotropic. Therefore, the stellar models are often assumed to be spherically symmetric, meaning that the quantities of a star are constant on spheres and depend only on the radial direction[6]. This assumption immensely simplifies the equations of stellar structure, because only one dimension has to be considered. The radius r could be the independent variable, however, often it is more convenient to use the mass m as the independent variable because, contrarily to the radius, the stellar mass remains almost constant, except for particular cases of heavy mass-loss. Therefore,

[6]The 3D character of physical processes, such as turbulent convection and rotation, was already outlined in Chapters I and II. Obviously, these processes are not spherically symmetric and their 1D approximative descriptions have to be thought of as a prediction of the average behaviour of the 3D processes.

MESA (and many other stellar evolution codes) uses the Lagrangian mass coordinates instead of the Eulerian coordinates.

The derivation of the stellar structure equations can be found in most stellar astrophysics textbooks (e.g. Kippenhahn & Weigert, 1994; Maeder, 2009). For completeness, the full set of the stellar structure equations is described below, following their implementation in MESA/star (Paxton et al., 2011):

$$\frac{\partial m}{\partial r} = 4\pi r^2 \rho, \tag{B.1}$$

$$\frac{\partial P}{\partial m} = \frac{1}{4\pi r^2}\left[-\frac{Gm}{r^2} - \frac{\partial^2 r}{\partial t^2}\right], \tag{B.2}$$

$$\frac{\partial l}{\partial m} = \epsilon_{\rm nuc} - \epsilon_{\nu,\rm thermal} + \epsilon_{\rm g}, \tag{B.3}$$

$$\frac{\partial T}{\partial m} = -\frac{GmT}{4\pi r^4 P}\nabla, \tag{B.4}$$

$$\left(\frac{dY_i}{dt}\right)_m = \frac{\partial}{\partial m}\left[\left(4\pi r^2 \rho\right)^2 D \frac{\partial Y_i}{\partial m}\right] + \left(\frac{\partial Y_i}{\partial t}\right)_{\rm nuc} \tag{B.5}$$

These are the equation of mass conservation, the equation of motion, the energy equation, the energy transport equation and the equations for the nuclear species, respectively. Eqs.(B.1) and (B.2) describe the mechanical part, which is coupled to the thermo-energetic part in Eqs.(B.3) and (B.4) only through the density ρ. Eq.(B.5) can be regarded as the chemical part. The variables have their usual physical meaning, either explained in the earlier Chapters or below.

The mass conservation equation, Eq.(B.1), relates the mass coordinate, the radius and the density of a given point in the star. It can also be used to translate the equations of stellar structure from Lagrangian to Eulerian coordinates.

The equation of motion, Eq.(B.2), also known as conservation of momentum, describes the opposing forces of gravity and the internal pressure gradient on a mass element. In the case of an imbalance, the mass element will receive an acceleration $\frac{\partial^2 r}{\partial t^2}$. However, the evolutionary timescale of the stellar interior is generally much longer than the sound crossing time and the star can be assumed to be in hydrostatic equilibrium. In certain cases, such as the evolution towards collapse, this assumption does not hold anymore and the hydrodynamic term needs to be included. In MESA it is possible to include the dynamical term via the boolean `v_flag`. This enables the use of implicit hydrodynamics, which also allows to simulate shocks (see Paxton et al., 2015, 2018, for more details).

The energy equation, Eq.(B.3), considers the conservation of energy by describing the luminosity of the stellar material enclosed within a mass m. Unless there is an energy source or sink in a shell there is no change in luminosity, i.e. $\frac{\partial l}{\partial m} = 0$. The energy equation in MESA considers three terms: thermonuclear energy, gravitational energy and energy loss by thermal neutrinos. The thermonuclear

energy generation rate, $\epsilon_{\rm nuc}$, is calculated as (Arnett & Thielemann, 1985)

$$\epsilon_{\rm nuc} = \frac{1}{\rho}\sum_{i,j} r_{i,j} Q_{i,j} \tag{B.6}$$

where $r_{i,j}$ is the reaction rate which turns nuclei i into nuclei j and $Q_{i,j}$ is the Q-value of the ij-reaction process. The gravitational energy generation rate, $\epsilon_{\rm g}$, is the specific amount of work done on or by the shell during expansion or contraction. It is theoretically calculated as (Kippenhahn & Weigert, 1994, p.23)

$$\epsilon_{\rm g} \equiv -T\frac{ds}{dt} = -c_P\frac{dT}{dt} + \frac{\delta}{\rho}\frac{dP}{dt}, \tag{B.7}$$

where s is the specific entropy. There are several options in `MESA` for how $\epsilon_{\rm g}$ is calculated. These alternatives are equivalent from an "*ideal*" physics viewpoint, but they can be very different numerically, depending on the situation[7]. The default form is

$$\epsilon_{\rm g} = -Tc_P\left[(1-\nabla_{\rm ad}\chi_T)\frac{d\ln T}{dt} - \nabla_{\rm ad}\chi_\rho\frac{d\ln\rho}{dt}\right], \tag{B.8}$$

with $\chi_T \equiv \frac{\partial \ln P}{\partial \ln T}\big|_\rho$ and $\chi_\rho \equiv \frac{\partial \ln P}{\partial \ln \rho}\big|_T$. $\epsilon_{\nu,\rm thermal}$ is the specific thermal neutrino-loss rate

The transport equation, Eq.(B.4), describes the temperature stratification as a function of mass coordinate. $\nabla \equiv d\ln T/d\ln P$ is the actual temperature gradient in terms of the pressure, taken from the corresponding theory - see Section II.1, in particular Eq.(II.15). An important note is that in Eq. (B.4), the right hand side is only valid in hydrostatic equilibrium. This is acceptable, since the local adjustment time in case of radiative transport is short and the mixing-length theory for convection assumes a hydrostatic equilibrium anyway - see Section II.1.2. `MESA/star` includes the option to switch off convective motions when the `v_flag` is switched on.

Eq.(B.5) describes the changes in abundance of the nuclear species i. The first term on the right hand side describes the change due to transport, for example by convection or rotation. The diffusion coefficient, D, sums up all transport processes of the nuclei which are treated as diffusive processes - see Sections B.1.3 and B.1.4. The second term describes the change in the abundance of nuclear species i due to nuclear burning processes (e.g. Arnett & Thielemann, 1985),

$$\left(\frac{\partial Y_i}{\partial t}\right)_{\rm nuc} = \sum_j c_i(j)\lambda_j Y_j + \sum_{j,k} c_i(j,k)\rho\lambda_{j,k}Y_jY_k + \sum_{j,k,l} c_i(j,k,l)\rho^2\lambda_{j,k,l}Y_jY_kY_l, \tag{B.9}$$

with $i = 1,\ldots,N$ and N is the total number of nuclei in the model (see e.g. Fig.(III.1)). Eq.(B.9) stands for the N equations that describe the temporal changes of the abundance of the N nuclear

[7] All the possible options are listed on the `MESA` documentation page.

species. The three terms on the right hand side stand, from left to right, for (1) β-decay, electron captures and photodisintegrations, (2) two-body reactions (e.g., ^{12}C(^{12}C,γ)^{24}Mg*) and (3) three-body reactions (e.g., the triple-α reaction), respectively. The rates of weak interactions and photodisintegration, (1), is represented by λ_j and the two- (or three-)body reaction rates, (2) and (3), are given by $\lambda_{j,k} = N_A\langle\sigma\nu\rangle_{j,k}$ and $\lambda_{j,k,l} = N_A^2\langle\sigma\nu\rangle_{j,k,l}$, respectively. N_A is Avogadro's number and $\langle\sigma\nu\rangle$ is the energy-integrated cross-section of the reaction (e.g. Kippenhahn & Weigert, 1994; Maeder, 2009). The coefficients c_i can be calculated, from left to right, by $c_i(j) = \pm N_i$, $c_i(j,k) = \pm N_i/(N_j!N_k!)$ and $c_i(j,k,l) = \pm N_i/(N_j!N_k!N_l!)$. Here N_i indicates how many particles of species i are involved in the reaction. The $\pm$ sign indicates whether the particle of species i is produced or destroyed (e.g. Arnett & Thielemann, 1985).

For a system with N different chemical species, Eq.(B.5) describes a set of N equations. Therefore, Eqs.(B.1)-(B.5) form a set of 4+N equations. In (B.5) one of the equations can be replaced by the normalisation of the mass fraction X_i, $\sum_i X_i = \sum_i A_i * Y_i = 1$, with the molar mass A_i. Eqs.(B.1)-(B.5) contain functions which describe the properties of the stellar material, such as

(i) an equation of state,

(ii) equations to describe the thermodynamic properties c_P, δ and $\nabla_{\rm ad}$,

(iii) the opacity κ,

(iv) the actual temperature gradient ∇,

as well as the nuclear reaction rates, the energy production and energy loss via neutrinos. By including these additional functions, which are described in the paragraphs further down, only 4+N variables, $r, P, T, l, Y_1, \cdots, Y_{\rm N}$ are left. Therefore, the system of Eqs.(B.1)-(B.5) can be solved numerically, with the independent variables m and t.

In a rotating star, spherical symmetry can no longer be assumed - see Sections I.4 and II.2. Therefore, the equations of stellar structure shown in Eqs.(B.1) - (B.5) are no longer valid. However, it is possible to write the stellar structure equations in one dimension; Kippenhahn & Thomas (1970) devised a method where they replaced the spherical stratification by a rotationally deformed stratification. The problem stays one dimensional if the potential of the star is conservative and an effective gravity can be derived from it. In this case, the pressure and density are constant on an equipotential - see Section I.4.1. The temperature is also constant, if the chemical composition is homogeneous on an equipotential. Therefore, the stellar structure equations can be written similarly to the non-rotating case if they are written on equipotentials.

Zahn (1992) and Chaboyer & Zahn (1992) showed that turbulence induced by differential rotation is anisotropic and acts much faster in the horizontal direction, i.e. perpendicular to gravity, than in the vertical one, i.e. parallel to gravity, which is a result from the stabilising effect of stratification. Conse-

quently, rotation is enforced to be constant on isobars. This shellular rotation law is not conservative and the method by Kippenhahn & Weigert (1994) is not valid anymore. However, Meynet & Maeder (1997) show that for the shellular rotation law surfaces with a constant total potential are isobars, but they are not equipotentials, and that Ω is constant on them. Therefore, the one-dimensional stellar structure equations can be written on isobars following Kippenhahn & Thomas (1970). The following set of stellar structure equations for the rotating case is implemented in the `MESA` code (Paxton et al., 2013):

$$\frac{\partial m_P}{\partial r_P} = 4\pi r_P^2 \bar{\rho}, \tag{B.10}$$

$$\frac{\partial P}{\partial m_P} = -\frac{G m_P}{4\pi r_P^4} f_P - \frac{1}{4\pi r_P^2}\left(\frac{\partial^2 r_P}{\partial t^2}\right)_{m_P}, \tag{B.11}$$

$$\frac{\partial l_P}{\partial m_P} = \epsilon_{\rm nuc} - \epsilon_\nu + \epsilon_{\rm g}, \tag{B.12}$$

$$\frac{\partial \ln T}{\partial \ln P} = \min\left[\nabla_{\rm MLT}, \nabla_{\rm rad}\frac{f_T}{f_P}\right]\left[1 + \frac{r_P^2}{G m_P f_P}\left(\frac{\partial^2 r_P}{\partial t^2}\right)_{m_P}\right]^{-1}, \tag{B.13}$$

with

$$f_P = \frac{4\pi r_P^4}{G m_P S_P}\frac{1}{\langle g^{-1}\rangle}, \qquad f_T = \left(\frac{4\pi r_P^2}{S_P}\right)^2 \frac{1}{\langle g\rangle\langle g^{-1}\rangle} \tag{B.14}$$

where S_P is the surface of an isobar and V_P its volume. The radius coordinate is defined as the radius of a sphere containing the same volume $V_P = (4/3)\pi r_P^3$. The index P refers to values on an isobar, $\langle x\rangle \equiv \frac{1}{S_P}\oint_{S_P} x d\sigma$ is the average of x on an isobaric surface and $\bar{x}$ is the average of x in the volume between two isobars. The two factors f_P and f_T account for the effects of rotation on the stellar structure - see Section I.4.1; f_P considers the change of the effective gravity due to centrifugal forces and f_T the change of the radiative flux with latitude. Furthermore, the consideration of isobars takes into account the deformation from spherical symmetry. The rotation-induced mixing of chemicals and transport of angular momentum is considered by including new terms into the equation for the transport of chemical elements and angular momentum, respectively - see Sections B.1.3 and B.1.4. The equation of energy, Eq. (B.3), does not change under the influence of rotation since the nuclear physics is unchanged. In Eq. (B.13) the two cases of radiative or convective energy transport are already summarised. $\nabla_{\rm MLT}$ is the temperature gradient from the corresponding mixing process in convective regions.

B.1.2.0.1 Equation of State and Opacities

The equation of state relates the thermodynamic properties of the stellar material, usually formulated

as $P \equiv P(\rho, T, Y_i)$. The equation of state for a gas can be written as

$$P_{\text{gas}}^{\alpha} = \frac{\rho}{\mu^{\varphi}} k T^{\delta} \tag{B.15}$$

with the Boltzmann constant $k = 1.38 \cdot 10^{-13}\,\text{cm}^2\,\text{g}\,\text{s}^{-2}\,\text{K}^{-1}$ and the thermodynamic quantities

$$\alpha \equiv \left(\frac{\partial \ln \rho}{\partial \ln P}\right)_{\mu,T} \qquad \delta \equiv -\left(\frac{\partial \ln \rho}{\partial \ln T}\right)_{P,\mu}, \qquad \varphi \equiv \left(\frac{\partial \ln \rho}{\partial \ln \mu}\right)_{P,T}. \tag{B.16}$$

In an ideal, non-interacting gas, $\alpha = \delta = \varphi = 1$. In a star, however, matter also interacts with radiation and can be found in extreme conditions such as degeneracy - see Section I.2.1.2. Therefore, a more general equation of state is used in stellar evolution codes, which needs to account for radiation and electron degeneracy pressure (e.g. Kippenhahn & Weigert, 1994; Maeder, 2009), i.e. $P = P_{\text{gas}} + P_{\text{rad}} + P_{\text{deg}}$, with

$$P_{\text{rad}} = \frac{a}{3} T^4 \tag{B.17}$$

and

$$P_{\text{deg}} = \begin{cases} \frac{h^2}{5 m_e} \left[\frac{3}{8\pi}\right]^{\frac{2}{3}} n_e^{\frac{5}{3}} & \text{non-relativistic} \\ \frac{hc}{4} \left[\frac{3}{8\pi}\right]^{\frac{1}{3}} n_e^{\frac{4}{3}} & \text{non-relativistic.} \end{cases} \tag{B.18}$$

where n_e is the electron number density and h the Planck constant. Furthermore, matter in the cooler layers of a star becomes partly ionised, which needs to be accounted for in the equation of state as well. Note that in massive stars, which are discussed in this thesis, the radiation pressure dominates. A general equation of state needs to cover an extreme range of values, from the interstellar medium with a density of about $10^{-23}\,\text{g}\,\text{cm}^{-3}$ to neutron stars with a density of $10^{15}\,\text{g}\,\text{cm}^{-3}$. While the computation of a massive star does not cover such an extreme range, there are still many orders of magnitude difference between the density in the core and the surface of the star. Therefore, determining the equation of state of the stellar material $P(\rho, T, Y_i)$ requires detailed calculations which can impose a substantial computational overhead. However, since $P(\rho, T, Y_i)$ is a fixed property of the material, its calculation can be pre-processed and provided to the stellar evolution calculation, which alleviates the computational burden. The `MESA` module `eos` provides the pressure as a function of density and temperature via tables. The coverage of the pre-computed tables is shown in Fig.(B.1a) in the log ρ - log T plane. If the density or temperature is outside of those ranges, the solution is computed during the runtime. The `MESA` equation of state tables are built from the OPAL tables (Rogers & Nayfonov, 2002). In order to rectify the treatment of the partially ionised region at high metallicity, i.e. $Z > 0.04$, new MacDonald equation of state tables have been computed (Paxton et al., 2013). At lower temperatures and densities (see Fig.(B.1a)), the SCVH tables (Saumon et al., 1995) are used, which account for partial dissociation and ionisation of the composition. There is a smooth

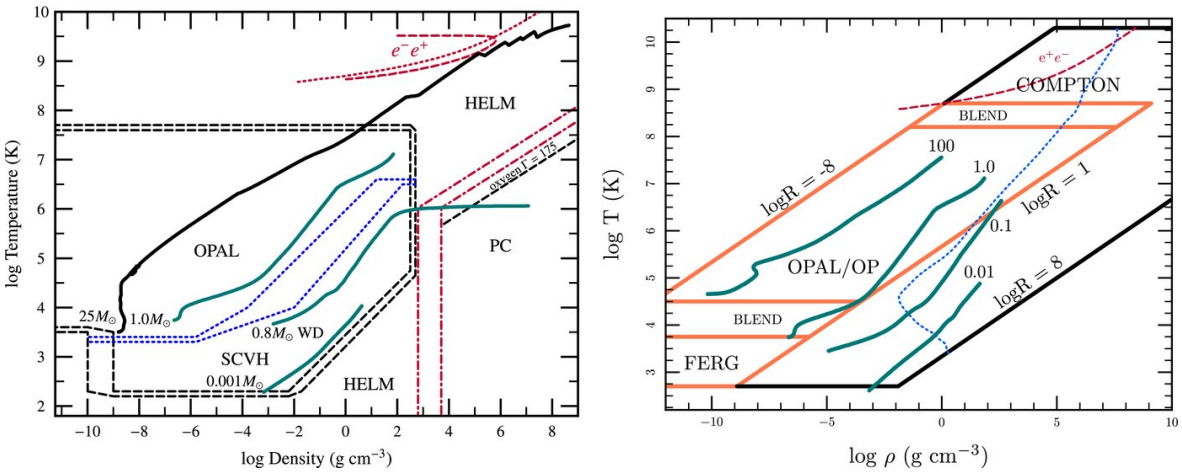

(a) (b)

Figure B.1: (a) The log ρ - log T plane showing the regions covered by the `MESA` equation of state tables. The details are explained in the text. The red dashed line bounds the region of pair creation. (b) Regions in the log ρ - log T plane which are covered by the `MESA` opacity tables. The orange lines surround the regions for which tabulated opacities are available and the black line extends to the region where the radiative opacity is taken at log $R = 1$ - see text for details. The red dashed line indicates where pair creation is dominant and the blue dotted line marks the region for which electron conduction becomes the dominant source of opacity. Both figures were taken from Paxton et al. (2011).

.

transition between the two tables, shown by the blue dotted lines in Fig.(B.1a), where the data is blended using a sinusoidal function for each of the physical quantities. Outside of the region covered by these tables, the HELM (Timmes & Swesty, 2000) and the PC (Potekhin & Chabrier, 2010) equation of states are employed. Again, the overlapping regions between the tables are blended together, indicated by the dashed black and red dash-dotted lines in Fig.(B.1a). The location of the smoothing region in the log ρ - log T plane can be modified by the user. The tables are interpolated in the independent variables using a bicubic function and separate quadratic interpolations are performed in the hydrogen and metal mass fraction (see Paxton et al., 2011, §4.2 for more details). `MESA eos` also has the flexibility to accept user-defined equation of state tables.

The opacity of stellar matter controls the rate at which light passes through a layer in the star, i.e. how fast the star loses its energy. Consequently, the luminosity of a star is determined by the opacity rather than its nuclear reactions, hence, it is a crucial ingredient for modelling stars. Opacity is a result of many processes in atomic physics that influence the transfer of radiation (see e.g. Kippenhahn & Weigert, 1994, §17), mainly

(i) electron scattering, where the energy of an electromagnetic wave is partly scattered by an electron,

(ii) free-free transitions, where a free electron moving in the Coulomb field of an ion can absorb and emit radiation,

(iii) bound-free transitions, where an incident photon ionises an atom (for example negative hydrogen absorption, where hydrogen can become a negative charged ion with a loosely-bound second electron which can absorb radiation, giving rise to a bound-free transition),

(iv) bound-bound transitions or line absorption, where an electron in an atom absorbs the radiation, reaches a higher energy level and re-emits it later in an arbitrary direction and

(v) electron conduction, where heat is transported by electrons via conduction, which is only important in degenerate matter.

The total opacity at a given frequency ν is the sum of all the various processes at frequency ν, where coefficients from points (ii)-(iv) are corrected by a term to account for stimulated emission[8].

In massive stars, (i) and (iv) dominate. Fig.(B.2a) presents the opacity profiles of massive stars with three different initial masses: 15, 25 and 60 $M_\odot$. In the interior the opacity has a relatively low value because at high temperatures the elements are fully ionised and electron scattering dominates. In the outer layers, at lower temperatures, there are three distinct peaks. The peak at $\log T \approx 5.3$, often called the *iron opacity bump*, is due to the many iron lines that originate in the M shell of iron which allow the element to efficiently absorb radiation (Iglesias & Rogers, 1993; Badnell et al., 2005). The much smaller bump around $\log T \approx 6.3$ originates from iron too, due to L shell bound-free transitions, and minor contributions from nickel and CNO elements. The peak at $\log T \approx 4.7$, the so-called *helium opacity bump*, results from the bound-free transition of ionised helium. The opacity profiles show similar features for all initial masses but more massive stars have a lower opacity in the envelope, which is because they have more compact envelopes and higher effective temperature, hence, the atoms are more ionised and the effectiveness of the process (iv) decreases. This leads to the disappearance of the *helium opacity bump* in the 60 $M_\odot$ model. Similarly to the equation of state, the opacity $\kappa(\rho, T, Y_i)$ is provided in tabular form from the `MESA` module `kap` as a function of density and temperature in order to avoid the computational burden. Fig.(B.1b) presents the coverage of the tables. The opacity tables are divided into a high-temperature, $\log(T/\mathrm{K}) \gtrsim 4$, and a low-temperature domain, in order to facilitate the use of different sources of low-T opacity data. The exact range of $\log T$ over which the tables are blended can be adjusted at runtime. The pre-processed opacity tables are constructed from several sources:

- The radiative opacities are covered by either Ferguson et al. (2005) or Freedman et al. (2008) for the low-temperature range, $2.7 \leq \log T \leq 4.5$, and OPAL (Iglesias & Rogers, 1993, 1996) for $3.57 \leq \log T \leq 8.7$. `MESA` offers the choice between OPAL Type 1 (Iglesias & Rogers, 1993) and OPAL Type 2 (Iglesias & Rogers, 1996). The latter accounts for varying abundances of carbon and oxygen, rather than assuming that they scale directly with metallicity. `MESA` also provides the option to use the OP tables (Seaton, 2005) in place of the OPAL tables. If $\log T \geq 8.7$, the radiative

[8] This is a process by which radiation of a specific energy can reduce the energy level of an excited atomic electron.
[9] http://cococubed.asu.edu

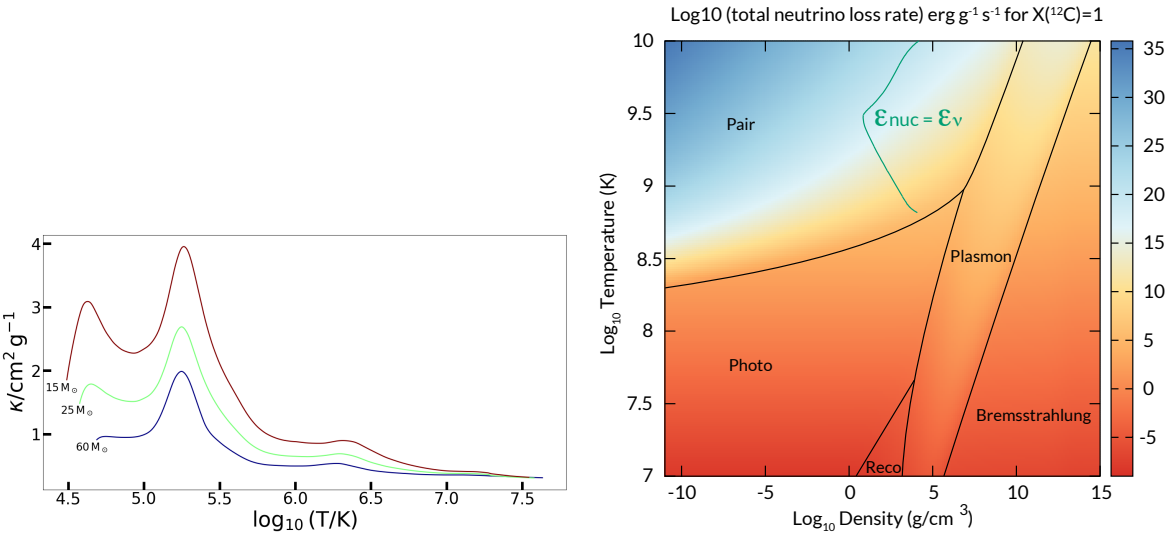

(a) (b)

Figure B.2: (a) The opacity κ at the zero-age main sequence for different initial masses as a function of the temperature. The non-rotating stellar models are presented in Chapter IV. (b) The log ρ - log T plane, showing the dominant mechanisms of neutrino production in case of ^{12}C matter. The colour indicates the total energy loss rate by the neutrinos obtained with the fitting formulae of Itoh et al. (1996). The figure was created using the tool `sneut5` provided by F.X. Timmes[9].

.

opacity is dominated by Compton scattering and is calculated with the equations from Buchler & Yueh (1976). In the region of pair production - see Section I.3.2 - the number of electrons and positrons per baryon is calculated with the HELM equation of state.

- The electron conduction opacities in the regions for $-6 \leq \log \rho \leq 11.5$ and $3 \leq \log T \leq 10$ are taken from Cassisi et al. (2007), including an expansion to cover higher temperatures and densities (see Paxton et al., 2013, A.3). Outside of this region two different fits to the electron conduction tables from Hubbard & Lampe (1969) are used; in the non-degenerate case the fits from Iben (1975) are applied, whereas the Yakovlev & Urpin (1980) fits are included for the degenerate case.

The various tables are blended together with a sinusoidal function (see Paxton et al., 2011, §4.2 for further details); the exact range of the blend can be adjusted. The tables are interpolated in log T and log R using a bicubic function and the user has the option to choose either linear or cubic interpolation in the hydrogen and metallicity mass fraction.

In the regions with no radiative opacity available, i.e. between log $R = 1$ and log $R = 8$ in Fig.(B.1b), the radiative opacities are fixed at their value at log $R = 1$ and combined with the electron conduction opacities (see Paxton et al., 2011, §4.2 for further details). Similarly, for the region left of log $R = -8$ and below log $T = 8.7$, where electron scattering dominates, the opacity from the table at log $R = -8$ and the appropriate value for log T is used. Above log $T = 8.7$, the production of electron-positron pairs becomes relevant. `MESA` incorporates the enhancement to the opacity from the increasing number of leptons per baryon.

1.2.1 Nuclear Reaction Rates

Both, the energy generation (Eq.(B.6)) and the change in the abundance of nuclear species due to thermonuclear burning (Eq.(B.9)) depend on the nuclear reaction rates. In MESA most reaction rates are taken from the REACLIB database[10] (Cyburt et al., 2010). This database is compiled from recommended reaction rates, including theoretical and experimentally measured contributions, and preference is given to the experimentally determined rates where applicable. Often the experimental rates are supplied by Caughlan & Fowler (1988) or the NACRE compilation (Angulo et al., 1999; Xu et al., 2013), with preference given to the latter. The REACLIB database provides each rate as a function of the temperature in GK, T_9,

$$\lambda_{<>} = \exp\left\{a_0 + \sum_{i=1}^{5} a_i T_9^{\frac{2i-5}{3}} + a_6 \ln T_9\right\}, \tag{B.19}$$

with a_i being fitting parameters from the database. For each reaction in the network, $\lambda_{<>}$ is computed from Eq.(B.19) and then used to determine the change in chemical species via Eq.(B.9). The units of $\lambda_{<>}$ differ, depending on the reaction type (Cyburt et al., 2010). For single-body reaction, λ_i has units of s^{-1}, whereas for two-body and three-body reactions λ_{ij} and λ_{ijk} have the units of $\mathrm{cm}^3\,\mathrm{mol}^{-1}\,\mathrm{s}^{-1}$ and $\mathrm{cm}^6\,\mathrm{mol}^{-2}\,\mathrm{s}^{-1}$, respectively. The REACLIB database also provides the Q-value for each reaction to calculate the corresponding release of thermonuclear energy (see Eq.(B.6)).

The reaction rate library in MESA includes significant updates to the NACRE rates for some of the key reactions. The $^{14}\mathrm{N}(\mathrm{p},\gamma)^{15}\mathrm{O}$ and $^{14}\mathrm{N}(\alpha,\gamma)^{18}\mathrm{F}$, which are important in the hydrogen-burning CNO cycle, are taken from Imbriani et al. (2005) and Görres et al. (2000), respectively. The updated rate of Fynbo et al. (2005) for the triple-α process and the rate of Kunz et al. (2002) for the $^{12}\mathrm{C}(\alpha,\gamma)^{16}\mathrm{O}$ are used in this work.

The weak reaction rates, i.e. the rates for lepton capture and β-decay reactions, are based on the tabulations of Fuller et al. (1985); Oda et al. (1994); Langanke et al. (2003) for isotopes with atomic mass numbers $45 < \mathrm{A} < 65$, where precedence is given to the tables in the latter publication.

1.2.2 Neutrino Energy Losses

During the advanced evolutionary phases of massive stars, the temperature in the centre is hot enough for non-negligible neutrino production - see Section I.2.1.3. Possible non-nuclear neutrino production processes are (Fowler & Hoyle, 1964; Itoh et al., 1996)

$$\begin{aligned}
\textit{Plasmon decay}: &\quad \gamma_{\mathrm{plasma}} \rightarrow \nu + \bar{\nu} \\
\textit{Pair annihilation/creation}: &\quad e^+ + e^- \rightarrow \nu + \bar{\nu} \\
\textit{Neutrino bremsstrahlung}: &\quad e^{\pm} + (Z,A) \rightarrow e^{\pm} + (Z,A) + \nu + \bar{\nu} \\
\textit{Photoneutrino process}: &\quad e^- + \gamma \rightarrow e^- + \nu + \bar{\nu}
\end{aligned}$$

[10] https://reaclib.jinaweb.org

Neutrinos have a very small cross-section and at the densities encountered in the stellar interior their mean free path is much longer than the stellar radius[11]. Therefore, any neutrino will immediately escape the star, resulting in a direct loss of energy in this region. `MESA` describes the energy loss from non-nuclear neutrino processes, ϵ_ν, with the fits of Itoh et al. (1996), which is used in Eq.(B.3). These fits do not include the energy loss by neutrinos created from weak nuclear reactions which are included in the $\epsilon_{\rm nuc}$ term - see Section (B.1.2.1).

Fig.(B.2b) illustrates the dominant neutrino production mechanisms in different regions in the log $\rho-$ log T plane and the corresponding neutrino energy loss rates. The neutrino pair creation dominates at high temperatures and low density. There black-body radiation produces e^-e^+-pairs in a equilibrium, which are converted directly to $\nu\bar{\nu}$-pairs (Chiu & Morrison, 1960). The photo-neutrino process dominates at lower densities and temperatures. Energy loss by plasmon neutrinos[12] depends strongly on the electron density, with a maximum in the domain where $\hbar\omega_0 \gg kT$, where ω_0 is the plasma frequency. Therefore, the plasma neutrino energy loss rate is peaked at higher electron densities for higher temperatures - see Fig.(B.2b) but also Beaudet et al. (1967). Bremsstrahlung neutrinos can be produced by electromagnetic radiation that is generated when an electron is slowed down in a Coulomb field of a charged nucleus. The emission rate depends on $\sim \rho T^6$ and is dominant at very high densities. Fig.(B.2b) shows that there is a small region where the recombination process dominates. There, a free electron transitions into a bound atomic state, which can generate a neutrino. However, these emission rates are very low and have little significance. Also, there are other neutrino emission processes, though only the above mentioned ones play a significant role in the conditions found in stellar evolution.

1.3 Thermally-Driven Mixing

`MESA/star` treats convective mixing as a time-dependent diffusive process. The diffusion coefficient D is determined following the mixing-length theory - see Sections II.1.2 and B.1.3.1. After the convective mixing has been solved, `MESA/star` computes the semiconvective and convective boundary mixing diffusion coefficients, according to Sections B.1.3.3 and B.1.3.2, respectively.

The change of the mass fraction $X_{i,k}$ of nuclear species i in cell k for a timestep δt in `MESA` is determined by (Paxton et al., 2011)

$$X_{i,k}(t+\delta t) - X_{i,k}(t) = \frac{dX_{i,k}}{dt}(t)\delta t + (F_{i,k+1} - F_{i,k})\frac{\delta t}{dm_k}, \tag{B.20}$$

[11] For example, the mean free path of an electron neutrino is $\ell_{\rm free} = \frac{1}{n\sigma_\nu}$ with its cross-section $\sigma_\nu \approx 10^{-44}\left(\frac{E_\nu}{m_e c^2}\right)^2$ cm^2, nuclei concentration n and energy E_ν (Maeder, 2009). Therefore, for 1 MeV electron neutrinos in ordinary lead the mean free path is about 20 light-years.

[12] A plasmon is a quantum of plasma oscillation, generated by an electromagnetic wave entering a dense plasma. Plasmons are unstable quasi-particles, the decay of which can produce a $\nu\bar{\nu}$-pair.

which is solved together with the other stellar structure equations - see Section B.1.2. $\frac{dX_{i,k}}{dt}(t)$ is the rate of change of species X_i in cell k due to nuclear burning (see Eq.(B.9)) and $F_{i,k}$ is the mass of chemical species i flowing across the boundary of cell k:

$$F_{i,k} = (X_{i,k} - X_{i,k-1})\frac{\sigma_k}{\overline{dm}_k} \tag{B.21}$$

with the averaged cell mass $\overline{dm}_k = \frac{1}{2}(dm_{k-1} + dm_k)$ and the Lagrangian diffusion coefficient, $\sigma_k = (4\pi\rho r^2)^2 D_{\rm tot}$, where $D_{\rm tot}$ is the sum of the diffusion coefficients of convection, semiconvection, convective boundary mixing and, if active, rotation. It should be noted that σ_k is calculated at the beginning of a timestep and held constant during the implicit solver iterations, which significantly improves the numerical convergence (Paxton et al., 2011). However, it can lead to small inconsistencies between the mixing boundary and the boundary of convection, which is determined at the end of a timestep.

1.3.1 Convection

The treatment of convection and mixing in stellar models arise from considerations of dynamical and secular stability, which was outlined in Section II.1, based on the mixing-length theory derived in Vitense (1953); Böhm-Vitense (1958). However, different flavours of the mixing-length theory have been developed over the years under different assumptions. `MESA` implements different variations of the mixing-length theory in the `mlt` module. In this paragraph, a short overview over the most commonly used versions is given.

The key equations of the mixing-length theory can be written in a general way (cf. Cox & Giuli, 1968; Ludwig et al., 1999), with the convective flux, Eq.(II.12),

$$F_{\rm conv} = f_2 \frac{\rho C_P \bar{v} T \ell_{\rm MLT}}{H_P}(\nabla - \nabla_{\rm int}), \tag{B.22}$$

the convective velocity, Eq.(II.14),

$$\bar{v}^2 = f_1 g \delta (\nabla - \nabla_{\rm int}) \frac{\ell^2_{\rm MLT}}{H_P} \tag{B.23}$$

and the convective efficiency, i.e. the ratio of the transported energy and the energy lost during the fluid element's lifetime,

$$\Gamma \equiv \frac{\nabla - \nabla_{\rm int}}{\nabla_{\rm int} - \nabla_{\rm ad}} = \frac{\rho C_P \bar{v} \tau_e}{f_3 \sigma T^3}\left(1 + \frac{f_4}{\tau_e^2}\right). \tag{B.24}$$

where σ is the Stefan-Boltzmann constant, $\ell_{\rm MLT} = \alpha_{\rm MLT} H_P$ is the mixing length, C_P the specific heat at constant pressure and the ∇s are the four temperature gradients discussed in Section II.1.

Table B.1: The f_i parameters for the various mixing-length theory versions implemented in `MESA`. The coefficients are hard-coded with the exception of $\nu_{\rm H}$ and $y_{\rm H}$ in the `Henyey` flavour which can be defined by the user during runtime, usually $\nu_{\rm H} = 8$ and $y_{\rm H} = \frac{1}{3}$ or $\frac{3}{4\pi^2}$, to adjust the opaqueness of the fluid element. The values were taken from Ludwig et al. (1999), Table 1.

mixing-length theory flavour	`MLT_option`	f_1	f_2	f_3	f_4
Cox & Giuli (1968)	`Cox`	$\frac{1}{8}$	$\frac{1}{2}$	24	0
Böhm-Vitense (1958)	`ML1`	$\frac{1}{8}$	$\frac{1}{2}$	24	0
Bohm & Cassinelli (1971)	`ML2`	1	2	16	2
Henyey et al. (1965)	`Henyey`	$\frac{1}{\nu_{\rm H}}$	$\frac{1}{2}$	$\frac{8}{y_{\rm H}}$	$\frac{1}{y_{\rm H}}$
Mihalas (1978); Kurucz (1979)	`Mihalas`	$\frac{1}{8}$	$\frac{1}{2}$	16	2

The optical thickness of a convective fluid element, τ_e, is defined as

$$\tau_e \equiv \kappa\rho\ell_{\rm MLT}. \tag{B.25}$$

The four dimensionless free parameters, f_1, f_2, f_3 and f_4, vary, depending on the underlying assumptions of the mixing-length theory flavour used. Table B.1 presents the f_i parameters for the various mixing-length theories implemented in `MESA`[13]. The `MESA` default version is `Cox`, which assumes optically thick material, hence, high optical depths and no radiative losses. In contrast, the `Henyey` flavour allows the convective efficiency to change with opaqueness of the fluid element, which is an important effect for convective layers in the envelope. In this work, the mixing-length theory option `Henyney` is chosen with $\nu_{\rm H} = 8$ and $y_{\rm H} = \frac{1}{3}$. `MESA` includes other flavours for specific situations such as atmospheres and white dwarfs (Paxton et al., 2013), listed in Table B.1 for completeness. Their discussion, however, will be omitted here.

Following the discussion in Section II.1.2, with (i) the knowledge of the total flux,

$$F_{\rm tot} = F_{\rm rad} + F_{\rm conv} \equiv \frac{4ac}{3}\frac{T^4}{\kappa\rho H_P}\nabla_{\rm rad}, \tag{B.26}$$

(ii) the adiabatic temperature gradient $\nabla_{\rm ad}$ and (iii) the knowledge of the physical variables C_P, κ, $\ell_{\rm MLT} = \alpha_{\rm MLT}H_P$, ρ and T, it is possible to form three equations with three unknowns,

$$\nabla_{\rm rad} = \nabla + a_0 A(\nabla - \nabla_{\rm int})^{\frac{3}{2}}, \tag{B.27}$$

$$\Gamma = A(\nabla - \nabla_{\rm int})^{\frac{1}{2}}, \tag{B.28}$$

$$\Gamma = \frac{\nabla - \nabla_{\rm int}}{\nabla_{\rm int} - \nabla_{\rm ad}}. \tag{B.29}$$

[13] A careful reader may notice that the f_i parameters in Table B.1 for the `MLT_option` `Cox` and `ML1` are identical. In the `MESA` code, both options are listed and two different implementations are used, however, they both are calculated exactly the same. According to the developers, "*the two options were implemented at different times and the availability of both is a relict of that (in accordance with the jumble of descriptions of different prescriptions strewn throughout the literature), for more detail follow the message thread*". Both options were kept in the table for completeness.

with the two quantities

$$a_0 = \frac{3}{16} \times \frac{f_2 f_3}{\left(1 + \frac{f_4}{\tau_e^2}\right)} \tag{B.30}$$

$$A^2 = \frac{f_1 g \delta \ell_{\mathrm{MLT}}^2}{H_P} \frac{\Gamma^2}{\bar{v}^2}. \tag{B.31}$$

This equation system allows to determine ∇, ∇_{int} and Γ via a cubic equation. The knowledge of the temperature gradient ∇ enables the computation of the convective velocity and finally the diffusion coefficient for chemical mixing (see Eq.(II.16)).

In the very centre of the star, with $r \to 0$ the definition of the pressure scale height, $H_P = \frac{P}{g\rho}$, diverges because $g \to 0$. MESA provides the option to include the alternative definition of the pressure scale height by Eggleton (1971), $H_{P,\mathrm{Eggl.}} = \sqrt{\frac{P}{G\rho^2}}$, when $H_{P,\mathrm{Eggl.}} < H_P$. In the centre of the star, $H_{P,\mathrm{Eggl.}} \sim r$, hence, the divergence is avoided.

1.3.2 Convective Boundary Mixing

The boundaries of a convective zone in a stellar model are determined either by the Ledoux or the Schwarzschild criterion - see Section II.1.1. MESA offers the choice between the two criteria. The boundary is determined as the location where the discriminant, $y = \nabla_{\mathrm{rad}} - \nabla_{\mathrm{ad}}$ or $y = \nabla_{\mathrm{rad}} - \nabla_{\mathrm{ad}} + B$, respectively, changes sign, where B is the composition term of the Ledoux criterion - see below. While this procedure works well if y is continuous at the interface of the convective and radiative region, problems arise if there is a discontinuity - see discussion in Section III.7 and Gabriel et al. (2014).

The adiabatic and radiative temperature gradient are determined according to Eqs.(II.8). ∇_{rad} is directly computed. In the atmosphere, i.e. where the optical depth drops below $\frac{2}{3}$, it is however multiplied by a factor to account for the dilution of stellar radiation following Paczyński (1969). On the other hand, ∇_{ad} is an output quantity from the `eos` module - see Appendix B.1.2.0.1 and Paxton et al. (2011). The chemical composition term in the Ledoux criterion explicitly takes into account the effect of composition gradients. In MESA, this term is implemented slightly differently to ensure that the description is both, numerically robust and simpler to implement (see Paxton et al., 2013, §3.3 for more details),

$$B = -\frac{1}{\chi_T} \sum_{i=1}^{N-1} \left(\frac{\partial \ln P}{\partial \ln X_i}\right)_{\rho,T,\{X_{j\neq i}\}} \frac{d \ln X_i}{d \ln P} \tag{B.32}$$

$$\equiv -\frac{1}{\chi_T} \lim_{\delta \ln P \to 0} \frac{\ln P(\rho, T, X + (dX/d\ln P)\,\delta \ln P) - \ln P(\rho, T, X)}{\delta \ln P}. \tag{B.33}$$

This term takes a directional derivative along the radial composition gradient, $dX/d\ln P$, in the stellar model. For the kth mesh point, indicated by the subscript, the chemical composition term is computed

as

$$B = -\frac{1}{\chi_T} \frac{\ln P(\rho_k, T_k, X_{k+1}) - \ln P(\rho_k, T_k, X_k)}{\ln P_{k+1} - P_k}. \tag{B.34}$$

This formulation requires only one numerical difference along the radial chemical composition, X. The Ledoux criterion for stability is then formulated as $\nabla_{\rm rad} < \nabla_{\rm ad} + B \equiv \nabla{\rm L}$. It should be noted that when the Schwarzschild criterion is used, the composition term is artificially set to zero.

The chemical composition profile often contains step-like features, a result of finite mesh grid and timesteps. This can lead to "numerical noise" in the chemical composition gradient; for example the radial profile of B can contain large peaks during the main-sequence evolution of a massive star in the region of the receding convective core. These peaks can lead to an over-stabilisation of the region and affect the later evolution of, e.g., the intermediate convective zone - see discussion in Section III.4. `MESA` implements a weighted smoothing routine - see Appendix C.1 - where the number of cells to be included in the smoothing are chosen by the user.

In an attempt to account for the problems with the identification of the convective boundary outlined by Gabriel et al. (2014), a "predictive mixing" scheme was implemented in `MESA` (Paxton et al., 2018). This scheme first locates the convective boundary by identifying the cells where the discriminant y changes sign. Next, the algorithm expands the convective boundary during a timestep, with the assumption of a uniform composition, until $\nabla_{\rm rad} = \nabla_{\rm ad}$ on the convective side of the boundary interface[14]. The expansion is achieved by modifying the convective diffusivity in the cells on the radiative side of the boundary. While "predictive mixing" is able to achieve $\nabla_{\rm rad} = \nabla_{\rm ad}$ on the convective side of the boundary in most cases, it fails in some scenarios such as the retreating main-sequence convective core in a $16\,{\rm M}_\odot$ model (see Paxton et al., 2019, §5.1 for details), showing the need for further work. For this reason, the "predictive mixing" scheme is not included in this thesis[15].

Convective boundary mixing and the different, commonly-used implementations have been discussed in Section II.1.3 to some extent. `MESA` adopts different schemes for convective boundary mixing in stellar models, from which the user can choose.

Exponentially-decaying diffusive scheme: Convective boundary mixing is implemented via an exponential decay of the convective diffusion coefficient beyond the convective boundary (see Eq.(II.17)). The user-specified parameters $f_{\rm ov}$ and f_0 determine the extent of the convective boundary mixing region and the location in the convective region where the exponential decay begins, respectively - see Section II.1.3 for more details. The convective boundary mixing is cut off once the diffusion coefficient drops below a certain value; the default is $D_{\rm cutoff} = 10^2\,{\rm cm^2\,s^{-1}}$, in order to avoid the infinite exponential tail.

[14] In the convective zone, the composition is assumed to be well mixed and $B = 0$, hence, the Ledoux and Schwarzschild criterion are identical in the convective region.

[15] Paxton et al. (2019) developed a new scheme for treating convective boundaries, "convective pre-mixing". This scheme, however, was developed in a later `MESA` revision and shall not be discussed here.

Step-overshoot: This options refers to the penetrative "overshoot" in Section II.1.3, where the fully mixed region is extended at the convective boundary for a fraction of the pressure scale height, $d_{\rm ov} = \alpha_{\rm ov} H_P$, with the user-adjusted free parameter $\alpha_{\rm ov}$. A constant user-defined diffusion coefficient is applied in this region: $D_{\rm ov} = D_{\rm user} + f_{\rm user} \cdot D_0$, where D_0 is the diffusion coefficient at the edge of the convective region. Similar to the exponentially-decaying diffusive scheme, the step-overshoot implementation depends on a second user-selected parameter, f_0, to determine the exact starting location of the step-overshoot.

Double-f: This scheme follows the exponentially-decaying diffusive scheme with the difference that it combines two regions with different scale lengths and starting value for the exponential decay. In this context, a diffusion coefficient is chosen, at which the code switches from the first exponential decay to the second one, which is in general shallower. The idea for this scheme is based on multi-dimensional hydrodynamic simulations, which report that the mixing efficiency after the convective boundary is best described with an initially steep slope followed by a shallower one (Herwig et al., 2007).

It is possible to combine the different convective boundary mixing schemes. In all cases, convective boundary mixing only mixes the chemical composition but not the entropy, thus $\nabla = \nabla_{\rm rad}$ in the convective boundary region.

In the very centre of the star, where the pressure scale increases immensely, convective boundary mixing is suppressed. This provides a simple way to avoid the problem with small convective regions in the core having an excessively large convective boundary mixing region. By default, convective boundary mixing is not allowed in regions with a mass fraction below 10^{-3} of the total star mass, a value that can be modified by the user. Also, convective boundary mixing is artificially omitted by default if the extra-mixed region is larger than the convective zone itself. This steers clear of potentially small convective regions being enlarged massively due to convective boundary mixing. Lastly, stabilising chemical composition gradients at the convective boundary might affect the amount of convective boundary mixing. `MESA` offers an optional user-chosen argument to terminate the convective boundary mixing region when a strong gradient in chemical composition is encountered by setting a maximum B for convective boundary mixing. However, strong chemical composition gradients might not entirely prevent convective boundary mixing from happening but only reduce its amount (Canuto, 1998).

1.3.3 Semiconvection

The theory of semiconvection was introduced in Section II.1.4. In `MESA/star` , semiconvection is implemented distinctly from convective boundary mixing, as a time-dependent diffusive process (Paxton et al., 2013). It is only applied if the Ledoux criterion for the convective boundary location is used.

In this case, if a cell is Ledoux stable but subject to an unstable temperature gradient it is mixed by semiconvection. `MESA` uses the scheme introduced by Langer et al. (1983), presented in Eq.(II.19). The implementation offers two options: (i) the actual temperature gradient ∇ in Eq.(II.19) is set to $\nabla_{\rm rad}$ or (ii) the actual temperature gradient in the semiconvective region is directly computed following Langer et al. (1983), in consistency with the theory of superadiabatic convection (Vitense, 1953; Böhm-Vitense, 1958), see Section II.1.2.

The semiconvective efficiency parameter, $\alpha_{\rm sc}$ - see Section II.1.4 - has to be specified by the user during runtime.

1.3.4 MLT++

Massive stars are dominated by radiation pressure, which can cause gas pressure and density inversion in their loosely-bound envelopes as the radiation approaches the Eddington luminosity (e.g. Joss et al., 1973). The inversion is more often present at higher metallicities because the iron opacity bumps are more pronounced - see Section B.1.2.0.1 - which cause the local radiation pressure to dominate and the local luminosity to approach the Eddington luminosity. These inflated envelopes are numerically unstable and the evolutionary timesteps become prohibitively short (of the order of hours). Furthermore, the energy transport by the classical mixing-length theory is clearly out of its range of applicability in such regions. The stability and treatment of such radiation-dominated envelopes is still an open question (Joss et al., 1973; Maeder, 1987b; Bisnovatyi-Kogan & Dorodnitsyn, 1999; Maeder, 2009; Paxton et al., 2013; Suárez-Madrigal et al., 2013; Sanyal et al., 2015, 2017) and stellar evolution codes apply different techniques for their computation, mostly numerical fixes of which none actually treats the true nature of the radiation-dominated envelope. This is yet another uncertainty in massive star evolution.

Following Joss et al. (1973); Paxton et al. (2013), an inversion of the gas pressure occurs if

$$\frac{dP_{\rm gas}}{dr} = \left(\frac{dP_{\rm rad}}{dr}\right)\left[\frac{L_{\rm Edd}}{L_{\rm rad}} - 1\right] > 0, \tag{B.35}$$

with the Eddington luminosity $L_{\rm Edd} = \frac{4\pi cGm}{\kappa} \approx 1.3 \times 10^4 \frac{1}{\kappa}\frac{M}{\rm M_\odot}{\rm L_\odot}$. Since $\frac{dP_{rad}}{dr} < 0$, a gas pressure inversion occurs for $L_{\rm rad} > L_{\rm Edd}$. On the other hand, a density inversion occurs when

$$\frac{L_{\rm rad}}{L_{\rm Edd}} > \frac{L_{\rm inv}}{L_{\rm Edd}} \equiv \left[1 + \left(\frac{\partial P_{\rm gas}}{\partial P_{\rm rad}}\right)_\rho\right]^{-1}, \tag{B.36}$$

where $L_{\rm inv}$ is the luminosity for the onset of the density inversion. Under the conditions of interest, i.e. in the envelope, $\left(\frac{\partial P_{\rm gas}}{\partial P_{\rm rad}}\right)_\rho > 0$, hence, density inversion can occur below the Eddington luminosity. Interestingly, for $L_{\rm inv} < L_{\rm rad} < L_{\rm Edd}$ a density inversion occurs without a gas pressure inversion.

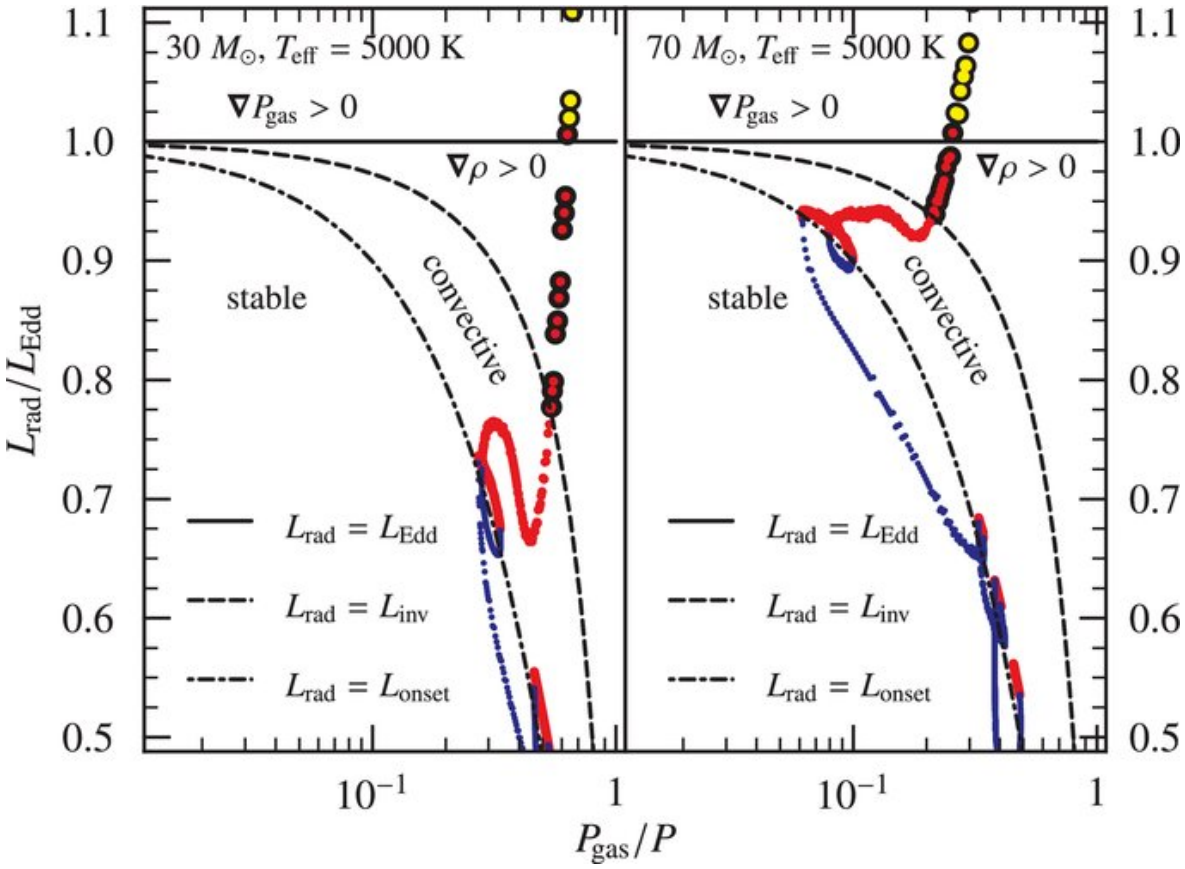

Figure B.3: (a) The critical luminosities $L_{\rm rad} = L_{\rm onset}$ (dot-dashed line) $L_{\rm rad} = L_{\rm inv}$ (dashed line) and $L_{\rm rad=L_{Edd}}$ (solid line) as a function of $P_{\rm gas}/P$ for an ideal gas-radiation mixture. For $L_{\rm rad} < L_{\rm onset}$ the gas is stable against convection; for $L_{\rm onset} < L_{\rm rad} < L_{\rm inv}$ the gas becomes convective; for $L_{\rm inv} < L_{\rm rad} < L_{\rm Edd}$ a density inversion occurs and for $L_{\rm Edd} < L_{\rm rad}$ a $P_{\rm gas}$ inversion occurs. The subplots include a part of the profile of a 30 $M_\odot$ (left) and 70 $M_\odot$ (right) model, respectively, at solar metallicity when the respective star meets $T_{\rm eff} = 5000$ K during its first crossing of the Hertzsprung gap. The blue dots represent radiatively stable layers and the red dots $\nabla_{\rm rad} > \nabla_{\rm ad}$. A black border around the dots indicates density inversion in the model and cells with a yellow dot have a gas pressure inversion. As the profile moves out from the stellar centre to the surface, it traces out the points on the plot from bottom to top. The figure is taken from Paxton et al. (2013).

.

Lastly, convection sets in when

$$\frac{L_{\rm rad}}{L_{\rm Edd}} > \frac{L_{\rm onset}}{L_{\rm Edd}} \equiv \left[1 - \frac{P_{\rm gas}}{P}\right] \left(\frac{\partial \ln P_{\rm rad}}{\partial \ln P}\right) \tag{B.37}$$

with $L_{\rm onset}$ the luminosity at which convection convection begins. Joss et al. (1973) argue that entropy decreases as density increases. Therefore a density inversion requires a superadiabatic temperature gradient, resulting in $L_{\rm onset} < L_{\rm inv}$. At high luminosities, where the gas is radiation dominated, the difference in $L_{\rm inv} - L_{\rm onset}$ becomes small and a small inefficiency in convection is enough to generate a density inversion. Indeed, in radiation-dominated, convective envelopes of massive star simulations such inefficient convection can arise (Paxton et al., 2013). Fig.(B.3) presents the critical onset luminosities as a function of $P_{\rm gas}/P$, showing that there is only a small gap between an adiabatically

stratified model and a model with a density inversion, i.e. the region between $L_{\rm rad} = L_{\rm onset}$ and $L_{\rm rad} = L_{\rm inv}$. On the other hand, a gas pressure inversion only occurs once $L > L_{\rm Edd}$, i.e. above the solid line in Fig.(B.3). The plot includes the profile of a 30 and 70 $M_\odot$ model during their first crossing of the Hertzsprung gap - see the caption for details.

Fig.(B.3) confirms several points. First, it shows the excellent agreement between the analytical conditions, Eqs.(B.36) and (B.37), and the detailed `MESA` evolutionary calculations. Second, it verifies that for massive stars, there is indeed a density inversion and, for even higher luminosity, a gas pressure inversion. Furthermore, the higher mass model enters deep into the low $P_{\rm gas}/P$, high $L_{\rm rad}/L$ regime. In this stellar model, the superadiabaticity $\nabla - \nabla_{\rm ad}$ increases to $\gtrsim 10^{-2}$ in the region with $L_{\rm rad} > L_{\rm Edd}$ and becomes larger than unity in the very outer layers. The large superadiabatic gradient encountered in its radiation-dominated envelopes leads to prohibitively short timesteps. Energy is mostly transported by radiation and the convective velocity in the framework of the mixing-length theory approach the speed of sound. In such a regime, the mixing length theory, as discussed in Sections II.1.2 and B.1.3.1, is out of its application domain. In fact, waves excited by the near-sonic turbulent convection (e.g. Maeder, 1987a), radiative diffusion enhanced by porous clumping of the envelope (e.g. Owocki et al., 2004) and other hydrodynamical instabilities become crucial for energy transport.

In order to calculate massive star models up to core collapse `MESA/star` offers the option of a treatment known as `MLT++`, which artificially reduces the superadiabaticity in a radiation-dominated convective region. The `MLT++` routine computes for every model two values,

$$\lambda_{\rm max} \equiv \max\left(\frac{L_{\rm rad}}{L_{\rm Edd}}\right) \qquad \text{and} \qquad \beta_{\rm min} \equiv \min\left(\frac{P_{\rm gas}}{P}\right). \tag{B.38}$$

If $\lambda_{\rm max}$ is large and $\beta_{\rm min}$ is small, and if the mixing-length routine yields a superadiabaticity, $\delta_\nabla \equiv \nabla - \nabla_{\rm ad}$, that is larger than a user-specified threshold $\delta_{\nabla,\rm thres}$, the `MLT++` routine artificially decreases the superadiabaticity. The default threshold value is $\delta_{\nabla,\rm thres} \sim 10^{-4}$, which is sufficiently large and convection is inefficient. The `MLT++` module reduces the superadiabaticity by setting ∇ so that it reduces $\delta_\nabla - \delta_{\nabla,\rm thresh}$ by a factor $f_\nabla \alpha_\nabla$, where f_∇ is a free parameter chosen by the user, which controls the maximum reduction of the superadiabaticity, and α_∇ is computed by the module at each time step as

$$\alpha_\nabla = \chi_\nabla \alpha_{\nabla,\rm old} + (1 - \chi_\nabla)\widetilde{\alpha_\nabla}, \tag{B.39}$$

a linear combination of the value from the previous time step, $\alpha_{\nabla,\rm old}$, and the current timestep, $\widetilde{\alpha_\nabla}\,(\lambda_{\rm max}, \beta_{\rm min})$. $\widetilde{\alpha_\nabla}$ is between 0 and 1 and depends on the strength of the density and gas pressure inversions. For a more extreme density and gas pressure inversion, i.e. large $\lambda_{\rm max}$ and small $\beta_{\rm min}$, $\widetilde{\alpha_\nabla} \to 1$. Vice versa, for small $\lambda_{\rm max}$ and large $\beta_{\rm min}$, i.e. no inversion occurs, $\widetilde{\alpha_\nabla} \to 0$. In a typical

Table B.2: Table listing the user-specified parameters of the MLT++ routine, their names in the MESA code, their default values and the values used in this work. An empty row in the last column indicates the use of the default value. The last six parameters are explained in Appendix C.2.

parameter	in-code name	default value	my value
$\delta_{\nabla,\mathrm{thres}}$	gradT_excess_f1	10^{-4}	
f_∇	gradT_excess_f2	10^{-3}	
χ_∇	gradT_excess_age_fraction	0.9	0.999
$\Delta_{\max}$	gradT_excess_max_change	not active	0.001
λ_1	gradT_excess_lambda1	1.0	
λ_2	gradT_excess_lambda2	0.5	
$\Delta\lambda$	gradT_excess_dlambda	0.1	
β_1	gradT_excess_beta1	0.35	
β_2	gradT_excess_beta2	0.25	
$\Delta\beta$	gradT_excess_dbeta	0.1	

model, the transition happens where $\lambda_{\max} \approx 0.5$ and $\beta_{\min} \approx 0.3$. Appendix C.2 demonstrates how the MLT++ module calculates $\widetilde{\alpha_\nabla}$. χ_∇ is a user-defined parameter, smoothing the change in α_∇ over time. α_∇ is further smoothed by limiting the maximum change at each timestep, i.e. $\alpha_\nabla = \min\{\alpha_\nabla, \alpha_{\nabla,\mathrm{old}} + \Delta_{\max}\}$. Table B.2 summarises all the free parameters used in the MLT++ module, how they are named in the code, the MESA default values and the values that are used in this work. It should be stressed that the radiatively dominated envelopes are physically unstable, which can result in strong enhancement of mass loss. Therefore, even if the use of MLT++ allows the computation of models up to core collapse, the prediction should be considered as highly uncertain.

1.4 Rotation-Induced Mixing

MESA includes the treatment of rotation if the rotation flag, rotation_flag, is activated by the user, either after a starting model has been created or after a restart. The implementation of rotation in MESA/star is derived from the stellar evolution code STERN (Langer et al., 1988; Heger et al., 2000; Petrovic et al., 2005; Yoon & Langer, 2005). The shellular approximation is adopted - see Sections I.4 and II.2 - and the stellar structure equations are modified due to the centrifugal acceleration as outlined in Section B.1.2. The rotation-induced transport of chemical elements is implemented in a diffusive approximation following Endal & Sofia (1978); Pinsonneault et al. (1989); Heger et al. (2000). The theory of the various instabilities is discussed in Section II.2. MESA/star has the capability to calculate the diffusion coefficient of five rotation-induced instabilities: the Solberg-Høiland instability, the Eddington-Sweet circulation, the dynamical and secular shear instability, the Goldreich-Schubert-Fricke instability as well as the mixing due to the Tayler-Spruit dynamo. Their implementation is based on Heger et al. (2000). The total diffusion coefficient is calculated as the sum of the diffusion

coefficient of each instability,

$$D_{\rm mix} = D_{\rm non-rot} + f_T \cdot f_c \times D_{\rm rot}$$
$$= D_{\rm non-rot} + f_T \cdot f_c \times [\alpha_{\rm SH} \cdot D_{\rm SH} + \alpha_{\rm ES} \cdot D_{\rm ES} + \alpha_{\rm DSI} \cdot D_{\rm DSI} + \alpha_{\rm SSI} \cdot D_{\rm SSI} + \alpha_{\rm GSF} \cdot D_{\rm GSF} + \alpha_{\rm TS} \cdot D_{\rm TS}] \,. \tag{B.40}$$

The free parameter f_c is introduced because the diffusion coefficients used are oder-of-magnitude estimates and are subject to large uncertainties. f_c allows to calibrate the diffusion coefficients with observational data. This parameter is only applied to compute the reduction of the diffusion coefficient but not the turbulent viscosity (see Eq.(B.46)). In addition, a second parameter, $f_\mu \in [0, 1]$, is used to describe the sensitivity of the rotation-induced mixing to chemical composition gradients by multiplying ∇_μ with it; the paragraphs below explain in which instabilities f_μ is included. The values used for the two parameters f_c and f_μ throughout the literature and in this work are discussed in Chapter IV. The user-chosen parameters αs allow to adjust the diffusion coefficient of each rotation-induced instability individually, where $\alpha = 0$ excludes the instability from the stellar model. Also, the diffusion coefficient profile of each instability can be spatially and temporally smoothed - see Appendix B.1.5.1.1. In this work, however, only the diffusion coefficient from the Tayler-Spruit instability is smoothed. f_T is another parameter that allows to manipulate the diffusion coefficient for rotation-induced chemical mixing. This parameter is equal to unity as long as the temperature is below a user-chosen temperature. If the temperature exceeds this specific value, $f_T = 0$, hence, it allows to turn off rotation above a temperature threshold, e.g., as the star approaches core collapse. The default value for the temperature limit is $\log T = 9.5$

The diffusion coefficient $D_{\rm mix}$ enters the abundance diffusion equation, Eq.(B.5), which is solved at each time step. In the following, the implementation of each rotation-induced instability is discussed.

1.4.1 Solberg-Høiland Instability

In `MESA` the condition for the Solberg-Høiland instability to occur, $R_{\rm SH}$ in Eq.(II.23), is formulated as

$$R_{\rm SH} = \frac{g}{\rho}\left[\left(\frac{d\rho}{dr}\right)_{\rm ad} - \frac{d\rho}{dr}\right] + \frac{9j}{2r^3}\frac{dj}{dr} < 0. \tag{B.41}$$

The first bracket term is equivalent to the first term containing the temperature gradients and the chemical composition gradient in Eq.(II.23) - see Section II.1.1. It should be noted that the stabilising stratification of the chemical composition is contained in the equation of state but its effect cannot be scaled via f_μ as in the other rotation-induced instabilities. The second term is equivalent to the second term in Eq.(II.23) under the assumption that the specific angular momentum j can be written for a thin spherical shell, hence, the specific moment of inertia is $i = \frac{2}{3}r^2$.

The computation of the diffusion coefficient follows Eq.(II.24), however, the maximum diffusion coefficient is limited by the product of the pressure scale height and the speed of sound. In reality, this limit is more than ten orders of magnitude larger than a typical value for $D_{\rm SH}$ and is therefore not met under normal circumstances.

Generally, in regions where the Solberg-Høiland instability is active, the condition for the dynamical shear instability is satisfied as well (see, e.g., Hirschi et al., 2004). Therefore, in this work the Solberg-Høiland instability is set to zero by $\alpha_{\rm SHI} = 0$.

1.4.2 Eddington-Sweet Circulation

The large scale meridional flows are implemented as a diffusive process in MESA called the Eddington-Sweet circulation - see Section II.2.2. The computation follows the diffusive procedure discussed there. In addition, the calculation of the circulation velocity $v_{\rm E}$ (Eq. (II.25)) limits the luminosity, mass and radius in the denominator of the fractions in the bracket by a thousandth of the respective solar value. This avoids the scenario where $v_{\rm E} \to \infty$ as the centre is approached. Also, the chemical composition gradient in the "stabilising" circulation velocity v_μ (Eq.(II.26)) is multiplied with f_μ to scale its importance. Finally, $v_{\rm ES}$ (Eq.(II.28)) is limited by the local sound speed and the diffusion coefficient from the Eddington-Sweet circulation is restricted by the product of the pressure scale height times the sound speed, which however is not reached under normal circumstances.

1.4.3 Dynamical Shear Instability

The Richardson number is computed according to Eq.(II.34), where the term $(\partial v/\partial z)^2$ is written in terms of the angular velocity ω, $(\partial z/\partial v)^2 = (\partial \ln z/\partial \omega)^2$. Also, the ∇_μ in Eq.(II.34) is scaled with f_μ, i.e. $f_\mu \cdot \nabla_\mu$. The Richardson number is artificially set to zero if $\nabla_{\rm ad} - \nabla < 0$, hence, the instability is switched off in convective regions.

In MESA the diffusion coefficient for the dynamical shear instability is calculated as

$$D_{\rm DSI} = \min\left[\frac{\min\left\{r_{\rm inst}, H_P\right\}^2}{t_{\rm dyn}}, H_P \cdot c_{sound}\right], \tag{B.42}$$

with the sound speed $c_{\rm sound}$ and the spatial extent of the instability $r_{\rm inst}$. This implementation differs from Eq.(II.34) with the facts that first, the mixing does not smoothly transition from the stable region and second, the mixing does not increase as the instability increases but is limited by the product of the pressure scale height scale and the speed of sound. However, the latter limit exceeds usual values of $D_{\rm DSI}$ by more than ten orders of magnitudes and is not reached in standard stellar models.

As discussed in Section II.2, the dynamical shear instability occurs on the dynamical timescale $\tau_{\rm dyn} \equiv \sqrt{r^3/(Gm)}$. Edelmann et al. (2017) compared 2D hydrodynamical simulation of the dy-

namical shear instability with the 1D prescription and concluded that most of the differences come from the fact that the evolutionary timescale in stellar evolution models is much longer than the dynamical timescale. Therefore, the estimated mixing efficiency in stellar models is overestimated. Another point is that the dynamical shear instability is often suppressed by the Brunt-Väisälä frequency. In rotating massive stars, only during the advanced pre-supernova phases the shear becomes strong enough to overcome the stable density stratification. Furthermore, the dynamical shear is only active over a very thin zone, because it needs very steep Ω gradients that arise only in very limited regions, where the μ-gradients are also very steep. Thus, despite the rather large diffusion coefficients from this instability, the global effect is minor. For these two reasons, the dynamical shear instability is excluded from the models in this work by setting $\alpha_{\rm DSI} = 0$.

1.4.4 Secular Shear Instability

The condition for the secular shear instability in `MESA` is determined similarly to Section II.2.4.2 with the following differences. First, the critical Reynolds number is $R_{\rm crit} = 2500$. Second, the Richardson number $\mathcal{R}i$ entering the first criterion $\mathcal{R}i_{\rm SSI,1}$, Eq.(II.36), is computed as $\mathcal{R}i \equiv \frac{g}{\rho}\frac{N_T^2}{(\partial v/\partial z)^2}$, where N_T^2 is the thermal part of the Brunt-Väisälä frequency, hence, the chemical stratification is ignored. Lastly, the chemical composition gradient in $\mathcal{R}i_{\rm SSI,2}$, Eq.(II.37), is multiplied by f_μ, reducing its effects.
The diffusion coefficient arising from the secular shear instability is computed as described in Eq.(II.39), with the exception that the maximal allowed diffusion coefficient is limited by the product of the pressure scale height and the speed of sound. In reality, this limit is more than ten orders of magnitude larger than a typical value for $D_{\rm SH}$ and is therefore not met under normal circumstances.

1.4.5 Goldreich-Schubert-Fricke Instability

In `MESA`, the activity of the Goldreich-Schubert-Fricke instability is checked with several conditions. First, the code compares the difference of the specific angular momentum between two neighbouring cells, which is equivalent to Eq.(II.40). If the angular momentum increases outwards, the local scale height of angular momentum is computed as

$$H_j \equiv \frac{dr}{d\ln j} > 0, \tag{B.43}$$

otherwise H_j is set to zero. If H_j is positive the velocity v_g is calculated following Eq.(II.41) if not v_g is set to zero. Finally, the code computes $v_{\rm GSF}$ following Eq.(II.42) and defines the instability as active only when $v_{\rm GSF} > 0$. The latter two conditions are numerical in nature. The computation of the diffusion coefficient follows the discussion in Section II.2.5.1. Similarly to the implementation of the Eddington-Sweet circulation, the chemical composition gradient in v_μ is multiplied with f_μ.

Furthermore, the maximal velocity of the Goldreich-Schubert-Fricke instability is limited by the sound speed and the diffusion coefficient $D_{\rm GSF}$ is controlled by the product of the sound speed and the pressure scale height. Again, this limit is many orders of magnitude larger than the values reached for $D_{\rm GSF}$ in standard stellar evolution models.

The Goldreich-Schubert-Fricke instability is strongly suppressed by μ-gradients and is only triggered in layers with an extremely strong shear. Both, Hirschi & Maeder (2010) and Caleo et al. (2016) independently investigated the instability and concluded that viscosity, either turbulent as in Hirschi & Maeder (2010) or molecular and radiative as in Caleo et al. (2016), suppresses the Goldreich-Schubert-Fricke instability. Hirschi & Maeder (2010) further show that the transport coefficient of the Goldreich-Schubert-Fricke instability during the late stages of stellar evolution can become larger than the shear instability and as large as the thermal diffusivity. However, the instability is confined to extremely narrow regions and there is not enough time left for siginificant mixing to occur before the core collapses, hence, its impact is insignificant. For these reasons, the Goldreich-Schubert-Fricke instability is excluded from the models in this work, i.e. $\alpha_{\rm GSF} = 0$.

1.5 Angular Momentum Transport

Angular momentum transport in MESA is implemented as a purely diffusive process,

$$\frac{dj}{dt} = \frac{d}{dm}\left[(4\pi r^2\rho)^2\left(\nu_\Omega \cdot i_{\rm rot}\frac{d\Omega}{dm} + \nu_j \frac{dj}{dm}\right)\right], \tag{B.44}$$

with $i_{\rm rot}$ the specific moment of inertia and ν_Ω and ν_j the turbulent viscosities for the rotation rate and the specific angular momentum, respectively. The two viscosities are calculated from the contribution of the rotating and non-rotating sources as

$$\nu_\Omega = f_{\Omega,{\rm non-rot}} \cdot \nu_{\rm non-rot} + f_{\Omega,{\rm rot}} \cdot \nu_{\rm rot} \tag{B.45}$$

$$\nu_j = f_{j,{\rm non-rot}} \cdot \nu_{\rm non-rot} + f_{j,{\rm rot}} \cdot \nu_{\rm rot}, \tag{B.46}$$

where $\nu_{\rm nonrot}$ is the sum of the turbulent viscosities for convection and semiconvection[16] and $\nu_{\rm rot}$ is the sum of the turbulent viscosities for the rotation-induced instabilities - see Section B.1.4 for a list - plus an additional user-chosen viscosity for angular momentum transport $\nu_{\rm visc}$,

$$\nu_{\rm rot} = \beta_{\rm DSI} \cdot \nu_{\rm DSI} + \beta_{\rm SSI} \cdot \nu_{\rm SSI} + \beta_{\rm SH} \cdot \nu_{\rm SH} + \beta_{\rm ES} \cdot \nu_{\rm ES} + \beta_{\rm GSF} \cdot \nu_{\rm GSF} + \beta_{\rm TS} \cdot \nu_{\rm TS} + \beta_{\rm visc} \cdot \nu_{\rm visc}. \tag{B.47}$$

[16] It is important to note that the convective boundary mixing is not included in this sum - see discussion in Chapter IV.

The viscosities are equal to the diffusion coefficients computed for the chemical mixing, with the exception for the magnetic dynamo (see below), times a free parameter β for each product to adjust the strength of the viscosity; they are set to unity by default. Contrarily to the diffusion coefficient for rotation-induced instabilities, the final rotational viscosity are not scaled with the f_c parameter. The fs are user-defined free parameters, by default $f_\Omega = 1$ and $f_j = 0$. Eq.(B.46) is equivalent to Eq.(46) in Heger et al. (2000) if $\nu_j = 0$. This implementation in `MESA` allows to (i) adjust the non-rotational and rotational viscosity and (b) adapt different specific angular momentum distributions, i.e. solid body rotation or uniform specific angular momentum in convective zones (see below and discussion in Zahn, 1992; Potter et al., 2012a).

In the radiative zones, shellular rotation can be assumed because the horizontal turbulence smooths out differential rotation along isobars. The large diffusion coefficient in the convective region leads to a rotation law which is not far from solid body rotation, a common assumption for convective regions in 1D stellar evolution codes (Pinsonneault et al., 1989; Heger et al., 2000; Eggenberger et al., 2008) which however is not true for, e.g., the solar convection zone (e.g. Brown et al., 1989). Currently, there are two treatments used in the convective regions: (a) convective regions are considered solid bodies, i.e. the turbulent viscosity $\nu_{\rm conv}$ in the convective zone is strong enough to homogenise the angular velocity distribution or (b) convective regions have a constant angular momentum distribution because the large-scale convective motions dominate and they conserve their angular momentum (Arnett & Meakin, 2010)[17].

`MESA/star` initialises rotation from a non-rotating model by adding a user-specified constant rotation rate - either a surface rotation velocity or a fraction of the critical rotation rate[18] - throughout the star, resulting in a solid body rotation. At each subsequent step, the angular momentum is changed according to Eq.(B.44), including remeshing and mass and radius adjustment (see Paxton et al., 2013, Appendix B.6 for more details). The evolution of angular momentum uses substeps from the stellar evolutionary time step and quad-precision linear algebra to obtain a high accuracy. Thus, it is performed as a separate operation after the structure and composition evolution. This also avoids additional operator splitting errors of the rotation rate.

1.5.1 Magnetic Dynamo

`MESA/star` offers the option to include a magnetic dynamo for the transport of angular momentum and chemical mixing. In `MESA`, magnetic fields generated by differential rotation in radiative regions - see Section II.3 - are implemented following the work of Spruit (2002) in a similar fashion to Petrovic et al. (2005) and Heger et al. (2005). The rotation-induced shear (see Eq.(II.51)) contains a differentiation

[17] However, reality is not as simple. 3D hydrodynamic simulation show that neither the angular velocity nor the angular momentum are constant in convective regions (e.g. Browning et al., 2004). Also, the convective motion depends on the rotation rate of the star (e.g. Brun & Palacios, 2009; Brun et al., 2017).

[18] $\Omega^2_{\rm crit} = (1 - \Gamma_{\rm Edd}) \frac{Gm}{r^3}$ with the Eddington factor $\Gamma_{\rm Edd} = \frac{\kappa L}{4\pi c G m}$.

and needs to be evaluated carefully. MESA calculates this dimensionless differential rotation rate in cell k as

$$q(k) = \frac{r(k)}{\Omega(k)} \cdot \frac{\Omega(k-1) - \Omega(k+1)}{r(k-1) - r(k+1)} \equiv \frac{\partial \ln \Omega}{\partial \ln r}(k), \tag{B.48}$$

where $k = 1$ is the cell at the surface. For numerical stability the shear is limited between 10^{-30} and 10^{30}. Similar to Spruit (2002) two cases are considered; if the chemical composition term of the Brunt-Väisälä frequency is dominant *case0* from Section II.3.1.2 is calculated and if the thermal term is dominant *case1* is computed. In the two limiting cases, only the respective *case* is taken for the determination of the magnetic viscosity and the magnetic diffusivity, i.e.

$$\nu_{\rm TS} = \begin{cases} \nu_0 \cdot f(q) & \text{if } \mathrm{N}_{\rm T}^2 \leq 0 \text{ and } \mathrm{N}_{\mu}^2 > 0 \\ \nu_1 \cdot f(q) & \text{if } \mathrm{N}_{\rm T}^2 > 0 \text{ and } \mathrm{N}_{\mu}^2 \leq 0 \end{cases} \qquad \eta_{\rm TS} = \begin{cases} \eta_0 \cdot f(q) & \text{if } \mathrm{N}_{\rm T}^2 \leq 0 \text{ and } \mathrm{N}_{\mu}^2 > 0 \\ \eta_1 \cdot f(q) & \text{if } \mathrm{N}_{\rm T}^2 > 0 \text{ and } \mathrm{N}_{\mu}^2 \leq 0 \end{cases}, \tag{B.49}$$

with the function $f(q)$ from Eq.(II.58). In the two limits, the Brunt-Väisälä frequency is always composed of the dominant term, either $N^2 = N_\mu^2$ or $N^2 = N_T^2$. In between, if $N_T^2 > 0$ and $N_\mu^2 > 0$ the patching formulae in Eqs.(II.56) and (II.59) are used. This is implemented in a way that the terms from the two limiting cases are calculated first, i.e. *case0* and *case1* outlined in Section II.3.1.2, and then are patched together. If $N_T^2 < 0$ and $N_\mu^2 < 0$ or $N^2 < 0$ the mixing by the Tayler-Spruit dynamo is artificially switched off by setting $\nu_{\rm TS} = 0$ and $\eta_{\rm TS} = 0$. Also, the Tayler-Spruit dynamo is artificially suppressed in convective zones and convective boundary mixing regions - see discussion in Chapter IV.

The tubulent viscosity in semiconvective regions is treated specially following Heger et al. (2005): The viscosity $\nu_{\rm TS,semiconv}$ is computed as the geometric mean between the semiconvective "effective viscosity" and the magnetic diffusivity ν_0 resulting from *case0*; *case1* is undefined in semiconvective layers. It is assumed that the flux is dominated by the convective flux and given by the local luminosity.

$$\begin{aligned} \nu_{\rm TS,semiconv} = (\nu_{\rm eff,semiconv} \cdot \nu_0)^{\frac{1}{2}} &\approx \left(\frac{1}{3} \bar{v} \ell_{\rm mix} \cdot \nu_0 \right)^{\frac{1}{2}} \\ &\approx \left(\frac{1}{3} H_P \left[\frac{g \delta H_P \cdot \max(0, L)}{64 \pi \rho C_P T r^2} \right]^{\frac{1}{3}} \cdot \nu_0 \right)^{\frac{1}{2}} \end{aligned} \tag{B.50}$$

The mixing length $\ell_{\rm mix}$ is assumed to be equal to the pressure scale height and $\bar{v}$ is computed from the mixing-length theory (Eqs.(II.14) and (B.22)).

Each of the composition term and the thermal term of the Brunt-Väisälä frequency, the effective diffusivity $D_{\rm TS}$ and the magnetic viscosity $\nu_{\rm TS}$, are multiplied with a factor that allows to adjust their strength. The default of each factor is set to unity.

B.1.5.1.1 Smoothing of the Tayler-Spruit Dynamo

The nature of the treatment of the chemical composition gradients in `MESA` can lead to a rapidly changing profile of the turbulent viscosity, in space and time, and the diffusion coefficients discussed above - see also discussion in Chapter IV. In order to avoid the jittery profiles, which arise due to numerics, improper treatment of the physics or the limitation to one-dimensional modelling, numerical smoothing routines are applied.

`MESA` implements a weighted smoothing routine - see Appendix C.1 - to spatially smooth the viscosity and diffusion coefficients derived for the Tayler-Spruit dynamo and the other rotation-induced instabilities discussed in Section B.1.4. The number of cells to be included in the smoothing routine are chosen by the user at runtime. By default, no spatial smoothing is applied.

`MESA` applies two time-smoothing processes for the viscosity and diffusion coefficient derived for the Tayler-Spruit dynamo and the other rotation-induced instabilities discussed above. The first scheme smooths the variable as

$$x = \max\left\{\frac{x_{\rm old}}{1+f_t},\ \min\left[x_{\rm new},\ \max\left(x_{\rm old}\cdot(1+f_t), x_{\rm old}+\delta\tau\right)\right]\right\} \tag{B.51}$$

where for cell k

$$\delta\tau(k) = f_r \cdot \frac{(r(k)-r(k+1))\cdot r(k-1)\cdot r(k)}{\Delta t}, \tag{B.52}$$

where $x_{\rm old}$ is the variable from the previous time step and $x_{\rm new}$ is as calculated for the current time step before time smoothing is applied. Δt is the time of the substep. f_t and f_r are user-defined parameters with the default of 0.2 and 0.001, respectively, for the Tayler-Spruit dynamo and $f_t = 0$ for the other instabilities. This smoothing prevents large changes in x by limiting the new value to be within a certain range of the old value, either defined by a pure numeral or the distancing of the neighbouring cells.

The second option calculates the arithmetic averages between the variable from the current and the old time step,

$$x = \frac{x_{\rm new}+x_{\rm old}}{2}, \tag{B.53}$$

where again $x_{\rm old}$ is the variable from the previous time step and $x_{\rm new}$ is as calculated for the current time step before time smoothing has been applied. This smoothing prevents fast changes between timesteps, but in contrast to the first scheme it allows for more changes and always considers half of the old value.

1.6 Mass Loss

In MESA/star, the adjustment of the mass due to mass loss or accretion is done at the beginning of each timestep, before the equations of stellar structure are solved (Paxton et al., 2011, 2013). There is a variety of prescriptions included in MESA to compute the mass-loss rate $\dot{M}$ - see also Section I.2.2. The available options for massive stars are the mass-loss rates by Kudritzki et al. (1989); Vink et al. (2000) and Vink et al. (2001) for main-sequence stars, Nugis & Lamers (2000) and Gräfener & Hamann (2008) for Wolf-Rayet stars and Nieuwenhuijzen & de Jager (1990) for cool supergiants. Further possibilities include the implementations from Reimers (1975) for red giants, Bloecker (1995) for asymptotic giant branch stars, van Loon et al. (2005) for dust-enshrouded red supergiants, de Jager et al. (1988) for a range of stars in the Hertzsprung-Russell diagram but often used for red supergiant branch stars, inspiration from Prialnik & Kovetz (1995) for supersonic mass loss and super-Eddington mass loss by Paczynski & Proszynski (1986). The *Dutch wind scheme* for massive stars combines two mass-loss prescriptions following Glebbeek et al. (2009); if $T_{\rm eff} > 10^4\,\mathrm{K}$ and the surface hydrogen mass fraction, $X_{\rm surf}(^1\mathrm{H})$, is larger than 0.4 the Vink et al. (2000, 2001) prescription is used, if $T_{\rm eff} > 10^4\,\mathrm{K}$ and $Y_{\rm surf}(^1\mathrm{H})< 0.4$ the formula by Nugis & Lamers (2000) is applied and for $T_{\rm eff} < 10^4\,\mathrm{K}$ the user can choose between the mass-loss prescriptions from either de Jager et al. (1988), van Loon et al. (2005) or Nieuwenhuijzen & de Jager (1990). MESA also offers the option of a constant mass-loss rate specified in the input file or a user-defined mass-loss rate. The mass-loss rate is multiplied with a user-defined wind-efficiency parameter, $\eta_{\rm wind}$.

The user can choose a wind scheme for three different regions, a "*hot wind scheme*" and a "*cool wind scheme*" for each, the red and the asymptotic giant branches. The code smoothly switches between the hot and cool wind prescriptions when a user-specified surface temperature is reached. The asymptotic giant branch wind is used over the red giant branch wind if the central hydrogen mass fraction is smaller than 0.01 and the helium abundance in the centre drops below a user-defined value - usually 10^{-4}.

In this work the *Dutch wind scheme* for massive stars is used, with the de Jager et al. (1988) option for the cool wind. The mass-loss recipe by Vink et al. (2000, 2001) is calculated in MESA as

$$\log_{10}\,\dot{M}_{\rm Vink} = \begin{cases} \log\,\dot{M}_{\rm Vink,1} & \text{if } \mathrm{T_{eff}} > 27500\,\mathrm{K} \\ \alpha_{\dot{M}}\cdot\log\,\dot{M}_{\rm Vink,1} + (1-\alpha_{\dot{M}})\cdot\log\,\dot{M}_{\rm Vink,2} & 22500\,\mathrm{K} \leq \mathrm{T_{eff}} \leq 27500\,\mathrm{K}\,, \\ \log\,\dot{M}_{\rm Vink,2} & \text{if } \mathrm{T_{eff}} < 22500\,\mathrm{K} \end{cases} \tag{B.54}$$

with

$$\log_{10} \dot{M}_{\mathrm{Vink},1} = -6.697 + 2.194 \log_{10} \left(\frac{L_{\mathrm{surf}}}{10^5 L_\odot} \right) - 1.313 \log_{10} \left(\frac{M_{\mathrm{surf}}}{30 M_\odot} \right) - 1.226 \log_{10} \left(\frac{v_\infty}{2 v_{\mathrm{esc}}} \right) + 0.933 \log_{10} \left(\frac{T_{\mathrm{eff}}}{4 \times 10^4\,\mathrm{K}} \right) - 10.92 \log_{10} \left(\frac{T_{\mathrm{eff}}}{4 \times 10^4\,\mathrm{K}} \right)^2 + 0.85 \log_{10} \left(\frac{Z}{Z_\odot} \right), \tag{B.55}$$

where v_∞ is the terminal velocity and v_{esc} the escape velocity, and

$$\log_{10} \dot{M}_{\mathrm{Vink},2} = -6.688 + 2.21 \log_{10} \left(\frac{L_{\mathrm{surf}}}{10^5 L_\odot} \right) - 1.339 \log_{10} \left(\frac{M_{\mathrm{surf}}}{30 M_\odot} \right) - 1.601 \log_{10} \left(\frac{v_\infty}{2 v_{\mathrm{esc}}} \right) + 1.07 \log_{10} \left(\frac{T_{\mathrm{eff}}}{2 \times 10^4\,\mathrm{K}} \right) + 0.85 \log_{10} \left(\frac{Z}{Z_\odot} \right). \tag{B.56}$$

This formulation includes the jump in the mass-loss rates around $T_{\mathrm{eff,jump}} = \frac{1}{3} \left\{ 61.2 + 2.59 \left[-13.636 + 0.889 \log \left(\frac{Z}{Z_\odot} \right) \right] \right\}$ due to a change in the main line-driving element iron, which recombines from Fe iv to Fe iii (Vink et al., 2000). Between $22500\,\mathrm{K} \leq \mathrm{T_{eff}} \leq 27500\,\mathrm{K}$ `MESA/star` smoothly computes the transition between the two mass-loss rates with

$$\alpha_{\dot{M}} = \begin{cases} 1 & \text{if } \mathrm{T_{eff}} > \mathrm{T_{eff,jump}} + 100 \\ \frac{T_{\mathrm{eff}} - (T_{\mathrm{eff,jump}} - 100)}{200} & T_{\mathrm{eff,jump}} - 100 < T_{\mathrm{eff}} < T_{\mathrm{eff,jump}} + 100 \\ 0 & \text{if } \mathrm{T_{eff}} < \mathrm{T_{eff,jump}} - 100 \end{cases} \tag{B.57}$$

The mass-loss rate by Nugis & Lamers (2000), which is applied to helium rich Wolf-Rayet stars, is computed as

$$\log_{10} \dot{M}_{\mathrm{NL}} = -11 + 1.29 \log_{10} \left(\frac{L_{\mathrm{surf}}}{L_\odot} \right) + 1.7 \log_{10} X_{\mathrm{surf}}(^4\mathrm{He}) + 0.5 \log \mathrm{Z}. \tag{B.58}$$

Lastly, the mass-loss scheme by de Jager et al. (1988) determines $\dot{M}$ by

$$\log_{10} \dot{M}_{\mathrm{J}} = -1.769 \log_{10} \left(\frac{L_{\mathrm{surf}}}{L_\odot} \right) - 1.676 \log_{10} T_{\mathrm{eff}} - 8.158 \tag{B.59}$$

This mass-loss recipe includes neither the mass nor the metallicity. While it is widely applied in models of red supergiants, it is one of the most uncertain mass-loss rates.

1.6.1 Rotation-enhanced Mass Loss

In Section I.4.1, it was discussed that rotation enhances the mass-loss rates. Following Langer (1998); Heger et al. (2000), `MESA/star` computes the enhancement of the mass-loss rate as

$$\dot{M}(\Omega) = \frac{\dot{M}_{\mathrm{non-rot}}}{\left(1 - \frac{\Omega_{\mathrm{surf}}}{\Omega_{\mathrm{surf,crit}}}\right)^{\xi}}, \tag{B.60}$$

with the adjustable parameter ξ - usually 0.43 (Langer, 1998) - and

$$\Omega^2_{\mathrm{surf,crit}} = (1 - \Gamma_{\mathrm{Edd}}) \frac{Gm}{r^3_{\mathrm{eq}}} = \left(1 - \frac{L}{L_{\mathrm{Edd}}}\right) \frac{Gm}{r^3_{\mathrm{eq}}}, \tag{B.61}$$

where $\Gamma_{\mathrm{Edd}} = \frac{\kappa L}{4\pi cGm}$ is the Eddington factor, $L_{\mathrm{Edd}} = \frac{4\pi cGm}{\kappa}$ the Eddington luminosity and r_{eq} the radius at the equator. `MESA` limits the boosting factor in Eq.(B.60) with a lower limit of 10^{-22} and a user-specified upper limit - the default is 10^4. Also, the change of the rotation-enhanced stellar wind during a timestep is not allowed to be larger than the wind from the previous timestep times a user-defined parameter - the default is 2.

As the star approaches critical rotation, i.e. $\Omega/\Omega_{\mathrm{crit}} \to 1$, Eq.(B.60) diverges. Luminous stars approach this limit without having to rotate fast because $\Omega_{\mathrm{crit}} \to 0$ as $L/L_{\mathrm{Edd}} \to 1$. `MESA/star` limits the mass-loss timescale to the thermal timescale of the star, τ_{KH}, following Yoon et al. (2010) as

$$\dot{M} = \min\left[\dot{M}(\Omega), f_{\dot{M}_{\mathrm{crit}}} \frac{M}{\tau_{\mathrm{KH}}}\right], \tag{B.62}$$

where $f_{\dot{M}_{\mathrm{crit}}}$ is an efficiency factor of order unity with the default value of 0.3.

Normally, the angular momentum removed from the stellar surface via winds corresponds to that contained in the removed layers. Since j can increase steeply in the very outer layers, very small timesteps are required to obtain a converged solution. `MESA/star` adjusts the angular momentum content of layers below the ones removed, an option which is applied by default but can be turned off by the user. The adjustment is such that

$$j_{\mathrm{lost}} = f_{\mathrm{adj}} \cdot \dot{M} j_{surf} + (1 - f_{adj}) \cdot j_{\mathrm{removed}} \tag{B.63}$$

where j_{removed} is the angular momentum contained in the removed layers of the star in the current step. It should be noted that while j_{surf} is the specific angular momentum of the surface cell, i.e. in units of angular momentum per mass, j_{removed} is in units of angular momentum. In the context of this scheme, the user defines the region from which angular momentum is removed by choosing a

maximal fraction of the total star mass, a fraction of $j_{\rm lost}$ that needs to be in this region and that is below a chosen optical depth. Angular momentum in this region is adjusted so that no artificial shear is generated at the inner boundary.

1.7 Resolution

Spatial and temporal resolutions are a crucial part of stellar evolution modelling. The model needs to be resolved to allow convergence and resolve the physical processes on their timescales.

The timesteps have to be small enough to allow convergence but large enough to allow for an efficient modelling. Furthermore, the length of a timestep needs to follow the rapid changes in the structure and composition conditions but, on the other hand, have to be controlled to avoid over-correcting which reduces the convergence.

The spatial resolution, given as a mesh grid, is a key ingredient of stellar modelling and requires careful settings. The resolution must properly render the gradients in the structure, chemical composition and energy generation, in order to give an accurate result. However, it should not be too tight to avoid an unnecessary computational cost and a reduction of the convergence due to numerical challenges with small differences.

The resolution settings chosen in the stellar models from this work are presented in Appendix B.3.

1.7.1 Temporal Resolution

`MESA/star` selects a timestep in two steps. First, a timestep for the next step, δt_{i+1}, is estimated as

$$\delta t_{i+1} = \delta t_i f \left[\frac{f(v_t/v_{c,i}) \cdot f(v_t/v_{c,i-1})}{f(dt_i/dt_{i-1})} \right]^{\frac{1}{4}} \tag{B.64}$$

with $f(x) = 1 + 2\tan^{-1}\left[\frac{1}{2}(x-1)\right]$. v_c is the control variable, which is the unweighted average over all cells of the relative changes in $\ln \rho$, $\ln T$ and $\ln R$. v_t is the target value with a default of 10^{-4}. Eq.(B.64) is a low-pass filter, that uses the results of the previous two timesteps indicated with the indices i and $i-1$. This control scheme allows for rapid changes in the timestep without undesirable fluctuations.

In a second step, the timestep computed from Eq.(B.64) can be reduced by a variety of tests that have hard and soft limits, which are specified by the user. If a change exceeds a specified hard limit, the current solution is rejected and the code forces a retry or backup. On the other hand, if a change exceeds its specified soft limit, the next timestep is reduced proportionally (see Paxton et al., 2011, 2013, for more details). The various classes of tests include changes in the limit of the relative or absolute mesh structure, limits in changes in composition, nuclear burning rates or changes in the luminosity resulting from nuclear burning and changes in other variables such as $T_{\rm eff}$, L, M, T_c, ρ_c.

A full list can be viewed in the MESA documentation.

1.7.2 Spatial Resolution

The mesh, i.e. the distribution of grid points, of the structure and composition profiles is checked at the beginning of each timestep and adjusted if necessary by either splitting a cell into two or more sub-cells or merging two or more adjacent cells into one. The code implements remeshing in a way that most cells are not changed during a remesh. This minimises the numerical diffusion and supports convergence. Remeshing is made in two stages; a planning stage and an adjustment stage. In the planning stage, the code determines which cells to split or merge based on allowed changes of certain mesh functions between adjacent cells. Mesh functions include gradients of m, r, P, T, $\nabla_{\rm ad}$, Ω and mass fractions above some threshold. Users can also specify regions in which the sensitivity is increased. In the adjustment stage the cells are merged or split by performing operations to calculate the value of the new basic variables for the remeshed cells. In doing so, physical principles such as mass and energy conservation, species conservation and conservation of angular momentum are accounted for (for more details see Paxton et al., 2011, 2013).

2 Code Alterations

Many of the modules in MESA are equipped with so called *hooks* which allow users to implement their own routines into the stellar evolution code. MESA also provides a way to override most of the physics routines via "*other hooks*" without having to change the core code. The use of *hooks* is beneficial because it allows an easier exchange of the code extensions with other users and simplifies the update process to a newer MESA revision[19].

The *hooks* can be used for many gimmicks, such as custom stopping conditions or additional model output when certain conditions are met. While I made extensive use of the *hooks* in this thesis, only two physically relevant extensions are presented in the following: the implementation of the Fuller-modified Tayler-Spruit dynamo and a modification of the mixing-length theory.

2.1 Implementation of the Fuller-modified Tayler-Spruit Dynamo

The theory of the Fuller-modified Tayler-Spruit dynamo is introduced in Section II.3.1.3 and the theoretical differences between the classic Tayler-Spruit dynamo and this modified version are discussed there. Here, the implementation of the Fuller-modified Tayler-Spruit dynamo, as published in Fuller

[19]The documentation on *hooks* provides more insight on how to use them.

et al. (2019), is discussed and differences in the numerics are highlighted.

First, the dimensionless rotational shear is smoothed. For cell k the shear becomes

$$q_{\rm smooth}(k) = \frac{1}{2n+1}\sum_{i=k-n}^{k+n} q(i), \tag{B.65}$$

with $q(i)$ calculated from Eq.(B.48) for cell i. n is an integer that controls the number of adjacent cells to be included in the smoothing process. In the current implementation $n = 5$ is hard-coded but this can easily be made a user-defined variable.

Next, the thermal diffusivity K is computed as

$$K = \frac{16\sigma T^3}{3\kappa\rho^2 C_V}, \tag{B.66}$$

which uses the specific heat at constant volume C_V, i.e. isochoric, instead of the specific heat at constant pressure C_P.

In contrast to the implementation of the Tayler-Spruit dynamo, the Fuller-modified version computes an effective Brunt-Väisälä frequency, $N_{\rm eff}$, where the thermal diffusion - which is efficient at the short radial length scales characteristic for the Tayler instability - mitigates the thermal stratification (Spruit, 2002; Maeder & Meynet, 2004). A fluid element displaced by a radial distance ℓ_r on the timescale $\tau_{\rm B}$ diffuses away its temperature fluctuations on a timescale $\tau_{\rm therm} \approx \frac{\ell_r^2}{K}$, with the maximum radial lengthscale for the Tayler instability, $\ell_r = \frac{r\omega_{\rm A}}{N_{\rm eff}}$ and the Alfvén frequency $\omega_A = \frac{B^2}{\sqrt{4\pi\rho r^2}}$. Therefore, after the time $\tau_{\rm B}$ thermal losses have reduced the fluctuation by a factor

$$f = \frac{\tau_{\rm B}}{\tau_{\rm therm}} + 1 = \tau_{\rm B}\cdot\frac{KN_{\rm eff}^2}{r^2\omega_{\rm A}^2} + 1. \tag{B.67}$$

The growth rate of the Tayler instability is largest for $m = 1$ - see Section II.3.1.1 - and is approximately $\sigma_{\rm B} = \frac{\omega_{\rm A}^2}{\Omega}$ for $w_{\rm A} \ll \Omega$ - see Section II.3.1.1 - hence, $\tau_{\rm B} = \sigma_{\rm B}^{-1} = \frac{\Omega}{\omega_{\rm A}^2}$. This allows to compute the effective Brunt-Väisälä frequency as

$$N_{\rm eff}^2 = N_\mu^2 + N_{\rm T,eff}^2 = N_\mu^2 + \frac{N_{\rm T}^2}{1+\frac{K}{r^2}\frac{N_{\rm eff}^2\Omega}{\omega_{\rm A}^4}} \quad\Rightarrow\quad N_{\rm eff}^2 - N^2 + (N_{\rm eff}^2 - N_\mu^2)\cdot\frac{K}{r^2}\frac{N_{\rm eff}^2\Omega}{\omega_{\rm A}^4} = 0, \tag{B.68}$$

with the saturated Alfvén frequency $\omega_{\rm A} = \alpha\Omega\left(\frac{q\Omega}{N_{\rm eff}}\right)^{\frac{1}{3}}$ and the Brunt-Väisälä frequency $N^2 = N_\mu^2 + N_T^2$. Eq.(B.68) can be solved to obtain the appropriate value of $N_{\rm eff}$ given a stellar structure. In the limits of the thermal diffusivity, the two cases of Spruit (2002) are recovered: for $K \to 0$, $N_{\rm eff}^2 = N^2$, for $K \to \infty$, $N_{\rm eff}^2 = N_\mu^2$ and if $N_\mu^2 \to 0$ and thermal diffusion is large, $N_{\rm eff}^2 \ll N^2$. In practice, however, an analytical solution to Eq.(B.68) includes a difficult root finding problem to solve for $N_{\rm eff}$ due to the dependence of $\omega_{\rm A}$ on $N_{\rm eff}$. Fuller et al. (2019) avoided this problem by using the Tayler instability

timescale of a non-rotating star, $\tau_{\rm B} = \tau_{\rm A} = \omega_A^{-1}$, which neglects the coriolis force that reduces the growth rate of the instability[20] - see Section II.3.1.1 - and using N^2 instead of $N^2_{\rm eff}$ to calculate ${}^*\omega_{\rm A}$, where the asterisk indicates the use of N^2 in the following. In this approximation, the thermal part of the effective Brunt-Väisälä frequency is written as

$$N^2_{\rm T,eff} = \frac{N^2_T}{1 + \frac{K}{r^2}\frac{N^2}{{}^*\omega^3_{\rm A}}}. \tag{B.69}$$

While this leads to a less accurate $N^2_{\rm eff}$, in reality, they found that in their models they are always in the limit with $\frac{K}{r^2}\frac{N^2}{{}^*\omega^2_{\rm A}} \gg {}^*\omega_{\rm A}$, such that the thermal component N^2_T is totally suppressed and only the compositional component matters (Fuller, priv. comm., see also Fig.(2) in Fuller et al. (2019)).

Maeder & Meynet (2004) derive an alternative formula to compute the effective Brunt-Väisälä frequency,

$$N^2_{\rm eff} = N^2_\mu + \frac{\frac{\eta}{K}}{\frac{\eta}{K} + 2} \cdot N^2_{\rm T} \approx N^2_\mu + \frac{\eta}{K} \cdot N^2_{\rm T}, \tag{B.70}$$

where in the last step it was assumed that $\eta \ll K$. In the implementation of the Fuller-modified Tayler-Spruit dynamo, both versions of the effective Brunt-Väisälä frequency, Eqs.(B.69) and (B.70), are considered and the final $N^2_{\rm eff}$ is calculated as

$$N^2_{\rm eff} = N^2_\mu + (N^2 - N^2_\mu) \cdot \max\left\{ \frac{1}{1 + \frac{K}{r^2}\frac{N^2\Omega}{{}^*\omega^3_{\rm A}}}, \min\left[1, \frac{\eta}{K}\right] \right\}. \tag{B.71}$$

Once $N^2_{\rm eff}$ is determined, $\omega_{\rm A}$ is re-evaluated using the effective Brunt-Väisälä frequency.

The magnetic viscosity generated by the dynamo action is computed in regions with $N^2_{\rm eff} > 0$, similar to Eq.(II.66), as

$$\nu_{\rm AM,TSF} = \mathcal{F}\left(\tfrac{\alpha\omega_{\rm A}}{\omega_{\rm min}}\right) \cdot \alpha^3 r^2 \Omega \left(\frac{\Omega}{N_{\rm eff}}\right)^2, \tag{B.72}$$

where $\mathcal{F}$ is a function to suppress the angular momentum transport if the saturated Alfvén frequency drops below the minimal frequency, $\omega_{\rm min}$, for the Tayler instability to occur (see Eq.(II.46)),

$$\mathcal{F}(x) = \frac{1}{2} + \frac{1}{2}\tanh\left(5 \cdot \log_{10}\left[x\right]\right). \tag{B.73}$$

The magnetic torque provided by the Fuller-modified Tayler-Spruit dynamo (Eq.(II.65)) $\mathcal{S}_{\rm B} \to \infty$ as $N^2_{\rm eff} \to 0$, which can happen in regions near the convective boundaries for example. Consequently, the torque generates an infinitely strong magnetic coupling. To prevent this, the viscosity computed in Eq.(B.72) is only applied above a limit for $N^2_{\rm eff}$. Since the magnetic dynamo was derived assuming $\Omega^2 \ll N^2_{\rm eff}$, the implementation in Fuller et al. (2019) only uses Eq.(B.72), if $N^2_{\rm eff} > 2q^2_{\rm smooth}\Omega^2$.

[20] The dynamo action by Spruit (2002) was established under the assumption of fast rotation, i.e. $\Omega \gg \omega_{\rm A}$, where the growth rate of the magnetic field is reduced by the coriolis force. However, in case of very slowly rotating stars, i.e. $\Omega \ll \omega_{\rm A}$, the timescale of the instability becomes $\tau_{\rm B} = \tau_{\rm A} = \omega_A^{-1}$ (Maeder & Meynet, 2005, Appendix A).

This limit is arbitrary and a similar expression such as $N^2_{\rm eff} > \Omega^2$ could have been used (Fuller, priv. comm.). Nevertheless, the choice only affects the torque in regions where $N^2_{\rm eff}$ is very small and the star is nearly rigidly rotating there, regardless of the limit. In the case the effective Brunt-Väisälä frequency is below this limit, $2q^2_{\rm smooth}\Omega^2 > N^2_{\rm eff} > 0$, the magnetic viscosity is calculated as

$$\nu_{\rm AM,TSF} = \alpha \cdot q_{\rm smooth}\Omega r^2. \tag{B.74}$$

It should be noted that in the current implementation the Fuller-modified Tayler-Spruit dynamo is computed without considering the $q_{\rm min}$ condition (Eq.(II.68)). Consequently, the dynamo action is also activated even if the shear is not strong enough, i.e. $q < q_{\rm min}$. This is contrarily to the Tayler-Spruit dynamo, where the dynamo is only active when $q > q_{\rm min}$, and could lead to an overestimation of $\nu_{\rm TSF}$ and consequently the angular momentum transport - see Section IV.6.1.

Finally, the magnetic viscosity is added to the total viscosity of all sources,

$$\nu_\Omega = \nu_{\Omega,\rm hydro} + \nu_{\rm AM,TSF} + 10^{-1}. \tag{B.75}$$

The factor 10^{-1} is added by default for numerical reasons; if the viscosity were reduced to zero, very sharp shear layers would develop which potentially cause numerical problems. That being said, this value is very small and does not affect the results.

It should be noted that the factor α, which is introduced in Section II.3.1.3 to account for the pre-factors in the magnetic energy dissipation balance (see Eqs.(II.66)) and (II.67), is only included in the computation of $\nu_{\rm TSF}$. Otherwise, the proportionality given in the equations in Section II.3.1.3 is taken as equal, e.g., for the saturated Alfvén frequency. Therefore, studies that compare different values for α with this current implementation of the magnetic dynamo (as in Fuller et al., 2019; den Hartogh et al., 2020) do not fully take into account the pre-factors of the magnetic energy dissipation in all equations, e.g., in the shear and $\omega_{\rm A}$, and it is assumed $\alpha = 1$.

In the end, the implementation provided by Fuller et al. (2019) applies a smoothing routine. However, instead of smoothing $\nu_{\rm TSF}$ the routine is applied to the total viscosity ν_Ω in Eq.(B.75). The "*other hook*" for angular momentum transport, in which this dynamo action is implemented, is called after all the other angular momentum transport discussed above, rotating and non-rotating, has been computed. Therefore, ν_Ω already contains the values for these mixing processes. Consequently, smoothing $\nu_{\Omega,\rm rot}$ instead of $\nu_{\rm TSF}$ not only smooths the transport of angular momentum by the magnetic torque but also the transport by all the other mechanisms. The smoothed rotation-induced processes can transport different amounts of angular momentum compared to the unsmoothed processes - see

also Section IV.3. The viscosity for cell k is smoothed as

$$\nu_{\Omega,\mathrm{smooth}}(k) = 10^x \quad \text{with} \quad x = \frac{1}{2n+1} \sum_{i=k-n}^{k+n} \log_{10}\left(\nu_\Omega(i)\right), \tag{B.76}$$

where again n is an integer that controls the number of adjacent cells to be included in the smoothing process and is hard-coded to be 5. The viscosity is not smoothed, if k is either a convective cell or if one of the $2n$ neighbouring cells is radiative[21], convective, semiconvective or a convective boundary region. In the implementation the viscosity in each cell is first divided by 5, except in convective cells, before they are added together following Eq.(B.76). The implementation of this separation into different regions is physically necessary, for example to not smooth the convective diffusivity into the radiative region, but it can lead to unexpected features as is discussed in Section IV.3.
As discussed in Section II.3.1.3, chemical mixing by the magnetic dynamo is negligible and is therefore excluded in this implementation.

2.2 Variant of the Mixing-Length Theory

The mixing-length theory - discussed in Sections II.1.2 and B.1.3.1 - predicts radial turbulent velocity and mixing profiles which are roughly constant throughout the convective zone. On the contrary, 3D hydrodynamic simulations show that these profiles have an "*n-shape*" (see e.g. Jones et al., 2017, their Fig.(21)), i.e. a faster radial velocity is predicted in the bulk of the convective region which slows down as the boundary is approached. Jones et al. (2017) analysed the mixing from their 3D hydrodynamic simulations in a 1D diffusive framework and provide a modified diffusion coefficient for the convective and the boundary region, which mimics the spherically averaged radial diffusion and velocity profiles from their 3D simulation. The best match is obtained in the following way. First, the diffusion coefficient is calculated as

$$D(r) = v_{\mathrm{MLT}} \times \min(\alpha_{\mathrm{MLT}} \cdot H_P, |r - r_{\mathrm{CB}}|), \tag{B.77}$$

where r_{CB} is the radius of the convective boundary as determined by the Ledoux or Schwarzschild criterion and v_{MLT} is the convective velocity estimated from MLT. This form limits the mixing near the boundary by limiting the mixing length with the distance from the convective boundary as suggested by Eggleton (1972). Second, the diffusion coefficient computed with the mixing-length theory, $D_{\mathrm{MLT}} = \frac{1}{3} v_{\mathrm{MLT}} \alpha_{\mathrm{MLT}} \cdot H_P$, is multiplied by a factor of 3, increasing the mixing and the convective velocity, v_{conv}, in the bulk of the convective zone. Third, the exponential decaying diffusive boundary mixing scheme has to be used (see Eq.(II.17)) and the two free parameters are set equal, $f_{\mathrm{CBM}} = f_0$. Jones

[21] i.e no rotation

et al. (2017) find the best fit to their oxygen burning shell simulations with $f_{\rm CBM} = f_0 = 0.03$.

3 Inlists

At the start of each run, MESA reads a file called *inlist*. The *inlist* contains controls to set up the numerical models such as options on how to evolve the star and initial conditions[22]. The inlists used for the stellar models in this work are all publicly available on the MESA marketplace:http://cococubed.asu.edu/mesa_market/inlists.html.

4 MESA Code Extensions

In the framework of this Thesis, I made use of MESA's hooks, i.e. including user-specified code, several times. The code alterations in Section B.2 are two examples that introduce new physics into the source code. In addition to new physics I also made use of the extensions to generate an artificial viscosity or modify the output, for example to generate additional output files when a specific condition is met or to provide the energy generation of a certain reaction. All these MESA Code Extensions can be found on my GitHub: hrefhttps://github.com/eddylegrand/MESA_run_star_extrashttps://github.com/eddylegrand/MESA_run_star_extras

[22] A full list is given on the MESA source page, for the star_job (http://mesa.sourceforge.net/star_job_defaults.html and the controls http://mesa.sourceforge.net/controls_defaults.html).

Appendix C

Numerics & Derivations

1 Weighted Smoothing

The weighted smoothing algorithm calculates the weighted average of the n neighbouring cells, where the original cell k received the maximum weight,

$$x_{\text{smooth}}(k) = \frac{\sum_{i=k-n}^{k+n} x_i * \text{weight(i)}}{\sum_{i=k-n}^{k+n} \text{weight(i)}}. \tag{C.1}$$

In `MESA` , the weight(i) is based on the binomial coefficients of Pascal's triangle. The rows in this triangle are numbered with n, starting with $n = 0$ at the top. Each row consists of m entries with $m = n + 1$. The first entry is one. Each subsequent row entry is constructed by adding the two numbers above, treating blank entries as zero,

$$\binom{n}{m} = \binom{n-1}{m-1} + \binom{n-1}{m}. \tag{C.2}$$

The first seven entries of Pascal's triangle are shown below.

$n = 0$: 1

$n = 1$: 1 1

$n = 2$: 1 2 1

$n = 3$: 1 3 3 1

$n = 4$: 1 4 6 4 1

$n = 5$: 1 5 10 10 5 1

$n = 6$: 1 6 15 20 15 6 1

$n = 7$: 1 7 21 35 35 21 7 1

2 MLT++: Calculation of $\widetilde{\alpha_\nabla}$

$\widetilde{\alpha_\nabla}$ is the parameter to reduce the superadiabaticity encountered during density and gas pressure inversions - see Section B.1.3.4. In the following, it is shown, how $\widetilde{\alpha_\nabla}$ is calculated as a function of $\lambda_{\max}$ and $\beta_{\min}$. `MESA` includes six user-chosen parameters to separate the $\lambda_{\max}$-$\beta_{\min}$ plane into different subsections, λ_1, λ_2, $\Delta\lambda$, β_1, β_2 and $\Delta\beta$ (see Table B.2), in order to determine the severity of the gas pressure and density inversion and compute $\widetilde{\alpha_\nabla}\left(\lambda_{\max}, \beta_{\min}\right)$ accordingly:

$$\widetilde{\alpha_\nabla} = \begin{cases} 1 & \text{if } \lambda_1 < 0 \\ & \\ & \text{if } \lambda_1 \leq \lambda_{\max}: \begin{cases} 1 & \text{if } \beta_{\min} \leq \beta_1 \\ \frac{\beta_1 + \Delta\beta - \beta_{\min}}{\Delta\beta} & \text{if } \beta_{\min} < \beta_1 + \Delta\beta \\ 0 & \text{if } \beta_1 + \Delta\beta \leq \beta_{\min} \end{cases} \\ & \\ & \text{if } \lambda_2 \leq \lambda_{\max}: \begin{cases} 1 & \text{if } \beta_{\min} \leq \beta_{\lim} \\ \frac{\beta_{\lim} + \Delta\beta - \beta_{\min}}{\Delta\beta} & \text{if } \beta_{\min} < \beta_{\lim} + \Delta\beta \\ 0 & \text{if } \beta_{\lim} + \Delta\beta \leq \beta_{\min} \end{cases} \\ & \\ & \text{if } \lambda_2 - \Delta\lambda < \lambda_{\max}: \begin{cases} 1 & \text{if } \beta_{\min} \leq \beta_2 \\ \frac{\lambda_{\max} - (\lambda_2 - \Delta\lambda)}{\Delta\lambda} & \text{if } \beta_{\min} < \beta_2 + \Delta\beta \\ 0 & \text{if } \beta_2 1\Delta\beta \leq \beta_{\min} \end{cases} \\ & \\ 0 & \text{if } \lambda_{\max} \leq \lambda_2 - \Delta\lambda \end{cases} \tag{C.3}$$

$\beta_{\lim}$ is a blend $\beta_{\lim} \equiv \beta_2 + \frac{(\lambda_{\max} - \lambda_2)(\beta_1 - \beta_2)}{\lambda_1 - \lambda_2}$. The code runs through a number of `if-else` statements, following the structure of Eq.(C.3), starting from top to bottom.

3 Derivations

In this section some of the formulae used in this work are derived from basic principles.

3.1 Diffusion Equation

Imagine particles of species i in presence of an abundance gradient along the radial direction and the other quantities constant in space. Particles i with mass fraction X_i and thermal velocity $v_{\mathrm{T,i}}$ can move a distance δr along the abundance gradient and enter or leave a sphere at coordinate r. This

results in an average flux of particles i

$$j_i^{\pm} = \frac{1}{6}\, v_{\mathrm{T,i}}(r \mp \delta r)\, X_i(r \mp \delta r) = -\frac{1}{6}\frac{\partial}{\partial r}(v_{\mathrm{T,i}} X_i)\delta r, \tag{C.4}$$

where the factor $\frac{1}{6}$ is the probability of the particles i at $r \mp \delta r$ with random motion to move towards the surface of the sphere. The + and − sign indicate particles i entering or leaving, respectively, which results in a total flux $j_i = j_i^+ + j_i^-$. The flux of particles i can also be expressed with the average diffusion velocity v_i,

$$j_i = \rho X_i v_i. \tag{C.5}$$

Eqs. (C.4) and (C.5) give the general expression of the diffusion velocity v_i. Since the diffusion is assumed to be a result of an abundance gradient the radial derivation of the thermal velocity can be neglected. Therefore the diffusion velocity of particles i can be expressed as

$$v_i = -\frac{D_i}{X_i}\frac{\partial}{\partial r} X_i, \tag{C.6}$$

with the diffusion coefficient $D_i = \frac{1}{3}\ell_i v_{\mathrm{T,i}}$. The minus sign indicates that the movement is in the opposite direction of the concentration gradient. Eq. (C.6) can similarly be derived for a turbulent medium, when appropriate expressions for v_{T} and ℓ are used.

The number of particles, $n_i = \rho X_i$, is conserved, hence, with the continuity equation and spherical symmetry

$$\frac{\partial}{\partial t}(\rho X_i) = -\frac{1}{r^2}\frac{\partial}{\partial r}(r^2 \rho X_i v_i) = \frac{1}{r^2}\frac{\partial}{\partial r}(r^2 \rho D_i \frac{\partial}{\partial r} X_i). \tag{C.7}$$

In the last step Eq. (C.6) is used. This equation can further be simplified by taking the sum over all particle species on both sides. The left hand side simplifies to

$$\sum_i \frac{\partial}{\partial t}(\rho X_i) = \frac{\partial}{\partial t}(\rho \sum_i X_i) = \frac{\partial}{\partial t}\rho. \tag{C.8}$$

The right hand side gives, using the fact that the total mass fraction is of unity ($\sum_i X_i = 1$),

$$\sum_i \frac{1}{r^2}\frac{\partial}{\partial r}(r^2 \rho D_i \frac{\partial}{\partial r} X_i) = \frac{1}{r^2}\frac{\partial}{\partial r}(r^2 \rho D_i \frac{\partial}{\partial r} \sum_i X_i) = 0. \tag{C.9}$$

Combining the left and right hand side results in

$$\frac{\partial}{\partial t}\rho = 0 \tag{C.10}$$

and Eq. (C.7) can be written in the form

$$\rho\frac{\partial}{\partial t}X_i = \frac{1}{r^2}\frac{\partial}{\partial r}(r^2\rho D_i\frac{\partial}{\partial r}X_i), \tag{C.11}$$

at a Lagrangian mass coordinate M_r. This is the diffusion equation in spherical symmetry as it is assumed in 1D stellar evolution. The diffusion equation can be written more generally,

$$\rho\frac{\partial}{\partial t}X_i = \nabla\cdot(\rho D\nabla X_i), \tag{C.12}$$

with an appropriate diffusion coefficient in any direction. In the case of a general fluid motion with velocity $\mathbf{u}$ the more general diffusion equation is written as (Landau & Lifschitz, 1966)

$$\rho\frac{d}{dt}X_i = \rho\frac{\partial}{\partial t}X_i + \rho\mathbf{u}\cdot\nabla X_i = \nabla\cdot(\rho D\nabla X_i). \tag{C.13}$$

The second term in the middle part is an advective term due to the motion of the fluid.

3.2 Angular Momentum Transport Equation

The torque $\mathcal{M}$ exerted by a force

$$\mathbf{F} = \frac{d}{dt}(m\mathbf{v}), \tag{C.14}$$

with the mass m and the velocity $\mathbf{v}$, about a fixed point $\mathbf{s}$ is

$$\mathcal{M} = \mathbf{s}\times\mathbf{F} = \mathbf{s}\times\frac{d}{dt}(m\mathbf{v}), \tag{C.15}$$

where $\times$ marks the cross-product of two vectors and $\frac{d}{dt}$ the Lagrangian time derivative. The angular momentum $\mathcal{L}$ of a point at $\mathbf{s}$ with respect to the centre on which the force $\mathbf{F}$ is applied is

$$\mathcal{L} = \mathbf{s}\times m\mathbf{v}. \tag{C.16}$$

The absolute time derivative of $\mathcal{L}$ is

$$\frac{d}{dt}\mathcal{L} = \frac{d}{dt}(\mathbf{s}\times m\mathbf{v}) = \frac{d}{dt}\mathbf{s}\times m\mathbf{v} + \mathbf{s}\times\frac{d}{dt}(m\mathbf{v}) = m\underbrace{(\mathbf{v}\times\mathbf{v})}_{=0} + \mathbf{s}\times\frac{d}{dt}(m\mathbf{v}) = \mathbf{s}\times\frac{d}{dt}(m\mathbf{v}), \tag{C.17}$$

thus, with Eq. (C.15),

$$\mathcal{M} = \frac{d}{dt}\mathcal{L}. \tag{C.18}$$

In spherical coordinates ($\hat{\mathbf{e}}_r$, $\hat{\mathbf{e}}_\theta$, $\hat{\mathbf{e}}_\varphi$), the distance $\mathbf{s}$ can be expressed as $\mathbf{s} = \mathbf{r}\sin(\theta)$. This allows to rewrite the time derivative of the angular momentum as

$$\frac{d}{dt}\mathcal{L} = m\frac{d}{dt}\left(\mathbf{s}\times\mathbf{v}\right) = m\frac{d}{dt}\left(s^2\mathbf{\Omega}\right) = m\frac{d}{dt}\left(r^2\sin^2(\theta)\mathbf{\Omega}\right), \tag{C.19}$$

where in the second step $s^2\mathbf{\Omega} = \mathbf{s}\times\mathbf{v}$ with the angular velocity $\mathbf{\Omega}$ was used.
The angular momentum of a volume element $dm = \rho\cdot dV$ is

$$d\mathcal{L} = \rho r^2\sin^2(\theta)\mathbf{\Omega}\cdot dV = \rho r^2\sin^2(\theta)\mathbf{\Omega}\cdot r^2\sin(\theta)d\theta d\varphi dr. \tag{C.20}$$

With Eq. (C.19) the time derivative of the angular momentum in Lagrangian coordinates becomes[1]

$$\rho\frac{d}{dt}\left(\mathcal{L}\right) = \rho\frac{d}{dt}\left(r^2\sin^2(\theta)\mathbf{\Omega}\right)_{M_r}\cdot r^2\sin(\theta)d\theta d\varphi dr, \tag{C.21}$$

where the subscript M_r is used to indicate a derivative in Lagrangian coordinates. The time derivative can be rewritten

$$\begin{aligned}\rho\frac{d}{dt}\left(r^2\sin^2(\theta)\mathbf{\Omega}\right)_{M_r} &= \frac{d}{dt}\left(\rho r^2\sin^2(\theta)\mathbf{\Omega}\right)_{M_r} - r^2\sin^2(\theta)\mathbf{\Omega}\frac{d}{dt}\left(\rho\right)_{M_r}\\ &= \frac{\partial}{\partial t}\left(\rho r^2\sin^2(\theta)\mathbf{\Omega}\right)_r + \mathbf{u}\nabla\cdot\left(\rho r^2\sin^2(\theta)\mathbf{\Omega}\right) - r^2\sin^2(\theta)\mathbf{\Omega}\frac{\partial}{\partial t}\left(\rho\right)_r - r^2\sin^2(\theta)\mathbf{\Omega}\cdot\mathbf{u}\cdot\nabla\rho,\end{aligned} \tag{C.22}$$

where the subscript r indicates a derivative in Eulerian coordinates and $\mathbf{u}$ is the speed of the co-moving system. Using the continuity equation,

$$\frac{\partial}{\partial t}\rho = -\nabla\cdot\left(\mathbf{u}\rho\right) \tag{C.23}$$

one can write

$$-\frac{\partial}{\partial t}\rho - \mathbf{u}\cdot\nabla\rho = \nabla\cdot\left(\mathbf{u}\rho\right) - \mathbf{u}\cdot\nabla\rho = \rho\nabla\cdot\mathbf{u}. \tag{C.24}$$

With this, Eq. (C.22) can be further simplified,

$$\begin{aligned}\rho\frac{d}{dt}\left(r^2\sin^2(\theta)\mathbf{\Omega}\right)_{M_r} &= \frac{\partial}{\partial t}\left(\rho r^2\sin^2(\theta)\mathbf{\Omega}\right)_r + \mathbf{u}\nabla\cdot\left(\rho r^2\sin^2(\theta)\mathbf{\Omega}\right) + \rho r^2\sin^2(\theta)\mathbf{\Omega}\nabla\mathbf{u}\\ &= \frac{\partial}{\partial t}\left(\rho r^2\sin^2(\theta)\mathbf{\Omega}\right)_r + \nabla\left(\rho r^2\sin^2(\theta)\mathbf{\Omega}\cdot\mathbf{u}\right)\end{aligned} \tag{C.25}$$

This expresses the temporal changes of angular momentum of a volume element in an Eulerian coordinate system. Eq. (C.15) indicates that the angular momentum only changes if there is a torque (see

[1] The volume can be considered continuous and steady. Therefore $\frac{d}{dt}\cdot\int(x) = \int\cdot\frac{d}{dt}(x)$.

Section II.3 for an example of a torque in a star).

In order to find the shear stress, the shear tensor has to be considered. The Navier-Stokes equation for incompressible fluids in tensor notation is

$$\rho\left(\frac{\partial v_i}{\partial t}+v_k\frac{\partial v_i}{\partial x_k}\right)=-\frac{\partial p}{\partial x_i}+\eta\frac{\partial^2 v_i}{\partial x_k^2} \tag{C.26}$$

with the shear tensor

$$\sigma_{ik}=-p\delta_{ik}+\eta\left(\frac{\partial v_i}{\partial x_k}+\frac{\partial v_k}{\partial x_i}\right). \tag{C.27}$$

δ_{ik} is the Kronecker symbol and η the dynamic viscosity.[2] . It was assumed that the velocity gradients are small (linearity of the derivations $\frac{\partial v_i}{\partial x_k}$) and that $\eta \cong$ const.

The tensor notation in Eq. (C.27) only holds in Cartesian coordinates and has therefore to be transformed into spherical coordinates (Landau & Lifschitz, 1966, Eq. (15.17)). In the context of a differentially rotating star we are interested in the vertical and tangential shear, hence we need the $\sigma_{r\varphi}$ and the $\sigma_{r\theta}$ component respectively. In spherical coordinates the vertical shear tensor component is written as

$$\sigma_{r\varphi}=\eta r\frac{\partial}{\partial r}\left(\frac{v_\varphi}{r}\right)+\eta\frac{1}{r\sin(\theta)}\frac{\partial v_r}{\partial\varphi}=\eta\left(\frac{\partial v_\varphi}{\partial r}-\frac{v_\varphi}{r}+\frac{1}{r\sin(\theta)}\frac{\partial v_r}{\partial\varphi}\right). \tag{C.28}$$

By using the identity $s^2|\mathbf{\Omega}|=|\mathbf{s}\times\mathbf{v}|$ and the fact that $\mathbf{v}=v\,\hat{\mathbf{e}}_\varphi$, Eq. (C.28) can be written as

$$\begin{aligned}\sigma_{r\varphi}&=\eta\left(\frac{\partial v_\varphi}{\partial r}-\frac{v_\varphi}{r}\right)=\eta\left(r\sin(\theta)\frac{\partial\Omega_\varphi}{\partial r}+\Omega_\varphi\frac{\partial r\sin(\theta)}{\partial r}-\frac{\Omega_\varphi r\sin(\theta)}{r}\right)\\&=\eta\left(r\sin(\theta)\frac{\partial\Omega_\varphi}{\partial r}+\Omega_\varphi\sin(\theta)-\Omega_\varphi\sin(\theta)\right)=\eta r\sin(\theta)\frac{\partial\Omega_\varphi}{\partial r}\end{aligned} \tag{C.29}$$

Similarly, the tangential shear tensor component is written as

$$\sigma_{r\theta}=\eta r\frac{\partial}{\partial r}\left(\frac{v_\theta}{r}\right)+\eta\frac{1}{r}\frac{\partial v_r}{\partial\theta}=\eta\left(\frac{\partial v_\theta}{\partial r}-\frac{v_\theta}{r}+\frac{1}{r}\frac{\partial v_r}{\partial\theta}\right)=\eta r\sin(\theta)\frac{\partial\Omega_\theta}{\partial r} \tag{C.30}$$

The force acting on a surface element $d\mathbf{f}=df\,\mathbf{n}$, where $\mathbf{n}$ is a unit vector along the surface's normal, is equal to the momentum flux through this element:

$$F_i=\Pi_{ik}d\mathbf{f}=\left(\rho v_i v_j-\sigma_{ij}\right)d\mathbf{f} \tag{C.31}$$

[2]The dynamic viscosity μ is the measurement of the fluid's internal resistance to flow while the kinematic viscosity ν refers to the ratio of dynamic viscosity to density. Simply put, μ gives information of the force needed to make the fluid flow at a certain rate, while ν states how fast the fluid is moving when a certain force is applied (Landau & Lifschitz, 1966, p.55).

In determining the force on a surface element, each surface element has to be considered in a frame where it is at rest (Landau & Lifschitz, 1966). Thus, the force per unit area acting on the surface element is

$$P_i = \sigma_{ij} n_i \tag{C.32}$$

This gives a force per unity surface (Maeder, 2009)

$$d\mathbf{F} = d\mathbf{A}\ \tau(\mathbf{u}) = d\mathbf{A}\nu\nabla\cdot\mathbf{v}. \tag{C.33}$$

The change of force of a volume element over a distance $d\ell = (dr, rd\theta, r\sin(\theta)d\varphi)$ is

$$d\mathcal{M} \equiv \nabla\cdot d\mathbf{F}d\ell = \left(\frac{\partial}{\partial r}dF_r + \frac{\partial}{r\partial\theta}dF_\theta + \frac{\partial}{r\sin(\theta)\partial\varphi}dF_\varphi\right)d\ell \equiv \nabla\cdot\left(d\mathbf{A}\nu\nabla\cdot\mathbf{v}\right)d\ell. \tag{C.34}$$

Therefore, combining Eqs. (C.18), (C.18), (C.21) and (C.34), an equation for the change of angular momentum is recovered,

$$\begin{aligned}\rho\frac{d}{dt}\left(r^2\sin^2(\theta)\mathbf{\Omega}\right)_{M_r}\cdot r^2\sin(\theta)d\theta d\varphi dr &= \nabla\cdot\left(d\mathbf{A}\nu\nabla\cdot\mathbf{v}\right)d\ell \\ &= \frac{1}{r^2}\frac{\partial}{\partial r}\left(r^2\sin(\theta)d\theta d\varphi\nu\frac{1}{r^2}\frac{\partial}{\partial r}v_r\right)dr\cdot\hat{e}_r + \frac{1}{r\sin(\theta)}\frac{\partial}{\partial\theta}\left(r\sin(\theta)drd\varphi\cdot\nu\frac{1}{r\sin(\theta)}\frac{\partial}{\partial\theta}v_\theta\right)\cdot rd\theta\cdot\hat{e}_\theta,\end{aligned} \tag{C.35}$$

where symmetry in $\hat{e}_\varphi$ was assumed. This can be simplified to

$$\rho\frac{d}{dt}\left(r^2\sin^2(\theta)\mathbf{\Omega}\right)_{M_r}\cdot r^2\sin(\theta) = \frac{1}{r^2}\frac{\partial}{\partial r}\left(\sin(\theta)\nu\frac{\partial}{\partial r}\cdot u_r\right)\cdot\hat{e}_r + \frac{1}{r\sin(\theta)}\frac{\partial}{\partial\theta}\left(\nu\frac{\partial}{\partial\theta}\cdot u_\theta\right)\cdot\hat{e}_\theta. \tag{C.36}$$

In the literature, there exist different descriptions and formulation for angular momentum transport. If in Eq. C.36 only the radial transport is considered one can further simplify,

$$\frac{d}{dt}\left(r^2\sin^2(\theta)\mathbf{\Omega}\right)_{M_r} = \frac{1}{\rho r^4\sin(\theta)}\frac{\partial}{\partial r}\left(\sin(\theta)\nu\frac{\partial}{\partial r}\cdot u_r\right)\cdot\hat{e}_r = \frac{1}{\rho r^4}\frac{\partial}{\partial r}\left(\nu\frac{\partial}{\partial r}u_r\right)\cdot\hat{e}_r. \tag{C.37}$$

When using the transformation (Eq. (1.7) from Kippenhahn & Weigert (1993))

$$\frac{\partial}{\partial r} = 4\pi r^2\rho\frac{\partial}{\partial m}, \tag{C.38}$$

it follows that

$$\frac{d}{dt}\left(r^2\sin^2(\theta)\mathbf{\Omega}\right)_{M_r} = \frac{d}{dt}(r^2\sin^2(\theta))_{M_r}\Omega + r^2\sin^2(\theta)\frac{d}{dt}(\Omega)_{M_r} = \frac{4\pi r^2\rho}{\rho r^4}\frac{\partial}{\partial m}\left(4\pi r^2\rho\nu\frac{\partial}{\partial m}u_r\right). \tag{C.39}$$

This can be rewritten as

$$\left.\frac{d\Omega}{dt}\right|_{M_r} = \frac{1}{r^4 \sin^2(\theta)} \frac{\partial}{\partial m} \left((4\pi)^2 r^2 \rho \nu \frac{\partial}{\partial m} u_r \right) - \frac{\Omega}{r^2 \sin^2(\theta)} \frac{d}{dt} (r^2 \sin^2(\theta))_{M_r}. \tag{C.40}$$